Modélisation des transferts de chaleur et masse pour des gouttes de carburant multi-composants

Artur Carvalho Santos

université
PARIS-SACLAY

On the modelling of heat and mass transfer for multi-component droplets

Modélisation des transferts de chaleur et masse pour des gouttes de carburant multi-composants

Thèse de doctorat de l'université Paris-Saclay

École doctorale n° 579, Sciences mécaniques et énergétiques, matériaux et géosciences (SMEMaG)
Spécialité de doctorat: Combustion
Graduate School: Sciences de l'ingénierie et des systèmes
Référent: CentraleSupélec

Thèse préparée dans l'unité de recherche Laboratoire EM2C (Université Paris-Saclay, CNRS, CentraleSupélec), sous la direction de Aymeric VIÉ, Maître de conférence.

Thèse soutenue à Gif-Sur-Yvette, le 2 décembre 2022, par

Artur CARVALHO SANTOS

Composition du jury

Membres du jury avec voix délibérative

Bénédicte CUENOT Chercheur Senior, CERFACS	Présidente & Rapporteur
Sergei SAZHIN Professeur, University of Brighton	Rapporteur & Examinateur
Christophe DUWIG Professeur, KTH Royal Institute of Technology	Examinateur
Chaouki HABCHI Docteur - HDR, IFP Energies nouvelles	Examinateur
Fernando Luiz SACOMANO FILHO Maître de conférences, Universidade de Sao Paulo	Examinateur

THESE DE DOCTORAT
NNT : 2022UPAST157

université PARIS-SACLAY

ÉCOLE DOCTORALE
Sciences mécaniques et énergétiques, matériaux et géosciences (SMEMAG)

Titre : Modélisation des transferts de chaleur et masse pour des gouttes de carburant multi-composants
Mots clés : Combustion multiphasique ; Gouttes ; Transition de phases ; Evaporation ; Biocarburants

Résumé : Les outils de simulation numérique en mécanique des fluides sont des outils importants pour la conception de chambres de combustion. Pour pouvoir prendre en compte une vaste gamme de phénomènes physiques y compris la turbulence, par exemple la combustion et l'injection de carburant liquide, des modèles ont été proposés. Si on se concentrent sur l'injection liquide, l'objectif est d'atomiser le carburant liquide le plus rapidement possible de sorte à générer un spray, c'est-à-dire un ensemble de gouttelettes qui se vaporiseront pour finalement alimenter la combustion. L'étape de vaporisation s'avère ainsi très importante pour la chaîne de simulation, étant donné qu'elle déterminera la disponibilité de carburant pour la combustion. Pour modéliser la vaporisation, des modèles bas-ordre ont été développés par la littérature, parmi lesquels le plus célèbre est celui de Abramzon et Sirignano (1989), fréquemment employé dans la communauté de combustion. Ce modèle à carburant mono-composant a été validé contre plusieurs études expérimentales, mais plusieurs éléments peuvent toujours être améliorés avec la littérature contemporaine. De plus, avec l'utilisation des biocarburants en tant que solution pour la combustion décarbonisée, il existe une grande demande pour la caractérisation précise de leur combustion, étant donné que leur composition varie par rapport aux carburants conventionnels. Ainsi, des modèles d'évaporation pour des carburants multi-composants sont requis. En revanche, il n'y a toujours pas de consensus pour une meilleure stratégie dans ce scénario multi-composant. Un premier objectif est ainsi de comprendre les stratégies existantes, en soulignant des potentielles faiblesses pour pouvoir proposer des améliorations. Pour y arriver, les différentes étapes de dérivation pour des modèles d'évaporation sont présentées. Les hypothèses simplificatrices fondamentales sont établies, conduisant à des expressions élémentaires qui posent ainsi une base théorique. Ensuite, les fermetures requises pour la diffusion massique et l'équilibre vapeur-liquide sont développées. Cette première partie vise à rassembler tous les modules principaux qui conduisent à la construction de modèles de changement de phase pour des gouttes, et le cadre qui s'en produit sera utilisé pour la dérivation de tous les modèles contenus dans ce manuscrit. Une deuxième partie est consacrée aux modèles mono-composant. Les contributions historiques sont établies et dérivées, avec les corrections pour prendre en compte l'écoulement de Stefan. Par la suite, l'incorporation des effets convectifs est étudiée avec l'emploi de la théorie de couche limite et le modèle d'Abramzon-Sirignano (A-S) en suit. Une recherche numérique est ensuite menée en utilisant le modèle A-S en variant les corrélations spécifiques aux effets convectifs. Une perspective est ainsi offerte pour les déviations parmi des corrélations fréquemment utilisées. La principale composante de ce travail est finalement la modélisation multi-composant, en se concentrant sur les modèles à composants discrets. Un modèle qui servira de référence basée sur la résolution des équations de Stefan-Maxwell est développé, couplé avec une nouvelle formulation pour l'énergie indépendante de la fermeture de diffusion massique. Ensuite, les principaux modèles multi-composant de la littérature sont présentés, avec des propositions pour leur extension contemplant des situations plus générales de changement de phase. Une étude complète est aussi menée pour la caractérisation des coefficients de diffusion. Tous les modèles étendus sont ainsi comparés dans des cas représentatifs pour des applications de combustion, afin de montrer leurs avantages et faiblesses et ainsi ouvrir des nouvelles perspectives pour la modélisation de changement de phase pour des gouttes multi-composant.

Title : On the modelling of heat and mass transfer for multi-component droplets
Keywords : Multiphase combustion ; Droplets ; Phase-change ; Evaporation ; Biofuels

Abstract : Currently, Computational Fluid Dynamics (CFD) solvers are among the most important tools to help design combustion chambers. To account for a wide range of physical phenomena including turbulence, combustion and liquid fuel injection for instance, modelling approaches have been proposed in the literature. Focusing on this last element, the objective is to atomize the liquid fuel as fast as possible to generate a spray, i.e. a collection of small droplets, which will vaporize and thus feed the combustion. The vaporization step is very important for the simulation chain, as it will determine the fuel availability for combustion. To model vaporization, low-dimensional models have been proposed in the literature. Among them, the most famous is the one of Abramzon and Sirignano (1989), widely used within the combustion community. This single-component model has been validated against many experiments, but still many elements can be improved with today's literature. Furthermore, due to the rise of biofuels as a solution for decarbonated combustion, there is a strong demand on the precise characterization of their combustion, for which the composition varies from conventional fuels. In this way, multi-component evaporation models are required. Unfortunately, there is still no consensus for best strategies in this multi-component scenario. The objective is thus to survey the existing strategies, highlighting possible weaknesses while proposing new improvements. To achieve this goal, the different derivation steps of evaporation models are first presented. Core simplifying hypotheses are stated, and baseline expressions are obtained to form a theoretical basis. Then, required closures are listed for mass diffusion and the vapor-liquid equilibrium. The goal of the first part is to summarize the building blocks for the construction of droplet models, and the resulting framework is used to derive all droplet phase-change models of this manuscript. The second part is devoted to single-component models. Historical contributions are stated and derived, with corrections to take Stefan flow effects into account detailed. Then, the incorporation of convective effects is studied through the use of boundary layer theory and the Abramzon-Sirignano (A-S) model is thus derived. To account for convective effects, a literature review is presented for correlations of drag coefficients and Nusselt/Sherwood numbers. A numerical investigation is then carried out using the A-S model by varying correlations specific to convection. An outlook is thus provided for deviations of results within up-to-date correlations, encouraging new developments and validation strategies. Finally, the third part tackles the multi-component modelling, focusing on discrete component models. We start by developing a model based on the Stefan-Maxwell equations, which serve as a reference, with the addition of an uncoupled, novel energy formulation that does not depend on the mass diffusion closure. Then, the main multi-component models of the literature are presented and are extended to account for all phase-change scenarios with no limitations in number of species. A thorough study for the characterization of diffusion coefficients is performed, highlighting that the most accurate strategy is the Wilke's rule. Finally, all extended models are compared in various cases relevant for combustion applications, showing their forces and weaknesses and thus opening new perspectives for multi-component droplet phase-change modelling.

Abstract

Currently, Computational Fluid Dynamics (CFD) solvers are among the most important tools to help design combustion chambers. To account for a wide range of physical phenomena including turbulence, combustion and liquid fuel injection for instance, modelling approaches have been proposed in the literature. Focusing on this last element, the objective is to atomize the liquid fuel as fast as possible to generate a spray, i.e. a collection of small droplets, which will vaporize and thus feed the combustion. The vaporization step is very important for the simulation chain, as it will determine the fuel availability for combustion.
To model vaporization, low-dimensional models have been proposed in the literature. Among them, the most famous is the one of Abramzon and Sirignano (1989), widely used within the combustion community. This single-component model has been validated against many experiments, but still many elements can be improved with today's literature. Furthermore, due to the rise of biofuels as a solution for decarbonated combustion, there is a strong demand on the precise characterization of their combustion, for which the composition varies from conventional fuels. In this way, multi-component evaporation models are required. Unfortunately, there is still no consensus for best strategies in this multi-component scenario. The objective is thus to survey the existing strategies, highlighting possible weaknesses while proposing new improvements.
To achieve this goal, the different derivation steps of evaporation models are first presented. Core simplifying hypotheses are stated, and baseline expressions are obtained to form a theoretical basis. Then, required closures are listed for mass diffusion and the vapor-liquid equilibrium. The goal of the first part is to summarize the building blocks for the construction of droplet models, and the resulting framework is used to derive all droplet phase-change models of this manuscript.
The second part is devoted to single-component models. Historical contributions are stated and derived, with corrections to take Stefan flow effects into account detailed. Then, the incorporation of convective effects is studied through the use of boundary layer theory and the Abramzon-Sirignano (A-S) model is thus derived. To account for convective effects, a literature review is presented for correlations of drag coefficients and Nusselt/Sherwood numbers. A numerical investigation is then carried out using the A-S model by varying correlations specific to convection. An outlook is thus provided for deviations of results within up-to-date correlations, encouraging new developments and validation strategies.
Finally, the third part tackles the multi-component modelling, focusing on discrete component models. We start by developing a model based on the Stefan-Maxwell equations, which serve as a reference, with the addition of an uncoupled, novel energy formulation that does not depend on the mass diffusion closure. Then, the main multi-component models of the literature are presented and are extended to account for all phase-change scenarios with no limitations in number of species. A thorough study for the characterization of diffusion coefficients is performed, highlighting that the most accurate strategy is the Wilke's rule. Finally, all extended models are compared in various cases relevant for combustion applications, highlighting their particular contributions and thus opening new perspectives for multi-component droplet phase-change modelling.

Synthèse en français

Introduction

Aujourd'hui, de plus en plus l'impact négatif de la surdépendance sur la combustion sont soulignés par la communauté scientifique. Ainsi, le pourcentage des applications qui s'utilisent de la combustion voient leur décroissance progréssive, comme montre les rapports annuels diffusés par la International Energy Agency e.g. (IEA 2021). Néanmoins, même si le pourcentage décroît, il y a toujours des applications qui ne peuvent pas cesser de s'utiliser de la combustion, comme par exemple dans le secteur aérospatiale en génerale. Ainsi, la recherche poursuit pour ces applications afin de minimiser tout de même leurs impacts.

Parmi les applications de combustion, on souligne ici la combustion biphasique, où le carburant liquide doit changer de phase i.e. évaporer avant de brûler dans la phase gazeuse pour alimenter la réaction de combustion. La combustion biphasique figure entre les phénomènes les plus complexes à analyser dû à une grande disparité d'échelles temporelles et spatiales, la présence de turbulence, réactions chimiques, rayonnement, changement de phase, atomisation etc. Ainsi, pour pouvoir étudier des applications complexes de combustion biphasique, il est possible de prendre trois voies différentes: expérimentale, théorique et numérique. Idéalement, la voie expérimentale doit être préferée, étant donné que ce sont ces résultats qui vérifieront la viabilité concrète d'une application spécifique. Cependant, il est aujourd'hui impossible d'avoir une certitude exacte sur toutes mésures importantes, et des erreurs associés demandent d'autres méthodes pour possibiliter leur vérification. D'un autre côté, la stratégie numérique nous permet d'avoir une précision plus importante sur les outils de mésure, mais il est aussi impossible de payer le coût numérique pour résoudre tous phénomènes qui sont fortement couplés. Pour faire le compromis entre une précision suffisante et un coût de calcul raisonnable, des modèles bas-ordre sont utilisés.

Pour les travaux de cette thèse, la modélisation s'est concentré plus particulièrement pour le changement de phase (évaporation mais aussi condensation) de gouttes individuelles dans le contexte de la combustion biphasique, i.e. souvent issues d'une injection par spray. Dans ce contexte, une attention particulière a été donné à des carburants hydrophiliques, c'est-à-dire, des carburants qui absorvent facilement de l'eau ambiante e.g. l'ethanol, à

cause de leur utilisation en tant que biocarburants. De même manière, la recherche s'est aussi concentrée sur des modèles qui peuvent prendre en compte plusieures espèces individuellement dans l'intérieur de la goutte et dans la phase gazeuse (i.e. gouttes multi-composantes), car ce traitement plus précis est requis dans ce contexte (en contraste à une analyse où tous carburants sont supposés homogénéisés dans une seule espèce par exemple). Ces modèles s'utilisent en part de correlations semi-empiriques obtenues par des expériences simplifiées pour des gouttes isolées mais aussi de résultats numériques, avec la hausse récente de l'utilisation des outils de Simulation Numérique Directe (DNS, en anglais). Le point de départ reste théorique, avec les équations de conservation de masse, espèces et énergie, et un point d'attention pour les travaux de cette thèse était justement de trouver un tronc commun d'où la plupart des modèles existantes dans la littérature peuvent être dérivés.

Le corps du manuscrit a été decoupé en 3 parties. Tout d'abord, les équations fondamentales ainsi que les hypothèses communes à tous modèles étudiés sont établies avec leurs justifications respectives. Dans ce moment, le problème de la diffusion massique ainsi que l'hypothèse d'équilibre vapeur-liquide à l'interface liquide-gaz sont aussi posés. Ensuite, dans la deuxième partie les modèles de changement de phase de gouttes mono-composants sont developpés, dans une ordre chronologique. Dans cette partie, les sous-modèles qui possibilitent la prise en compte des effects de convection sont aussi détaillés. Après avoir posé la base des modèles mono-composant, il est ainsi possible de passer aux modèles multi-composant, ce qui est fait dans la troisième partie. C'est dans cette partie où les contributions nouvelles de cette thèse les plus importantes sont offertes. Un modèle de changement de phase basé sur une intégration analytique directe des équations de Stefan-Maxwell est proposé pour un nombre quelconque d'espèces et pour des applications convectives. Ensuite, un modèle basé sur l'intégration générale de l'équation de conservation d'énergie est proposé de façon générale pour tous modèles basés sur l'intégration des espèces, ce qui permet une comparaison aisée entre ceux-ci. Les chapitres suivants sont consacrés à une étude approfondie sur la fermeture de diffusion massique et la comparaison entre les modèles proposés et ceux de la littérature.

Partie I

Dans le premier chapitre, les fondations nécessaires pour la modélisation des transferts de chaleur et masse pour des gouttes sont developpés. Tout d'abord, les équations de conservation sont posées dans leur forme la plus générale. Ensuite, des hypothèses classiques sont appliqués, menant à une structure de référence pour tous modèles étudiés dans ce manuscrit. Suivant cette structure, une première intégration analytique est menée pour les équations de conservation simplifiées ce qui apporte des résultats qui introduiront quelques paramètres importants, tel quel le taux de transfert de masse et de chaleur entre la goutte et la phase gazeuse.

Une fois cette première intégration réalisée, la fermeture de la diffusion massique se mon-

tre nécessaire, ce qui justifie le sujet du deuxième chapitre. Concrètement, cette fermeture apparaît sous forme de vitesses de diffusion, présentes dans les équations des espèces ainsi que celle de l'énergie (terme de diffusion d'enthalpie). Dnas ce chapitre, une formulation simplifiée suivant les hypothèses classiques appliqués aux modèles de changement de phase de goutte est obtenue, nommée les équations de Stefan-Maxwell. Ces équations sont utilisées pour lier le gradient de fraction molaire aux vitesses de diffusion, et doivent être utilisées pour le cas le plus général, celui des gouttes multi-composantes. Cependant, dans ce chapitre on se concentre à obtenir la loi de Fick, classique pour un mélange à deux espèces, ainsi qu'aux corrélations semi-empiriques qui permettent le calcul des coefficients de diffusion dans ce cas binaire.

Pour tous modèles de changement de phase de ce manuscrit, une quantité clé c'est la fraction de chaque espèce participante dans les deux cotés de l'interface liquide-gaz. Le troisième chapitre fait donc l'effort de développer l'hypothèse de l'équilibre vapeur-liquide, qui est acceptée pour des applications typiques de combustion en spray (pression atmospherique), et si la goutte n'est pas trop petite. En cas de basse pression ou des petits groupements liquides par exemple, le non-équilibre sera présent et des modèles cinétiques (théorie de Boltzmann) seront plus appropriés. L'équilibre vapeur liquide établit que les fugacités de chaque espèce doivent être identiques, du coté liquide ainsi que du coté gazeux. La fugacité quant à elle peut être calculé par exemple à travers de modèles de coefficient d'activité, et l'objectif de ce chapitre est aussi de détailler quelques modèles utilisés dans la pratique, comme par exemple le UNIFAC, pour calculer ces coefficients d'acitivtés, y compris pour des mélanges liquides non-ideaux (e.g. eau-ethanol, car azeotrope).

Partie II

Dans le quatrième chapitre, les modèles de Maxwell, Fuchs et Spalding sont développés. Ce sont les premiers modèles d'évaporation de goutte amplement diffusés dans la litterature, utilisés pour des gouttes mono-composants. Particulière contribution a été faite pour l'inclusion de l'écoulement de Stefan (flux de masse dû aux changement de phase) pour les modèles de Fuchs (mass/espèces) et Spalding (énergie). Tous ces modèles n'avaient pas encore pris en compte des effects convectifs.

Le chapitre cinq se concentre sur l'extension aux applications convectives. Une des raisons pour laquelle cela a été mis de coté pour les premiers modèles c'est car c'est directement contraire à l'hypothèse de symmétrie sphérique, nécessaire pour permettre l'intégration analytique. L'absence de convection s'avère trop restrictif pour quelques applications, et la prise en compte de ces effects est nécessaire pour la combustion en spray. Un des modèles le plus célèbres qui a réussi à incorporer cela c'est le modèle de Abramzon-Sirignano, qui est ainsi dérivé et détaillé dans ce chapitre, avec aussi la théorie de filme (couche limite mince sphérique autour de la goutte). Il est aussi remarqué que le modèle de Abramzon-Sirignano a pris en compte des effets d'enthalpie de diffusion dans le cas mono-composant.

Le sixième chapitre se consacre à approfondir les corrélations évoquées par les sous-modèles de convenction forcée. Dans un premier temps, l'influence de la trainée est analysée, et ensuite les principales corrélations des nombres non-dimensionnels de Nusselt et Sherwood sont listées. Enfin, Dans le chapitre sept, quelques comparaisons numériques sont menées dans le contexte d'une goutte évaporante, afin de quantifier la sensabilité de quelques paramètres clé par rapport aux choix des sous-modèles de convection.

Partie III

Pour les modèles de changement de phase de gouttes multi-composantes, il n'y existe pas encore de consensus dans la littérature, surtout pour les modèles à composants discrets (DCM, en anglais), sur lesquels ce manuscrit se concentre. De ce fait, le chapitre huit développe d'abord un modèle basé sur l'intégration directe des équations de Stefan-Maxwell pour un cas convectif avec nombre arbitraire d'espèces inertes et évaporantes. Le résultat final répresente une nouvelle contribution de ce manuscrit, comme extension des travaux originaux de (**?**) avec une formulation de plus simple implémentation numérique ainsi que l'absence d'une hypothèse supplémentaire pour les coefficients de diffusion binaires. Ensuite, similairement ce chapitre cherche à poser un modèle de référence pour la formulation d'énergie et répresente également une nouvelle contribution. L'inclusion des effets de diffusion d'enthalpie est rigouresement prise en compte à travers de l'intégration analytique, avec inclusion des effets d'écoulement de Stefan et convection. La différence finale peut être materialisée à travers la chaleur spécifique moyen du mélange gazeux, ce qui apporte un résultat analytique très important, et montré conséquent pour des applications à haute temperature (important pour des applications de combustion en spray).

Le neuvième chapitre rassemble les contributions passées de la litterature pour les DCMs multi-composants, notamment les modèles de Tonini-Cossali, Newbold-Amundson, Law et Ebrahimian-Habchi. Tous ces modèles sont rigouresement dérivés et detaillés, avec leurs forces et faiblesses. Le modèle de Law est proposé comme le plus simple en termes de structure, vu qu'il suppose que toutes espèces doivent avoir le même coefficient de diffusion dans la phase gazeuse. Ensuite, les modèles de Tonini-Cossali et Newbold-Amundson sont montrés être équivalents en terme de structure finale. Celui de Tonini-Cossali est obtenu à travers d'une deuxième intégration de l'équation des espèces, produisant une formulation en terme de quantités massiques, alors que celui de Newbold-Amundson vient d'une deuxième intégration des équations de Stefan-Maxwell simplifiés, produisant une formulation en terme de quantités molaires. Particulière attention est donnée au modèle d'Ebrahimian et Habchi, qui réussit a éviter une deuxième intégration spatiale. Cela évite notamment l'hypothèse de propriétés thermodynamiques et de transport constantes dans le space, ainsi que la nécessité de développer une méthode de moyenemment de ces propriétés. Le chapitre dix qui en suit cherche à étendre tous ces modèles de la littérature, pour prendre en compte notamment des effets convectifs, un nombre arbitraire d'espèces ainsi que la condensation en regime général.

Le onzième chapitre détaille les méthodes utilisés pour obtenir les coefficients de diffusion moyennés entre chaque espèce et le mélange gazeux, utilisés pour les modèles de Tonini-Cossali, Newbold-Amundson et Ebrahimian-Habchi. Notamment, les modèles de Blanc, Wilke et Hirschfelder-Curtiss sont tous dérivés à partir des équations de Stefan-Maxwell suivant quelques hypothèses liés aux vitesses moleculaires ainsi qu'aux vitesses de diffusion massique et de diffusion molaire. Il est montré que la structure analytique du modèle de Wilke est la plus bien-comporté. Ce chapitre répresente aussi une contribution originale dans la mesure où l'obtention de ces coefficients ainsi que les hypothèses nécessaires pour leur obtention n'a jamais été rassemblé de cette manière. Il montré aussi que systematiquément le modèle de Wilke s'approche plus du modèle de réference et donc ce modèle est utilisé par la suite.
Enfin, le douzième chapitre réalise des simulations comparatives entre tous modèles, montrant qu'en général le modèle de réference (Stefan-Maxwell) coûte systematiquément une ordre de grandeur de plus en terme de temps par rapport aux approches simplifiées, surtout à cause de la necessité de calculer une matrice exponentielle. Également, il est montré que le modèle de Law, même si trop simple en terme de physique de diffusion quand comparé aux autres, coûte systematiquément le même en terme de temps de calcul par rapport aux autres modèles simplifiés. Le modèle d'Ebrahimian-Habchi est aussi presenté comme une stratégie prometteuse, vu qu'il est plus simple à être calibré (moins de degré de libertés). Toutes investigations numériques sont conduites avec gouttes présentant des compositions liquides réalistes, avec ethanol, acetone, n-dodecane et de l'eau.

Acknowledgements

Completing a PhD thesis is a journey that few people undertake, and I am quite conscious of that. It is quite distant from the typical structured "job", and a major reason for this comes from the highly personal character it entails. One of the main takeaways for me, from this experience, is autonomy: I now feel way more capable to undertake personal or professional projects that might come my way. Autonomy, however, is not synonimous to loneness - far from being exhaustive, this is where I dedicate some words to all beings that were pivotal for the completion of this journey. First and foremost, I would like to thank my sole supervisor, Aymeric, for believing in me from the start. My first internship was with Aymeric, just after having completed the main engineer cycle at École Centrale Paris. Here, I also thank Sébastien, EM2C's director, who was also always supportive and allowed for my adventures to happen, and Léo, the Brazilian inspiration that pushed me to pursue a PhD. I firmly decided that I wanted my first internship to be somewhat related to my specialty - aeronautical engineering - and so, a research internship studying acoustic instabilities inside aeronautical combustion chambers was perfectly valid. I started that internship with no intent to stay in academia, and little did I knew, it was the start of something special. At the end of that internship, I already knew I wanted to pursue a PhD, and this guided me to my first international conference, ICNC Orlando, which was amazing - thank you to everyone involved back then. The natural path was to come back to EM2C, the lab that first greeted me, in such positive ways. After a lot of resistance, I was able to get a summer internship again with Aymeric, this time on uncertainty quantification and its applications for particle-laden flows. This gave me further experience, and a second domain that I was sure that I would NOT want to dedicate many years of my life doing - I would need a third try. It is therefore time to thank Fernando. My third internship was with him, at the LETE lab, where I discovered the modeling techniques used in fuel droplet evaporation. The coupling between fluid mechanics, analytical and computational tools, and models, persuaded both my scientist side as well as my engineer side, and thus I finally discovered what I wanted to do my PhD on. During this experience, Fernando was always very reachable and helpful, and this marked the start of a very fruitful cooperation that would last up until the last day of my thesis (and still continues for my Post-Doc position...). I also would like to thank Guenther, who also welcomed me with open arms and was determined to make things work. Finally, I went back to France and Aymeric was able to secure not only a funding for my thesis, but also was open to slowly allow my thesis to converge towards the theme

I wanted to explore the most: droplet phase-change modeling. I also would like to thank Benedetta, as without your initial support, things would surely have gone differently, and I was honored to have you as my supervisor, even if for such a brief moment.
Then, I would like to thank my partner, Lana, for being ever-present, always understanding, and always listening to the new small detail that I had discovered and wanted to share, always challenging me, and always being by my side. Also, for understanding the way I work, respecting it and encouraging it. I also thank here my direct family, Ana Edith, Ernesto, Rafaela, Alexandre, for the continuous support and words of encouragement, and for always showing interest in what I was researching. I extend these thoughts to my grandmother, Edmar, and the rest of my close family, Guibson, Magali, Gilberto, Paulinha, Bernardo, Miguel, Dudu, Gabriel, Ana Beatriz, Gustavo, Ana Rita, Fabiano, Rafael, Ana Cristina, Victor, Ana Lúcia, Marcos, Mariana, Juliana, Bibi, Pedro, Mateus, Dani Dani, Isinha, Elmar, Luiz Carlos, Carlos Antônio, Décio Luiz, Edith Zulmira, Edlamar and also my new "second" family, Jany, Orlando, Iasha, Ulisses, Lília, Marcelo, Totti, Dani, Ayla, Gabs, André, Tainá, Yanko, Lucca, Julia for all gatherings that were really important to me. I also would like to thank my closest friends, Andrew, Nara, Juarez, Novaes, Felipe, Caio, Santos, Luiz, Bella, Vanessa, Lidia, Jacques, Rafinha, Rafael, Diogo, Guto. From the lab, I would like to thank specially the people from my bureau, Victor, Jan, Max, Marie, Julie and Lorenn, but also Pierre, Ulysse, Preethi, David, Guillaume, Victorien, Roxane, Yuri, Suzane, Livia, Junghwa, Jean, Karl, Alexandre, Valentin and the employees Sébastien, Jean-Michel, Nathalie, Noï and Brigitte. Then, I also thank my neighbours, Camille, Bertrand, Lilian and Marion, for being so receptive, kind and generous. I would also specially like to thank my dog, Saduk, my best friend in life, who passed away during my final year at the PhD program, after a long and happy life. Thank you, and you have taught me many lessons that will accompany me for the rest of my life. Thank you for the serenity you brought me, the companionship, for always listening, being available, and next to me. You taught me about life and death, the joy and the sadness within each one. I also would like to thank my great grandmother Bisa Edith, my grandfather Esmael and my little bird Falcão, all bright stars in the night sky - even though you were not here for this journey, your presence will always be with me, for the rest of my life. I dedicate this work to all these people, and hope that will serve as a useful reference for many students in the future. Finally, I wanted to thank special companions that were there passively for me throughout my thesis, with the gift of music: The Beatles, Paul McCartney, Wings, Janis Joplin, Metallica, Pink Floyd, Led Zepellin and Supertramp, all of whom gave me energy and motivation during different times of this work, and also Jamey Stegmaier for fostering the game designer inside me and being an important mentor, and Sean "Day [9]" Plott for being a good friend in good times but also in times of adversity, and one of the greatest entertainers that I know. I cannot thank all of you enough, for being part of one of the greatest achievements of my life, that I will never forget.

Contents

Introduction

Ever since the breakthrough caused by the so-called "Industrial Revolution", human civilization has been highly dependant on energy. In this way, within the context of energy generation, combustion quickly rose to popularity, due to its high energy potential per mass and the relative abundance of required fuels. The subsequent focus on manufacturing and efficiency placed even more emphasis in combustion, creating a complex chain of developments that solidified a continuous reliance on combustion as a form of energy that lasts until today (Mohr, Wang, Ellem, Ward, and Giurco 2015). However, the abundance of resources is more questionable by today's metrics, and the negative impact of an over-reliance on combustion as a primary source of energy is evident (IEA 2021). Progress towards renewable forms of energy has been advancing steadily over the years, and global regulations on overall emissions have become more strict. Still, some applications cannot avoid using combustion, and so studies must be carried out to reduce all potential harms, including fuel choice, formation of pollutants or acoustic noise for instance. In this context, some applications are concerned with internal combustion engines, as is the case for vehicles, aircraft and spacecraft (Faeth 1977). Specifically for aircraft and spacecraft, the high burst of energy that combustion provides is fundamentally necessary for critical operations such as take-off, landing, and launches.

Spray combustion and point-droplet modelling

To better understand these applications, it is still quite difficult to establish experimental apparatus that can reproduce scenarios representative of real-life applications (Chauveau, Halter, Lalonde, and Gökalp 2008). Therefore, the strategy has often leaned towards computational fluid dynamics (CFD) simulations (Sazhin 2014). However, even for this approach, discretizing a three-dimensional domain in a complex geometry and solving for all the physics (turbulence, chemistry, liquid injection...) is too expensive (Alis 2018), (Boniou, Schmitt, and Vié 2022). An acceptable compromise is to use models for the closure of some physical phenomena.

If we focus on the liquid phase, injection systems in internal combustion engines are designed to promote a fast atomization (Marmottant and Villermaux 2004). As seen in Fig. 1, the liquid phase evolves from a separated phase with a dense core and liquid

ligaments, to a disperse phase with individual droplets which will eventually evaporate and feed the combustion. Owing to the droplets small sizes, the modeller can resort to the widely-used "point-particle" (Kuerten 2016) assumption: as the droplet scale is significantly smaller than any other scale of the flow, we can consider point-wise droplets, thus neglecting their volume occupation in the CFD solver. In this way, we only need to track their position along with specific variables such as their mass, velocity or temperature, and compute their influence on the carrier phase through models derived separately. Each droplet will then be characterized by a set of mathematical equations that represent its heat, mass, and momentum transfer rates with respect to its surrounding gaseous phase. To that extent, these droplet models are often referred to as "zero-dimensional" (Gradinger and Boulouchos 1998), since the host solver only sees these droplets through these localized source terms, and not as the physical objects that they are. The main question becomes therefore how to provide accurate models for the droplet evolution in the carrier phase.

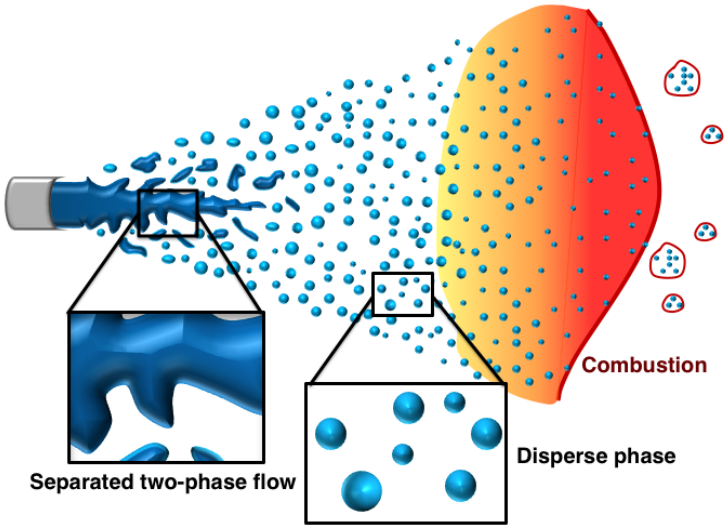

Figure 1: Schematic representation of the different phases of the spray evolution (Extracted from (Mercier 2021)).

Droplet physics in combustion chambers

Before modelling the droplet, we first have to identify the underlying physics, and so it is helpful to have some order of magnitude for droplet-related quantities in typical combustion chamber operations. For this, we extract the following reference data from (Mesquita 2021), which will guide our analyses in this manuscript:

- Droplet radii sizes within range of $10 - 100 \mu m$

- Relative velocities spanning $0 - 100 m/s$
- Gas temperatures spaning $300 - 1600 K$.

Among the possible physics, the droplet can be subjected to various exchanges due to a non-equilibrium with its surroundings:

- Mass exchanges through vaporization or condensation;
- Energy exchanges through heating or cooling;
- Momentum exchanges through drag forces, possibly with the occurence of secondary breakup for strong aerodynamics efforts.

Focusing on momentum exchanges, many correlations have been provided in the literature for solid spheres (Michaelides 2006), which aim to mimic the standard drag curve represented in Fig. 2. This has led to very accurate models, such as the widely used Schiller-Naumann correlation (Schiller and Naumann 1935).

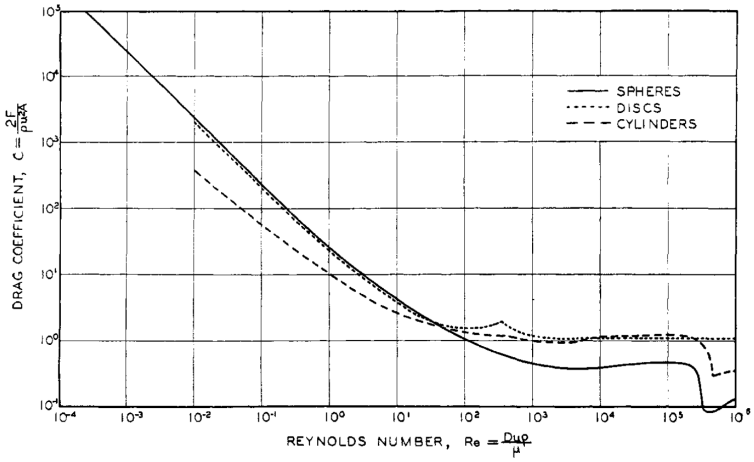

Figure 2: Standard Drag force curve: drag coefficient as a function of the Reynolds number. Image from (Lapple and Shepherd 1940))

As for the heat and mass exchanges in the case of droplets i.e. liquid spheres, additional models are required to incorporate these effects, and possibly the effect of inernal recirculation. Furthermore, the physics will depend on the composition of the droplet. Overall, the core of this manuscript will adress the modelling possibilities for the heat and mass exchanges.

Multicomponent droplets

Liquid fuels are typically composed of hundreds of chemical species. Still, classical fuels such as aeronautical kerosene contain blends that tend to follow an ideal behavior, with similar molecular structures which attenuates the complexity of species interactions. One common strategy to model the evaporation of such fuels has been to lump all species as a single, “surrogate” one which is deemed to represent the whole mixture

accurately enough. An example of a such surrogate description is given in Fig. 3, where the discrete species model (DSM) and the continuous thermodynamic model (CTM; the surrogate approximation) are plotted for the composition of a typical hydrocarbon. The main advantage of such approach comes from the fact that well-established models exist to describe single-component evaporating droplets. For instance, among the most widely used models in CFD solvers for combustion applications is the one of (Abramzon and Sirignano 1989), which is devoted to the evaporation of fuel droplets in convective environments. Therefore, when following the surrogate strategy, the attention would be more focused towards evaluating proper surrogate descriptions, instead of the droplet phase-change models themselves.

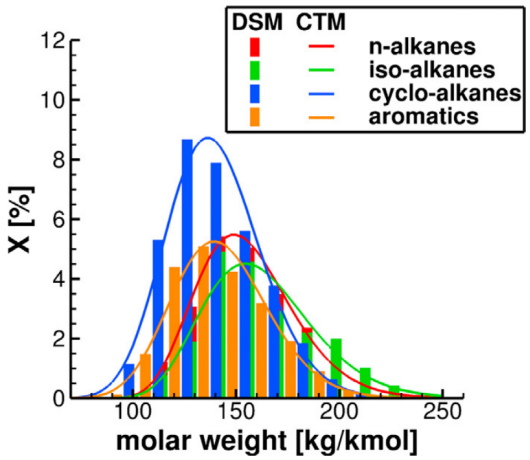

Figure 3: Example of surrogate fuel composition of aeronautical kerosene. Extracted from (Eckel, Grohmann, Cantu, Slavinskaya, Kathrotia, Rachner, Clercq, Meier, and Aigner 2019)

However, from the previously mentioned strict emission constraints, biofuels have been emerging as more sustainable options (Farrell, Plevin, Turner, Jones, O'Hare, and Kammen 2006), (Liu, Jia, Xi, Liu, and Yi 2022). In contrast to typical hydrocarbon-chained fuels, these contain species that present high levels of non-ideal behavior and complex interactions (Filho, Santos, Vié, and Filho 2022), making it difficult to still use surrogate models and capture the required phenomena. For that matter, even for fuels that tend to be better represented through surrogates, different internal groups can be classified (as seen in Fig. 3), and a more thorough analysis would benefit from having individual descriptions for each group of species. To answer this question, discrete component models (DCMs) have emerged (Abianeh and Chen 2012), to describe droplets that can have 2 or more species - here labeled as multi-component droplets. In this situation, there is no real consensus on the phase-change model to use, as the picture becomes far more complex than for single-component evaporation, because of the following challenges:

- Fick's law, exact for binary diffusion, is no longer valid for multi-component problems with more than 2 species;

- The vapor-liquid equilibrium requires more complex physics, as the standard Raoult's law used in single-component evaporation may be not valid anymore.
- Analytical integrations that were possible for single-component droplets may now not be possible, and sometimes non-linear equation solvers are required.

In this context, some contributions of the literature have attempted to solve each of the issues. Among them, we can state four contributions that are of interest:

- Law (Law 1976) proposed a simplified strategy based on Fick's law, which avoids the use of a non-linear solver by a strong simplification of the non-linear system. This model has been notably used in combustion applications, for instance in (Shastry, Cazeres, Rochette, Riber, and Cuenot 2021) or (Bonanni and Ihme 2022).
- Ebrahimian and Habchi (Ebrahimian and Habchi 2011) proposed a model based on the Hirschfelder and Curtiss approximation (Hirschfelder and Curtiss 1949) for diffusion velocities which uses only a single spatial integration, avoiding the assumption of constant properties in space;
- Tonini and Cossali (Tonini and Cossali 2015) developed a full multi-component model based on a often employed binary analogy Fick's law as seen in (Zhang and Kong 2012) for instance;
- Tonini and Cossali (Tonini and Cossali 2016; Tonini and Cossali 2022) also developed evaporation models for spheroidal droplets based on the Stefan-Maxwell equations for the diffusion velocities.

As already stated, among all these contributions, no consensus exist on the best model to use. This is where the present manuscript starts.

Objectives of this work

The present manuscript focuses on the description of the droplet heat and mass transfer and, therefore, the associated models, first laying out the required theoretical tools and surveying the main developments carried out for single-component droplet models. Then, a core focus is given to DCMs for multi-component droplets, with the main strategies proposed in the literature but also with the proposition of novel, more robust formulations that seek to obtain general application regimes. As for the momentum, the spherical symmetry assumption and the zero-dimensional coupling with CFD solvers allows for a more straightforward momentum coupling. The main complexity thus arises from the degrees of freedom generated from such an approach, mainly the correlations of droplet drag and relevant non-dimensional numbers. Still, a study is carried out to pinpoint the main contributions from the literature for droplet and solid sphere momentum closures, and a phenomenological investigation is made to clarify to the reader the impact of such choices.

Throughout the text, a particular emphasis is given on the rigorous derivation for the studied models based on a unified framework of equations, all while highlighting the main contributions and advantages of each model. For the multi-component part, new, more

suitable alternatives for both mass and heat transfer formulations are proposed keeping in mind a pragmatic approach with regards to numerical cost and implementation, but also the required procedure of validation. The objective of such approach is to consolidate a rigorous and universal framework for the different models and sub-models related to droplet phase-change, with a focus on combustion applications and the surrounding literature, to better inform the interested reader in their choice as to which models and/or sub-models to use and when, following their advantages and limitations.

Also, throughout this manuscript, the terms "mass transfer model", "heat and mass transfer model", or "phase-change model" are preferred contrary to "evaporation model". This choice is made to reinforce that condensation, when vapor species are also able to enter the droplet, may also occur, and this can be quite important especially when considering multi-component droplets and the influence of ambient humidity.

Outline of the manuscript

This manuscript is organized as follows.

In Part I, the baseline equations and derivations, as well as standard closures are presented. First, Chap. 1 shows the equations of conservation and the first spatial integration that leads to baseline equations. Chap. 2 is devoted to the modelling of species diffusion as its is the main driver of evaporation. Chap. 3 presents how to handle the vapor-liquid equilibrium that is commonly assumed at the droplet interface.

In Part II, single-component models are investigated. First, in Chap. 4, classical models for static droplets are presented. Then, the film-theory extension for convective environments is detailed in Chap. 5, leading to the Abramzon-Sirignano model. The required closures for momentum, heat and mass transfers are reviewed in Chap. 6. Finally, a numerical investigation for possible choices among correlation models is presented in Chap. 7.

In Part III, multi-component developments are presented. First, Chap. 8 shows the development of a reference multicomponent model based on the Stefan-Maxwell equations. Chap. 9 reviews the existing models of the literature based on approximations of the Stefan-Maxwell equations. In Chap. 10, extensions to multi-component models of this manuscript are presented based on new contributions on energy and species diffusion treatments. Chap. 11 analyses the impact of the choices for diffusion coefficients on phase-change modelling. Finally, Chap. 12 shows comparisons between extended modelling strategies proposed in this manuscript for various multi-component droplet phase change scenarios representative of spray combustion.

Part I

Theoretical framework for the droplet heat and mass transfer

Chapter 1

Baseline developments from conservation equations

In this chapter, the building blocks for modelling the heat and mass transfer processes for droplets are developed. First, the conservation equations are written in their general form. Then, classical simplifying hypotheses are applied, leading to a framework of reference for all models studied in this manuscript. These hypotheses are typically established from the perspective of computational fluid dynamics (CFD) simulations based on the point paricle approach, and so they aim to preserve the most critical aspects of the underlying physics whilst also allowing for an analytical integration.

Following this framework, a first analytical integration is carried out for the relevant conservation equations leading to results that introduce the reader to some key quantities, most notably the droplet mass transfer rate and heat transfer rate. This first integration is a core part of all droplet phase-change models of this manuscript. Typically, a second integration can also be carried out, and this is where additional hypotheses and/or specificities of each model appear, and so this second integration will be left to subsequent chapters.

In this way, the goal of this chapter is to better equip the reader with the fundamental knowledge necessary to better understand the derivation and particular contribution of each model shown in this manuscript.

1.1 Conservation equations and main hypotheses

The general conservation equations of mass, species, momentum and energy (represented here through the sensible enthalpy) for a mixture composed of $i = 1, 2, ..., N$ species in the gaseous phase are written below, respectively (Poinsot and Veynante 2012; Williams 2018; Klingenberg 2015):

$$\frac{\partial \rho}{\partial t} + \nabla \cdot [\rho \mathbf{u}] = 0, \tag{1.1a}$$

$$\frac{\partial \rho Y_i}{\partial t} + \nabla \cdot [\rho Y_i \mathbf{v}_i^m] = \dot{\omega}_i, \tag{1.1b}$$

$$\frac{\partial \rho \mathbf{u}}{\partial t} + \nabla \cdot [\rho \mathbf{u}\mathbf{u}] = -\nabla \mathbf{p} + \nabla \cdot \boldsymbol{\tau} + \rho \sum_{k=1}^{N} Y_k \boldsymbol{f}_k, \tag{1.1c}$$

$$\begin{aligned} \frac{\partial \rho h_s}{\partial t} + \nabla \cdot \left[\rho \left(\mathbf{u} h_s + \sum_{k=1}^{N} Y_k \mathbf{v}_k^D h_{s,k} \right) \right] &= \frac{D\mathbf{p}}{Dt} + \boldsymbol{\tau} : \nabla \mathbf{u} + \nabla \cdot \mathbf{q}_R + \\ + \rho \sum_{k=1}^{N} Y_k \mathbf{v}_k^D \boldsymbol{f}_k + \nabla \cdot \left[RT \sum_{j=1}^{N} \sum_{k=1}^{N} \left(\frac{X_k D_j^T}{W_j \tilde{D}_{j,k}} \right) \left(\mathbf{v}_j^{D,Y} - \mathbf{v}_k^{D,Y} \right) \right] &+ \\ + \nabla \cdot \lambda \nabla \mathbf{T} + \dot{\omega}_c, & \end{aligned} \tag{1.1d}$$

where ρ is the total density, $\mathbf{u}$ is the mass convective velocity, Y_i is the mass fraction, $\mathbf{v}_i^m$ is the average molecular velocity, $\dot{\omega}_i$ is the species source term for chemical reactions, $h_s = \sum_{k=1}^{N} h_{s,k} Y_k$ is the sensible enthalpy, $h_{s,k}$ is the sensible enthalpy of species k, $\mathbf{v}_i^{D,Y}$ is the mass diffusion velocity, $\mathbf{p}$ is the pressure, $\boldsymbol{\tau}$ is the viscous tensor, $\mathbf{q}$ is the conductive heat flux, λ is the thermal conductivity, T is the temperature, $\boldsymbol{f}_i$ are the volumic forces, R is the universal gas constant, X_i is the molar fraction, D_j^T is the thermal diffusion coefficient, W_i is the molecular weight, $\tilde{D}_{i,k}$ is the binary diffusion coefficient in a multi-component mixture, $\boldsymbol{q}_R$ is the radiative flux and $\dot{\omega}_c$ is the energy source term due to chemical reactions.

In Eq. 1.1, the molecular velocity is defined as

$$\mathbf{v}_i^m = \mathbf{u} + \mathbf{v}_i^{D,Y}. \tag{1.2}$$

In the introduction, it was stated that droplets are usually described through spheroidal shapes. It may be useful therefore to show the gradient and divergence operators in spherical coordinates. For a general ζ field decomposed as follows:

$$\zeta = \zeta_r \hat{r} + \zeta_\theta \hat{\theta} + \zeta_\phi \hat{\phi}, \tag{1.3}$$

the gradient and divergence operators are computed as:

$$\nabla \zeta = \frac{\partial \zeta}{\partial r} \hat{r} + \frac{1}{r} \frac{\partial \zeta}{\partial \theta} \hat{\theta} + \frac{1}{r \sin\theta} \frac{\partial \zeta}{\partial \phi} \hat{\phi}, \tag{1.4a}$$

$$\nabla \cdot \zeta = \frac{1}{r^2} \frac{\partial \left(r^2 \zeta_r \right)}{\partial r} + \frac{1}{r \sin\theta} \frac{\partial \left(\zeta_\theta \sin\theta \right)}{\partial \theta} + \frac{1}{r \sin\theta} \frac{\partial \zeta_\phi}{\partial \phi}. \tag{1.4b}$$

To derive droplet phase-change models, typically we depart from the conservation equations Eqs. 1.1 for the gaseous phase, effectively decoupling the treatment of the liquid and the gaseous phases. Also, for an analytical integration, a set of hypotheses is needed, which are described below. All of these assumptions are common-place when deriving droplet phase-change models.

1. Quasi-steadiness, also called quasi-stationarity i.e. all temporal derivatives are neglected for the gaseous phase.
2. Spherical symmetry, i.e. contributions in the polar and azimuthal components are neglected; only radial ones are retained.
3. No chemical reaction i.e. $\dot{\omega}_k = 0, \ \forall k$ and $\dot{\omega}_c = 0$;
4. Constant-pressure Low-Mach, dilatable flow i.e. negligible viscous contributions such that $\boldsymbol{\tau} = 0$ and also $\frac{D\mathbf{p}}{Dt} = 0$;
5. Volumetric forces neglected i.e. $\boldsymbol{f}_k = 0, \ \forall k$;
6. Negligible Dufour effect: $RT \sum_{j=1}^{N} \sum_{k=1}^{N} \left(\frac{X_k D_j^T}{W_j \tilde{D}_{j,k}} \right) (\mathbf{v}_j - \mathbf{v}_k) \approx 0$;
7. No radiation, i.e. $\mathbf{q}_R \approx 0$.

By employing hypotheses #1-#7 defined before, the conservation equations Eqs. 1.1 then become greatly simplified, and the momentum conservation Eq. 1.1c brings only redundant information; it can therefore be omitted. In this way, Eqs. 1.1a-1.1d are recast below in their simplified form:

$$\frac{1}{r^2}\frac{d}{dr}\left[r^2 \rho \mathrm{u}\right] = 0, \tag{1.5a}$$

$$\frac{1}{r^2}\frac{d}{dr}\left[r^2 \rho Y_i \mathrm{v}_i^m\right] = 0, \tag{1.5b}$$

$$\frac{1}{r^2}\frac{d}{dr}\left[r^2 \rho \left(\mathrm{u} h_s + \sum_{k=1}^{N} Y_k \mathrm{v}_k h_{s,k} \right)\right] = \frac{1}{r^2}\frac{d}{dr}\left[r^2 \lambda \frac{dT}{dr}\right], \tag{1.5c}$$

Eqs. 1.5a-1.5c above represent the main point of departure for most droplet heat and mass transfer models. Before starting to develop models, a brief discussion of the hypotheses leading to these equations is provided in the next section to contextualize the reader.

1.2 Discussion on the baseline assumptions

1.2.1 Quasi-steadiness

Quasi-stationarity, also sometimes referred to as quasi-steadiness, is typically justified from a phenomenological standpoint. One analysis for instance consists in checking orders of magnitude for diffusivities in the liquid and the gaseous phase. In (Sazhin 2014), the author makes a quick computation for Diesel droplets, obtaining that liquid diffusivities are around two orders of magnitude smaller than the gaseous counterpart. Effectively, this means that it is sensible to "decouple" the analysis of the liquid and gaseous phases and treat them separately, but also, that the gaseous phase can be seen

to adapt infinitely fast, relative to the liquid. This is a key characteristic of this assumption, in that it is stated for the gaseous phase, but can often be regarded as valid only within the context of the two phases.

In (Bellan and Summerfield 1976), more criteria are offered that allow the use of the quasi-stationarity hypothesis even when disregarding comparisons with the liquid phase; overall for typical pressures the assumption holds well. Still, for a more quantitatively precise approach, in Appendix B we provide the analytical solution of the diffusion equation (for both temperature and species) including temporal derivatives. This is not a comprehensive solution, since it neglects Stefan flow and external convection effects, but it already provides a solid framework and further reassurance that this assumption is in principle reasonable.

One recent study that proposes a fully transient solution for single-component droplets with typical assumptions can be found in (Finneran, Garner, and Nadal 2021). Therein, the author classifies the quasi-steady approach as when the droplet temperature is fixed at a single temperature, constant in time and homogeneous inside the droplet. Therefore, a great difference was found when comparing the quasi-steady approach with the fully transient one. In (Talbot, Sobac, Rednikov, Colinet, and Haut 2016), another transient study was perfomed and again, the quasi-steady approach was defined as constant temperature for the liquid droplet. In (Williams 1960), the author classifies the quasi-stationary approach as when the droplet radius is assumed to be constant during the integration procedure (which is generally not the case for a droplet undergoing phase-change).

In this manuscript, "quasi-stationarity" refers exclusively to the gaseous phase. The treatment used for the liquid phase is separate, and some details are shared in Appendix A. For that matter, we employ the infinite conductivity approach for the liquid phase, which still allows for the update of the droplet temperature (time-variable, but still homogeneous in space), and we also assume constant radius during integration, which is sensible for CFD applications. A rather similar model employed in (Talbot, Sobac, Rednikov, Colinet, and Haut 2016) was there named as the "quasi-homogeneous" model. When comparing this approach with the full transient solution, not much difference was reported. The final temperatures of the droplets were predicted to be the same, and the overall temperature profile in time was found to be in good agreement, with deviations increasing as the surrounding temperature increases. The same trend of results was reported in (Aggarwal, Tong, and Sirignano 1984), where the authors referred to the present treatment also as the "infinite conductivity model".

1.2.2 Spherical symmetry

The spherical symmetry hypothesis can be justified also through a phenomenological observation with the aid of dimensionless numbers, with a first analysis justified through

the Bond number:

$$Bo = \frac{2(\rho_l - \rho_g)gR_d^2}{\sigma}, \tag{1.6}$$

where g is the acceleration due to gravity, σ the surface tension and R_d the droplet radius. This number compares surface tension and gravity forces. For small Bo, surface tension dominates and the droplet will have the equilibrium spherical shape. For fuel droplets in cases of interest for this manuscript $Bo < 0.002$ is obtained which generally justifies the spherical shape.

We can also employ the Weber number to see whether the droplet will be atomized or not:

$$We = \frac{2\rho_g U^2 R_d}{\sigma}, \tag{1.7}$$

where U is the relative velocity between the droplet and the surrounding gas velocity field. A Weber number below 12 leads to a stable droplet. For this parameter, the conclusion is not as straightforward for our parameter range. In Fig. 1.1, the Weber number is plotted against droplet radius and relative velocity.

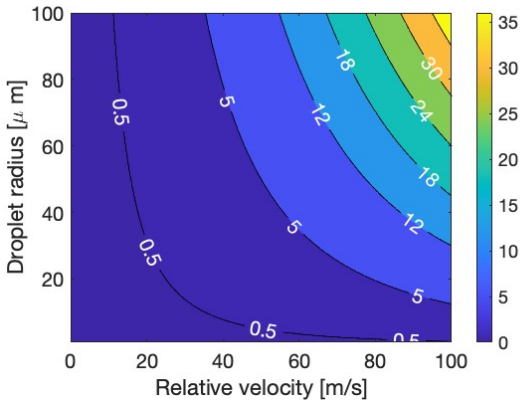

Figure 1.1: Weber number range for the evaporating condition considered in the present manuscript. Droplet with a Weber number below 12 are considered stable with respect to atomization. Droplet with a Weber number below 0.5 may be considered as spherical.

From this figure, we can see that a large part of our operating conditions is concerned with stable droplets, while the extreme conditions for high velocities and large diameter could require the modelling of an atomization process, which would mean that the spherical symmetry would no longer be an accurate representation. The validity of this assumption can be discussed even further: even below the stable Weber number the spherical shape may be not preserved, as its shape may be oscillating, leading to an spheroidal shape. Following the TAB model of (O'rourke and Amsden 1987), we can define the deviation

to the spherical shape x by using this formula:

$$\frac{x}{R_d} = \frac{C_F}{C_k}\frac{We}{2}, \tag{1.8}$$

where $C_F = \frac{1}{3}$ and $C_k = 8$ are constants of the model. Using this formula, we see that we require a Weber number below 5 if we accept a deviation below 10%, and a Weber number below 0.5 if we accept a deviation of 1%.

On the other side, if the size decreases too much, kinetic effects may start to play a larger role when the droplet diameter starts to become of the same order of magnitude as the mean free path l_{coll}. To measure this, one criteria was offered by (Sazhin 2014) in that if the Knudsen number for the droplet respects $Kn = l_{coll}/R_d < 0.01$, then the continuum approach is verified. Here we place ourselves in the context of droplets having radius in the range $R_d > 10^{-8}m$ which should satisfy this lower limit.

1.2.3 Dufour effect

As for the Dufour effect, it describes the physical behaviour that species gradients tend to induce temperature gradients, which should be incorporated in the energy conservation balance. Quantitative analyses usually reveal that its impact relative to other terms on the equations tends to be negligible (Williams 2018). Some studies have considered the impact of the Dufour effect in other systems, including spheres as seen for instance in (Bég, Prasad, Vasu, Reddy, Li, and Bhargava 2011). Unfortunately, no precise studies for the Dufour effect specifically for droplets undergoing phase-change have been carried out to our knowledge. This is also the case for the Soret effect, which conversely introduces effects of temperature gradients on the species gradients. The Soret effect which appears later on for the mass diffusion closure equation in Chap. 2, is therefore also neglected in this manuscript. However, as will be shown in Chap. 8, one proposed contribution is a general energy model uncoupled from the mass transfer model and its choices. Therefore, such general energy formulation could also be used in conjunction with an alternative mass transfer model that incorporates Soret effects (the Dufour effects are still neglected).

1.2.4 Chemical reactions

The absence of chemical reactions might seem counterintuitive for spray combustion applications. This can be best justified by understanding the typical flame structures that appear for two-phase combustion, as detailed for instance in (Reveillon and Vervisch 2005) and (Jenny, Roekaerts, and Beishuizen 2012). Following the classification of Reveillon et al., often in spray combustion scenarios droplets are confined into pockets of "pure vaporization" regimes, with the flame only at the exterior. Since most droplet phase-change models are concerned with spatial integrations, it is typically reasonable to assume that no influence of source terms is expected on the integration procedure for the vast majority of droplets. In this case, only the "indirect" presence of the flame appears, through high specified temperatures and surrounding chemical species, for example. Still, in an

extremely diluted region, or for a small subset of droplets, individual spherical flames may develop. In this case, the integration procedure can be modified to include the influence of heat and mass transfer source terms due to combustion. This was developed for some simple droplet models, such as the ones in (Spalding 1953), (Godsave 1953), (Wood, Wise, and Inami 1960), (Law 1976). However, to include the explicit impact of the flame, a number of other simplifications are enforced, such as the unitary Lewis number hypothesis. For this manuscript we focus on the case without source terms, as it prevails for a wide variety of scenarios within spray combustion. Both scenarios can be seen in Fig. 1.2 below; at the left, the outer droplets have spherical flames attached to them, whereas at the right, the whole group is surrounded by a single flame.

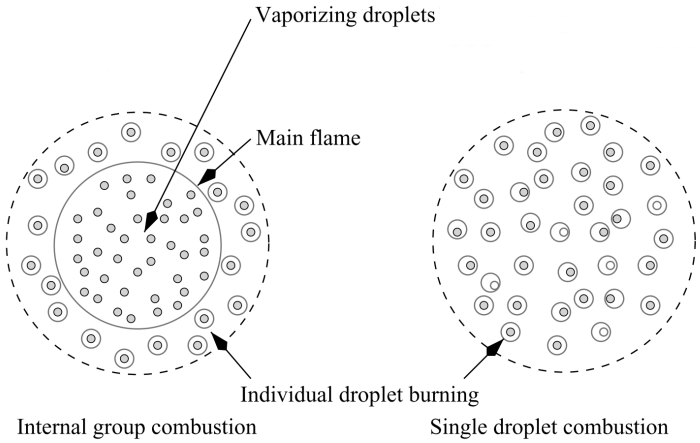

Figure 1.2: Flame envelopes for droplet combustion. Extracted from (Reveillon and Vervisch 2005)

1.2.5 Low-Mach number assumption

Finally, the low-Mach and dilatable flow is more of an extrinsic characterisctic to the problem, i.e. it does not directly depend on the droplets themselves but rather on the surrounding conditions. Many aeronautical engines operate in this regime, at least for stable conditions of operation. Studies of droplet vaporization or more generally phase-change with compressible effects are also of paramount importance for some key spray combustion applications, but are out of the scope of this manuscript.

1.3 Dimensionality reduction: a first integration

Below are developed some main results that make the core of all droplet heat and mass transfer models studied in this manuscript. The main strategy consists in taking advantage of the quasi-steadiness and spherical symmetry hypotheses allow for the integration to have functional dependencies on a single differential variable, the radial coordinate r. In this way, the integration procedure of Eqs. 1.5 is referred to here as an integration

over the spatial coordinate.

First, the global mass conservation Eq. 1.5a when integrated once over the spatial coordinate leads to:

$$r^2 \rho \mathrm{u} = \text{constant}. \tag{1.9}$$

In Eq. 1.9 above, the integration constant can in particular be evaluated as a boundary condition at the surface of the droplet. The LHS represents a flux of mass on the gaseous phase, being transported through the advective velocity field u. Therefore, from the typical definition of a mass flux, the constant can be evaluated as being:

$$\boxed{r^2 \rho \mathrm{u} = \frac{\dot{m}}{4\pi}} \tag{1.10}$$

where $\dot{m}$ is the mass transfer rate from the droplet to the gaseous phase. In this way, $\dot{m} > 0$ if there is evaporation, and $\dot{m} < 0$ if there is condensation. The radial velocity field u that arises solely from the mass transfer depicted in Eq. 1.10 is commonly referred to as the *Stefan flow*.

The species conservation Eq. 1.5b for species i when integrated over the spatial coordinate yields the following:

$$r^2 \rho Y_i \mathrm{v}_i^m = \frac{\dot{m}_i}{4\pi}, \tag{1.11}$$

where the constant of integration is also evaluated analogously to the procedure described for Eq. 1.10. In this case, the mass flux is the one represented by the single species i. It is also common to represent the mass transfer rate of Eq. 1.11 above through a fractional evaporation rate ϵ, which is defined as being:

$$\epsilon_i = \frac{\dot{m}_i}{\dot{m}}. \tag{1.12}$$

The trivial results $\sum_{k=1}^{N} \dot{m}_k = \dot{m}$ and $\sum_{k=1}^{N} \epsilon_k = 1$ are also of note here. In this manuscript, inert species are defined such that they do not participate in phase-change, namely, the species k that respect $\dot{m}_k = 0$. Note that from Eq. 1.11, this implies that the net average molecular velocity v_i^m for inert species is zero. For a more general treatment, it would be possible to allow for a dissolution from the inert species into the liquid phase, but this is out of scope for this manuscript.

The molecular velocity v_i^m in Eq. 1.11 can also be split into its advective and diffusive components following Eq. 1.2. In this way, another common form of Eq. 1.11 is retrieved:

$$r^2 \rho Y_i \left(\mathrm{u} + \mathrm{v}_i^{D,Y} \right) = \frac{\dot{m}_i}{4\pi}, \tag{1.13}$$

Then, the result of Eq. 1.10 may be substituted for the velocity u to yield:

$$\boxed{Y_i \frac{\dot{m}}{4\pi} + r^2 \rho Y_i \mathrm{v}_i^{D,Y} = \frac{\dot{m}_i}{4\pi}} \tag{1.14}$$

Eq. 1.14 above is the main point of depature to obtain most droplet mass transfer results.

Finally, the energy conservation i.e. Eq. 1.5c when integrated similarly over the radial coordinate leads to:

$$r^2 \rho \mathrm{u} h_s + r^2 \rho \left(\sum_{k=1}^{N} Y_k \mathrm{v}_k h_{s,k} \right) - r^2 \lambda \frac{dT}{dr} = \text{constant} = \frac{\dot{\mathcal{Q}}}{4\pi}, \tag{1.15}$$

where $\dot{\mathcal{Q}}$ is the heat exiting the gas-phase towards the liquid phase, defined following the same logic as that for Eq. 1.10. It is also possible to substitute for the integrated result of global mass conservation Eq. 1.10 in Eq. 1.15 to have:

$$\frac{\dot{m}}{4\pi} h_s + r^2 \rho \left(\sum_{k=1}^{N} Y_k \mathrm{v}_k h_{s,k} \right) - r^2 \lambda \frac{dT}{dr} = \frac{\dot{\mathcal{Q}}}{4\pi}. \tag{1.16}$$

Most droplet heat transfer models express the energy result of Eq. 1.15 in terms of temperature instead of sensible enthalpy. To do so, we perform an additional assumption that only ideal gases are present, and so the definition of the sensible enthalpy for this case is recalled as being:

$$h_{s,k} = \int_{T^0}^{T} c_{p,k} dT + h_{s,k}^0 \tag{1.17}$$

where T^0 is a reference temperature, $h_{s,k}^0$ is the sensible enthalpy at that reference temperature, and c_p is the specific heat at constant pressure. It is also common to make a further assumption that $\int_{T^0}^{T} c_{p,k} dT \approx c_{p,k}(T - T^0)$, meaning, constant specific heat with respect to the temperature. For most CFD codes this is reasonable, as argued for instance in (Sazhin 2017). This is because the CFD integration procedures are typically carried out with explicit schemes, and so the properties are all evaluated only once at each time-step and so regarded as being constant already. For droplet models, the reference temperature is also typically taken to be the one at the surface of the droplet, namely $T^0 = T^s$.

Substitution of the simplified expression $h_{s,k} = c_{p,k}(T - T^0)$ for the sensible enthalpy onto Eq. 1.15 leads to:

$$r^2 \rho \mathrm{u} c_p (T - T^s) + r^2 \rho \left(\sum_{k=1}^{N} Y_k \mathrm{v}_k^{D,Y} c_{p,k} (T - T^s) \right) - r^2 \lambda \frac{dT}{dr} = \frac{\dot{\mathcal{Q}}}{4\pi}, \tag{1.18}$$

where the specific heat of the gaseous mixture is defined as:

$$c_p = \sum_{k=1}^{N} Y_k c_{p,k}. \tag{1.19}$$

Similarly, substitution of the integrated global mass conservation Eq. 1.10 on Eq. 1.18 above yields:

$$\boxed{\frac{\dot{m}}{4\pi} c_p (T - T^s) + r^2 \rho \left(\sum_{k=1}^{N} Y_k \mathrm{v}_k^{D,Y} c_{p,k} (T - T^s) \right) - r^2 \lambda \frac{dT}{dr} = \frac{\dot{\mathcal{Q}}}{4\pi}} \tag{1.20}$$

As mentioned before, the next step for most droplet phase-change models developed in this manuscript is to perform a second integration of Eqs. 1.13/1.14 for mass transfer developments or Eqs. 1.18/1.20 for energy developments. To perform this second integration, a closure for the diffusion velocities v_k^D is needed, since they represent an additional parameter. This closure will be introduced in Chap. 2.

This second integration procedure is also typically carried out through a definite integral, namely, using specified limits of integration. As will be shown on the next chapter, this is typically done from the surface of the droplet $r = R_d$ towards a far-away coordinate $r \to \infty$. Also, since one of the bounds of integration is at the surface, some quantities must be evaluated there, in particular the mass fraction of each species k at the gaseous side Y_k^s. This is done here through the vapor-liquid equilibrium hypothesis, in Chap. 3. Finally, even though the assumption of spherical symmetry does not allow for a generic, three-dimensional velocity field to be taken account, the film theory strategy has been used to allow for convection effects to be taken into account through boundary layers. The required correlations for convection scenarios are discussed in Chap. 6 whereas the film theory is formally introduced in Chap. 5.

1.4 Summary of expressions

The baseline equations for droplet phase-change models are summarized in Table 1.3 below for reference.

Mass transfer rate	$r^2 \rho \mathrm{u} = \dfrac{\dot{m}}{4\pi}$
Species mass transfer rate	$Y_i \dfrac{\dot{m}}{4\pi} + r^2 \rho Y_i \mathrm{v}_i^{D,Y} = \dfrac{\dot{m}_i}{4\pi}$
Heat transfer rate	$\dfrac{\dot{m}}{4\pi} c_p (T - T^s) + r^2 \rho \left(\sum_{k=1}^{N} Y_k \mathrm{v}_k^{D,Y} c_{p,k} (T - T^s) \right) - r^2 \lambda \dfrac{dT}{dr} = \dfrac{\dot{\mathcal{Q}}}{4\pi}$

Figure 1.3: Summary of the baseline equatons for droplet phase-change models.

Chapter 2

Species diffusion velocities

In Chap. 1, the main hypotheses required for deriving the droplet heat and mass transfer models have been established, creating the foundation for these models. However, as pointed out, it is still necessary to add closures for the diffusion velocities v_k^D of each species, that appear both on the species conservation (Eq. 1.14) and the energy conservation (Eq. 1.16) equations for instance.

In the present chapter, we first show a general formulation, obtained from the Boltzmann equations in the gaseous phase, that ties the difference of molecular velocities as well as other terms to the molar fraction gradient. Simplifications inline with those assumed in the first chapter are then performed, leading to the so-called Stefan-Maxwell equations. These in turn can be used to characterize the species diffusion velocities. The chapter structure will first present a general scope. Then, particular developments are performed for the binary case, since it is used for single-component droplet models. This includes the computation of binary diffusion coefficients. Finally, a brief overview is given towards the multi-component extension.

2.1 The Stefan-Maxwell equations

The molecular velocity of a given species can be decomposed either through mass-related velocities or molar-related ones:

$$\mathbf{v}_i^m = \mathbf{u} + \mathbf{v}_i^{D,Y} = \mathbf{u}^X + \mathbf{v}_i^{D,X}, \tag{2.1}$$

with the mass and molar advective velocities defined respectively as:

$$\mathbf{u} = \sum_{k=1}^{N} Y_k \mathbf{v}_k^m, \tag{2.2}$$

$$\mathbf{u}^X = \sum_{k=1}^{N} X_k \mathbf{v}_k^m. \tag{2.3}$$

In this way, superscripts Y or X are used for velocities related to mass or molar fluxes, respectively.

Also, to retrieve global mass conservation when summing the contributions of all species, it must follow that:

$$\sum_{k=1}^{N} Y_k \mathrm{v}_k^{D,Y} = 0. \tag{2.4}$$

As shall be further explored in this manuscript, this two-fold decomposition of the molecular velocity can lead to different closures for the diffusion velocities. Regardless of the simplifying strategies, the most general closure for the molecular velocities can be traced back to the following equation, derived from the Boltzmann equations in kinetic theory (Sazhin 2014), (Klingenberg 2015):

$$\nabla X_i = -\sum_{k=1}^{N} \frac{X_i X_k}{\tilde{D}_{i,k}} [\mathbf{v}_i^m - \mathbf{v}_k^m] + (Y_i - X_i)\frac{\nabla \mathbf{p}}{\mathbf{p}} + \frac{\rho}{\mathbf{p}} \sum_{k=1}^{N} Y_i Y_k (\boldsymbol{f}_i - \boldsymbol{f}_k) + \\ + \sum_{k=1}^{N} \left[\left(\frac{X_i X_k}{\rho \tilde{D}_{i,k}} \right) \left(\frac{D_k^T}{Y_k} - \frac{D_i^T}{Y_i} \right) \right] \left(\frac{\nabla T}{T} \right). \tag{2.5}$$

Eq. 2.5 above directly connects the gradient of the molar fractions of each species to the pair-wise difference of all molecular velocities, as well as multiple other terms. If hypotheses #4 (low Mach, dilatable flow) and #5 (no volumetric forces) from Chap. 1 are applied in conjunction with:

8. Negligible Soret effect: $\sum_{k=1}^{N} \left[\left(\frac{X_i X_k}{\rho \tilde{D}_{i,k}} \right) \left(\frac{D_k^T}{Y_k} - \frac{D_i^T}{Y_i} \right) \right] \left(\frac{\nabla T}{T} \right) \approx 0$,

then, Eq. 2.5 becomes:

$$\nabla X_i = -\sum_{k=1}^{N} \frac{X_i X_k}{\tilde{D}_{i,k}} [\mathbf{v}_i^m - \mathbf{v}_k^m]. \tag{2.6}$$

The hypothesis of negligible Soret effect was briefly mentioned in Chap. 1 as well.

It is then possible to recast Eq. 2.1 in terms of differences of velocities between two species i, j as being:

$$\mathbf{v}_i^m - \mathbf{v}_j^m = \mathbf{v}_i^{D,Y} - \mathbf{v}_j^{D,Y} = \mathbf{v}_i^{D,X} - \mathbf{v}_j^{D,X}, \tag{2.7}$$

and so Eq. 2.6 can also be recast in terms of differences of mass or molar diffusion velocities:

$$\nabla X_i = -\sum_{k=1}^{N} \frac{X_i X_k}{\tilde{D}_{i,k}} [\mathbf{v}_i^{D,Y} - \mathbf{v}_k^{D,Y}], \tag{2.8}$$

$$\nabla X_i = -\sum_{k=1}^{N} \frac{X_i X_k}{\tilde{D}_{i,k}} [\mathbf{v}_i^{D,X} - \mathbf{v}_k^{D,X}] \tag{2.9}$$

Eqs. 2.6, 2.8 and 2.9 are often referred to as the Stefan-Maxwell equations. It is also possible to find these equations written in terms of molar fluxes. For instance, Eq. 2.6 can be recast as:

$$\nabla X_i = -\sum_{k=1}^{N} \frac{[X_k \mathcal{N}_i - X_i \mathcal{N}_k]}{c\tilde{D}_{i,k}}, \tag{2.10}$$

with $\mathcal{N}_i = c_i \mathbf{v}_i^m = cX_i \mathbf{v}_i^m$ being the molar flux of species i, and c being the molar density.

Finally, due to the difficulty of evaluating the generalized multi-component binary diffusion coefficients $\tilde{D}_{i,k}$, it also customary to make the following hypothesis:

9. Binary diffusion coefficients in the multi-component gas-phase are taken to be the same as if each pair of species was in a binary mixture, i.e. $\tilde{D}_{i,j} \approx D_{i,j}$.

In (Mason and Marrero 1970), it is mentioned that a first approximation $[D_{i,j}]_1$ for the multi-component binary diffusion coefficients would be the Chapman-Enskog result, Eq. 2.13 in the next section. Then, a second approximation could be expressed as:

$$[D_{i,j}]_2 = \frac{[D_{i,j}]_1}{1 - \Delta_{i,j}}, \tag{2.11a}$$

$$\Delta_{i,j} = \frac{(6C^*_{i,j} - 5)^2}{10} \left[\frac{X_i^2 P_i + X_j^2 P_2 + X_i X_j P_{i,j}}{X_i^2 Q_i + X_j^2 Q_2 + X_i X_j Q_{i,j}} \right], \tag{2.11b}$$

where $\Delta_{i,j}$ is a correction factor, P and Q are algebraic expressions containing different types of collision integrals and C^* is a dimensionless ratio of collision integrals. In (Sandler and Mason 1968) it was shown that for most typical cases the $\Delta_{i,j}$ factor is of the order of experimental errors and could therefore be neglected. However, some specific gaseous mixture combinations can exhibit larger deviations, and so a particular study concerning droplet in spray combustion applications would be of interest.

If hypothesis #2 of spherical symmetry is also made, the Stefan-Maxwell equations become:

$$\frac{dX_i}{dr} = -\sum_{k=1}^{N} \frac{X_i X_k}{D_{i,k}} \left[\mathrm{v}_i^m - \mathrm{v}_k^m \right], \tag{2.12a}$$

$$\frac{dX_i}{dr} = -\sum_{k=1}^{N} \frac{X_i X_k}{D_{i,k}} \left[\mathrm{v}_i^{D,Y} - \mathrm{v}_k^{D,Y} \right], \tag{2.12b}$$

$$\frac{dX_i}{dr} = -\sum_{k=1}^{N} \frac{X_i X_k}{D_{i,k}} \left[\mathrm{v}_i^{D,X} - \mathrm{v}_k^{D,X} \right], \tag{2.12c}$$

$$\frac{dX_i}{dr} = -\sum_{k=1}^{N} \frac{[X_k \mathcal{N}_i - X_i \mathcal{N}_k]}{cD_{i,k}}. \tag{2.12d}$$

The results represented through Eqs. 2.12a-2.12d are mostly used for multi-component droplet models, where more than two species are present in the gaseous phase.

2.2 Computing binary diffusion coefficients

For all mass diffusion closures used in this manuscript and highlighted below, the binary diffusion coefficient for each pair of species in the gas-phase is necessary. To compute these, most methods are based on the Chapman-Enskog equation, derived from solving the Boltzmann equation in kinetic theory (Poling, Prausnitz, and O'Connell 2001):

$$D_{i,j} = \frac{3}{16}\frac{\left(4\pi kT/\bar{W}_{ij}\right)^{1/2}}{n\pi\sigma_{ij}^2\Omega_D} f_D, \tag{2.13}$$

where k is the Bolzmann's constant, $\bar{W}_{ij} = 2(W_i^{-1} + W_j^{-1})^{-1}$ is an average molecular weight between those of species i, j, n is the molecular number density, σ_{ij} is a characteristic length given in angstoms (Å), Ω_D is the collision integral for diffusion and f_D is a correction factor. As noted by Poling et al., f_D is of the order of one; if we assume $f_D \approx 1$ and that n can be obtained by supposing an ideal gas law, then Eq. 2.13 becomes:

$$D_{i,j} = 0.00266\left[\frac{T^{3/2}}{\mathrm{p}\bar{W}_{ij}^{1/2}\sigma_{ij}^2\Omega_D}\right], \tag{2.14}$$

where the pressure p is expressed in bar. This modelling approach usually comes paired with the Lennard-Jones potential to theoretically approximate the intermolecular energy ψ between two molecules at a distance R from each other:

$$\psi = 4\epsilon\left[\left(\frac{\sigma}{R}\right)^{12} - \left(\frac{\sigma}{R}\right)^{6}\right], \tag{2.15}$$

where ϵ and σ here are the characteristic Lennard-Jones energy and length, respectively. Poling et al. note that it is also possible to demonstrate that Ω_D is a function that depends only on kT/ϵ_{ij}. If the following rules are chosen to represent the decomposition of $\epsilon_{ij}, \sigma_{ij}$:

$$\epsilon_{ij} = (\epsilon_i\epsilon_j)^{1/2}, \tag{2.16a}$$

$$\sigma_{ij} = \frac{\sigma_i + \sigma_j}{2}, \tag{2.16b}$$

then it is possible to to correlate the expression of Ω_D in particular following the methodology of (Neufeld, Janzen, and Aziz 1972) using:

$$\Omega_D = \frac{A}{(T^*)^B} + \frac{C}{\exp(DT^*)} + \frac{E}{\exp(FT^*)} + \frac{G}{\exp(HT^*)}, \tag{2.17}$$

where $T^* = kT/\epsilon_{ij}$, $A = 1.06036$, $B = 0.1561$, $C = 0.193$, $D = 0.47635$, $E = 1.03587$, $F = 1.52996$, $G = 1.76474$, $H = 3.89411$.

In practice, methods further based on empirical correlations are often preferred in conjunction with some other simplifying assumptions. The Wilke and Lee equation, first published in (Wilke and Lee 1955) is one of such correlations that has been often used:

$$D_{i,j} = 10^{-7} \frac{(3.03 - 0.98\bar{W}_{ij}^{-1/2})T^{3/2}}{\mathrm{p}\bar{W}_{ij}^{1/2}\sigma_{ij}^2\Omega_D}, \tag{2.18}$$

where the parameters σ_{ij} and ϵ_{ij} are obtained from Eqs. 2.16 and the individual σ_i and ϵ_i of species i given by:

$$\sigma_i = 1.18V_{b,i}^{1/3}, \tag{2.19a}$$

$$\epsilon_i = 1.15kT_{b,i}, \tag{2.19b}$$

where $T_{b,k}$ is the boiling temperature of species i at 1 atm and $V_{b,i}$ the liquid molar volume at this temperature, both of which are determined experimentally.

Then, the Fuller equation, after the publications (Fuller and Giddings 1965), (Fuller, Schettler, and Giddings 1966), (Fuller, Ensley, and Giddings 1969) consolidated the following correlation to modify Eq. 2.14:

$$D_{i,j} = 0.00143 \left(\frac{T^{1.75}}{\mathrm{p}}\right) \left[\frac{\left(\frac{1}{W_i} + \frac{1}{W_j}\right)^{1/2}}{\sqrt{2}\left(\delta_i^{1/3} + \delta_j^{1/3}\right)^2}\right] \mathrm{x}10^{-4}, \tag{2.20}$$

where the pressure p must be expressed in bar and the 10^{-4} factor appears to convert from cm^2/s to m^2/s. The factors $\delta_{i,j}$ represent the sum of atomic volumes, and they are correlated semi-empirically. For this manuscript, we prefer the methodology of Fuller et al. due to its recurrent use, which led to improvements for its correlations over the years, and due to the numerical flexibility it provides when implementing new species. An updated list for relevant parameters can be found in (e. V. 2010) for instance.

2.3 Binary case: Fick's law of diffusion

For single-component droplets, a classical hypothesis is to assume that only one inert species is also present in the gas-phase, such that the gaseous mixture is composed of only two species. In this way, the Stefan-Maxwell Eqs. 2.12a-2.12d become considerably simplified, as shown below.

For the binary case, the indexes $1, 2$ can be used for each species instead of the conventional $k = 1, 2, ..., N$ for multi-component mixtures. The following relations are then

true concerning mass/molar fractions and their gradients:

$$Y_{1,2} = 1 - Y_{2,1}, \tag{2.21}$$

$$X_{1,2} = 1 - X_{2,1}, \tag{2.22}$$

$$Y_1 = \frac{X_1}{X_1 + (1 - X_1)W_2/W_1}, \tag{2.23}$$

$$\nabla Y_{1,2} = \left[\frac{Y_1 Y_2}{X_1 X_2}\right] \nabla X_{1,2}, \tag{2.24}$$

$$\nabla X_{1,2} = \left[\frac{X_1 X_2}{Y_1 Y_2}\right] \nabla Y_{1,2}. \tag{2.25}$$

Due to Eqs. 2.21 and 2.22, the species conservation equations would need to be solved for only one species.

Eq. 2.12a for a binary mixture leads to, for species 1:

$$\frac{dX_1}{dr} = -\frac{X_1 X_2}{D_{1,2}} \left[\mathrm{v}_1^{D,Y} - \mathrm{v}_2^{D,Y}\right] \tag{2.26}$$

Substituting Eq. 2.25 leads to:

$$\frac{dY_1}{dr} = -\frac{Y_1 Y_2}{D_{1,2}} \left[\mathrm{v}_1^{D,Y} - \mathrm{v}_2^{D,Y}\right]. \tag{2.27}$$

Therefore it is possible to see that, for binary mixtures, a direct replacement of molar to mass fractions on the Stefan-Maxwell equations is possible. Further, for the binary case Eq. 2.4 yields $\mathrm{v}_2 Y_2 = -\mathrm{v}_1 Y_1$. Substituting this on the RHS of Eq. 2.27 above yields:

$$Y_1 \mathrm{v}_1^{D,Y} = -D_{1,2} \frac{dY_1}{dr}. \tag{2.28}$$

Eq. 2.28 above is typically referred to as Fick's law of diffusion. The condition presented through Eq. 2.4 also implies that the binary diffusion coefficients are interchangeable as well i.e. $D_{1,2} = D_{2,1}$.

2.4 The multi-component case

To be able to integrate the conservation equations for a multi-component gaseous phase, usually the strategy has been to seek for simplified expressions for the mass diffusion velocities v_D^Y. The two most common strategies for CFD solvers have been well documented in (Poinsot and Veynante 2012).

The first one consists in supposing that all species in the gaseous mixture have the same diffusion coefficient $\bar{D}$ between each other. In this case, the Stefan-Maxwell Eq. 2.8 for mass diffusion velocities become:

$$X_i \mathbf{v}_i^{D,Y} = X_i \sum_{k=1}^{N} X_k \mathbf{v}_k^{D,Y} - \bar{D} \nabla X_i. \tag{2.29}$$

Multiplying the above equation by Y_i/X_i yields:

$$Y_i \mathbf{v}_i^{D,Y} = Y_i \sum_{k=1}^{N} X_k \mathbf{v}_k^{D,Y} - \bar{D} Y_i \frac{\nabla X_i}{X_i}. \tag{2.30}$$

Eq. 2.30 is then summed for all species N:

$$\sum_{j=1}^{N} Y_j \mathbf{v}_j^{D,Y} = \sum_{j=1}^{N} \left[Y_j \sum_{k=1}^{N} X_k \mathbf{v}_k^{D,Y} \right] - \bar{D} \sum_{j=1}^{N} Y_j \frac{\nabla X_j}{X_j}. \tag{2.31}$$

In the LHS, $\sum_{j=1}^{N} Y_j \mathbf{v}_j^{D,Y} = 0$ to ensure global mass conservation. The first term in the RHS can be split as:

$$\sum_{j=1}^{N} \left[Y_j \sum_{k=1}^{N} X_k \mathbf{v}_k^{D,Y} \right] = \left[\sum_{j=1}^{N} Y_j \right] \left[\sum_{k=1}^{N} X_k \mathbf{v}_k^{D,Y} \right] = \sum_{k=1}^{N} X_k \mathbf{v}_k^{D,Y}. \tag{2.32}$$

Eq. 2.31 then becomes:

$$\sum_{k=1}^{N} X_k \mathbf{v}_k^{D,Y} = \bar{D} \sum_{k=1}^{N} Y_k \frac{\nabla X_k}{X_k}. \tag{2.33}$$

Substituting Eq. 2.33 into the left term of the RHS in Eq. 2.29 leads to:

$$\mathbf{v}_i^{D,Y} = \bar{D} \left[\sum_{k=1}^{N} Y_k \frac{\nabla X_k}{X_k} - \frac{\nabla X_i}{X_i} \right] \tag{2.34}$$

Now, the following expression can be developed for the ratio of gradients of molar fractions to molar fractions:

$$\frac{\nabla X_i}{X_i} = \frac{\nabla (Y_i W)}{X_i W_i} = \frac{W \nabla Y_i + Y_i \nabla W}{X_i W_i} = \frac{\nabla Y_i}{Y_i} + \frac{\nabla W}{W}. \tag{2.35}$$

Substituting this result on Eq. 2.34 leads to:

$$\mathbf{v}_i^{D,Y} = \bar{D} \left[\sum_{k=1}^{N} \nabla Y_k + \sum_{k=1}^{N} Y_k \frac{\nabla W}{W} - \frac{\nabla Y_i}{Y_i} - \frac{\nabla W}{W} \right] \tag{2.36}$$

By noting that $\sum_{k=1}^{N} \nabla Y_k = 0$ and that $\sum_{k=1}^{N} Y_k \frac{\nabla W}{W} = \left(\sum_{k=1}^{N} Y_k \right) \frac{\nabla W}{W} = \frac{\nabla W}{W}$, the molar weight terms cancel out leading to the following formulation:

$$Y_i \mathbf{v}_i^{D,Y} = -\bar{D} \nabla Y_i, \tag{2.37}$$

which preserves the same structure as Fick's law for binary diffusion, Eq. 2.28. This means that the supposition that all species have the same diffusional behaviour, characterised through an equal diffusion coefficient $\bar{D}$, allows for a multi-component mass

diffusion closure that has the same structure as the single-component one, and thus any integration techniques that benefit from Fick's law would also carry over to the multi-component case. In particular, Fick's law organically enforces the conservation of global mass' relation with respect to the diffusion velocities, Eq. 2.4.

Of course, the main challenge of this approach resides then in how to compute this average diffusion coefficient. One possibility is to use an analogy for the single-component case, where a single fuel species and a single inert species are present. In the multi-component case, the diffusion could then be described by clumping all fuel vapors together as a single "average" one and all inert species as a single one as well. Then, as proposed for instance in (Liu, Liu, Mi, Wang, and Jiang 2016), it would be still possible to use the Wilke and Lee formula, Eq. 2.18. To achieve their strategy, the quantities W, ϵ and σ are computed as follows for each "average species" F and I:

$$W_F = \sum_{k=1}^{N_F} X_k^n W_k, \forall k \in \text{fuels}, \tag{2.38a}$$

$$W_I = \sum_{k=1}^{N_I} X_k^n W_k, \forall k \in \text{inerts}, \tag{2.38b}$$

$$\epsilon_F = \sum_{k=1}^{N_F} X_k^n \epsilon_k, \forall k \in \text{fuels}, \tag{2.38c}$$

$$\epsilon_I = \sum_{k=1}^{N_I} X_k^n \epsilon_k, \forall k \in \text{inerts}, \tag{2.38d}$$

$$\sigma_F = \sum_{k=1}^{N_F} X_k^n \sigma_k, \forall k \in \text{fuels}, \tag{2.38e}$$

$$\sigma_I = \sum_{k=1}^{N_I} X_k^n \sigma_k, \forall k \in \text{inerts}. \tag{2.38f}$$

where the normalized molar fractions X^n are obtained for species within each group, fuel and inert, as follows:

$$X_i^n = \frac{X_i}{\sum_{k=1}^{N_F} X_k}, \forall i \in \text{fuels}, \tag{2.39a}$$

$$X_j^n = \frac{X_j}{\sum_{k=1}^{N_I} X_k}, \forall j \in \text{inerts}, \tag{2.39b}$$

with N_F, N_I being the number of fuel and inert species, respectively. The Wilke and Lee formula can then be employed between average species F and I to yield a diffusion coefficient that can be used for all species.

Conversely, the main drawback of the above approach is that the diffusional behaviour of all species is clumped together, which represents a great loss of information, given the multi-component context. A second approach that has been often used is to relax the hypothesis of same diffusion coefficient to another one where each species now has its own diffusion coefficient, but the same towards all other species, i.e. $D_{i,j} = D_i$. It will also be shown in Chap. 11 that when such approach is taken, the Stefan-Maxwell equations are simplified to the following:

$$Y_i \mathrm{v}_i^{D,Y} = -D_i \frac{dY_i}{dr}, \tag{2.40}$$

again for each species i in the gaseous mixture.

The key difference between Eqs. 2.40 and 2.37 is of course the diffusion coefficients, and the expression of used models in the litterature for these diffusion coefficients is such that Eq. 2.4 is no longer attained. Namely, mass conservation is no longer organically guaranteed when using this approach. To counter this, it is possible to solve for all species except for one, and enforce this last species to obey the rule $\sum_{k=1}^{N} Y_k = 1$. In this way, we are effectively making this last species absorb all eventual deviations that come from such an approach.

Another approach consists in enforcing a correction velocity, which has typically been associated with the Hirschfelder-Curtiss (H-C) diffusion velocity (or coefficient). This will also be explored in detail when the Ebrahimian and Habchi droplet mass transfer model is derived, in Chap. 9. The (H-C) approximation for the diffusion velocities is:

$$X_i \mathbf{v}_i^{D,Y} = -\frac{(1 - Y_i)}{\sum\limits_{\substack{k=1 \\ k \neq i}}^{N} X_k / D_{i,k}} \frac{dX_i}{dr}, \tag{2.41}$$

and this has motivated the definition of a diffusion coefficient that reads:

$$D_i = \frac{(1 - Y_i)}{\sum\limits_{\substack{k=1 \\ k \neq i}}^{N} X_k / D_{i,k}}. \tag{2.42}$$

In parallel, if a mass correction velocity $\mathbf{u}_c$ defined as follows:

$$\mathbf{u}_c = -\sum_{k=1}^{N} Y_k \mathbf{v}_k^{D,Y}. \tag{2.43}$$

is introduced in the species conservation equation before the integration, then Eq. 2.4 would be once again attained.

Finally, the last approach is to directly try and integrate the Stefan-Maxwell equations by employing some simplifying hypotheses. The main advantage of this strategy is that no simplifying hypotheses are needed for the diffusion coefficients; however typically these methods tend to be more expensive computationally. Formulations that directly integrate the Stefan-Maxwell equations will be discussed in Chap. 8 and Chap. 9.

2.5 Summary

In this chapter, the Stefan-Maxwell equations were obtained, from a simplification of the Boltzmann equations of kinetic theory with simplifying hypothesis consistent with those of droplet phase-change models. These equations represent the foundation of the the mass diffusion velocities closure, which is required for all droplet phase-change models, as shown in Chap. 1. Then, a brief discussion was carried out for the computation of the binary diffusion coefficients, which are useful not only for the binary case but also for multi-component treatments. The Fuller method emerged as the preferred one for this manuscript due to its flexibility. Concerning the extension towards the multi-component modelling, two common approaches were highlighted, one that directly degenerates to the binary formulation, and another one that operates in analogy with the binary case. Therein, the Hirschfelder-Curtiss approximation was also shown. These topics will be further detailed in Chaps. 8, 9, and 11.

Chapter 3

The vapor-liquid equilibrium

For all droplet phase-change models, a quantity that is always needed is the mass (or molar) fraction of each participating fuel species evaluated at the surface of the droplet, see Fig. 3.1. This is because of the subsequent integration of the species conservation Eq. 1.14, which is typically carried out between the surface of the droplet and another coordinate $R > R_d$, as seen in Fig. 3.1 below for instance. At the surface of the droplet, $Y_i(r) = Y_i(R_d) = Y_i^s$, and this quantity is obtained using a vapor-liquid equilibrium (VLE) assumption.

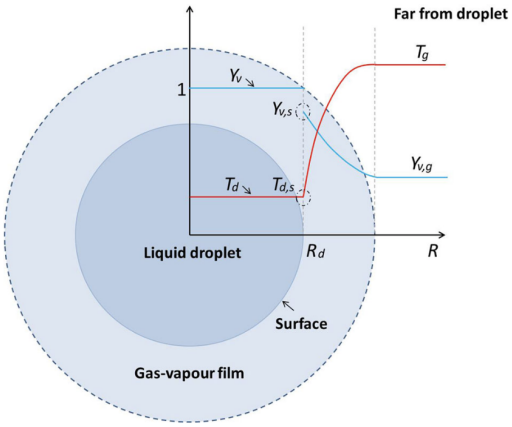

Figure 3.1: Schematic for typical integration region for droplet modelling. Extracted from (Pinheiro and Vedovoto 2019)

The VLE hypothesis is usually accepted for typical spray combustion applications, provided that the droplet is not too small, as discussed in the Introduction. In a constant pressure and temperature problem, the VLE states that there is an equality of fugacities between both liquid and gaseous phases, for each species:

$$f_i^l = f_i^v, \tag{3.1}$$

where the index v for vapor is used to differentiate from inert species. The fugacities f

can be seen as an "effective partial pressure" for real gases in multi-component gaseous mixtures for the general case. They are equal to the pressure of an ideal gas having the same temperature and molar Gibbs free energy as the associated real gas, and so they have the units of pressure. The objective of this chapter is to show how to set this VLE using fugacity expressions.

3.1 General formulation: activity coefficient approach

In order to develop the general framework of Eq. 3.1, it is customary to define the fugacity coefficients for each phase, liquid l or vapor v:

$$\phi_i^{l,v} = \frac{f_i^{l,v}}{X_i^{l,v}\mathrm{p}}, \tag{3.2}$$

where p is the ambient pressure. Then, one possible way to expand Eq. 3.1 is through activity coefficient models (Poling, Prausnitz, and O'Connell 2001). To do that, activity coefficients γ are defined for each species as:

$$\gamma_i = \frac{1}{X_i^l}\frac{f_i^l}{f_i^{0,l}}, \tag{3.3}$$

where $f_i^{0,l}$ is a standard-state fugacity which is commonly taken to be the one of a pure liquid from species i. If this choice is made, it is possible to directly see that $\gamma = 1.0$ if there is only one liquid species, which is the case for single-component droplets. Following the developments in (Poling, Prausnitz, and O'Connell 2001), Eq. 3.1 can then be expanded as:

$$X_i^g\mathrm{p} = X_i^l\gamma_i\mathrm{p}_i^{sat}\mathcal{F}_i, \tag{3.4}$$

where p_i^{sat} is the saturation vapor pressure and $\mathcal{F}_i$ is a correction factor defined as:

$$\mathcal{F}_i = \frac{\phi_i^{sat}}{\phi_i^v}\exp\int_{\mathrm{p}_i^{sat}}^{\mathrm{p}}\frac{v_i^l}{RT}d\mathrm{p}, \tag{3.5}$$

where ϕ_i^{sat} is the saturation fugacity coefficient, typically computed from correlations using volumetric data and equations of state, v is the specific volume and R is the universal gas constant. As pointed out in (Poling, Prausnitz, and O'Connell 2001), for low-pressure applications, $\mathcal{F}_i \approx 1.0$ and so Eq. 3.4 can be simplified.

From Eq. 3.4 it is possible to compute molar fractions for each species at the gaseous side of the interface. The additional challenges of this approach then lie on the computation of the saturation vapor pressure and the activity coefficients.

In particular, for the case of single-component droplet evaporation, only the fugacity of species 1 is relevant. For this case, $X_1^l = 1.0$, $\gamma_1 = 1.0$ as discussed before and by assuming $\mathcal{F}_i = 1.0$, Eq. 3.4 reduced to:

$$X_1^g = \frac{\mathrm{p}_1^{sat}}{\mathrm{p}}, \tag{3.6}$$

which is sometimes referred to as Henry's law. Therefore, essentially, the vapor-liquid equilbrium hypothesis allows for a direct computation of the molar fraction of the fuel species at the surface of the droplet through its saturation vapor pressure p_i^{sat}. For multi-component mixtures, other approaches will be discussed further.

3.2 Saturation vapor pressure

In this section, three approaches are discussed for the computation of the saturation vapor pressure of a liquid species. First, the Clausius-Clapeyron equation is developed. It is one of the most used methods to compute the saturation vapor pressure, since it comes from an analytical formulation which avoids the tabulation of specific coefficients. In contrast, the Antoine and Wagner equations require fine-tuning of coefficients with experimental data, typically translating into more precise results at the expense of the laborious task of building a coefficient database.

3.2.1 The Clausius-Clapeyron equation

To fully derive the hypotheses behind the Clausius-Clapeyron closure, we start from the first law of thermodynamics:

$$dU = dQ - dW, \tag{3.7}$$

where dU is the infinitesimal variation of internal energy, dQ is the infinitesimal amount of heat supplied to the system by its surroundings and dW is the infinitesimal work done by the system on its surroundings. For a reversible process, the first law can be developed to obtain:

$$dG = VdP - SdT, \tag{3.8}$$

where S is the entropy, T the absolute temperature, p is the pressure and V the volume.

In the case of vapor-liquid equilibrium between two phases, if vaporization takes place at constant pressure and temperature, Eq. 3.8 tells us that $dG = 0$. This translates to equal Gibbs' free energies between the liquid and vapor phases, namely $G^l = G^v$ at the given vapor-liquid equilibrium temperature. This would still hold true for a new state with a different temperature and different pressure, translating to:

$$dG^l = dG^v. \tag{3.9}$$

Substituting Eq. 3.8 for each phase and rearranging yields:

$$(S^v - S^l)dT = (V^v - V^l)d\mathrm{p}_{sat}, \tag{3.10}$$

where the saturation vapor pressure p_{sat} has appeared due to the hypothesis of vapor-liquid equilibrium. Now, using $G = H - TS$ for both phases leads to:

$$H^v - TS^v = H^l - TS^l \rightarrow H^v - H^l = (S^v - S^l)T. \tag{3.11}$$

Substituting the change of entropy above into Eq. 3.10 and casting the enthalpy difference as $\Delta H_{vap} = H^v - H^l$ leads to:

$$\frac{\Delta H_{vap}}{T(V^v - V^l)}dT = d\mathrm{p}_{sat}. \tag{3.12}$$

As noted in (Poling, Prausnitz, and O'Connell 2001), this is known as the Claperyon equation. However, this is typically further developed for droplet evaporation problems. Two simplifications are made:

1. Vapor behaves like ideal gas, such that $V^v = RT/\mathrm{p}_{sat}$ for this case;
2. Low pressure applications, such that the approximation $V^v >> V^l$ can be made.

These simplifications lead to:

$$\frac{\Delta H_{vap}}{RT^2}dT = \frac{d\mathrm{p}_{sat}}{\mathrm{p}_{sat}}. \tag{3.13}$$

By noting that $d(1/T) = -1/T^2 dT$ and that $d\ln\mathrm{p}_{sat} = d\mathrm{p}_{sat}/\mathrm{p}_{sat}$, this can finally be rearranged as the Clausius-Clapeyron equation:

$$-\frac{\Delta H_{vap}}{R}d\left(\frac{1}{T}\right) = d\left(\ln\mathrm{p}_{sat}\right). \tag{3.14}$$

By further making the hypothesis that ΔH_{vap} is constant with respect to the temperature, which is true for small ranges of temperatures, this equation can be integrated. Of note is that is customary to express the enthalpy difference ΔH_{vap} between vapor and liquid states as a latent heat of vaporization, or simply, an enthalpy of vaporization. In this sense, in terms of notation, ΔH_{vap} will be expressed as L_{vap} from now on to follow the convention of this manuscript for clarity. To do that, we note that if the system at ambient pressure p is at vapor-liquid equilibrium, then, when $\mathrm{p}_{sat} = \mathrm{p}$, the temperature must be that of boiling, $T = T^b$.

$$-\frac{L_{vap}}{R}\int_T^{T_b} d\left(\frac{1}{T}\right) = \int_{\mathrm{p}_{sat}}^{\mathrm{p}} d\left(\ln\mathrm{p}_{sat}\right). \tag{3.15}$$

Integrating and rearranging leads to:

$$-\frac{L_{vap}}{R}\left(\frac{1}{T_b} - \frac{1}{T}\right) = \ln\left(\frac{\mathrm{p}}{\mathrm{p}_{sat}}\right). \tag{3.16}$$

Now, Eq. 3.16 above can be rearranged to yield:

$$\frac{\mathrm{p}^{sat}}{\mathrm{p}} = \exp\left[-\frac{\Delta H^{vap}}{R}\left(\frac{1}{T_b} - \frac{1}{T}\right)\right]. \tag{3.17}$$

For a single-component droplet, the supposition of ideal gases allows us to compute molar fractions through partial pressures, such that:

$$X_1^s = \exp\left[-\frac{\Delta H^{vap}}{R}\left(\frac{1}{T_b} - \frac{1}{T}\right)\right], \tag{3.18}$$

with X_1^s being the molar fraction of species 1 at the gaseous side of the surface of the droplet.

This result has been extensively used for the closure of droplet evaporation problems, as seen for example in (Miller, Harstad, and Bellan 1998). Now, it is also important to note that this result has been obtained supposing that the pressure in which the boiling temperature has been measured is the same pressure as the droplet is evaporating. Typically, boiling temperatures are measured at a reference pressure p^{atm} of 1 atm. Denoting the boiling temperature at that pressure as T_b^{atm}, the result of 3.17 can be recast as:

$$\frac{\mathrm{p}^{sat}}{\mathrm{p}^{atm}} = \exp\left[-\frac{\Delta H^{vap}}{R}\left(\frac{1}{T_b^{atm}} - \frac{1}{T}\right)\right]. \tag{3.19}$$

Another possibility as seen in (Poling, Prausnitz, and O'Connell 2001) is to take the reference through the pair of critical pressure and temperature, p_c, T_c:

$$X_1^s = \frac{\mathrm{p}_c}{\mathrm{p}}\exp\left[-\frac{\Delta H^{vap}}{R}\left(\frac{1}{T_c} - \frac{1}{T}\right)\right]. \tag{3.20}$$

Regardless of the strategy of choice, once the molar fraction has been obtained, a simple conversion to mass fractions allows for the obtention of the vapor mass fraction at the surface of the droplet, which appears throughout the mass-related derivations of the next chapters.

3.2.2 The Antoine equation

A different strategy when compared to the purely analytical Clausius-Clapeyron equation is the one first proposed in (Antoine 1888). Therein, the author devises a semi-empirical method by noticing that saturation vapor pressure data could be fitted using parabolas and exponentials. Part of the reasoning comes from the realization that the Clausius-Clapeyron equation could be approximated as:

$$\log_{10}\mathrm{p}_{sat} = c_1 - \frac{c_2}{T}, \tag{3.21}$$

with c_1 and c_2 being two constants that vary for each substance. However, this equation is valid only for small temperature ranges, and was thus deemed not practical enough, as

discussed for instance in (Rodgers and Hill 1978). After some developments, the equation was finally calibrated and expressed as:

$$\log_{10} \mathrm{p}_{sat} = A - \frac{B}{C+T}, \tag{3.22}$$

where A, B and C are all constants to be fitted depending on the substance. Eq. 3.22 contains a rather straightforward link between saturation vapor pressure and temperature. As mentioned before, one possible drawback of this approach when compared to the Clausius-Clapeyron equation is that the coefficients must be fitted for each substance. Fortunately, these coefficients are widely available today and one excellent source is the NIST webbook (Linstrom and Mallard 2014) where the user can search a vast database of species.

Still, this equation is known to not fit well over the complete range for the liquid phase (from melting point to boiling point) of a given species, even for classical species such as water. One possibility to overcome this is to have multiple sets of coefficients for each species. This can represent an even more cumbersome implementation, since more coefficients need to be implemented and a check must be made to choose which ones to use. Moreover, typically these coefficients create discontinuities at the temperature of transition, which can create numerical sensitivities.

3.2.3 The Wagner equation

Due to the above mentioned impracticalities for the Antoine equation, the Wagner equation as published in (Wagner 1973) has emerged as one robust candidate for the saturation vapor pressure. The general structure is:

$$\ln\left(\frac{\mathrm{p}_{sat}}{\mathrm{p}_c}\right) = \frac{1}{T_r}\left(A(1-T_r) + B(1-T_r)^{1.5} + C(1-T_r)^3 + D(1-T_r)^6\right), \tag{3.23}$$

where A,B,C and D are coefficients and $T_r = T/T_c$ is the reduced temperature.

Comparing Eq. 3.23 with Eq. 3.22 it is possible to see that Wagner's equation has a much more complex form, a fourth coefficient and also a reference based on the critical state p_c, T_c. In consequence, its results are typically way more robust; as mentioned in (e. V. 2010), its results can describe the temperature range from the triple point to the critical point, with a weakness only for low temperature extrapolations. Therefore, for spray combustion applications, this seems like an improvement choice when compared to the Clausius-Clapeyron and the Antoine equations.

Still, Eq. 3.23 has been steadily calibrated over the years and in (e. V. 2010) an improved version is oferred, where the last two exponents are changed:

$$\ln\left(\frac{\mathrm{p}_{sat}}{\mathrm{p}_c}\right) = \frac{1}{T_r}\left(A(1-T_r) + B(1-T_r)^{1.5} + C(1-T_r)^{2.5} + D(1-T_r)^5\right), \tag{3.24}$$

Coefficients for Eq. 3.24 (which are naturally not the same as those of Eq. 3.23) can be found in (e. V. 2010) for 275 substances, including all of the ones used in the investigations of this manuscript. Due to this improved behavior, this shall be the vapor pressure closure of choice for this manuscript.

In Fig. 3.2 below, the three different models for the saturation vapor pressure described above are compared for pure water, ethanol, acetone and n-dodecane. The comparison is performed by setting the Wagner equation Eq. 3.23 as a reference, since it is the most precise, and computing the following deviation metric:

$$\tilde{\Delta}\mathrm{p}_{sat} = \frac{\mathrm{p}_{sat}^{\mathrm{Wagner}} - \mathrm{p}_{sat}^{*}}{\mathrm{p}_{sat}^{\mathrm{Wagner}}}, \tag{3.25}$$

where p_{sat}^{*} is computed using either the Clausius-Claperyon Eq. 3.19 (black) or the Antoine Eq. 3.22 (red). Results are ploted starting from $T = 300K$ and going to 99% of each species' boiling temperature (see Appendix C).

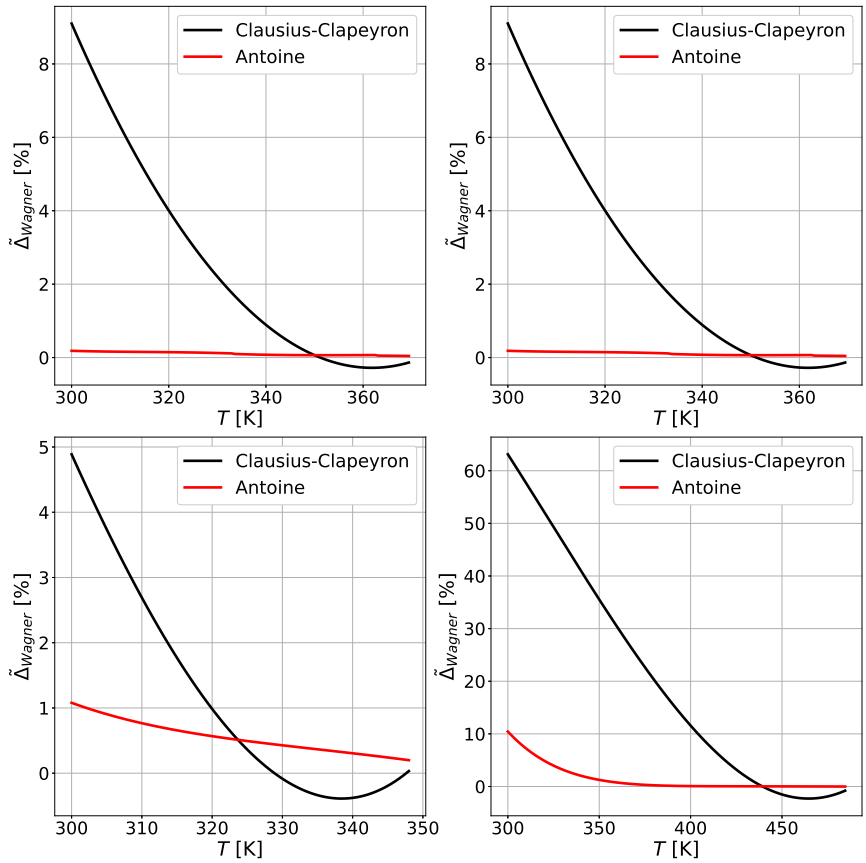

Figure 3.2: Normalized deviation from Wagner's equation for water (top-left), ethanol (top-right), acetone (bottom-left) and n-dodecane (bottom-right)

In Fig. 3.2, it is directly possible to see that the Antoine equation presents less deviations from the Wagner equation than Clausius-Clapeyron. Furthermore, the farther away from the boiling point, the worse the Clausius-Clapeyron equation performs. Acetone and n-dodecane represent the species with the lowest and highest boiling point respectively, and this is why the worst deviation for Clausius-Clapeyron for acetone is around 5% whereas n-dodecane can go as far as 60%.

Multiple studies in the litterature have shown that these deviations translate into great impacts in predicting droplet phase-change characteristics, such as the droplet lifetime, as seen in (Filho, Filho, van Oijen, Sadiki, and Janicka 2019) for instance. In this way, the Clausius-Clapeyron is generally not recommended due to its lack of flexibility.

3.3 Activity coefficient computations

Eq. 3.3 establishes that $\gamma_1 = 1$ for when species 1 is the only species inside the droplet, if the standard state fugacity is that of the pure liquid (assumed to be the case here). Therefore, the modelling of activity coefficients is only relevant for multi-component applications. One simple approach is to use a first approximation by direct analogy and impose that $\gamma = 1$ for all fuel species. This methodology is referred to as Raoult's law, and from Eq. 3.4 it provides the following result, assuming that $\mathcal{F} = 1$:

$$X_i^g = X_i^l \left(\frac{\mathrm{p}_i^{sat}}{\mathrm{p}} \right). \tag{3.26}$$

Raoult's law is reasonably valid for mixtures wherein all species have similar molecular structures and volatilities (Poling, Prausnitz, and O'Connell 2001), since in this case the activity coefficients are close to unity. One example would be a mixture of hydrocarbons of similar weight, for example n-hexane, h-heptane and n-octane. However, for non-ideal mixtures, a large departure from the unitary activity coefficient can be observed. This is the case for instance for polar/non-polar mixtures, and a realistic example would be ethanol mixed with n-octane. The situation becomes even more complex when water is incorporated, which is the case if hydrophilic substances such as alcohols are present. These absorb water from the surrounding atmosphere due to the presence of relative humidity resulting in water condensation towards the liquid phase. Therefore, even if liquid water was present at extremely low quantities at the beggining of a droplet lifetime, its transient composition can vastly differ.

To solve for this, more complex and robust activity coefficient models that correct Raoult's law have been developed. To better understand where they come from, we postulate below the general, multi-component Gibbs-Duhem relation:

$$\sum_{k=1}^{N} n_k d\ln\gamma_i = 0, \tag{3.27}$$

Most activity coefficient models actually come from expressions that seek to model the Gibbs free energy G^E. It can be seen as an excess energy that exists only in the non-ideal case i.e. as $\gamma \to 1$ then $G^E \to 0$, and it is defined as:

$$G^E = RT \sum_{k=1}^{N} n_k \ln\gamma_k, \tag{3.28}$$

It is also common to normalize the excess Gibbs energy by the total number of moles, with the notation $g^E = G^E / \sum_{k=1}^{N} n_k$.

The combination of Eqs. 3.27 and 3.28 leads to:

$$RT\ln\gamma_i = \left.\frac{\partial G^E}{\partial n_i}\right|_{T,\mathrm{p},n_k \forall k \neq i}, \tag{3.29}$$

where $n_k \forall k \neq i$ is to signal that all other mole numbers are kept constant during the differentiation. From Eq. 3.29 it is possible to predict activity coefficients if a model for the Gibbs excess energy is provided. This is typically done through semi-empirical closures.

Here, a similar consideration to that of the binary diffusion coefficients appears. In Chap. 2, a simplifying assumption was made that binary diffusion coefficients in the multi-component mixture can be assumed to be the same as those of a binary mixture. Namely, all influence of the surrounding species on the evaluation of the pair-wise diffusion coefficients was neglected. A similar assumption is often made when tabulating parameters for multi-component activity coefficient models. This is very useful since data for binary mixtures is much more practical to gather and tabulate, and so the description of any mixture could be extrapolated only from binary data. For instance, supposing a ternary liquid mixture composed of species $1, 2, 3$, a new experiment would not need to be carried out if binary data for pairs $1-2$, $1-3$ and $2-3$ is already available. When even more species are present, it is straightforward to notice the how practical this assumption can be.

3.3.1 The NRTL and UNIQUAC methods

Below are listed two among the most accurate activity coefficient models that follow this procedure, the NRTL and UNIQUAC models. They both are semi-empirical in the sense that there will be calibrated coefficients collected from experimental data. The NRTL model has three parameters for calibration, whereas UNIQUAC has two. Ideally, more parameters leads to higher precision; however, good experimental data obtention is hard enough such that a third parameter can sometimes result in worst results, since more "good" data points to create the correlation would be needed.

Also, for this manuscript a choice was made to not include the Wilson model, even though it was often used, as seen in (Law, Xiong, and Wang 1987) for instance. This

is because, as noted in (Poling, Prausnitz, and O'Connell 2001), Wilson's model cannot handle miscibility gaps, when two liquid phases can be formed, whereas the NRTL and UNIQUAC can in principle include this physical behavior. In this way, these two can be seen as among the most accurate and general, and they are described below.
The nonrandom two-liquid (NRTL) model was first published in (Renon and Prausnitz 1968). It has three semi-empirical parameters τ_{ij}, τ_{ji} and G, and the general formula is:

$$\frac{g^E}{RT} = \sum_{i=1}^{N} \left(X_i \frac{\sum_{j=1}^{N} \tau_{ji} G_{ji} X_j}{\sum_{k=1}^{N} G_{ki} X_k} \right), \tag{3.30a}$$

$$\ln\gamma_i = \frac{\sum_{j=1}^{N} \tau_{ji} G_{ji} X_j}{\sum_{k=1}^{N} G_{ki} X_k} + \sum_{j=1}^{N} \left(\frac{X_j G_{ij}}{\sum_{k=1}^{N} G_{kj} X_k} \left(\tau_{ij} - \frac{\sum_{k=1}^{N} X_k \tau_{kj} G_{kj}}{\sum_{k=1}^{N} G_{kj} X_k} \right) \right). \tag{3.30b}$$

The τ parameter is described as a non-dimensional interaction energy between species i and j, and can be computed by:

$$\tau_{ij} = \frac{\Delta g_{ij}}{RT} = \frac{U_{ij} - U_{ji}}{RT}, \tag{3.31}$$

where U_{ij} is one measure for the energy between species i and j and $U_{ij} \neq U_{ji}$. It is still useful to write the intermediary variable for the difference Δg_{ij} because often correlations are obtained for this parameter. Note that $\Delta g_{ij} \neq \Delta g_{ji}$ in general and therefore $\tau_{ij} \neq \tau_{ji}$.

The parameter G is actually also defined for each pair ordering i, j and j, i, however it represents only a single parameter since it is computed through:

$$G_{ij} = \exp(-\alpha_{ij}\tau_{ij}), \tag{3.32}$$

and the usual approximation is to have $\alpha_{ij} = \alpha_{ji}$, making G_{ij} sensitive to pair ordering because τ_{ij} also is. Therefore, in practice correlations are given for α_{ij}.

The universal quasi-chemical (UNIQUAC) model was published later, in (Abrams and Prausnitz 1975). It has two semi-empirical coefficients τ_{ij} and τ_{ji} and the formulation is:

$$\frac{g^E}{RT} = \sum_{i=1}^{N} X_i \ln\frac{\Phi_i}{X_i} + \frac{z}{2} \sum_{i=1}^{N} q_i X_i \ln\frac{\theta_i}{\Phi_i} - \sum_{i=1}^{N} q_i X_i \ln\left(\sum_{j=1}^{N} \theta_j \tau_{ji} \right), \tag{3.33a}$$

$$\Phi_i = \frac{r_i X_i}{\sum_{k=1}^{N} r_k X_k}, \tag{3.33b}$$

$$\theta_i = \frac{q_i X_i}{\sum_{k=1}^{N} q_k X_k}, \tag{3.33c}$$

for the excess Gibbs energy and:

$$\ln\gamma_i = \ln\frac{\Phi_i}{X_i} + \frac{z}{2}q_i\ln\frac{\theta_i}{\Phi_i} + l_i - \frac{\Phi_i}{X_i}\sum_{j=1}^{N} x_j l_j - q_i\ln\left(\sum_{j=1}^{N}\theta_j\tau_{ji}\right) + \tag{3.34a}$$

$$+q_i - q_i\sum_{j=1}^{N}\left(\frac{\theta_j\tau_{ji}}{\sum_{k=1}^{N}\theta_k\tau_{kj}}\right),$$

$$l_i = z/2(r_i - q_i) - (r_i - 1). \tag{3.34b}$$

for the activity coefficients. For this model, τ has a similar but not identical meaning to the NRTL definition. It is computed as:

$$\tau_{ij} = \exp\left(-\frac{\Delta u_{ij}}{RT}\right), \tag{3.35}$$

and u_{ij} is another measure for the interaction energy between molecules i and j. Therefore, the τ parameter between the NRTL and the UNIQUAC methods is not the same. Again, $\Delta u_{ij} \neq \Delta u_{ji}$ and so $\tau_{ij} \neq \tau_{ji}$. The inner parameters r and q are purely based on the molecular geometry:

$$r_i = \sum_{g=1}^{N_{s,i}} \nu_{s,i} R_s, \tag{3.36a}$$

$$q_i = \sum_{g=1}^{N_{s,i}} \nu_{s,i} Q_s, \tag{3.36b}$$

with g being a molecular group, $N_{s,i}$ the total number of secondary molecular groups in species i, $\nu_{s,i}$ the number of times the secondary group s appears in the molecule of species i and R_s, Q_s being parameters that describe the volume and surface areas of each secondary group s, respectively. These are conveniently tabulated for example in (Poling, Prausnitz, and O'Connell 2001). Finally, the coordination number z is the number of close interacting molecules around a central molecule. The cubic packing configuration with molecules represented by spheres yields $z = 6$ and the hexagonal configuration yields $z = 12$, and so $z = 10$ is a typical general approximation.

The distinction between secondary and primary group follows the treatment in (Poling, Prausnitz, and O'Connell 2001); essentially, more than one secondary molecular group can be part of the same primary group. It should be noted that Poling et al. use the denomination "main group" instead of "primary group", but in this work the word primary is opted for better clarity of notation.

To illustrate, Ethanol has the chemical formula C_2H_5OH. It is composed of the secondary groups CH_3, CH_2 and OH, and each one appears only once on the molecule. Therefore, $N_{s,Ethanol} = 3$ (3 different types of secondary groups) and $\nu_{CH_3} = \nu_{CH_2} = \nu_{OH} = 1$.

N-heptane, on the other hand is written C_7H_{16} and is made of 2 CH_3 secondary groups and 5 CH_2 secondary groups. Therefore, $N_{s,N-heptane} = 2$, $\nu_{CH_3} = 2$ and $\nu_{CH_2} = 5$. Both ν_{CH_3} and ν_{CH_2} are part of primary group #1 and OH is part of primary group #5.

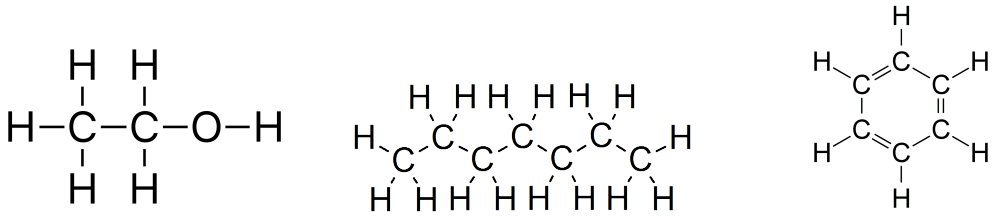

Figure 3.3: Molecular structures for ethanol (left), n-heptane (center) and benzene (right)

From (Poling, Prausnitz, and O'Connell 2001), it is possible to extract the R_s, Q_s factors for each of the secondary groups (data for 108 secondary groups is available). These secondary groups can be quite complex, or comprise entire molecules; for example, ACH also denotes a CH group but inside an aromatic ring, such that benzene (C_6H_6, see Fig. 3.3) is composed of 6 ACH, and not 6 CH. These parameters can therefore be tabulated and implemented for a range of molecular groups that make part of the substances of interest.

3.3.2 The UNIFAC method

The practical aspect of the molecular group part of the UNIQUAC method motivated an analogous extension called the UNIQUAC functional-group activity coefficients (UNIFAC) method, published shortly afterwards (Fredenslund, Jones, and Prausnitz 1975). It essentially borrows all of the already present secondary group structure part from UNIQUAC while also incorporating interactions between primary groups and from secondary groups between each species and the whole mixture. In this way, all parameters can be tabulated and become only a function of molecular geometry, significantly simplificating the data collection procedure, and serving as a reference.

Following the reasoning of Poling et al., the UNIQUAC method Eq. 3.33 can be divided into two parts for the activity coefficients, a combinatorial $\ln\gamma_i^c$ and a residual one $\ln\gamma_i^r$:

$$\ln\gamma_i = \ln\gamma_i^c + \ln\gamma_i^r, \tag{3.37a}$$

$$\ln\gamma_i^c = \ln\frac{\Phi_i}{X_i} + \frac{z}{2}q_i\ln\frac{\theta_i}{\Phi_i} + l_i - \frac{\Phi_i}{X_i}\sum_{j=1}^{N} x_j l_j, \tag{3.37b}$$

$$\ln\gamma_i^r = q_i\left[1 - \ln\left(\sum_{j=1}^{N}\theta_j\tau_{ji}\right) - \sum_{j=1}^{N}\left(\frac{\theta_j\tau_{ji}}{\sum_{k=1}^{N}\theta_k\tau_{kj}}\right)\right]. \tag{3.37c}$$

The UNIFAC method preserves the combinatorial part Eq. 3.37b directly, and the residual part Eq. 3.37c is replaced by a solution-of-groups concept:

$$\ln\gamma_i^r = \sum_{s=1}^{N_s} \nu_{s,i} \left(\Gamma_g - \Gamma_{s,i}\right), \tag{3.38}$$

with particular attention drawn to the fact that the summation is now made for all secondary groups in the whole liquid mixture, and not only among those of each species i molecule. In this way, Γ_s is a parameter related to the molecular groups of the whole mixture whereas $\Gamma_{s,i}$ is a parameter that has the same structure but only with contributions related to the secondary groups of species i. One of the consequences of this is that $\Gamma_g \to \Gamma_{s,i}$ as $X_1 \to 1.0$ in order to retrieve $\gamma_i \to 1$ for the single-component limit.

The Γ_s factor for the whole mixture can be computed as follows:

$$\ln\Gamma_s = Q_s \left[1 - \ln\left(\sum_{m=1}^{N_s} \theta_m \Psi_{p(m),p(s)}\right) - \sum_{m=1}^{N_s} \frac{\theta_m \Psi_{p(s),p(m)}}{\sum_{n=1}^{N_s} \theta_n \Psi_{p(n),p(m)}}\right], \tag{3.39a}$$

$$\theta_\alpha = \frac{Q_\alpha X_\alpha}{\sum_{\beta=1}^{N_s} Q_\beta X_\beta}, \tag{3.39b}$$

$$\Psi_{p(\alpha),p(\beta)} = \exp\left[-\frac{a_{p(\alpha),p(\beta)}}{T}\right], \tag{3.39c}$$

where θ_α is analogous to a secondary group volume fraction (since Q_α represents a volume) and $\Psi_{p(\alpha),p(\beta)}$ is a primary group parameter. Essentially, each secondary group can be mapped to a primary group p; this mapping is represented for instance as $p(\alpha)$ for the secondary group α. The $\Psi_{p(\alpha),p(\beta)}$ factor is representative of the energy of interaction between groups and depends on the liquid temperature and also on $a_{p(\alpha),p(\beta)}$, which is a 2-dimensional matrix that correlates data between each primary group. This matrix can also be found in (Poling, Prausnitz, and O'Connell 2001) for 50 primary groups.

It is possible to see a great resemblance between Eqs. 3.39 above and the residual part of the UNIQUAC method, Eq. 3.37c. However, the summations now go through the secondary groups s, instead of the species i, and $\Psi_{p(\alpha),p(\beta)}$ substitutes the empirical quantity τ_{ij}. It has units of Kelvin, in general $a_{mn} \neq a_{nm}$ and all values can be tabulated from experimental data, which is also done in (Poling, Prausnitz, and O'Connell 2001).

As for $\Gamma_{s,i}$, it is computed as follows:

$$\ln\Gamma_{s,i} = Q_s \left[1 - \ln\left(\sum_{m=1}^{N_s \in i} \theta_m \Psi_{p(m),p(s)}\right) - \sum_{m=1}^{N_s \in i} \frac{\theta_m \Psi_{p(s),p(m)}}{\sum_{n=1}^{N_s \in i} \theta_n \Psi_{p(n),p(m)}}\right], \tag{3.40a}$$

$$\theta_\alpha = \frac{Q_\alpha X_\alpha}{\sum_{\beta=1}^{N_s \in i} Q_\beta X_\beta}. \tag{3.40b}$$

The only concrete difference is that now the summations are only carried out for the secondary groups that are part of species i, $N_s \in i$. The Ψ factor is computed identically and is therefore omitted.

Due to the practical reasons mentioned in this subsection, mainly that empirical coefficients such as those inside NRTL and UNIQUAC are not needed anymore, in this manuscript the UNIFAC method will be preferred.

Part II

Single-component droplet phase-change models

Chapter 4

Maxwell-Fuchs-Spalding single-component models

In this chapter, most of the results can be directly obtained from the work of (Fuchs 1959). The author has performed his developments by extending and/or improving the first conclusions published in (Maxwell 1877). In that work, Maxwell devises some theoretical procedures and hypotheses that were further consolidated and clarified in the works of Fuchs. Also, there is only a brief mention of a spherical application, and so Fuchs converted some of these results to a spherical system of coordinates that could then apply to droplet heat and mass transfer models. Then, Fuchs also introduced an improvement to the mass-related derivations of Maxwell to account for the Stefan flow. Finally, Spalding extended the addition of Stefan flow effects for the energy-related derivations in (Spalding 1953) (notice that Fuchs' work cited here was published in its second edition, and so technically Spalding's contributions came after it). In this chapter we focus on mass-related derivations first and then the energy-related derivations.

4.1 Mass-related derivations

4.1.1 Diffusion-regulated mass transfer: Maxwell's model

In (Maxwell 1877), the author stipulates that evaporation is driven by a diffusion process where liquid molecules diffuse towards the gas-phase via the interface, thus becoming vapor molecules. The main results were derived for only two species, vapor (index 1) and an inert non-vapor (index 2) species such that only species 1 contributes to the mass transfer rate. The composition of species $1 + 2$ forms the gas-phase mixture which is referred to as "air" in the original work of Maxwell; this is not to be confused with air as an inert species, which is commonly the case in the litterature and also the case here.

For this mass transfer model, the author neglects the presence of any advective velocity for the species conservation equations, namely, $\mathrm{u} = 0$ in Eq. 1.13, representing absence of Stefan flow. No equation can be found for this diffusion-controlled mass transfer model

in (Maxwell 1877), but in (Fuchs 1959) the author quantitatively expressed those main results, the derivation of which are detailed below. It should be noted that all the results in (Maxwell 1877) and (Fuchs 1959) are given as functions of a species density $\rho_i = \rho Y_i$ instead of mass fractions Y_i as done here, but the results apply equivalently. The gas-phase species conservation equation for species 1 in the binary case is reproduced below:

$$r^2 \rho \mathrm{v}_1 Y_1 = \frac{\dot{m}}{4\pi}. \tag{4.1}$$

As shown in Chap. 2, Fick's law of diffusion (Eq. 2.28) can be used for a binary mixture for the closure of diffusion velocities. Substitution of this result in Eq. 4.1 leads to:

$$-r^2 \rho D_{1,2} \frac{dY_1}{dr} = \frac{\dot{m}}{4\pi} \tag{4.2}$$

This can be further rearranged to allow for an integration as follows:

$$-\rho D_{1,2} dY_1 = \frac{\dot{m}}{4\pi} \frac{dr}{r^2} \tag{4.3}$$

This equation is integrated in the gas-phase from the surface of the droplet indicated by s, where the radial coordinate is $r = R_d$ to an arbitrary coordinate R, as indicated in Fig. 4.1.

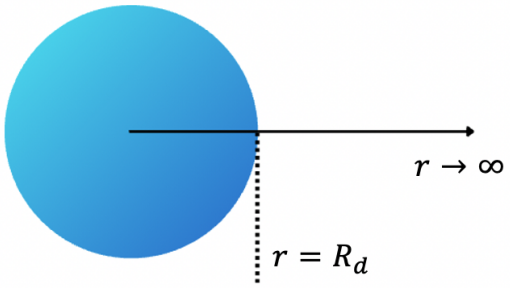

Figure 4.1: Gaseous domain outside droplet without Stefan flow.

To do this, it is common to further suppose that the product $\rho D_{1,2}$ is constant in space, yielding:

$$-\rho D_{1,2} \int_{Y_1^s}^{Y_1(R)} dY_1 = \frac{\dot{m}}{4\pi} \int_{R_d}^{R} \frac{dr}{r^2}. \tag{4.4}$$

Recalling from Eq. 1.10 that $\dot{m}$ is constant in space. Integration of both sides leads to:

$$-\rho D_{1,2} (Y_1(R) - Y_1^s) = \frac{\dot{m}}{4\pi} \left(\frac{1}{R_d} - \frac{1}{R} \right), \tag{4.5}$$

Rearranging for the mass transfer rate, we get:

$$\dot{m} = 4\pi \left(\frac{1}{\frac{1}{R_d} - \frac{1}{R}} \right) \rho D_{1,2}(Y_1^s - Y_1). \tag{4.6}$$

The main result of this model, however, is typically shown by performing an integration towards a point far away from the surface of droplet, namely $R \to \infty$ such that $1/R \approx 0$. This far-away point, commonly referred to as "infinity", is mathematically defined as a point where all spatial gradients are zero, including in this case the mass fraction gradient. In this case, Eq. 4.6 reduces to:

$$\boxed{\dot{m} = 4\pi R_d \rho D_{1,2}(Y_1^s - Y_1^\infty)} \tag{4.7}$$

which is actually present in (Fuchs 1959).

Due to the similar treatment in (Langmuir 1918), sometimes this result is also attributed to Langmuir. If one supposes that $Y_1^\infty = 0$, it is easy to see that the mass transfer rate is strictly positive $\dot{m} > 0$ since $Y_1^s > 0$, which signifies vaporization (mass being released into the gas phase). Otherwise, this model predicts that condensation will occur if $Y_1^\infty > Y_1^s$.

4.1.2 Adding Stefan-flow effects to the species formulation: Fuchs' model

Fuchs suggests that a first improvement to Maxwell's model could be the inclusion of Stefan flow effects, essentially keeping the radial velocity term u in Eq. 1.13. As noted by (Tonini and Cossali 2012) and (Sazhin 2014), this suggestion probably first appeared in the works of (Fuchs 1959), and so this will be named Fuchs' model in this manuscript. For a binary gaseous mixture, Eq. 1.14 becomes:

$$\frac{\dot{m}}{4\pi} Y_1 - r^2 \rho D_{1,2} \frac{dY_1}{dr} = \frac{\dot{m}}{4\pi}, \tag{4.8}$$

which can be rearranged to allow for integration:

$$-\rho D_{1,2} \frac{dY_1}{1 - Y_1} = \frac{\dot{m}}{4\pi} \frac{dr}{r^2}. \tag{4.9}$$

The assumption of product $\rho D_{1,2}$ constant in space done for Maxwell's model is made here as well. Then, the integration is performed first from the surface s of the droplet ($r = R_d$) to an arbitrary coordinate R, as indicated in Fig. 4.2:

$$-\rho D_{1,2} \int_{Y_1^s}^{Y_1(R)} \frac{dY_1}{1 - Y_1} = \frac{\dot{m}}{4\pi} \int_{R_d}^{R} \frac{dr}{r^2}. \tag{4.10}$$

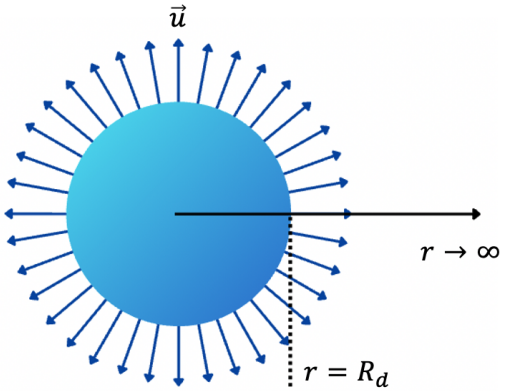

Figure 4.2: Gaseous domain outside droplet with Stefan flow u.

Integration on both sides leads to:

$$\rho D_{1,2} \ln\left(\frac{1-Y_1(R)}{1-Y_1^s}\right) = \frac{\dot{m}}{4\pi}\left(\frac{1}{R_d} - \frac{1}{R}\right). \tag{4.11}$$

Rearranging for the mass transfer rate leads to:

$$\dot{m} = 4\pi \left(\frac{1}{\frac{1}{R_d} - \frac{1}{R}}\right) \rho D_{1,2} \ln\left(\frac{1-Y_1(r)}{1-Y_1^s}\right). \tag{4.12}$$

The most common way to express this result is to integrated towards infinity, as done before with $1/R \to 0$, leading to:

$$\dot{m} = 4\pi R_d \rho D_{1,2} \ln\left(\frac{1-Y_1^\infty}{1-Y_1^s}\right). \tag{4.13}$$

This equation is also commonly presented with the Spalding mass transfer number B_M:

$$\boxed{\dot{m} = 4\pi R_d \rho D_{1,2} \ln\left(1 + B_M\right)} \tag{4.14}$$

with B_M defined as:

$$B_M = \frac{Y_1^s - Y_1^\infty}{1 - Y_1^s} \tag{4.15}$$

If $\dot{m}_D$ is defined as the mass transfer rate retrieved by only taking mass diffusion into account (Eq. 4.7) and $\dot{m}_{\mathrm{u},D}$ is defined as the one that takes into account both Stefan flow effects and mass diffusion (Eq. 4.12), their ratio then yields:

$$\frac{\dot{m}_{\mathrm{u},D}}{\dot{m}_D} = \frac{\ln\left(\frac{1-Y_1^\infty}{1-Y_1^s}\right)}{(Y_1^s - Y_1^\infty)}, \tag{4.16}$$

and this ratio represents a "correction" factor measuring the impact of taking or not Stefan-flow effects into account. From the definition of B_M in Eq. 4.15, the above result can also be rearranged as:

$$\boxed{\frac{\dot{m}_{\mathrm{u},D}}{\dot{m}_D} = \frac{\ln(1+B_M)}{B_M}\frac{1}{(1-Y_1^s)}} \tag{4.17}$$

4.2 Energy-related derivations

4.2.1 Maxwell's contributions

In (Maxwell 1877), the author's first approach for energy conservation in the gaseous phase is to assume that all heat transfer is driven by advection, through the transport of the carrier gas enthalpy. The energy conservation equation Eq. 1.18 with only advective terms is reproduced below:

$$r^2 \rho \mathrm{u}^Y c_p (T - T^s) = \frac{\dot{\mathcal{Q}}}{4\pi}, \tag{4.18}$$

with the same notation as in Chapter 1, namely, c_p being the specific heat for the gaseous mixture and $\mathcal{Q}$ the heat transfer rate traversing the droplet's surface. Substituting the results from global mass conservation Eq. 1.10 and rearranging for the gas-phase heat transfer rate $\dot{\mathcal{Q}}$ leads to:

$$\dot{\mathcal{Q}} = \dot{m} c_p (T - T^s). \tag{4.19}$$

Supposing that the far-away gas is at a temperature T^∞, then the total heat transfer rate given to the droplet is:

$$\boxed{\dot{\mathcal{Q}} = \dot{m} c_p (T^\infty - T^s)} \tag{4.20}$$

and this constitutes a simple way of computing the heat reaching the droplet by neglecting heat conduction.

However, following (Maxwell 1877) the author actually develops this expression for the wet-bulb configuration. This is the physical situation wherein the droplet reaches a stable temperature T_{wb} below that of boiling T_b, where any excess energy given to it is used exclusively for phase change and not to further modify its temperature. Therefore, all incoming heat is converted to the latent component, i.e. $\dot{\mathcal{Q}}_d = \dot{\mathcal{Q}}_{d,L}$ for the liquid droplet heat balance Eq. A.1, and the following ideal relation is obtained:

$$c_p (T^\infty - T^s) = L_{vap}. \tag{4.21}$$

The conducted reasoning does not translate to concrete computations for the droplet heat and mass transfer, since these quantities are functionally eliminated. However, this can

still be used to compute latent heats of vaporization; alternatively, deviations from this result can be computed in order to account for other heat losses in a non-ideal scenario, or to see how far from this condition the current scenario is, providing a reference.

Maxwell then proceeds to present a possible improvement to this model: dropping advection (or Stefan-flow effects) in exchange for conduction and radiation, with radiation being added as an integrated term. Below, only the heat conduction term is developed, to highlight the contribution of its analytical integration since we do not consider radiation effects in this manuscript. The energy conservation Eq. 1.18 in this case reduces to:

$$-r^2\lambda\frac{dT}{dr} = \frac{\dot{\mathcal{Q}}}{4\pi}. \tag{4.22}$$

By supposing that the thermal conductivity λ is constant in space, this can be rearranged and integrated from $r = R_d$ at the surface of the droplet to an arbitrary coordinate R:

$$-\lambda\int_{T^s}^{T(R)} dT = \frac{\dot{\mathcal{Q}}}{4\pi}\int_{R_d}^{R}\frac{dr}{r^2}. \tag{4.23}$$

Rearranging for the heat transfer rate:

$$\dot{\mathcal{Q}} = \frac{4\pi\lambda}{\left(\frac{1}{R_d}-\frac{1}{R}\right)}(T^s - T(R)) \tag{4.24}$$

If this is integrated towards infinity, $1/R \to 0$ leading to the classical form:

$$\boxed{\dot{\mathcal{Q}} = 4\pi R_d\lambda(T^s - T^\infty)} \tag{4.25}$$

The result of the integrated mass transfer rate from the species counterpart Eq. 4.7 may now be used, recalling that it was also developed by neglecting advection contributions. Substitution of Eq. 4.7 on Eq. A.3 for the wet-bulb limit leads to:

$$\dot{\mathcal{Q}} = 4\pi R_d\rho D_{1,2}(Y_1^s - Y_1^\infty)L_{vap}, \tag{4.26}$$

and combining Eqs. 4.25 and 4.26 leads to the version of Eq. 4.21 that only accounts for heat and mass diffusion, neglecting advection:

$$\frac{\lambda}{\rho D_{1,2}}\left(\frac{T^s - T^\infty}{Y^s - Y^\infty}\right) = L_{vap}, \tag{4.27}$$

and so in a sense, dividing Eq. 4.21 by Eq. 4.27 can give a rough estimate of the relative strength of advection to diffusion terms in a more general condition.

4.2.2 Adding Stefan-flow effects to the energy formulation: Spalding's model

Even though Fuchs proposes the inclusion of Stefan flow effects in the species conservation results, no such proposition is given for the energy counterpart of the conservation equations. To our knowledge, the first time this was proposed was in (Spalding 1953), where the author specifically derived results for a sphere of fuel in an infinite stagnant atmosphere of gas. The derivations of this section are thus referred to as Spalding's model in this manuscript.

The results in (Spalding 1953) are given without derivation, and so departing from the integrated energy conservation equation Eq. 1.20, we deduce that, to obtain their results, the term containing diffusive velocities and the enthalpies of each species, also referered to as "enthalpy diffusion", needs to be neglected. This leads to the following formulation:

$$\frac{\dot{m}}{4\pi}c_p(T-T^s) - r^2\lambda\frac{dT}{dr} = \frac{\dot{\mathcal{Q}}}{4\pi}, \tag{4.28}$$

Eq. 4.28 can now be integrated from the surface of the droplet $r = R_d$ where $T = T^s$ to an arbitrary coordinate r with temperature T. To do this, it is assumed that the specific heat and the thermal conductivity λ of the gaseous mixture c_p are constant in space. The equation is then rearranged leading to:

$$4\pi\lambda\int_{T^s}^{T}(R)\frac{dT}{\dot{m}c_p(T-T^s)-\dot{\mathcal{Q}}} = \int_{R_d}^{R}\frac{dr}{r^2}. \tag{4.29}$$

Carrying the integration procedure yields:

$$4\pi\frac{\lambda}{\dot{m}c_p}\ln\left(\frac{\dot{m}c_p(T^s-T(R))+\dot{\mathcal{Q}}}{\dot{\mathcal{Q}}}\right) = \left(\frac{1}{R_d}-\frac{1}{R}\right). \tag{4.30}$$

Rearranging for the mass transfer rate leads to:

$$\dot{m} = 4\pi\left(\frac{1}{\frac{1}{R_d}-\frac{1}{R}}\right)\frac{\lambda}{c_p}\ln\left(\frac{\dot{m}c_p(T^s-T)+\dot{\mathcal{Q}}}{\dot{\mathcal{Q}}}\right). \tag{4.31}$$

In (Spalding 1953), the integration is carried out to infinity $1/R \to 0$, yielding:

$$\dot{m} = 4\pi R_d\frac{\lambda}{c_p}\ln\left(\frac{\dot{m}c_p(T^s-T^\infty)+\dot{\mathcal{Q}}}{\dot{\mathcal{Q}}}\right). \tag{4.32}$$

Also in (Spalding 1953), the author defines the now called Spalding heat transfer number B_T, which allows Eq. 4.32 above to be recast as:

$$\boxed{\dot{m} = 4\pi R_d\frac{\lambda}{c_p}\ln(1+B_T)} \tag{4.33}$$

with B_T defined with our notation as:

$$B_T = \frac{\dot{m} c_p (T^s - T^\infty)}{\dot{\mathcal{Q}}}. \tag{4.34}$$

When looking at Eqs. 4.33 and 4.32, we see that the mass transfer rate cannot be isolated analytically, as it is also present inside the logarithm term. Therefore, if the mass transfer rate was to be computed using this expression, an iterative procedure would be necessary.

To understand the impact of the inclusion of Stefan-flow effects, it is useful to isolate for the heat transfer rate $\dot{\mathcal{Q}}$ in Eq. 4.32:

$$\boxed{\dot{\mathcal{Q}} = \frac{\dot{m} c_p (T^s - T^\infty)}{\exp\left(\frac{\dot{m} c_p}{4\pi R_d \lambda}\right) - 1}} \tag{4.35}$$

Now labeling the heat transfer rate computed only using heat conduction Eq. 4.25 as $\dot{\mathcal{Q}}_\lambda$ and the heat transfer rate that does include both Stefan flow effects and conduction Eq. 4.35 as $\dot{\mathcal{Q}}_{\mathrm{u},\lambda}$, we see that:

$$\frac{\dot{\mathcal{Q}}_{\mathrm{u},\lambda}}{\dot{\mathcal{Q}}_\lambda} = \frac{\left(\frac{\dot{m}_{\mathrm{u},D} c_p}{4\pi R_d \lambda}\right)}{\exp\left(\frac{\dot{m}_{\mathrm{u},D} c_p}{4\pi R_d \lambda}\right) - 1}, \tag{4.36}$$

where $\dot{m}$ from Eq. 4.35 has been recast as $\dot{m}_{\mathrm{u},D}$ as a reminder that this is the mass transfer rate that takes Stefan flow effects into account. Then from the definition of B_T in Eq.4.33, the ratio provided by Eq. 4.36 above can now be recast as:

$$\boxed{\frac{\dot{\mathcal{Q}}_{\mathrm{u},\lambda}}{\dot{\mathcal{Q}}_\lambda} = \frac{\ln(1 + B_T)}{B_T}} \tag{4.37}$$

And so the RHS of Eq. 4.37 can be seen as a correcting factor for predicting the heat transfer rate when including Stefan flow effects when compared to a purely conductive approach, analogously to the result of Eq. 4.17 for the mass transfer rate.

4.3 Coupling mass transfer rates from species and energy formulations

As developed throughout this Chapter, it is possible to obtain two different formulations for the mass transfer rates when using the same set of hypotheses; one from the species conservation equation, and one from the energy conservation. Therefore, since these represent the same phenomenom, for consistency these two independently obtained

expressions must be equal. This equality was first sugested in (Spalding 1953).

For the Stefan-flow corrected coupling, equating Eqs. 4.14 and 4.33 leads to:

$$\rho D_{1,2} \ln(1 + B_M) = \frac{\lambda}{c_p} \ln(1 + B_T). \tag{4.38}$$

This can be further developed as:

$$\boxed{1 + B_T = (1 + B_M)^{\phi}} \tag{4.39}$$

with the coefficient ϕ defined as:

$$\phi = \frac{\rho D_{1,2} c_p}{\lambda} = \frac{1}{Le}, \tag{4.40}$$

and Le being the Lewis number defined for this gaseous phase (notice the use of the specific heat of the global mixture c_p for these developments).

Further, in (Spalding 1953) the author states that both Spalding transfer numbers B_M and B_T must be always equal. From Eq. 4.39 above, this statement can only be true if a unitary Lewis number is assumed. This is a common assumption made in implementations of droplet phase-change models since the Lewis number for air rovers around 1.0 for room temperatures; one example of such approach can be seen in (Bader, Keller, and Hasse 2013) and this is also highlighted in (Sazhin 2006).

4.4 Summary of expressions

Throughout this chapter, derivations were conducted for single-component non-moving droplets with and without the presence of the Stefan-flow, with particular focus on the works of (Fuchs 1959) and (Spalding 1953). In this way, it was shown how to quantitatively compute the influence of this effect on the droplet heat and mass transfer rates. The coupling between these transfer rates was also laid out, and the equations developed in this chapter will serve as a useful reference for the derivations of Chap. 5.

In Table 4.3 below, we now summarize all the main expressions derived in this chapter.

Mass transfer rate with only diffusion	$\dot{m}_D = 4\pi R_d \rho D_{1,2}(Y_1^s - Y_1^\infty)$
Mass transfer rate with diffusion and Stefan flow	$\dot{m}_{\mathrm{u},D} = 4\pi R_d \rho D_{1,2} \ln(1 + B_M)$
Mass transfer correction factor for Stefan flow	$\frac{\dot{m}_{\mathrm{u},D}}{\dot{m}_D} = \frac{\ln(1+B_M)}{B_M} \frac{1}{(1-Y_1^s)}$
Heat transfer rate with only Stefan flow	$\dot{\mathcal{Q}}_{\mathrm{u}} = \dot{m} c_p (T^\infty - T^s)$
Heat transfer rate with only conduction	$\dot{\mathcal{Q}}_\lambda = 4\pi R_d \lambda (T^s - T^\infty)$
Heat transfer rate with diffusion and Stefan flow	$\dot{\mathcal{Q}}_{\mathrm{u},\lambda} = \frac{\dot{m} c_p (T^s - T^\infty)}{\exp\left(\frac{\dot{m} c_p}{4\pi R_d \lambda}\right) - 1}$
Heat transfer correction factor for Stefan flow	$\frac{\dot{\mathcal{Q}}_{\mathrm{u},\lambda}}{\dot{\mathcal{Q}}_\lambda} = \frac{\ln(1+B_T)}{B_T}$
Mass transfer rate computed from energy with Stefan flow	$\dot{m} = 4\pi R_d \frac{\lambda}{c_p} \ln(1 + B_T)$
Heat and mass transfer relation	$1 + B_T = (1 + B_M)^\phi$

Figure 4.3: Summary of single-component droplet expressions for for Chap. 4.

Chapter 5

Accounting for convective effects: the Abramzon-Sirignano model

The results obtained in Chap. 4 were derived for non-moving droplets. One of the reasons for this limitation is the assumption of spherical symmetry, which establishes that velocity fields can only exist in the radial direction. This is too restrictive for any real application, and taking convection effects into account is of paramount importance for spray combustion applications, which will always contain moving droplets. As will be discussed in Chap. 6, convection effects can be quite pronounced for droplets, with additional effects concerning the inner recirculation and phase-change also taking place.

To take these effects into account, one of the most used approaches is the proposed droplet heat and mass transfer model from (Abramzon and Sirignano 1989) which will be detailed and derived here. To better understand its contributions, it is first necessary to lay the basis of the film theory. The film represents a thermal or mass transfer boundary layer that describes a behaviour with steep variations over small distances, after which no further impact from the body of interest, in this case the droplet, can be detected. For spray combustion scenarios, the main use of the boundary layer theory is to allow for modelling tools that have been previously developed under non-convective environments to be extended to convective applications. One example of this film region, delimited by the Stefan flow, can be seen in Fig. 5.1.

After establishing the principles of the film theory, we highlight a second contribution in the Abramzon-Sirignano model in that the specific heat of the fuel vapor, instead of that of the whole gaseous mixture, appears in the energy formulation. As will be shown throughout the derivation, this subtle difference arises from the incorporation of enthalpy diffusion fluxes for the energy conservation.

Finally, it was shown that droplet heat and mass transfer models often make hypotheses concerning constant properties in space. However, for spray combustion applications, strong thermal gradients can be expected between the surface of the droplet, bounded

to be smaller than the liquid's boiling temperature $T^s < T_b$, and the temperature at the far-field T^∞, which means that properties can vary by a substantial margin. Therefore, a discussion is carried out about how to average the thermodynamic and transport properties inside the film. This is done here through the one-third rule framework, as proposed in (Hubbard, Denny, and Mills 1975) and (Yuen and Chen 1976), since this was the modelling approach used in the Abramzon-Sirignano model as well.

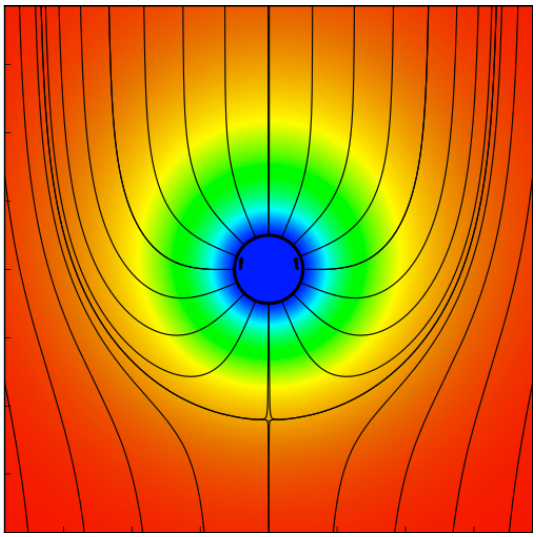

Figure 5.1: Moving droplet with surrounding convective velocity field and inner Stefan flow velocity field. Extracted from (Alis 2018)

5.1 Boundary layer results without Stefan flow

The first appearace of film theory, or the use of boundary layer analytical tools for droplet phase-change modelling, was suggested in (Spalding 1953). Therein, the author employs a "stagnant film theory", where an evaporative boundary layer between the droplet and the outer region is considered, inside of which only diffusive fluxes are to be taken into account.

Concretely, this means that Stefan-flow effects are neglected inside the film. The general procedure used to obtain the film-theory results is therefore similar to the heat and mass transfer models from Chapter 2 that neglect Stefan-flow effects. The main difference is that the integration operation on the conservation equations is now performed in a finite distance, instead of up to infinity, as seen in Fig. 5.2. The physical limits of integration can then be defined as $r = R_d + \delta_M$ and $r = R_d + \delta_T$, with δ_M being the thickness of the mass transfer boundary layer and δ_T the thickness of the thermal transfer boundary layer.

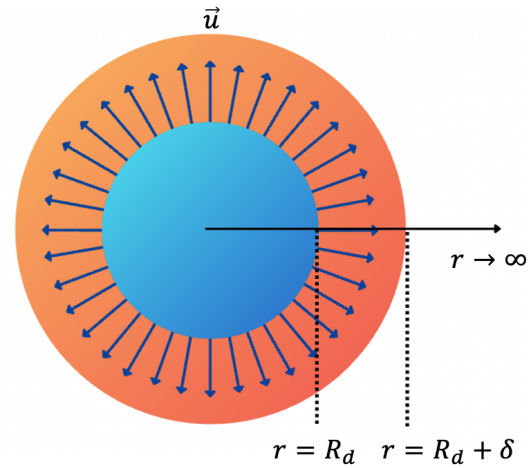

Figure 5.2: Gaseous domain outside droplet with Stefan flow u and film region.

In this way, Eqs. 4.4 and 4.23 become:

$$-\rho D_{1,2} \int_{Y_1^s}^{Y_1^\infty} dY_1 = \frac{\dot{m}}{4\pi} \int_{R_d}^{R_d+\delta_M} \frac{dr}{r^2}, \tag{5.1a}$$

$$-\lambda \int_{T^s}^{T^\infty} dT = \frac{\dot{\mathcal{Q}}}{4\pi} \int_{R_d}^{R_d+\delta_T} \frac{dr}{r^2}. \tag{5.1b}$$

The integration procedure leads to:

$$\dot{m} = 4\pi R_d^2 \left[\frac{R_d + \delta_M}{R_d \delta_M}\right] \rho D_{1,2}(Y_1^s - Y_1^\infty), \tag{5.2a}$$

$$\dot{\mathcal{Q}} = 4\pi R_d^2 \left[\frac{R_d + \delta_T}{R_d \delta_T}\right] \lambda(T^s - T^\infty). \tag{5.2b}$$

From another perspective, the boundary layer theory allows for the representation of the mass and heat transfer rates through average mass and heat transfer coefficients h_M, h_T respectively (Newton's law of cooling). The general expression for these coefficients, as seen in (Klingenberg 2015) for instance, can be inferred for spherical droplets from the folowing equations:

$$\dot{m} = 4\pi R_d^2 h_M (Y_1^s - Y_1^\infty), \tag{5.3a}$$

$$\dot{\mathcal{Q}} = 4\pi R_d^2 h_T (T^s - T^\infty). \tag{5.3b}$$

These coefficients represent therefore the proportionality between a potential (of mass fraction or temperature) to a surface flux, and introduce alternative ways to compute the droplet heat and mass transfer rates. Most notably, these coefficients are typically expressed in terms of the non-dimensional Sherwood Sh and Nusselt Nu numbers, which as will be shown in Chap. 6 are the main way to concretely incorporate convection

effects. For spherical droplets in our current framework, the relationship between the transfer coefficients and these non-dimensional numbers is:

$$h_M = \frac{\rho D_{1,2} Sh}{2R_d}, \tag{5.4a}$$

$$h_T = \frac{\lambda Nu}{2R_d}, \tag{5.4b}$$

Combining Eq. 5.3 with Eq. 5.2 leads to:

$$h_M = \left[\frac{R_d + \delta_M}{R_d \delta_M}\right] \rho D_{1,2}, \tag{5.5a}$$

$$h_T = \left[\frac{R_d + \delta_T}{R_d \delta_T}\right] \lambda. \tag{5.5b}$$

Substituting the alternative definitions of Eq. 5.4 into Eq. 5.5 and rearranging for the thicknesses of the mass and thermal boundary layers leads to, finally:

$$\delta_M = \frac{2R_d}{Sh - 2}, \tag{5.6a}$$

$$\delta_T = \frac{2R_d}{Nu - 2}. \tag{5.6b}$$

The result above was not shown for spherical droplets in (Spalding 1953). One of the first appearances of this explicit result was possibly in (Faeth 1968), where the author essentially expressed that $(R_d + \delta_T)/R_d = Nu/(Nu - 2)$.

The values of the boundary layer thicknesses given by 5.6 when substituted onto 5.2 lead to:

$$\dot{m} = 2\pi R_d Sh \rho D_{1,2} (Y_1^s - Y_1^\infty), \tag{5.7a}$$

$$\dot{\mathcal{Q}} = 2\pi R_d Nu \lambda (T^s - T^\infty). \tag{5.7b}$$

At this point, it might be useful to revisit the non-convective scenario. Comparison between the results for the mass and heat transfer rates in the non-convective case i.e. Eqs. 4.7 and 4.25 with Eqs. 5.7 above leads to:

$$Sh = 2, \tag{5.8a}$$

$$Nu = 2. \tag{5.8b}$$

Namely, for an evaporating sphere that neglects Stefan flow and with no convection, the Sherwood and Nusselt numbers must be $Sh = Nu = 2$. This is also the classical result for the Nusselt number for non-moving solid spheres. It is therefore possible to see that, to retrieve this result, the boundary layers extend to infinity, taking the limit $\delta_{M,T} \to \infty$ in the non-convective case.

Now, from Eqs. 4.2 and 4.22, the gradients at the surface of the droplet for the case without Stefan-flow can be isolated to be:

$$\left.\frac{dY_1}{dr}\right|^s = -\frac{\dot{m}}{4\pi R_d^2 \rho D_{1,2}} \tag{5.9a}$$

$$\left.\frac{dT}{dr}\right|^s = -\frac{\dot{\mathcal{Q}}}{4\pi R_d^2 \lambda} \tag{5.9b}$$

Therefore, combining the sets of equations 5.9 with 5.7 leads to a formal definition of the local Sherwood and Nusselt numbers for spherical droplets:

$$Sh = -\frac{2R_d}{(Y^s - Y^\infty)}\left.\frac{\partial Y_1}{\partial r}\right|^s \tag{5.10a}$$

$$Nu = -\frac{2R_d}{(T^s - T^\infty)}\left.\frac{\partial T}{\partial r}\right|^s \tag{5.10b}$$

5.2 Boundary layer results considering Stefan flow

The next step is to consider the addition of Stefan flow effects. To start, we focus on the species conservation equations. The integration step is reproduced below for the results without Stefan flow (Eq. 4.4) and with Stefan flow (Eq. 4.10). For the integration limits, the boundary layer thicknesses for the two cases are represented, with δ_M for the purely diffusive one and δ_M^* for the one with Stefan flow effects:

$$-\rho D_{1,2}\int_{Y_1^s}^{Y_1} dY_1 = \frac{\dot{m}}{4\pi}\int_{R_d}^{R_d+\delta_M}\frac{dr}{r^2}, \tag{5.11a}$$

$$-\rho D_{1,2}\int_{Y_1^s}^{Y_1} \frac{dY_1}{1-Y_1} = \frac{\dot{m}}{4\pi}\int_{R_d}^{R_d+\delta_M^*}\frac{dr}{r^2}. \tag{5.11b}$$

The blowing/sucking phenomenom on a boundary layer and how it can affect its thicknesses is a well-documented fact in the litterature; see (Schlichting and Gersten 2017) for instance. Therefore, in general $\delta_M \neq \delta_M^*$ since the Stefan-flow represents blowing for evaporation $\dot{m} > 0$ and sucking for condensation $\dot{m} < 0$.

An analogous reasoning can be extended to energy-related integrations Eqs. 4.23, 4.29

now using the thicknesses δ_T, δ_T^* respectively:

$$-4\pi\lambda \int_{T^s}^{T} dT = \dot{\mathcal{Q}} \int_{R_d}^{R_d+\delta_T} \frac{dr}{r^2}, \tag{5.12a}$$

$$4\pi\lambda \int_{T^s}^{T} \frac{dT}{\dot{m}c_p(T-T^s) - \dot{\mathcal{Q}}} = \int_{R_d}^{R_d+\delta_T^*} \frac{dr}{r^2}, \tag{5.12b}$$

and therefore in general $\delta_T \neq \delta_T^*$ on the above.

However, in (Spalding 1953) the author makes a first approximation by stating that these boundary layer thicknesses can be regarded as the same. In particular, since they have developed an energy model, their developments are concentrated only on that front. By making this assumption, substitution of the thicknesses 5.6 in Eqs. 5.11b,5.12b after integration yields:

$$\dot{m} = 2\pi R_d Sh \rho D_{1,2} \ln\left(\frac{1-Y_1^\infty}{1-Y_1^s}\right), \tag{5.13a}$$

$$\dot{m} = 2\pi R_d Nu \frac{\lambda}{c_p} \ln\left(\frac{\dot{m}c_p(T^s - T^\infty) + \dot{\mathcal{Q}}}{\dot{\mathcal{Q}}}\right). \tag{5.13b}$$

Or, in terms of Spalding numbers:

$$\boxed{\dot{m} = 2\pi R_d Sh \rho D_{1,2} \ln(1+B_M)} \tag{5.14a}$$

$$\boxed{\dot{m} = 2\pi R_d Nu \frac{\lambda}{c_p} \ln(1+B_T)} \tag{5.14b}$$

which leads to an updated version of the ϕ coefficient for consistency relation between heat and mass transfer derivations Eq. 4.39:

$$\boxed{\phi = \left(\frac{1}{Le}\right)\left(\frac{Sh}{Nu}\right)} \tag{5.15}$$

Eq. 5.13b can also be recast through the heat transfer rate $\dot{\mathcal{Q}}$ to update Eq. 4.35:

$$\boxed{\dot{\mathcal{Q}} = \frac{\dot{m}c_p(T^s - T^\infty)}{\exp\left(\frac{\dot{m}c_p}{2\pi R_d Nu \lambda}\right) - 1}} \tag{5.16}$$

The equations represented by 5.14, 5.15 and 5.16 are sometimes referred to as the "classical model", as done for instance in (Abramzon and Sirignano 1989).

For this case with Stefan flow effects, the gradients at the surface are now recast from rearranging Eqs. 4.8, 4.28 to:

$$\left.\frac{dY_1}{dr}\right|^s = -\frac{\dot{m}(1-Y_1)}{4\pi R_d^2 \rho D_{1,2}} \tag{5.17a}$$

$$\left.\frac{dT}{dr}\right|^s = -\frac{\dot{m}c_p(T^s - T^\infty) + \dot{\mathcal{Q}}}{4\pi R_d^2 \lambda} \tag{5.17b}$$

5.3 Including enthalpy diffusion effects

One difference found in the Abramzon-Sirignano model when comparing their results with other droplet heat transfer models is the appearance of a specific heat for the fuel vapor species $c_{p,v}$ on the final structure of the energy equation, instead of one for the whole gaseous mixture, c_p. This was possibly among the first publications to explicitly bring forward this change; However, the lack of clarity on the notations used might mean that other authors had already proposed this change, including the aforementioned publication of (Spalding 1953).

To retrieve the results shown by Abramzon-Sirignano, it is necessary to depart from the quasi-steady equation for energy conservation which preserves enthalpy diffusion terms, Eq. 1.18. For a binary mixture composed of species $1, 2$, the middle term of the LHS can be opened up leading to:

$$\frac{\dot{m}}{4\pi}c_p(T-T^s) - r^2\rho\left(D_{1,2}\frac{dY_1}{dr}c_{p,1} + D_{2,1}\frac{dY_2}{dr}c_{p,2}\right)(T-T^s) - r^2\lambda\frac{dT}{dr} = \frac{\dot{\mathcal{Q}}}{4\pi}. \tag{5.18}$$

For the binary mixture, the gradients respect the following relationship $dY_2/dr = -dY_1/dr$. Also, the equality between diffusion coefficients must hold i.e. $D_{2,1} = D_{1,2}$. With these, Eq. 5.18 above becomes:

$$\frac{\dot{m}}{4\pi}c_p(T-T^s) - r^2\rho D_{1,2}\frac{dY_1}{dr}(c_{p,1}-c_{p,2})(T-T^s) - r^2\lambda\frac{dT}{dr} = \frac{\dot{\mathcal{Q}}}{4\pi}. \tag{5.19}$$

In parallel, the conservation equation for species 1 with the same set of hypotheses Eq. 4.8 can provide the following expression for the mass fraction gradient:

$$\frac{dY_1}{dr} = -\frac{\dot{m}(1-Y_1)}{4\pi r^2 \rho D_{1,2}}. \tag{5.20}$$

Substituting Eq. 5.20 into Eq. 5.19 leads to the following:

$$\frac{\dot{m}}{4\pi}c_p(T-T^s) + \frac{\dot{m}}{4\pi}(c_{p,1}-c_{p,2})(1-Y_1)(T-T^s) - r^2\lambda\frac{dT}{dr} = \frac{\dot{\mathcal{Q}}}{4\pi}. \tag{5.21}$$

Recall that from Eq. 1.19, for a binary mixture $c_p = c_{p,1}Y_1 + c_{p,2}Y_2$. Substituting this on the above and using $1 - Y_1 = Y_2$ to cancel out the relevant terms leads to, finally:

$$\dot{m}c_{p,1}(T - T^s) - 4\pi r^2 \lambda \frac{dT}{dr} = \dot{\mathcal{Q}}. \tag{5.22}$$

Comparing this equation and Eq. 4.28 shows that the only difference on the expressions is the appearance of the specific heat of the fuel species $c_{p,1}$ instead of the specific heat of whole the binary mixture, c_p. Effectively, the use of the fuel species' specific heat, as employed in (Abramzon and Sirignano 1989), equates to an inclusion of enthalpy diffusion effects. It should be highlighted that nevertheless the authors never mention the enthalpy diffusion importante and/or its inclusion throughout their work. It is straightforward to see that, from Eq. 5.19, if $c_{p,1} = c_{p,2}$ the enthalpy diffusion term also disappears, which is a hypothesis sometimes made, as seen in (Renksizbulut and Yuen 1983b) for instance.

The above result is valid for a binary gaseous mixture, but for the rest of this chapter the notation $c_{p,v}$ instead of $c_{p,1}$ is preferred to highlight the fuel vapor. By analogy, the same integration procedure as done for Eq. 4.28 can be carried out for Eq. 5.22. First, the integration towars infinity yields:

$$\dot{m} = 4\pi R_d \frac{\lambda}{c_{p,v}} \ln(1 + B_T), \tag{5.23}$$

with an updated Spalding heat transfer number given by:

$$B_T = \frac{c_{p,v}(T^s - T^\infty)}{\dot{\mathcal{Q}}}. \tag{5.24}$$

This is again reflected on the ϕ coefficient of Eq. 4.39 which should be updated to:

$$\phi = \frac{\rho D_{1,2} c_{p,v}}{\lambda} = \left(\frac{c_{p,v}}{c_p}\right)\left(\frac{1}{Le}\right), \tag{5.25}$$

and accordingly the heat transfer rate in the gas-phase $\dot{\mathcal{Q}}$ Eq. 4.35 is updated to:

$$\dot{\mathcal{Q}} = \frac{\dot{m}c_{p,v}(T^s - T^\infty)}{\exp\left(\frac{\dot{m}c_{p,v}}{4\pi R_d \lambda}\right) - 1} \tag{5.26}$$

Similarly, when integrating inside the film, the classical model result from Eq. 5.14b becomes:

$$\dot{m} = 2\pi R_d Nu \frac{\lambda}{c_{p,v}} \ln\left(1 + B_T\right) \tag{5.27}$$

with the same Spalding heat transfer number of Eq. 5.24. The ϕ coefficient for the heat and mass transfer relation Eq. 5.15 is naturally updated to include enthalpy diffusion effects leading to:

$$\phi = \left(\frac{\rho D_{1,2} c_{p,v}}{\lambda}\right)\left(\frac{Sh}{Nu}\right) = \left(\frac{c_{p,v}}{c_p}\right)\left(\frac{1}{Le}\right)\left(\frac{Sh}{Nu}\right), \tag{5.28}$$

And finally, the heat transfer rate from film theory Eq. 5.26 is changed to:

$$\dot{\mathcal{Q}} = \frac{\dot{m}c_{p,v}(T^s - T^\infty)}{\exp\left(\frac{\dot{m}c_{p,v}}{2\pi R_d Nu\lambda}\right) - 1} \tag{5.29}$$

5.4 The Abramzon-Sirignano model

Having now exposed the main characteristics of the film theory, as well as the inclusion of enthalpy diffusion effects, it is now possible to show the contribution in (Abramzon and Sirignano 1989) in its final form. Therein, the authors circumvented the classical model assumption that the boundary layer thicknesses do not change when taking into account Stefan flow effects. To do so, the same functional structure is imposed for their boundary layer thicknesses as showcased in the set of equations 5.6, but now they are multiplied by a correction factor. This leads to the following corrected boundary layer thicknesses δ_M^*, δ_T^*:

$$\delta_M^* = F_M \delta_M, \tag{5.30a}$$
$$\delta_T^* = F_T \delta_T, \tag{5.30b}$$

where the correction factors $F_{M,T}$ are computed through:

$$F_M = (1 + B_M)^{0.7} \frac{(1 + B_M)}{B_M}, \tag{5.31a}$$
$$F_T = (1 + B_T)^{0.7} \frac{(1 + B_T)}{B_T}. \tag{5.31b}$$

According to the authors, these correction factors were derived by solving a laminar boundary layer problem with a a flow past a vaporizing wedge; no further details were given. The range of parameters for which they consider the correction to be valid is $0 \leq B_{M,T} \leq 20$, $1 \leq (Sc, Pr) \leq 3$ and $0 \leq \beta \leq 2\pi$ where β is the wedge angle and Sc, Pr are the Schmidt and Prandtl dimensionless numbers.

By coupling the previous definitions of the boundary layer thicknesses Eqs. 5.6 with the updated ones in Eqs. 5.30, the correction factors Eqs. 5.31 can also be recast as:

$$F_M = \frac{Sh - 2}{Sh^* - 2}, \tag{5.32a}$$
$$F_T = \frac{Nu - 2}{Nu^* - 2}, \tag{5.32b}$$

where the Stefan-flow corrected Sherwood and Nusselt numbers Sh^*, Nu^* now appear. They can therefore be isolated leading to:

$$Sh^* = 2 + \frac{Sh - 2}{F_M}, \tag{5.33a}$$
$$Nu^* = 2 + \frac{Nu - 2}{F_T}, \tag{5.33b}$$

which is the result presented in (Abramzon and Sirignano 1989). Therein, the authors referred to Sh^* and Nu^* as the modified Sherwood and Nusselt numbers.

From the definition of the thicknesses in Eq. 5.30, it is possible to integrate Eqs. 5.11b and 5.12b with the updated specific heat for the fuel vapor to obtain:

$$\dot{m} = 2\pi R_d Sh^* \rho D_{1,2} \ln(1 + B_M) \tag{5.34a}$$

$$\dot{m} = 2\pi R_d Nu^* \frac{\lambda}{c_{p,v}} \ln(1 + B_T) \tag{5.34b}$$

where the Spalding transfer numbers are defined from Eqs. 4.15 and 5.24. This once again updates the ϕ coefficient of Eq. 5.28, recast below:

$$\phi = \left(\frac{c_{p,v}}{c_p}\right)\left(\frac{1}{Le}\right)\left(\frac{Sh^*}{Nu^*}\right) \tag{5.35}$$

And the same update must be applied to the heat transfer rate, Eq. 5.29:

$$\dot{\mathcal{Q}} = \frac{\dot{m} c_p (T^s - T^\infty)}{\exp\left(\frac{\dot{m} c_p}{2\pi R_d Nu^* \lambda}\right) - 1} \tag{5.36}$$

As for the gradients at the surface of the droplet, notice that the set of equations 5.17 is constructed before the final integration, and therefore before introducing the boundary layer thicknesses. Therefore, the gradients are unchanged between the classical model and the Abramzon-Sirignano model.

5.5 The one-third rule

The droplet phase-change models derived up until now all make assumptions for constant thermodynamic and transport properties in space. Since the integration procedure is done between the surface of the droplet and the far-away state, it is reasonable to assume that the properties should reflect a compromise between these two locations. However, for spray combustion applications, there could be a great difference between such states, due to the potential temperature and composition differences. The first droplet models never properly detailed how to average these properties, showing that not much attention was dedicated to this subject.

The publication of (Hubbard, Denny, and Mills 1975) was perhaps one of the first to highlight the impact of this choice. Therein, the authors carried out numerical experiments

for fully transient simulations of octane droplets, spanning typical spray combustion conditions. The authors proposed that the properties could be averaged using a reference temperature T_R and reference compositions Y_R, X_R computed as:

$$T_R = T^s + \gamma_T(T^\infty - T^s); \tag{5.37a}$$
$$Y_R = Y^s + \gamma_c(Y^\infty - Y^s); \tag{5.37b}$$
$$X_R = X^s + \gamma_c(X^\infty - X^s), \tag{5.37c}$$

where $0 < (\gamma_T, \gamma_c) < 1$ are averaging parameters to be established depending on whether the surface or the far-away conditions have more or less "influence" on the computation of the properties. Their results showed that a good correlation between models and numerical data was obtained if $\gamma_T = \gamma_c = 1/3$, and this result has been globally referred to as the one-third rule, being also adopted in (Abramzon and Sirignano 1989).

Shortly afterwards, the work of (Yuen and Chen 1976) further cemented this result, this time around focusing on droplet drag correlations. Yuen and Chen showed that a good agreement is found between experimental data and the "standard drag curve" correlation if the one-third rule is used to compute the gaseous viscosity used in the Reynolds number computation. They further argue that this is reasonable since the Reynolds number represents a ratio of inertial to viscous forces, and that viscous forces should be evaluated close to the body of interest (instead of that at infinity). At the time, some authors such as (Eisenklam, Arunachalam, and Weston 1967) argued that it was necessary to correct for phase-change effects in the drag coefficient for evaporating droplets, but the modification proposed by Yuen and Chen also shows good agreement with the data of Eisenklam et al. To that extent, an alternative way was being presented to study drag correlations: fix a known model of drag and vary the way the properties are computed, instead of assuming a fixed method to compute properties and trying different drag laws. The authors' conclusions have also generally corroborated the findings of (Hamielec, Hoffman, and Ross 1967) and (Coats and Fendell 1968), which provided quantitative data for drag coefficients but no correlations.

Even though the one-third rule has been universally accepted, there is no analytical basis to assume that the averaging parameters should be constant throughout a droplet's lifetime, especially for general spray combustion scenarios with such critical variations of the surrounding atmosphere. One new study (Finneran 2021) has tried to relax the hypothesis of constant parameter, finding that in general $0 < (\gamma_T, \gamma_c) < 1/2$ and that this factor is highly dependant on the temperature, such that $\gamma_T, \gamma_c \to 0$ as $T^\infty \to \infty$. Still, there is no concrete basis to support that the parameter for the temperature rule γ_T must be identical to the one of the composition rules γ_c, even though this has often been assumed to be the case for simplicity.

In this manuscript, the one-third rule will be applied for all investigations due to its simplicity and broad acceptance, leading to clearer comparisons. More studies on this are encouraged specially as fully solved single droplet DNS tools become more accessible.

5.6 Summary of expressions

In this chapter, the single-component droplet phase-change model of (Abramzon and Sirignano 1989) was derived. It was shown that its main contributions was the inclusion of Stefan-flow effects into the boundary layer thicknesses, as well as the inclusion of enthalpy diffusion effects, materialized through the specific heat of the fuel vapor $c_{p,v}$. To do that, the film theory and its main characteristics were developed. Updated expressions for the heat and mass transfer rates were provided and will serve as a reference for single-component results in this manuscript. The topic of average properties in space and the one-third rule was also exposed, and this framework for the properties will also be applied for the remainder of the manuscript, due to its simplicity and universal acceptance.

In Table 5.3 below, we now summarize all the main expressions derived in this chapter.

Surface mass fraction gradient w/o Stefan-flow	$\left.\frac{dY_1}{dr}\right\|^s = -\frac{\dot{m}}{4\pi R_d^2 \rho D_{1,2}}$
Surface mass fraction gradient w/ Stefan-flow	$\left.\frac{dY_1}{dr}\right\|^s = -\frac{\dot{m}(1-Y_1)}{4\pi R_d^2 \rho D_{1,2}}$
Surface temperature gradient w/o Stefan-flow	$\left.\frac{dT}{dr}\right\|^s = -\frac{\dot{\mathcal{Q}}}{4\pi R_d^2 \lambda}$
Surface temperature gradient w/ Stefan-flow	$\left.\frac{dT}{dr}\right\|^s = -\frac{\dot{m} c_p (T^s - T^\infty) + \dot{\mathcal{Q}}}{4\pi R_d^2 \lambda}$
Droplet surface local Sherwood number	$Sh = -\frac{2R_d}{(Y^s - Y^\infty)} \left.\frac{\partial Y_1}{\partial r}\right\|^s$
Droplet surface local Nusselt number	$Nu = -\frac{2R_d}{(T^s - T^\infty)} \left.\frac{\partial T}{\partial r}\right\|^s$
Classical model mass transfer rate (species)	$\dot{m} = 2\pi R_d Sh \rho D_{1,2} \ln(1 + B_M)$
Classical model mass transfer rate (energy)	$\dot{m} = 2\pi R_d Nu \frac{\lambda}{c_p} \ln(1 + B_T)$
Classical model heat transfer rate	$\dot{\mathcal{Q}} = \frac{\dot{m} c_p (T^s - T^\infty)}{\exp\left(\frac{\dot{m} c_p}{2\pi R_d Nu \lambda}\right) - 1}$
Classical model ϕ coefficient for Eq. 4.39	$\phi = \left(\frac{1}{Le}\right)\left(\frac{Sh}{Nu}\right)$
Abramzon-Sirignano mass transfer rate (species)	$\dot{m} = 2\pi R_d Sh^* \rho D_{1,2} \ln(1 + B_M)$
Abramzon-Sirignano mass transfer rate (energy)	$\dot{m} = 2\pi R_d Nu^* \frac{\lambda}{c_{p,v}} \ln(1 + B_T)$
Abramzon-Sirignano heat transfer rate	$\dot{\mathcal{Q}} = \frac{\dot{m} c_p (T^s - T^\infty)}{\exp\left(\frac{\dot{m} c_p}{2\pi R_d Nu^* \lambda}\right) - 1}$
Abramzon-Sirignano ϕ coefficient for Eq. 4.39	$\phi = \left(\frac{c_{p,v}}{c_p}\right)\left(\frac{1}{Le}\right)\left(\frac{Sh^*}{Nu^*}\right)$

Figure 5.3: Summary of single-component droplet expressions for Chap. 5.

Chapter 6

Accounting for convective effects: sub-modelling choices

In Chap. 5, the film theory was described to incorporate convective effects, culminating on the Abramzon-Sirignano modelling strategy. Therein, multiple sub-modelling degrees of freedom were left unanswered, such as how to model the droplet drag and how to actually compute the Nusselt and Sherwood numbers. In this chapter, the main characteristics for the different sub-modelling choices concerning moving droplets are detailed. This is of paramount importance for spray combustion applications, since both the droplets and the surrounding gas velocities are expected to not only be non-zero but also to vary significantly during the droplet's lifetime.

First, the distinction between forced and natural convection is made, with the definition of the Reynolds and Grashof numbers, respectively. Then, a brief overview is given to the equation for the droplet momentum from the lagrangian point-particle perspective. Concretely, this equation allows for the update of the droplet's velocity, effectively defining its trajectory. Finally, analytical, empirical and numerical correlations are offered for the modelling of the droplet drag coefficient from its momentum equation as well as for the Nusselt and Sherwood numbers, which essentially describe the thicknesses of the thermal and mass boundary layers, respectively.

6.1 Forced and natural convection

First, it may be useful to dinstinguish between forced and natural convection. Forced convection occurs when external means influence the fluid motion. This is typically the case for spray combustion applications, since the flow at the spray injection point is typically generated or at least altered using mechanical means. Forced convection can be described through the Reynolds non-dimensional number:

$$Re = \frac{\rho U l}{\mu}, \tag{6.1}$$

where ρ and μ are the density and dynamic viscosity on the gaseous phase respectively, l is a characterisctic length or spatial dimension and U a characteristic velocity. For the case of a moving droplet, the Reynolds numbers is usually writen as:

$$Re_d = \frac{\rho^\infty |U^\infty - U_d| \mathcal{D}_d}{\mu^\infty}, \tag{6.2}$$

where ρ^∞ and μ^∞ are the gas density and dynamic viscosity evaluated at the far-field, the characteristic length is the droplet's diameter $\mathcal{D}_d$ and the characteristic velocity is the difference between the velocity of the droplet U_d and that of the far-field U^∞. For simplicity, for the remainder of this chapter we use the notation Re for the droplet Reynolds number.

The Reynolds number is also described as the ratio of inertial to viscous forces. In (Yuen and Chen 1976) and (Abramzon and Sirignano 1989), the authors argued then the viscous forces should be evaluated close to the body of interest. For the film theory approach, concretely this means that the viscosity should be evaluated inside the boundary layer i.e. μ^f with a superscript f for film instead of μ^∞. To compute this average viscosity inside the film, the spatial averaging formalism of Eqs. 5.37, or the one-third rule, can be used. The Reynolds number definition would then be updated to:

$$Re_d = \frac{\rho^\infty |U^\infty - U_d| \mathcal{D}_d}{\mu^f}. \tag{6.3}$$

Some correlations also make use of the Péclet number, which represents the ratio between convective and diffusive transports. In this way, it is possible to define one Péclet number for mass and another for heat transfer Pe_M, Pe_T, respectively using the Schmidt and Prandtl numbers:

$$Pe_M = ReSc, \tag{6.4}$$
$$Pe_T = RePr. \tag{6.5}$$

Natural convection, on the other hand, happens by natural means, which for droplet motion means the gravitational force. Due to the small size of droplets for typical modelling applications, the explicit influence of volumic forces including gravity is neglected; this was formalized through hypothesis #5 in Chap. 1. It has been shown both experimentally and numerically, for instance in (Chauveau, Chesneau, and Gökalp 1995), (Daïf, Bouaziz, Chesneau, and Chérif 1998), (Gogos, Soh, and Pope 2003), (Habchi and Ebrahimian 2012), (Verwey and Birouk 2018) that natural convection can be influential in droplets. Two main correlations have been highlighted: the droplet's size, which is expected as discussed in the introduction (bigger droplets will see increased influence), but also the ambient pressure; starting at 5-10 bar, the impact of natural convection becomes more influential.

To better understand these impacts, it is useful to define the Grashof number, the equivalent of the Reynolds number, but for natural convection. It represents the ratio of

gravitational forces to viscous forces, and is usually defined for droplets as:

$$Gr_T = \frac{g\rho_\infty^2 \mathcal{D}_d^3}{\mu^2} \frac{|T^\infty - T^s|}{T^\infty}, \tag{6.6}$$

where g is the gravitational acceleration and T^∞, T^s are temperatures evaluated far away and at the surface of the body of interest, respectively. The density is usually taken to be at the far-away state $\rho = \rho_\infty$ and the viscosity can be evaluated likewise $\mu = \mu_\infty$ or at the film $\mu = \mu_f$ (subscripts are used due to the squared operator). The coefficient of thermal expansion can be approximated to $\beta = 1/T$ for ideal gases, and customarily this temperature is evaluated at infinity such that $\beta = 1/T^\infty$.

However, following (Verwey and Birouk 2018), it is also possible to define a "mass-equivalent" form of the Grashöf number, that would measure the buoyancy through mass instead of thermal considerations. For droplets, it is defined as:

$$Gr_M = \frac{g\rho^\infty |\rho^\infty - \rho^s| \mathcal{D}_d^3}{\mu^2}, \tag{6.7}$$

where ρ^s is the gas density evaluated at the surface of the droplet.

The mentioned works all studied the impact of natural convection isolated from forced convection. This impact is often measured as a linear deviation from the $\mathcal{D}_d^2$-law (see Appendix A), since the Grashof number presents a depedency on $\mathcal{D}_d^3$. The correlation with size and pressure is reassuring in that we could potentially neglect the inclusion of natural convection effects for spray combustion scenarios.

Furthermore, in (Verwey and Birouk 2018) the authors state that under purely evaporative conditions, the effect is even less impactful, when compared to burning conditions; however, for extremely small droplet-to-droplet spacings, the effect can start to be more impactful again. Some authors i.e. (Fedorenko, Antonov, Strizhak, and Sazhin 2022) and (Ebrahimian and Habchi 2011) have suggested that it is possible to use correlations obtained for Reynolds number in forced convection scenarios and substitute the Grashof number in place of the Reynolds number for forced convection applications. This was also suggested in (Ranz and Marshall 1952).

This would imply that a direct comparison between these numbers can be relevant to quantify their relative influence. Assuming a pure water droplet with initial diameter of $\mathcal{D}_{d,0} = 100\mu m$ immersed in an atmosphere with pure air, 1 atm pressure and with a velocity difference $U^\infty - U_d = 10m/s$, we find that $Re \approx 6.93$, $Gr_T \approx 3.77\text{x}10^{-4}$ and $Gr_M \approx 1.85\text{x}10^{-4}$, which shows a difference of multiple orders of magnitude even for a large droplet, considering spray combustion applications. For this same situation, the velocity difference would have to be around 0.01 (which would be even more difficult for a big droplet moving in spray combustion scenarios, due to its high relaxation time) for these numbers to have the same order of magnitude. Even if the choice of the velocity

difference is arbitrary here, the large difference spanning multiple orders of magnitude can illustrate the proposed argumentation. It was shown however in (Pinheiro and Vedovoto 2019) that the direct substitution of Grashof numbers instead of Reynolds may lead to deviations from experimental data, which signals that this direct comparison is not perfect.

Still, following this simplified quantitative analysis we neglect natural convection effects in this manuscript, and so the correlations presented for the remainder of this chapter are only related to forced convection.

6.2 Droplet momentum: Stoke's law

For the zero-dimensional modelling coupling described in the first chapter, each droplet is tracked as a point-wise particle. In this way, the particle tracking is perfectly described if it has a starting position, velocity and a law for its velocity evolution. In this section, the general framework for the velocity evolution is presented.

The most basic case corresponds to Stoke's flow. This flow represents the limiting case $Re << 1$ for solid spheres, with an analytical solution presented in (Stokes 1850), and can be seen in Fig. 6.1. Even though this case is not very representative for spray combustion applications, it has spawned various improvements and can be used as a assymptotic case.

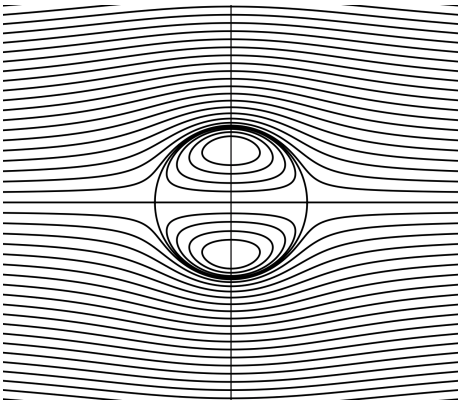

Figure 6.1: Stokes flow around droplet. Extracted from (Kallendorf, Fath, Oberlack, and Wang 2015)

One of the main results from the Stokes theory is the following simplified equation of the velocity evolution for the spherical body:

$$\frac{dU_d}{dt} = \frac{3C_D}{2R_d}\frac{\rho^\infty}{\rho_d}|U^\infty - U_d|\left(U^\infty - U_d\right), \tag{6.8}$$

with the drag coefficient defined as:

$$C_D = \frac{24}{Re} \tag{6.9}$$

and the Reynolds number following Eq. 6.2.

Eq. 6.8 can also be conveniently formulated as:

$$\frac{dU_d}{dt} = \frac{(U^\infty - U_d)}{\tau_d}, \tag{6.10}$$

in order to define a characteristic momentum relaxation time τ_d:

$$\tau_d = \frac{\rho_d R_d^2}{18\mu^\infty}. \tag{6.11}$$

The results of Stoke's flow mark the cornerstone for droplet drag models, particularly Eqs. 6.8 and 6.10. However, its results have been derived for quite restrictive conditions, and so improvements have been carried out over the years, including for droplets with or without the phase-change context. Typically, these have come through correction factors and/or updated drag coefficients, and historically through correlations with phenomenological studies. The first analyses have been based on analytical developments, particularly for low Reynolds numbers, but also experimental data, and more recently numerical correlations have also emerged as potential strategies.

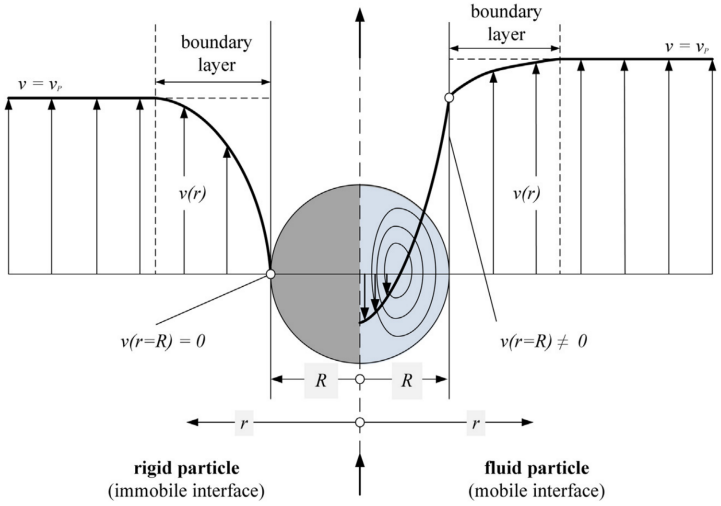

Figure 6.2: Surrounding boundary layer for solid and fluid spheres. Extracted from (Wegener, Paul, and Kraume 2014)

To that extent, we now list some of these correlations and their general characteristics, first for solid spheres and then for fluid spheres (with/without phase change). Due to internal recirculation for fluid spheres, a qualitative difference can be expected for the boundary layer depending on the viscosity ratio, as seen for instance in Fig. 6.2.

It should be noted that most droplets in spray combustion applications will typically have a Reynolds number spanning $0 < Re < 1000$ throughout its lifetime, since droplets of various diameters will be present and in different flow regimes. To that extent, correlations mentioned here focus on that range. Also, for simplicity of notation, all parameters here will be assigned to the droplet i.e. Reynolds number Re etc. even for the studies that have considered solid spheres, since it has been argued that a droplet can behave like a solid sphere for drag stresses under some conditions (Grace and Clift 1978).

6.3 Solid sphere drag correlations

6.3.1 Oseen (1910) and Proudman-Pearson (1957)

The main hypothesis on the formulation of Stokes was that the Reynolds number must be small, but it was later shown that this could not be guaranteed for arbitrarily large distances. This critique was formalized in (Oseen 1910), where the author shows that the Stokes solution contains ill-posed derivatives of the velocity far away from the body of interest. Oseen then offered a more robust solution to correct for this, which when applied to the sphere leads to the following "corrected" drag coefficient:

$$C_D = \frac{24}{Re}\left[1 + \frac{3}{8}Re\right]. \tag{6.12}$$

Later on, (Proudman and Pearson 1957) indeed confirm that Oseen's solutions represent a good starting point for analysing low Reynolds flows, but they propose an even more robust method that is able to take into account expansions following the forms from both Oseen's and Stokes' treatments. Their work is quite remarkable in that it summarizes the main contributions from both preceding authors as well as proposing a new strategy. Essentially, Stoke's flow would be represented when solving the following simplified form of the Navier-Stokes equations:

$$\nu\nabla^2\mathbf{v} = \nabla \mathrm{p}, \tag{6.13}$$

with ν being the kinematic viscosity and ∇^2 the laplacian operator, while Oseen's treatment changes the above to:

$$\mathrm{U}\cdot\nabla\mathbf{v} - \nu\nabla^2\mathbf{v} = -\nabla \mathrm{p}, \tag{6.14}$$

with U being the uniform stream.

Proudman and Pearson then further state that Oseen's result for the drag coefficient Eq. 6.12 would need to include higher order terms and so that this would be inconsistent with

its original derivation procedure. They then combined an improved solution for Oseen's flow far away from a sphere with an improvement for Stokes' solution close to the sphere, mathcing them in a common regime of validity, to derive the following improved result, that includes terms of even higher order:

$$C_D = \frac{24}{Re}\left[1 + \frac{3}{8}Re + \frac{9}{40}Re^2 \ln Re\right]. \tag{6.15}$$

Therefore, for low Reynolds droplets i.e. ideally $Re \leq 0.1$, this analytical result for the drag coefficient should in principle be preferred.

6.3.2 Schiller and Naumann (1935) and Putnam (1961)

In (Schiller and Naumann 1935), the authors have offered one of the first correlations that is able to better extrapolate the Stokes drag coefficient Eq. 6.9 into higher Reynolds numbers. Their correlation is expressed as:

$$\begin{gathered} C_D = \frac{24}{Re}\left[1 + 0.15Re^{0.687}\right], \text{for } Re \leq 1000; \\ C_D = 0.44, \text{ for } Re > 1000. \end{gathered} \tag{6.16}$$

A similar, but more recent contribution can also be traced back to (Putnam 1961), and brief mentions to Putnam's work can be found in the review of (Faeth 1977). Therein, Faeth reports that this result is quite accurate for $Re < 1000$ supposing that properties can be computed accurately enough. Putnam's development essentially consists in a correction for Eq. 6.9 leading to the following improved result for drag of spheres:

$$C_D = \frac{24}{Re}\left[1 + \frac{Re^{2/3}}{6}\right] \tag{6.17}$$

It is straightforward to see that Eq. 6.17 is basically quantitatively identical to Eq. 6.16. Also, as $Re \to 0$ both corrections tends to be negliglibe, approaching the original Stokes drag coefficient. In this way, the correction tends to be more impactful for larger Reynolds numbers, with the drag coefficient plateauing at around $C_D = 0.44$ for large Reynolds. Due to the popularity of Schiller and Naumann's (or Putnam's) model, and possibly to the fact that it essentially encapsulates all relevant regimes for droplets in spray combustion applications, it has sometimes been referred to as the standard drag curve, as done in (Yuen and Chen 1976) and (Abramzon and Sirignano 1989) for instance. For simplicity, throughout this manuscript we refer to Eq. 6.17 as the standard drag curve.

6.3.3 Morsi and Alexander (1972)

In (Morsi and Alexander 1972), Morsi et al. followed a straightforward procedure to obtain correlations for drag coefficients on different ranges of Reynolds numbers. The authors first note that the drag coefficient for a solid sphere follows the behaviour depicted in Fig. 6.3. Then, the next step was to subdivide a curve from gathered experimental

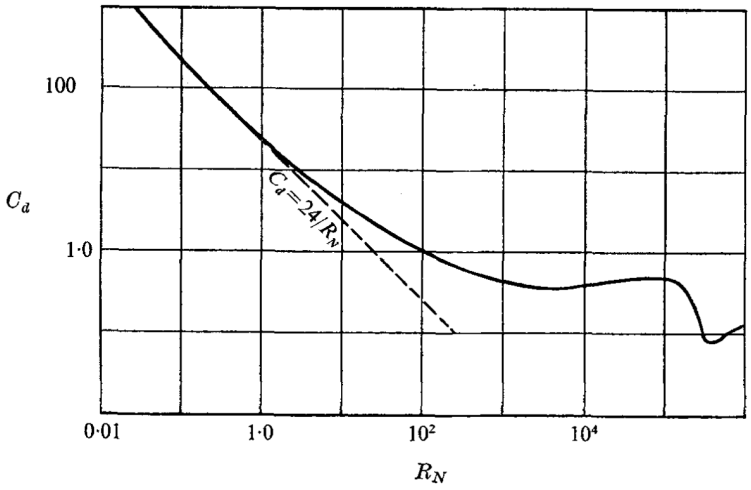

Figure 6.3: Drag coefficient versus sphere Reynolds number - the extended standard drag curve. Extracted from (Morsi and Alexander 1972)

data for drag in a sphere into 8 different regions, spanning Reynolds numbers up until 50000. Each region was then fitted to a third-order inverse polynomial, and the results are shown below for Reynolds up to 1000:

$$
\begin{aligned}
C_D &= \frac{24}{Re} \text{ for } Re < 0.1; \\
C_D &= \frac{22.73}{Re} + \frac{0.0903}{Re^2} + 3.69 \text{ for } 0.1 \leq Re < 1; \\
C_D &= \frac{29.1667}{Re} - \frac{3.8889}{Re^2} + 1.222 \text{ for } 1 \leq Re < 10; \\
C_D &= \frac{46.5}{Re} - \frac{116.67}{Re^2} + 0.6167 \text{ for } 10 \leq Re < 100; \\
C_D &= \frac{98.33}{Re} - \frac{2778}{Re^2} + 0.3644 \text{ for } 100 \leq Re < 1000.
\end{aligned}
\tag{6.18}
$$

The equations are not exactly continuous at the intersection point, but the results are relatively close; for example at $Re = 0.1$, the first expression yields $C_D = 240$ while the second one yields $C_D = 240.02$. These correlations were used for instance in (Law, Prakash, and Sirignano 1977), with the corrections suggested in (Eisenklam, Arunachalam, and Weston 1967) to account for phase-change, explained in the Sect. 6.4.

6.4 Fluid sphere drag correlations

The correlations for fluid spheres have historically been focused either on taking into account effects of inner vortices, or phase-change effects. Therefore this section is subdivided into those two categories.

6.4.1 Incorporating inner flow effects for the droplet drag

Hadamard-Rybczynski (1911)

In two studies published independently, (Hadamard 1911) and (Rybczynski 1911) developed essentially the same results, as reported in (Grace and Clift 1978). These analytical results are among the most important for low Reynolds fluid spheres, which could be bubbles (gas sphere surrounded by liquid medium) or droplets (liquid sphere surrounded by gaseous medium). One of the most important distinctions between solid and fluid spheres is the internal recirculation as seen in Fig. 6.4, and this can affect drag stresses. Typically, this recirculation phenomena is analytically taken into account through the so-called Hill vortices, as was done by Hadamard and Rybczynski.

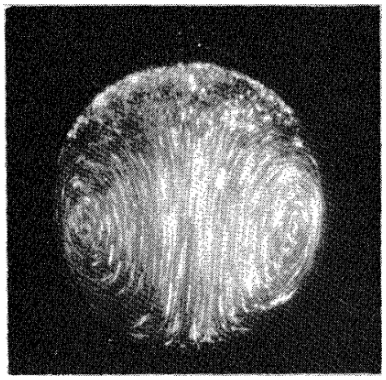

Figure 6.4: Recirculation inside liquid water droplet. Extracted from (Grace and Clift 1978)

One parameter that helps describing the expected behaviour from fluid spheres is the viscosity ratio κ:

$$\kappa = \frac{\mu_{fs}}{\mu_{sp}}, \tag{6.19}$$

with μ_{fs} being the viscosity of the fluid sphere and μ_{sp} that of the surrounding phase. The two extremes for the viscosity ratio are $\kappa \to 0$ for bubbles and $\kappa \to \infty$ for solid spheres.

The analytical results by Hadamard and Rybczynski were derived for low Reynolds numbers and also taking some other restrictions into consideration and particular attention is

given to the hypothesis of no surface-active contaminants; this will be discussed shortly afterwards. The main result for the drag coefficient is:

$$C_D = \frac{8}{Re}\left(\frac{2+3\kappa}{1+\kappa}\right). \tag{6.20}$$

It is possible to see that, when $\kappa \to \infty$ then the Stokes drag coefficient Eq. 6.9 is retrieved, as expected.

As noted in (Grace and Clift 1978), this result for the drag coefficient often does not correlate well with experimental data. One justification given is that for the small droplets typically used for experiments, the amount of recirculation would not be sufficient to cause major departures from solid spheres laws. One criteria to measure the amount of recirculation is through the Bond number, also called Eötvös number, computed as follows for a spherical droplet with diameter $\mathcal{D}_d$:

$$Bo = \frac{|\rho_{fs} - \rho_{sp}| g \mathcal{D}_d^2}{\sigma}, \tag{6.21}$$

with ρ_{fs}, ρ_{sp} being the densities of the fluid sphere and surrounding phase, respectively and σ the surface tension. The criteria offered is that for $Bo < 4$, not much recirculation can be expected. However, its pointed out that even this criteria does not comprehend all compared scenarios, revealing a quite complex situation.

In (Grace and Clift 1978), one alternative way to explain the lack of circulation for small droplets is given, related to surface-active substances. These tend to accumulate at the interface, and the overall effect is to reduce the surface tension. As the droplet moves, adsorbed surface-active materials tend to be swept to the rear part, reducing the contaminants at the front. Tangential gradients of surface then appear, and these are more pronounced for small droplets, further reducing their inner recirculation. The overall conclusion is that surface contaminants may play a larger role, and since real-life applications will typically have surface contaminants, a lesser inner recirculation should be expected.

Feng and Michaelides (2001) and Saboni and Alexandrova (2002)

These two contributions were published at around the same time and seek to present a solution for fluid spheres without phase-change that spans a larger range of Reynolds numbers and viscosity ratios while still aiming concrete applications. Details from (Feng and Michaelides 2001) can also be found in the book (Michaelides 2006), where the author

proposes the following correlation:

$$\begin{aligned} C_D^{Re<5} &= \left(\frac{2+3\kappa}{1+\kappa}\right)\left(\frac{8}{Re}\left[1+0.05\left(\frac{2+3\kappa}{1+\kappa}\right)Re\right]-0.01Re\ln Re\right); \\ C_D^{Re>5} &= \left(\frac{2-\kappa}{2}\right)C_D^{\kappa=0}+\left(\frac{4\kappa}{6+\kappa}\right)C_D^{\kappa=2},\ \text{for } 0<\kappa<2; \\ C_D^{Re>5} &= \left(\frac{4}{2+\kappa}\right)C_D^{\kappa=2}+\left(\frac{\kappa-2}{\kappa+2}\right)C_D^{\kappa=\infty},\ \text{for } 2<\kappa<\infty. \end{aligned} \tag{6.22}$$

where $C_D^{Re<5}$ is the expression for the drag coefficient when $0 < Re < 5$ and $C_D^{Re>5}$ is for the range $5 < Re < 1000$. The drag coefficients $C_D^{\kappa=0}, C_D^{\kappa=2}$ and $C_D^{\kappa=\infty}$ are expressions specifically obtained for those viscosity ratios. The authors suggest the following expressions for them:

$$C_D^{\kappa=0} = \frac{48}{Re}\left[1+\frac{2.21}{Re^{1/2}}-\frac{2.14}{Re}\right], \tag{6.23a}$$

$$C_D^{\kappa=2} = 17Re^{-2/3}, \tag{6.23b}$$

$$C_D^{\kappa=\infty} = \frac{24}{Re}\left[1+\frac{Re^{2/3}}{6}\right]. \tag{6.23c}$$

The analytical structure is such that for $Re \to 0$, the form of (Hadamard 1911) and (Rybczynski 1911) is retrieved. Also, these results cover the expression of (Oliver and Chung 1987) and this is why those results are omitted in this manuscript. The logarithmic term of (Proudman and Pearson 1957) for the Reynolds number is also embedded for that equation. In fact, Eq. 6.22 correlates well with experimental data up until $Re \approx 20$. Also, the authors systematically tested for the density ratio ρ_{fs}/ρ_{sp} and found that their functional inclusion is not necessary. Finally, they also note that the expressions neglect the presence of contaminants at the surface.

The study of (Saboni and Alexandrova 2002) provided the following expression, general for the range $0 < Re < 400$ and $0 < \kappa < 1000$:

$$C_D = \frac{\left[\kappa\left(\frac{24}{Re}+\frac{4}{Re^{1/3}}\right)+\frac{14.9}{Re^{0.78}}\right]Re^2+40\left(\frac{2+3\kappa}{Re}\right)+15\kappa+10}{(1+\kappa)(5+Re^2)} \tag{6.24}$$

This expression could be seen as preferable if the Reynolds range is limited to $Re < 400$ because it also retrieves the Hadamard-Rybczynski limit for $Re \to 0$ and because the authors argue that axisymmetry holds only until that Reynolds number, approximately; Also, a single expression is provided, which simplifies the implementation procedure. For the Reynolds number range that is common to both models, a good agreement in (Saboni

and Alexandrova 2002) is reported with the results of (Feng and Michaelides 2001) and (Oliver and Chung 1987) as well. Still, in (Wegener, Paul, and Kraume 2014) a better agreement for the terminal velocity with liquid droplets surrounded by liquid mediums was found by using the expressions of (Feng and Michaelides 2001), except for a droplet with high surface tension and high viscosity ratio, with high absolute viscosities.

6.4.2 Incorporating phase-change effects for the droplet drag

Eisenklam et al. (1967)

Eisenklam et al. were one of the first to consider the explicit influence of transfer numbers related to phase-change for convection-related correlations. In (Eisenklam, Arunachalam, and Weston 1967), they present correlations obtained from experimental data for single-component evaporating and burning droplets, for a range of initial droplet diameters $25 < d_0 < 500\mu m$, Reynolds number $0.01 < Re < 15$ and transfer number $0.06 < B_{T,L} < 12.3$. The Spalding thermal transfer number $B_{T,L}$ is not quite the original from Eq. 4.34; it is defined as the one from the wet-bulb condition, where all heat is being used for phase-change only. In this case, the formulation is no longer dependant on the mass transfer rate for a single-component droplet. The full procedure using Eqs. A.1, A.3 is detailed below:

$$B_T = \frac{\dot{m}c_p(T^s - T^\infty)}{\dot{\mathcal{Q}}} = -\frac{\dot{m}c_p(T^s - T^\infty)}{\dot{\mathcal{Q}}_d} = -\frac{\dot{m}c_p(T^s - T^\infty)}{\dot{m}L_{vap}} = -\frac{c_p(T^s - T^\infty)}{L_{vap}}, \quad (6.25)$$

leading to the following formulation:

$$B_{T,L} = \frac{c_p(T^\infty - T^s)}{L_{vap}}. \quad (6.26)$$

This latent-heat Spalding transfer number was consistently used for many correlations, possibly due to the elimination of the mass transfer rate and the sensible heat, considerably simplifying its computation. It should also be noted that the gas-phase average specific heat c_p was computed at an average temperature $T = (T^\infty + T_d)/2$.
Their results for the drag coefficient for both purely evaporating as well as burning droplets are:

$$C_D = \frac{24}{Re}\frac{1}{(1 + B_{T,L})}, \quad (6.27)$$

and this can essentially be viewed as a correction factor of $1/(1 + B)$ for phase-change for the Stokes drag Eq. 6.9.

Renksizbulut and Yuen (1983)

In (Renksizbulut and Yuen 1983b), the authors have performed numerical simulations for single-component droplets with a quasi-stationarity hypothesis enforced for the gas-phase. They have also neglected any inner motion for the droplet and supposed that the

droplet temperature is constant at its wet-bulb temperature. They also neglect radiation, gravity and chemical reactions, and these hypotheses are typically aligned with those for droplet phase-change models. Finally, they suppose that the flow is axisymmetric, and state that this hypothesis may become less valid starting at $Re \approx 130$, limiting their study to the intermediary Reynolds number regime. Still, they show good correlation with experimental data for $10 < Re < 260$ and propose the following formula:

$$C_D = \frac{24}{Re} \frac{1}{(1 + B_{T,L})^{0.2}} \left[1 + 0.2Re^{0.63}\right] \tag{6.28}$$

where the latent-heat Spalding thermal transfer $B_{T,L}$ is defined from Eq. 6.26.

It is possible to see that this expression essentially encapsulates the results of Schiller-Naumann/Putnam Eqs.6.16 and 6.17 with the correction procedure proposed by Einseklam Eq. 6.27, but with an exponent of 0.2 for the denominator containing the transfer number B. This formula was also validated with numerical simulations in (Haywood, Nafziger, and Renksizbulut 1989) for $10 < Re < 300$.

Bellan and Harstad (1987)

(Miller, Harstad, and Bellan 1998) proposed a correlation for a correction factor to Eq. 6.10 that can be rewritten in terms of a drag coefficient as being:

$$\begin{gathered} C_D = \frac{24}{Re}\left[\frac{C_{D,0}}{1 + \alpha Re_{d,b}^{\beta}}\right], \\ C_{D,0} = 1 + 0.0545Re + 0.1Re^{1/2}(1 - 0.03Re), \\ \alpha = 0.09 + 0.077\exp(-0.4Re), \\ \beta = 0.4 + 0.77\exp(-0.04Re). \end{gathered} \tag{6.29}$$

In the above, we note the appearance of the droplet's blowing Reynolds number $Re_{d,b}$, included as an alternative instead of the Spalding transfer number B proposed by (Eisenklam, Arunachalam, and Weston 1967) to explicitly quantify the Stefan flow influence. It is defined as being:

$$Re_{d,b} = \frac{\rho^{\infty}|U_b|\mathcal{D}_d}{\mu}, \tag{6.30}$$

where $U_b = \dot{m}/(4\pi R_d^2 \rho^f)$ is the blowing velocity obtained from global mass conservation, Eq. 1.10 and $\mu = \mu^{\infty}$ or $\mu = \mu^f$ depending on the choice of viscosity. Note that the density used for the blowing velocity is ρ^f, since it is based on the constant property arising from the spatial integration inside the film, and not from the inertial forces.

The set of equations 6.29 actually originates from (Bellan and Harstad 1987b), which is a correlation to the numerical results of (Cliffe and Lever 1985) that incoporated Stefan-flow effects. Cliffe et al. solved an axisymmetric problem for the flow past a blowing sphere, to create an analogy with a droplet undergoing phase-change while also neglecting any internal effects.

Miller et al. report that this correlation was derived over the range $0 < Re < 100$ and with $0 < Re_{d,b} < 10$, and that this would be reasonable for spray combustion applications wherein dense clustering of droplets form, since in this case the Reynolds number would not be expected to be much bigger. In (Bellan and Summerfield 1978) however it is noted that the correlation should be valid for $1 < Re < 100$, and this range should in principle be preferred since results focused for low Reynolds numbers are available. Also, the authors compared their approach with those of Eisenklam et al. and (Yuen and Chen 1976) and concluded that the choice of drag coefficient model was insensitive with regards to their droplet phase-change model.

Finally, in (Michaelides 2006), the author points out that if if $0 < Re < 10$ the α coefficient equation should be changed to the following:

$$\alpha = 0.06 + 0.077\exp(-0.4Re). \tag{6.31}$$

Chiang et al. (1992)

In (Chiang, Raju, and Sirignano 1992), the authors extended the correlation of (Renksizbulut and Yuen 1983b) and (Haywood, Nafziger, and Renksizbulut 1989) with a new, more robust numerical method. The Navier-Stokes equations were solved both for the inner and outer region with essentially the same hypotheses except for quasi-steadiness. A nonlinear regression using least squares was carried out leading to the following updated formulation:

$$C_D = \frac{24}{Re}\frac{1}{(1+B_{T,L})^{0.32}}\left[1+0.325Re^{0.474}\right] \tag{6.32}$$

for the ranges $0.4 < B_{T,L} < 13$ and $30 \leq Re \leq 200$. Similarly to Eisenklam et al. and Renksizbulut et al., a latent-heat Spalding transfer number $B_{T,L}$ was used, defined in Eq. 6.26. This transfer number was computed using properties from the film, but no specifications were given as to how exactly the average properties were computed.

6.5 Nusselt and Sherwood non-dimensional numbers

In Chap. 5, the Nusselt and Sherwood numbers were introduced as a way to represent the boundary layer thicknesses for the integration inside the film region. Therein, analytical expressions were given for the local Nusselt and Sherwood numbers computed at the

surface of the droplet, through gradients of temperature and mass fractions, respectively.

In practice, these gradients are not available when computing heat and mass transfer models, and so an external methodology is used. These numbers are typically evaluated from correlations similar to those of the drag coefficients that were just mentioned. In this way, we now list some useful contributions and models that are frequently used in the litterature.

We also note that, due to the similarity between heat and mass diffusion (Fick's law and Fourier's law), typically results that are derived for the Nusselt number are extended to the Sherwood number (and vice-versa), via the non-dimensional boundary layer Prandlt and Schmidt numbers. Some correlations use Péclet numbers, and accordingly for the Nusselt number the thermal Pe_T should be used whereas for the Sherwood number the mass transfer Pe_M should be used.

The different models will be subdivided into those that do not include the explicit influence of phase-change (no Stefan flow effects) and those that do include these effects. For cases where the droplet heat and mass transfer models include Stefan flow effects, expressions that do not take Stefan flow effects into account must be corrected to include them. One possibility is to correct them to the modified Nusselt and Sherwood numbers using the methodology of Eqs. 5.33 from the Abramzon-Sirignano model.

6.5.1 Correlations without Stefan flow effects

Frössling (1938) and Ranz and Marshall (1952)

In (Fuchs 1959) the main contributions for the experimental work of (Frössling 1938) are presented. First, it is noted that the experimental apparatus contained droplets of water, aniline and nitrobenzene, as well as spheres of naphtalene. The observed droplets possessed initial radii spanning $0.1 < R_{d,0} < 0.9mm$ and were suspended from glass fibres except for water, which was suspended from a thermocouple. The chamber contained an aerodynamic tube which injected air towards the droplets at a variable velocity $0.2 < U^{\infty} < 7m/s$, leading to a range of Reynolds numbers $2.3 < Re < 1280$ when considering all cases.

Frössling results were mostly concerned to mass transfer, and therefore the Sherwood number. The results showed that the Sherwood number globally respected the following fitting formula:

$$Sh = 2(1 + \alpha Re^{1/2} Sc^{1/3}), \tag{6.33}$$

with α being a constant. The proportionality to $Sc^{1/3}$ is also positively reinforced from a theoretical perspective, due to similarity results using boundary layer theory (Schlichting and Gersten 2017). From the experimental data, it was found that $\alpha = 0.276$, leading to

the final formula:

$$Sh = 2 + 0.552 Re^{1/2} Sc^{1/3} \tag{6.34}$$

which is typically the main result attributed to Frössling's work.

Frössling also reported a large scatter for experimental data concerning water, and attributed this to the surrounding air's relative humidity. For the naphtalene sphere, Frössling obtained that the Sherwood number (and therefore, the mass transfer rate) may vary of a ten-fold factor when considering the front versus the rear point of the sphere, and a factor of more than 30 when also considering the sides of the sphere. This can be a critical consideration for some applications, given the spherical symmetry assumed by droplet mass transfer models.

The functional structure of Frössling's results was also extended to the heat transfer and the analogous Nusselt number, by using the Prandtl number Pr instead of the Schmidt number:

$$Nu = 2 + 0.552 Re^{1/2} Pr^{1/3} \tag{6.35}$$

We now present the results of Ranz and Marshall. Their contribution was summarized in a paper split in parts I and II, but only part I (Ranz and Marshall 1952) is readily available. Fuchs also details its main characteristics.

Experiments were ran for water droplets with $R_{d,0} \approx 0.5mm$ at room temperature and suspended from a microburette, with a thermocouple inserted at the side of the droplet to measure its temperature. The Reynolds numbers varied in the range $0 < Re < 200$ approximatively. The air flow was oriented vertically, similar to Frössling's approach, and it could push air with varying temperature T^{∞} spanning approximately $360 - 500K$. The mass transfer was measured either through the rate with which water must be injected through the burette to keep a constant diameter for the droplet, or through an extrapolation from the diameter's variation through microphotography at various instants. The authors argue that corrections for radiation and heat flow along the capillary were performed, as well as a correction for the heat flow from the added water through the burette, which does not share the same temperature as the water droplet.

In general, a proportionality to $Re^{1/2} Pr^{1/3}$ was also observed for the Nusselt number, however the constant in Eq. 6.33 that fitted the results was found to be $\alpha = 0.3$, leading to the following formulae:

$$\begin{aligned} Nu &= 2 + 0.6 Re^{1/2} Pr^{1/3}, \\ Sh &= 2 + 0.6 Re^{1/2} Sc^{1/3}, \end{aligned} \tag{6.36}$$

which are here referred to as the Ranz-Marshall correlations. Since the same functional structure is preserved with a similar constant, not much difference is expected from these correlations to those of Frössling.

Acrivos and Taylor (1962)

(Acrivos and Taylor 1962) followed the analytical procedure by some authors, for instance (Proudman and Pearson 1957), to develop analytical series for the Nusselt or Sherwood number. Acrivos and Tayloy develop their results for $Re << 1$ in the limit of Stokesian flow, providing an important analytical benchmark for low Reynolds flows. They further subdivided their study into small and large Péclet number regimes, and it is noted that in order to have small Reynolds and large Péclet numbers, it must follow that either the Prandtl or Schmidt numbers must be large, and this is the case for surrounding liquid phases. For spray combustion applications, the important results are for small Reynolds and small Péclets, and the following truncated expression is provided:

$$Nu = 2 + \frac{1}{2}Pe + \frac{1}{4}Pe^2 \ln Pe + 0.03404 Pe^2 + \frac{1}{16}Pe^3 \ln Pe, \tag{6.37}$$

which should be valid for $Pe \leq 1$. They also inform that for increasing Reynolds numbers, moving away from the limit $Re \to 0$ but if the restriction $Pe \leq 1$ is still respected, then the following formula would still preserve some accuracy up to $O(Pe^2 \ln Pe)$:

$$Nu = 2 + \frac{1}{2}Pe. \tag{6.38}$$

It is noted in (Grace and Clift 1978) that when Eq. 6.38 is divided by the Nusselt number representative of no phase-change and pure diffusion i.e. $Nu = 2$, then the resulting "correction factor" would be analogous to the Oseen correction factor Eq. 6.12 for the Stokes drag coefficient.

Whitaker (1972)

A study to correlate a great number of experimental data for different shapes, including spheres, was put together in (Whitaker 1972). Therein, the authors forced a correlation structure that ensures $Nu \to 2$ as $Re \to 0$, but also extend the functional form further from the laminar regime.

In the laminar regime, the classical proportionality following Frössling and Ranz-Marshall is offered i.e. $Re^{1/2}Pr^{1/3}$, whereas in the wake region they argue that a proportionality to $Re^{2/3}Pr^{1/3}$ would be more suitable due to the installment of turbulence effects. Moreover, the exponent on the Prandtl number is changed to 0.4 instead of 1/3 to better fit the data. They further added a ratio of surface to far-away gaseous viscosities, essentially expliciting the impact of variable properties for this property.

The following final expression is provided:

$$Nu = 2 + (0.4Re^{1/2} + 0.06Re^{2/3})Pr^{0.4}\left(\frac{\mu^{\infty}}{\mu^{s}}\right) \tag{6.39}$$

The fit is shown to be valid from $Re \approx 4$ to $Re \approx 10^5$, with a bigger deviation from some experimental data on the range $200 < Re < 4000$ and better overall agreement on the extremes.

Clift and Weber (1978)

In the book (Grace and Clift 1978), the authors specifically state an equivalence between Nusselt and Sherwood numbers and decided to show most of their results in terms of Sherwood numbers.

First for solid spheres, an extension is proposed for all Péclet numbers to Eq. 6.38 (using Sherwood number to keep the notation of Clift et al.), which is derived for $Re << 1$:

$$Sh = 1 + (1 + Pe)^{1/3}, \tag{6.40}$$

and they note that this can be done because the heat and mass transfer formulations are less sensitive to errors from vorticity expressions than the drag counterparts.

For the range $1 \leq Re \leq 400$ and $0.25 \leq Sc \leq 100$, they correlate numerical data from six sources reasonably well with the following expression:

$$Sh = 1 + \left[1 + \left(\frac{1}{Pe}\right)\right]^{1/3} Re^{0.41} Sc^{1/3}. \tag{6.41}$$

In (Abramzon and Sirignano 1989), the authors condensed Eqs. 6.40 and 6.41 into a single one:

$$\begin{gathered} Sh = 1 + f(1 + ReSc)^{1/3}, \\ f = 1 \text{ for } Re \leq 1, \\ f = Re^{0.077} \text{ for } 1 \leq Re \leq 400. \end{gathered} \tag{6.42}$$

The following expression was also provided to fit all ranges of Schmidt numbers and a general range for κ and for $Re > 70$:

$$Sh = \frac{2}{\sqrt{\pi}} Pe^{1/2} \left[1 - \frac{\left(\frac{2+3\kappa}{3+3\kappa}\right)}{\left(1 + \left[\frac{(2+3\kappa)Re^{1/2}}{(1+\kappa)(8.67+6.45\kappa^{0.64})}\right]^{n}\right)^{1/n}}\right]^{1/2}, \tag{6.43}$$

with $n = 4/3 + 3\kappa$.

Feng and Michaelides (2001) and Saboni et al. (2007)

Similar to their drag work counterpart, in (Feng and Michaelides 2001) and in (Saboni, Alexandrova, Spasic, and Gourdon 2007), the authors sought for numerical correlations spanning the full viscosity ratio κ for fluid spheres. Feng and Michaelides provided global expressions for two regimes of viscosity ratios, and limited their correlations to the range $10 < Pe < 1000$. Their formulas are provided for the Nusselt number, specifically:

$$\begin{aligned} Nu &= \left(\frac{2-\kappa}{2}\right) Nu^{\kappa=0} + \left(\frac{4\kappa}{6+\kappa}\right) Nu^{\kappa=2} \text{ for } 0 \leq \kappa \leq 2; \\ Nu &= \left(\frac{4}{2+\kappa}\right) Nu^{\kappa=2} + \left(\frac{\kappa-2}{\kappa+2}\right) Nu^{\kappa=\infty} \text{ for } 2 \leq \kappa \leq \infty, \end{aligned} \tag{6.44}$$

where $Nu^{\kappa=0}, Nu^{\kappa=2}, Nu^{\kappa=\infty}$ are correlations obntained specifically for bubbles, low-viscosity droplets and solid spheres, respectively; the ones that they provide for their correlations are:

$$Nu^{\kappa=0} = 1.6 - \frac{0.61Re}{Re+21} + 0.651Pe^{1/2}\left(1.032 + \frac{0.61Re}{Re+21}\right), \tag{6.45a}$$

$$Nu^{\kappa=2} = 1.41 - 0.15Re^{0.287} + 0.64Pe^{0.43}(1 + 0.233Re^{0.287}), \tag{6.45b}$$

$$Nu^{\kappa=\infty} = 1.3 - 0.182Re^{0.355} + 0.852Pe^{1/3}(1 + 0.233Re^{0.287}). \tag{6.45c}$$

Saboni et al. relaxed the Péclet restriction, extending the range to $0 < Pe < 10^6$, but concentrating their correlation on the Reynolds regime $10 < Re < 400$, with the justification that past $Re = 400$ the hypothesis of axisymmetry would not longer be valid. Their viscosity ratio covers the range $0 < \kappa < 1000$ and a single all-encompassing expression is provided for the Sherwood number:

$$\begin{aligned} Sh = \frac{1}{3+\kappa}\Bigg[1.65 + 0.67\left(Pe^{1/2} + \left(\frac{0.67Re}{Re+15}\right)(Pe^{1/2}-1)\right) + \\ +\kappa(1 - 0.12Re^{1/3} + (1+Pe)^{1/3}(1+0.12Re^{1/3}))\Bigg] \end{aligned} \tag{6.46}$$

6.5.2 Correlations with Stefan flow effects

Downing (1966)

Downing correlated experimental data for single-component droplets composed of acetone, hexane, benzene and water, at surrounding temperatures spanning $300 < T^\infty < 613K$. Similar to Ranz and Marshall, in (Downing 1966) the droplets were suspended and received a stream of air from below, with corresponding Reynolds numbers $24 < Re < 325$. A correction factor based on the transfer number $B_{T,L}$ appears explicitly, to incorporate phase-change effects. A latent-heat Spalding thermal transfer number was

used, as defined in Eq. 6.26.

However, the author also added an explicit dependance on the non-dimensional temperature difference, arguing that this would correct for the fact that properties are supposed constant but that they should vary with temperature in practice. Their final correlation for the Nusselt number is:

$$\begin{aligned} Nu &= MN\frac{\ln(1+B)}{B}\left(2+0.6Re^{1/2}Pr^{1/3}\right), \\ M &= 1-0.4\left(1-\frac{T^s}{T^\infty}\right), \\ N &= 1-0.4\left(1-\frac{\ln(1+B)}{B}\right). \end{aligned} \tag{6.47}$$

It is straightforward to see that this correlation can be seen as three multiplicative factors inserted to correct for the Nusselt correlation of (Ranz and Marshall 1952). Ignoring the M, N factors, the other correction factor is $\ln(1+B)/B$, which has been suggested in (Spalding 1953) for the inclusion of Stefan-flow effects.

The authors report fairly good agreement between the above correlation and their experimental data, but that it must be used carefully following the same treatment as they did. In particular, for the properties computation, they state that they were evaluated using a reference temperature and composition defined as that of Eqs. 5.37 with $\gamma = 0.6$, which is quite different from the one-third rule that would later appear.

Eisenklam (1967)

In (Eisenklam, Arunachalam, and Weston 1967), the author provided two correlations for Nusselt numbers, one for evaporating and another for burning droplets. Experiments were carried out for droplets of corresponding Reynolds numbers in the range $0.01 < Re < 15$ and transfer numbers $0.06 < B_{T,L} < 12.3$, and formulations based on boundary-layer theory were used for the correlations. Since overall the presence of strong phase-change was seen to decrease Nusselt numbers, a functional dependency on $1/(1+B)$ was elected to correct for this, leading to the following expression for the Nusselt number of an evaporating droplet:

$$Nu = \frac{2+1.6Re^{1/2}}{1+B_{T,L}}. \tag{6.48}$$

They note that their correlations are based on an arimethic mean for gaseous properties between surface and far-field for the evaporative case. The proposed expression retrieves $Nu \to 2$ as $Re \to 0$ only if $B \to 0$ as well.

Faeth (1977)

In the review (Faeth 1977), the author lists the steps necessary to correlate Nusselt or Sherwood numbers for droplet in spray combustion applications. First, it is noted that the functional behaviour should retrieve $Nu, Sh \to 2$ as $Re \to 0$, with a functional dependency on the Reynolds number and the Prandtl or Schmidt number, for the Nusselt or Sherwood number respectively, as customary. Then, the author enforces that the phase-change correction should mimic the one proposed by (Spalding 1953), namely with a correction factor of $\ln(1+B)/B$, but instead of using the thermal transfer number as done by Spalding, they opt for the mass transfer number B_M. They then propose to unite the correlations for low Reynolds numbers made by (Acrivos and Taylor 1962) with the one of (Frössling 1938) for the greater Reynolds range, yielding the following result:

$$\begin{aligned} Nu &= \left[\frac{\ln(1+B_M)}{B_M}\right]\left(2+\frac{0.555Re^{1/2}Pr^{1/3}}{\left(1+1.232/(RePr^{4/3})\right)^{1/2}}\right), \\ Sh &= \left[\frac{\ln(1+B_M)}{B_M}\right]\left(2+\frac{0.555Re^{1/2}Sc^{1/3}}{\left(1+1.232/(ReSc^{4/3})\right)^{1/2}}\right). \end{aligned} \tag{6.49}$$

It should be noted that the coefficient 0.555 was used instead of 0.552 for the classical Frössling result.

The author still notes the uncertainties for the properties' evaluation, and that the correction factor for including phase-change effects has been also used in the form of $1/(1+B)$ as done in (Eisenklam, Arunachalam, and Weston 1967), instead of $\ln(1+B)/B$ as they propose. It is noted that if the original treatment of properties is followed, actually the factor $1/(1+B)$ agrees better with experimental data, but that it would be theoretically inconsistent because in the limit of no convection the boundary layer would extend to infinity and the ratio of heat and mass transfers when including or not Stefan flow (and thus, phase-change) should contain the $\ln(1+B)/B$ structure instead.

Renksizbulut et al (1983,1988,1989,1991)

In the series of papers (Renksizbulut and Yuen 1983a), (Renksizbulut and Yuen 1983b), (Renksizbulut and Haywood 1988), (Haywood, Nafziger, and Renksizbulut 1989) and (Renksizbulut, Nafziger, and Li 1991), authors Renksizbulut et al. performed a series of experimental and numerical investigations and produced dedicated expressions for both Nusselt and Sherwood numbers, indicating that a different behaviour may be expected regardless of the functional similitude between species and heat diffusion. They note that, for their correlations, the Reynolds number is to be computed using a viscosity evaluated in the film, using the same reasoning as in (Abramzon and Sirignano 1989). However, different from (Abramzon and Sirignano 1989), they use a $\gamma = 1/2$ coefficient instead of the one-third rule proposed in (Yuen and Chen 1976).

In (Renksizbulut and Yuen 1983a), the following correlation has been proposed for the Nusselt number, for $24 < Re < 2000$ and temperatures up to $T^{\infty} = 1273K$:

$$Nu = \frac{(2 + 0.57Re^{1/2}Pr^{1/3})}{(1 + B_{T,L})^{0.7}} \tag{6.50}$$

and they also compute the Prandtl number and the latent-heat thermal transfer number $B_{T,L}$ using properties evaluated at the film with the same averaging rule. The studied substances were water, methanol and n-heptane. In a subsequent numerical study (Renksizbulut and Yuen 1983b), they focused on the Reynolds range $10 < Re < 150$ and found a slightly different correlation:

$$Nu = \frac{(2 + 0.9Re^{1/2}Pr^{1/3})}{(1 + B_{T,L})^{0.7}}, \tag{6.51}$$

which indicates that the coefficients should be tuned differently for the lower and the higher part of the intermediate Reynolds number regime. The correlation represented through Eq. 6.50 also reappeared in a later study (Renksizbulut and Yuen 1983b), and due to its more general range of Reynolds numbers it should be preferred.

As for the Sherwood number, both studies of (Haywood, Nafziger, and Renksizbulut 1989) and (Renksizbulut, Nafziger, and Li 1991) provide the same correlation:

$$Sh = \frac{(2 + 0.87Re^{1/2}Sc^{1/3})}{(1 + B_{T,L})^{0.7}} \tag{6.52}$$

which was verified for both numerical and experimental data for $10 < Re < 2000$, for a surrounding temperature $T^{\infty} = 800K$. The authors argue that the ratio $\ln(1 + B)/B$, even though predicted theoretically for the non-convective regime, would fail to capture the correct physics for higher Re, corroborating the findings of (Faeth 1977) and the overall structure suggestion of (Eisenklam, Arunachalam, and Weston 1967).

The unified Nusselt and Sherwood correlations of Eqs. 6.50,6.52 were also found to be satisfactory in the study of (Chiang, Raju, and Sirignano 1992). However, a worse agreement was found with the data of (Schwarz and Smolík 1994), wherein experiments were ran for water droplets in low temperature environments $314 < T^{\infty} < 449$ and for $30 < Re < 80$, indicating that the mass transfer correction possible does not converge well in the limit $B \to 0$. In the study of Schwarz et al., a better agreement was found with the expression of (Downing 1966), which was also derived for a closer set of conditions.

6.6 Summary of expressions

In this chapter, concepts related to convection were introduced, with a focus on forced convection for droplets in spray combustion scenarios. A general expression for the

droplet momentum was provided in the context of the point-particle assumption. Multiple correlations were then presented for the drag coefficient for this equation, as well as for the Nusselt and Sherwood numbers that correct the heat and mass transfer formulations in the scope of the film theory. In Table 6.5 below we summarize the main drag coefficient expressions, and in Table 6.6 the main Nusselt number correlations. A sensitivity analysis for the models of both of these tables will follow in Chap. 7. For conciseness, we only showcase expressions for the Nusselt number.

Schiller-Naumann	$C_D = \frac{24}{Re}\left[1 + 0.15Re^{0.687}\right], \text{for } Re \leq 1000$ $C_D = 0.44, \text{ for } Re > 1000$
Putnam	$C_D = \frac{24}{Re}\left[1 + \frac{Re^{2/3}}{6}\right]$
Morsi and Alexander	$C_D = \frac{24}{Re} \text{ for } Re < 0.1$ $C_D = \frac{22.73}{Re} + \frac{0.0903}{Re^2} + 3.69 \text{ for } 0.1 \leq Re < 1$ $C_D = \frac{29.1667}{Re} - \frac{3.8889}{Re^2} + 1.222 \text{ for } 1 \leq Re < 10$ $C_D = \frac{46.5}{Re} - \frac{116.67}{Re^2} + 0.6167 \text{ for } 10 \leq Re < 100$ $C_D = \frac{98.33}{Re} - \frac{2778}{Re^2} + 0.3644 \text{ for } 100 \leq Re < 1000$
Feng and Michaelides	$C_D^{Re<5} = \left(\frac{2+3\kappa}{1+\kappa}\right)\left(\frac{8}{Re}\left[1 + 0.05\left(\frac{2+3\kappa}{1+\kappa}\right)Re\right] - 0.01Re\ln Re\right)$ $C_D^{Re>5} = \left(\frac{2-\kappa}{2}\right)C_D^{\kappa=0} + \left(\frac{4\kappa}{6+\kappa}\right)C_D^{\kappa=2}, \text{ for } 0 < \kappa < 2$ $C_D^{Re>5} = \left(\frac{4}{2+\kappa}\right)C_D^{\kappa=2} + \left(\frac{\kappa-2}{\kappa+2}\right)C_D^{\kappa=\infty}, \text{ for } 2 < \kappa < \infty$
Saboni et al.	$C_D = \frac{\left[\kappa\left(\frac{24}{Re} + \frac{4}{Re^{1/3}}\right) + \frac{14.9}{Re^{0.78}}\right]Re^2 + 40\left(\frac{2+3\kappa}{Re}\right) + 15\kappa + 10}{(1+\kappa)(5+Re^2)}$
Renksizbulut and Yuen	$C_D = \frac{24}{Re}\frac{1}{(1+B)^{0.2}}\left[1 + 0.2Re^{0.63}\right]$
Bellan and Harstad	$C_D = \frac{24}{Re}\left[\frac{1 + 0.0545Re + 0.1Re^{1/2}(1 - 0.03Re)}{1 + \alpha Re_{d,b}^{\beta}}\right]$
Chiang, Raju and Sirignano	$C_D = \frac{24}{Re}\frac{1}{(1+B)^{0.32}}\left[1 + 0.325Re^{0.474}\right]$

Figure 6.5: Summary of main drag coefficient models for Chap. 6.

Frössling	$Nu = 2 + 0.552 Re^{1/2} Pr^{1/3}$
Ranz-Marshall	$Nu = 2 + 0.6 Re^{1/2} Pr^{1/3}$
Whitaker	$Nu = 2 + (0.4 Re^{1/2} + 0.06 Re^{2/3}) Pr^{0.4} \left(\frac{\mu^{\infty}}{\mu^{s}}\right)$
Clift, Grace and Weber	$Nu = 1 + f(1 + RePr)^{1/3}$ $f = 1$ for $Re \leq 1$ $f = Re^{0.077}$ for $1 \leq Re \leq 400$
Feng and Michaelides	$Nu = \left(\frac{2-\kappa}{2}\right) Nu^{\kappa=0} + \left(\frac{4\kappa}{6+\kappa}\right) Nu^{\kappa=2}$ for $0 \leq \kappa \leq 2$ $Nu = \left(\frac{4}{2+\kappa}\right) Nu^{\kappa=2} + \left(\frac{\kappa-2}{\kappa+2}\right) Nu^{\kappa=\infty}$ for $2 \leq \kappa \leq \infty$
Saboni et al.	$Nu = \frac{1}{3+\kappa}\left[1.65 + 0.67\left(Pe^{1/2} + \left(\frac{0.67Re}{Re+15}\right)(Pe^{1/2}-1)\right) + \right.$ $\left. + \kappa(1 - 0.12 Re^{1/3} + (1+Pe)^{1/3}(1 + 0.12 Re^{1/3}))\right]$
Downing	$Nu = MN \frac{\ln(1+B)}{B}\left(2 + 0.6 Re^{1/2} Pr^{1/3}\right)$
Faeth	$Nu = \left[\frac{\ln(1+B)}{B}\right]\left(2 + \frac{0.555 Re^{1/2} Pr^{1/3}}{\left(1 + 1.232/(RePr^{4/3})\right)^{1/2}}\right)$
Renksizbulut et al.	$Nu = \frac{(2 + 0.57 Re^{1/2} Pr^{1/3})}{(1+B)^{0.7}}$

Figure 6.6: Summary of main Nusselt number correlations for Chap. 6.

Chapter 7

Numerical investigation for convection sub-models

In Chap. 6, correlations were listed for the drag coefficient as well as for the Nusselt and Sherwood non-dimensional numbers. The drag coefficient is used mainly for the update of the droplet velocity, determining its relaxation time. As for the Nusselt and Sherwood numbers, they incorporate convection effects into the heat and mass transfer formulations, respectively, regulating the boundary layer thicknesses.

In total, eight drag coefficient correlations were highlighted in Table 6.5 and nine Nusselt (or Sherwood, equivalently) correlations were listed in Table 6.6. Among these correlations, overlaps for the parameter ranges occur, and some of them incorporate different physics than others. This indicates that a study to identify the impact of these choices would be useful, and this is the purpose of this chapter.

First, we make a preliminary analysis to qualitatively infer which models present the largest differences. Then, we move to full droplet numerical investigations, seeking to show what are the maximum deviations expected for typical droplet metrics when varying different convection sub-models. To isolate the influence of each sub-model, the Abramzon-Sirigano droplet heat and mass transfer model described in Chap. 5 is used. As explained in Chap. 6, models for Nusselt and Sherwood numbers that do not take Stefan-flow effects into account will be corrected via the procedure suggested by Abramzon and Sirignano, i.e. Eqs. 5.33.

In this chapter the work previously developed in (Santos, Filho, and Vié 2021) is conducted in a more focused manner. The goal is still to draw attention to the fact that a sensitivity exists concerning different sub-modelling strategies in this front, and that no universal answer is present today; therefore, we also seek to encourage further studies, especially as direct numerical solution (DNS) tools become more practical.

7.1 Preliminary analysis

As seen in Chap. 6, different convection sub-models include different physics, and to incorporate them, different parameters are employed. From Tables 6.5 and 6.6, the parameters that can be varied are:

- The Reynolds number Re_d (all models);
- The blowing Reynolds number $Re_{d,b}$ (Bellan et al.);
- The Spalding transfer numbers B_M, B_T (Renksizbulut et al., Bellan et al., Chiang et al., Downing, Faeth);
- The Schimdt, Prandtl and Péclet numbers Sc, Pr, Pe_M, Pe_T (Nusselt and Sherwood models)
- The viscosity ratio κ (Feng et al., Saboni et al.)
- The film and the far-away viscosity μ^f, μ^∞ (Whitaker)
- The temperature at the surface and far-away T^s, T^∞ (Downing)

For this a priori analysis, only the Reynolds number will be varied. For all other parameters, we first conduct a simple numerical investigation to provide realistic baseline values. For the Péclet numbers, since they are a product between the Schmidt/Prandtl number and the Reynolds number, tracking the Sc and Pr is sufficient.

Simulations are conducted for pure droplets composed of ethanol, acetone, water and n-dodecane in an extreme scenario which should magnify the differences between models, thus providing an outlook to the maximum expected impacts. The initial conditions can be seen in Table 7.1. The atmosphere is composed of pure air. To gauge these reference values, we use the standard drag curve (Eq. 6.17) for the drag coefficient and the Frössling equations (Eqs. 6.34 and 6.35) for the Sherwood and Nusselt numbers respectively. The Reynolds number is computed using the film viscosity μ^f.

Parameter	Value
Initial droplet diameter $\mathcal{D}_{d,0}$	$100\mu m$
Initial droplet temperature $T_{d,0}$	$300K$
Surrounding gas temperature T^∞	$1600K$
Initial droplet velocity $U_{d,0}$	$0m/s$
Surrounding gas velocity U^∞	$100m/s$
Atmospheric pressure p	$101325Pa$

Figure 7.1: Common initial conditions for reference investigation.

In Fig. 7.3, we see that the maximum Reynolds number is obtained for the acetone droplet and is less than 80. We also see that all droplets manage to relax towards the far-field velocity, $U^\infty = 100m/s$ despite their initial large size, as they finally completely

evaporates and thus reach very small diameters. The maximum blowing Reynolds number is obtained for acetone and rovers around $Re_{d,b} \approx 3$. As for the viscosity ratio, we are interested in the minimum values, since a small κ will lead to higher recirculation and thus bigger deviations from the solid sphere models. We see that the minimum $\kappa \approx 10$ is obtained for both n-dodecane and acetone. Concerning the Spalding transfer numbers, the highest values are obtained for n-dodecane, and we see that the droplets stabilize at their maximum value for most of their lifetime. Also, systematically the thermal transfer number B_T is around double that of the mass transfer number B_M. Finally, the Prandtl number stabilises at maximum value $Pr^f \approx 0.945$ for n-dodecane and minimum value $Pr^f \approx 0.77$ for water, and the Schmidt number stabilises at a maximum of $Sc^f \approx 1.0$ obtained for n-dodecane and a minimum $Sc^f \approx 0.7$, obtained for the water droplet.

Since the n-dodecane droplet systematically outputs parameters that would lead to the greatest deviations, we choose this droplet for the following investigations. In Table 7.2 we summarize reference values for all parameters relevant to convection with the exception of the Reynolds number Re_d, which will be left as a degree of freedom. These reference values have been arbitrarily evaluated at $t = 5ms$ (dotted lines in Fig. 7.3) where most of them have reached stable values and the blowing Reynolds number $Re_{d,b}$ is still near its peak value, where its impact should be the highest. Also, at $t = 5ms$, the Reynolds number was measured to be $Re_d \approx 18$.

To obtain the gas viscosity ratio used in the Whitaker model, the viscosity at the film was evaluated to be $\mu^f \approx 2.56\text{x}10^{-5}\ kg/(m \cdot s)$ at $t = 5ms$, and the viscosity for the far-field is computed as $\mu^\infty = 3.50\text{x}10^{-5}\ kg/(m \cdot s)$ for air at $1600K$. As for the temperature ratio required for the Downing model, at $t = 5ms$ the system has already reached its wet-bulb temperature, evaluated as $T^s \approx 464$ and therefore $T^s/T^\infty = 464/1600$.

Parameter	Reference value
Blowing Reynolds number	$Re_{d,b} = 2.15$
Spalding mass transfer number	$B_M = 6.34$
Spalding heat transfer number	$B_T = 14.37$
Prandtl number	$Pr = 0.94$
Schmidt number	$Sc = 0.98$
Viscosity ratio	$\kappa = 9.62$
Gas viscosity ratio	$\mu^\infty/\mu^f = 1.37$
Temperature ratio	$T^s/T^\infty = 0.29$

Figure 7.2: Reference parameter values for a priori analysis.

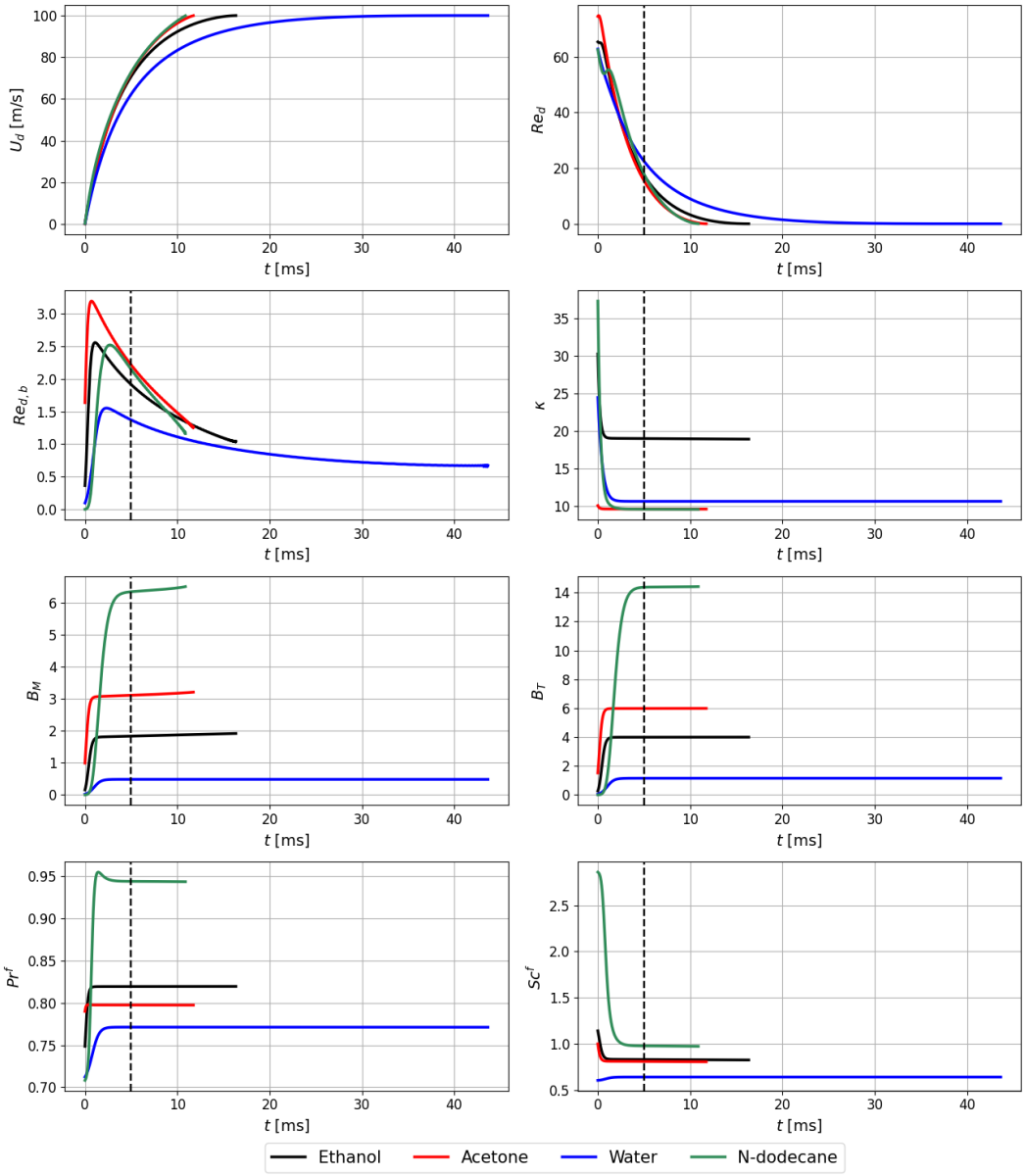

Figure 7.3: Simulations using the Abramzon-Sirignano model for ethanol, acetone, water and n-dodecane droplets surrounded by pure air with initial conditions listed in Table 7.1. The droplet drag followed the Putnam model whereas the Nusselt/Sherwood numbers followed the Frössling correlations corrected for Stefan-flow using the Abramzon and Sirignano framework. Results are displayed for the droplet velocity U_d, its Reynolds number Re_d, its blowing Reynolds number $Re_{d,b}$, the viscosity ratio κ, the Spalding transfer numbers B_M and B_T and the Prandtl and Schmidt numbers evaluated at the film Pr_f,Sc_f. Dotted vertical lines are marked for $t = 5ms$, where values from the n-dodecane curves were extracted.

In Fig. 7.4 we now see the results of this a priori analysis. For the drag coefficient, it is possible to see that the Schiller-Naumann, Putnam, Morsi-Alexander, Feng-Michaelides and Saboni-Alexandrova models all behave in similar ways. The Renksizbulut-Yuen, Bellan-Harstad and Chiang-Raju-Sirignano are the models that incorporate the impact of phase-change, and these manifest the largest deviation from the other models. Towards $Re_d \approx 200$, the Bellan-Harstad formulation starts to decay abruptly but that should not be an issue since this correlation was derived for a maximum of $Re_d = 100$ and the extreme conditions of Table 7.1 show that droplets will seldom cross this limit.

As for the Nusselt number, again the models that do not naturally incorporate phase-change i.e. the Frössling, Ranz-Marshall, Whitaker, Clift et al., Feng-Michaelides and Saboni-Alexandrova models, are grouped together. It should be noted that all of them are being corrected with the Abramzon-Sirignano correction factor (which is the same for all of them, since it will only depend on B_T and so no relative differences are expected). The difference between this set of models and the models of Downing, Faeth and Renksizbulut et al. is again expressive.

The pronounced difference for highly evaporation conditions motivated us to produce the same analysis but by fixing the evaporation-related quantities i.e. $B_M, B_T, Re_{d,b}$ to an extremely low value e.g. $1\text{x}10^{-5}$. The result of this analysis can be seen in Fig. 7.5. Indeed, this time around we see a better agreement between all models; still, for the Nusselt number appreciable differences can be seen.

7.2 Complete droplet heat and mass transfer investigations

As previously seen in Figs. 7.4 and 7.5, a preliminary analysis has shown that a certain sensitivity can be expected when varying droplet drag coefficient and Nusselt/Sherwood numbers. We now conduct full droplet evaporation simulations where we vary only a single sub-model at a time, to see whether the preliminary sensitivity is increased or damped during a realistic scenario.

The initial conditions of Table 7.1 are preserved. We also conducted simulations for the n-dodecane droplets, since these systematically represent situations with the most deviations. For the investigations where the drag coefficient was varied, the Nusselt and Sherwood numbers were computed using the Frössling correlation corrected for Stefan flow effects using the procedure in (Abramzon and Sirignano 1989) i.e. Eqs. 5.33. Conversely, for the simulations where the Nusselt and Sherwood numbers were varied, we fixed the droplet drag using the standard drag curve of (Putnam 1961) i.e. Eq. 6.17. Also, for the Nusselt and Sherwood simulations for simplicity we employ the same modelling structure for both, only changing the Schmidt number for the Prandtl number (or vice-versa) and the same for the Péclet numbers. The only exception for this can be observed with the models described by Renksizbulut et al. Eqs. 6.50 and 6.52 which were specifically provided for the Nusselt and Sherwood numbers separately. Results are

summarized in Figs. 7.6 and 7.7.

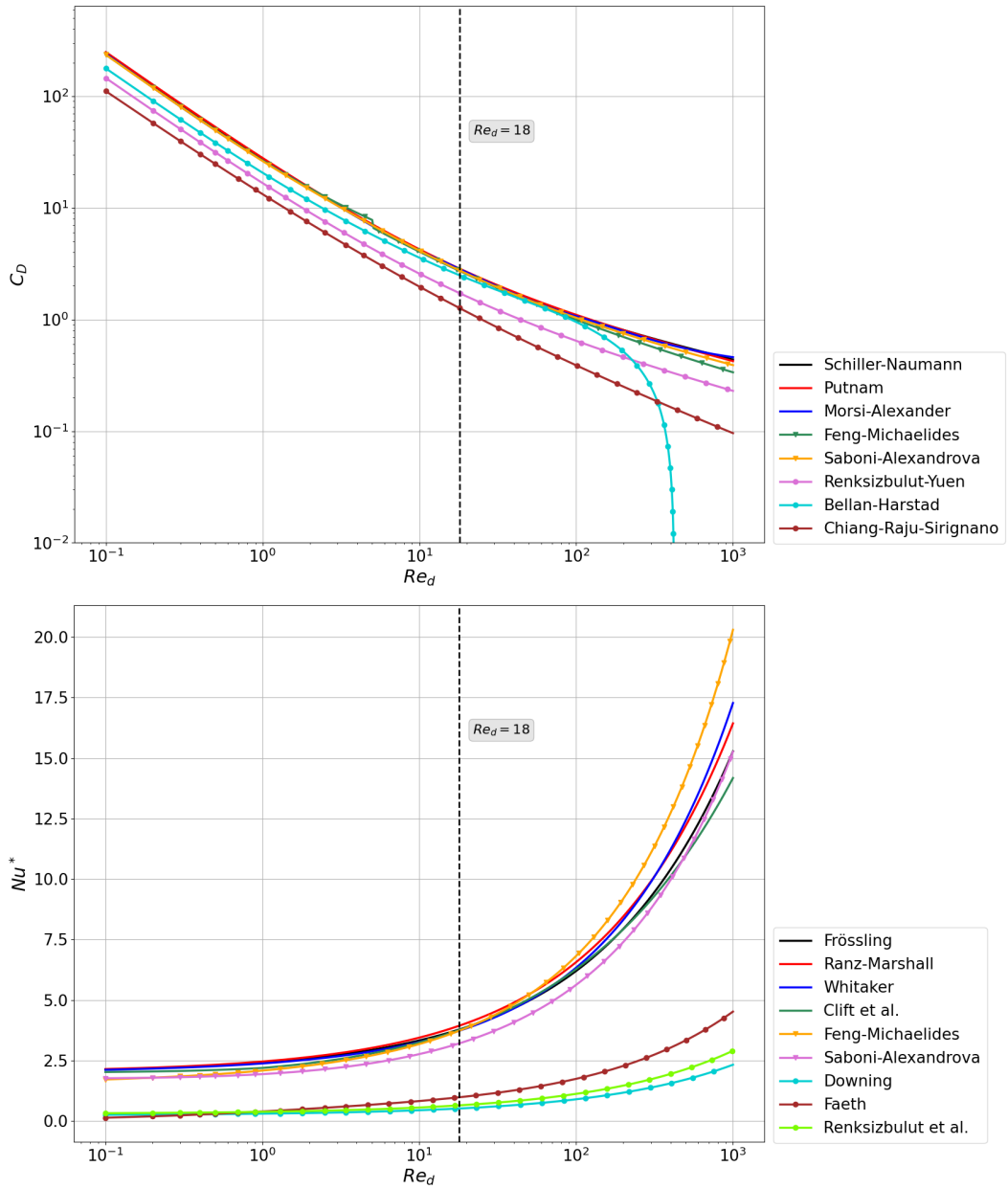

Figure 7.4: Results for droplet drag coefficient models (top, log-log plot) and Nusselt number models (bottom - semilog plot) using parameters from Table 7.2 while varying the Reynolds number in the range $0.1 < Re_d < 1000$. The dotted line corresponds to $Re_d = 18$ where parameters were extracted from the n-dodecane preliminary simulation.

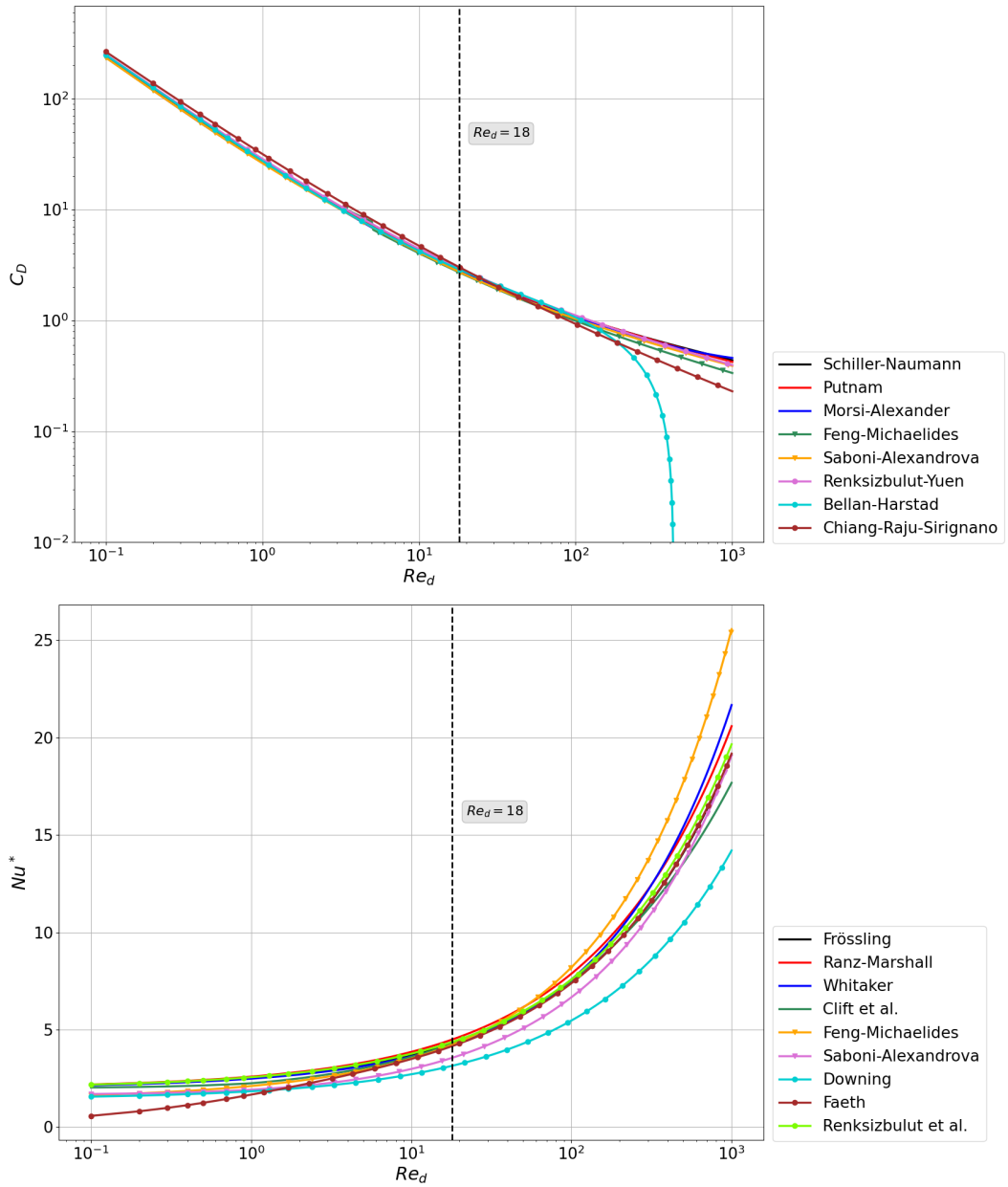

Figure 7.5: Results for droplet drag coefficient models (top, log-log plot) and Nusselt number models (bottom - semilog plot) using parameters from Table 7.2 except for $B_M, B_T, Re_{d,b}$ which are all fixed at $1\text{x}10^{-5}$. The Reynolds number is varied in the range $0.1 < Re_d < 1000$. The dotted line corresponds to $Re_d = 18$ where parameters other than $B_M, B_T, Re_{d,b}$ were extracted from the n-dodecane preliminary simulation. Models that do not have Stefan flow effects (those with plain lines and lines with triangles) have been corrected using the modified Nusselt formulation of Abramzon and Sirignano.

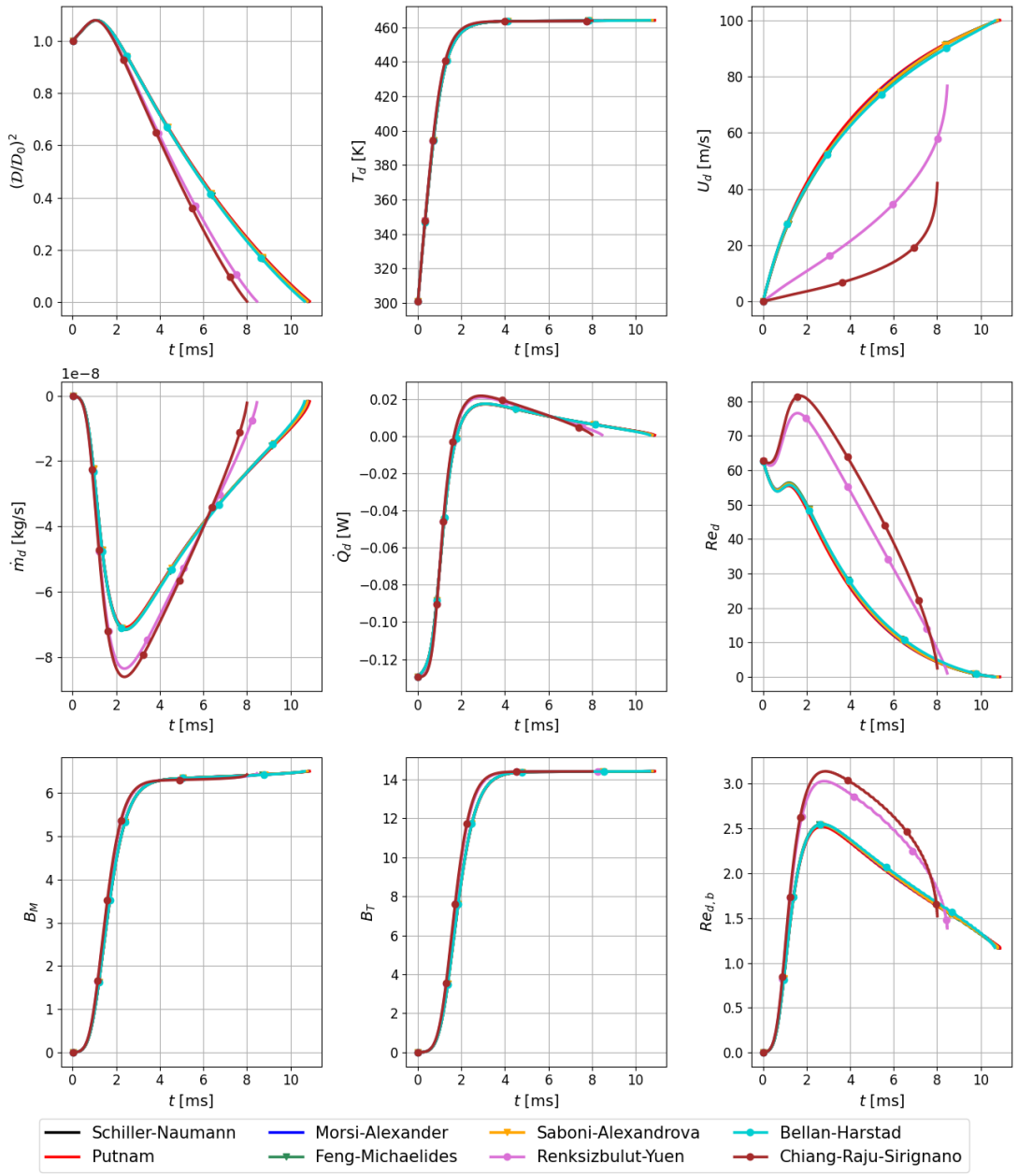

Figure 7.6: Results for droplet drag coefficient models using parameters from Table 7.1 for a n-dodecane droplet surrounded by pure air using the Abramzon-Sirignano model. The Nusselt and Sherwood numbers were computed using the Frössling model with the Abramzon-Sirignano correction for Stefan-flow effects.

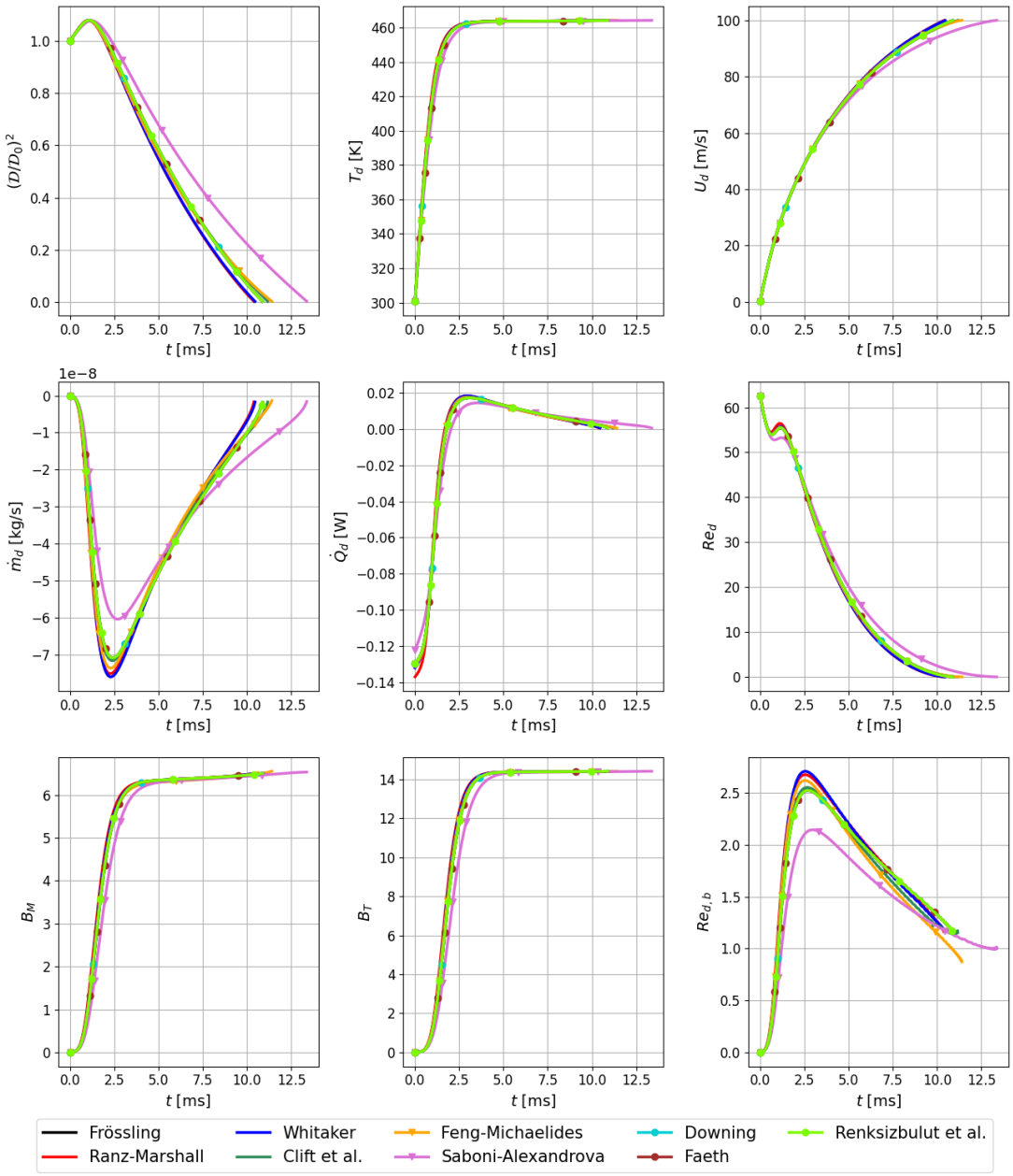

Figure 7.7: Results for droplet Nusselt and Sherwood models using parameters from Table 7.1 for a n-dodecane droplet surrounded by pure air using the Abramzon-Sirignano model. The drag coefficient was computed using Putnam's standard drag curve.

In Fig. 7.6 we see first the results for the drag coefficients. The models can be classified in three categories. The Schiller-Naumann, Putnam and Morsi-Alexander fall under the solid sphere (SS) category, the Feng-Michaelides and Saboni-Alexandrova are part of the fluid sphere with recirculation (FSR) category, and finally the Renksizbulut-Yuen, Bellan-Harstad and Chiang-Raju-Sirignano are classified as fluid sphere with phase-change (FSPC) models. In general, we see that all SS and FSR models behave similarly in all metrics. For the FSPC category, the Bellan-Harstad model performs similar to other models, possibly justified by the small values for the blowing Reynolds number.

As for the two remaining models, they both behave substantially differently from other models, predicting for instance that the droplet is not able to relax to the far-field velocity. Due to the consistently higher relative velocity for these two models, the droplet lifetime is predicted to be around 20 % lesser than other models. We also see that the Reynolds number increases past its initial value, and a different inflection is observed both for the Reynolds number as well as for the droplet velocity. A sharper peak is observed for the global mass transfer rate, and this does not translate to the heat transfer rate and thus the droplet temperature. This may be because no deviations are observed for the mass transfer number B_M, and since the Abramzon-Sirignano model computes the thermal transfer Spalding number B_T directly from B_M, no deviations are propagated from these terms to the heat transfer rate.

In Fig. 7.7 we now see the isolated impact for the Nusselt and Sherwood numbers. Following the same classification from the drag models, the Frössling, Ranz-Marshall, Whitaker and Clift et al. are part of the SS group, Feng-Michaelides and Saboni-Alexandrova again represent the FSR group and the Downing, Faeth and Renksizbulut et al. finally compose the FSPC category. This time around, the only model that clearly distantiates itself from the other ones is the Saboni-Alexandrova one from the FSR group. The main impact can be traced to the mass transfer rate, which has a smaller peak, translating to a smaller peak for the blowing Reynolds number and a longer droplet lifetime. Still, among the remaining models, the Feng-Michaelides which is also an FSR model, predicts the longest droplet lifetime, whereas the models from the SS group predict the shortest droplet lifetime. The maximum difference for the droplet lifetime among this group is around 10 %. Different from the drag coefficients, all models preserve the same trends for physical behaviours.

7.3 Summary

In this chapter, we sought to compare the different strategies for convection sub-models proposed in Chap. 6. To do this, first we established in Table 7.1 initial conditions that represent an extreme scenario for moving droplets, while still aiming for realistic scenarios considering spray combustion applications. Then, a preliminary analysis was conducted. The n-dodecane droplet was isolated as the one representative of the largest expected deviations, and a first intuition of expected differences was developed in Figs. 7.4, 7.5.

Finally, in Figs. 7.6 and 7.7 we show results for complete simulations, showing that for the droplet drag coefficient the correction for phase-change can be quite impactful, whereas for the Nusselt and Sherwood numbers, the correction for inner recicirculation merits further investigation. This suggests that ideally a universal correlation should be developed that takes into account both the recirculation as well as phase-change, aiming general scenarios for droplet in spray combustion scenarios.

Part III

Multi-component droplet phase-change models

Chapter 8

A reference multi-component droplet heat and mass transfer model

In Part II, a comprehensive treatment was given first to single-component droplet heat and mass transfer models, leading up to the (Abramzon and Sirignano 1989) formulation. Considering the set of hypothesis layed out in Part I, the Abramzon-Sirignano model is today broadly considered as a reference for single-component applications, or even as a framework for multi-component surrogate based models.

However, when more than one species is present, there is still no consensus for discrete component models (DCMs), that solve for each species individually. Therefore, it is the purpose of this chapter to provide a DCM reference framework, for both the mass and the heat transfer separately.

For the mass transfer, a formulation based on the work of (Tonini and Cossali 2016) is proposed, where the full Stefan-Maxwell equations are integrated. In this way, no simplifying hypotheses must be made for the diffusion velocities closure, as explained in Chap. 2. However, the Stefan-Maxwell formulation proposed by Tonini-Cossali presented some drawbacks considering general spray combustion applications: only a non-convective formulation was presented, and only a single inert species could be present in the gaseous phase. Our proposed formulation is able to incorporate convection effects following the film theory treatment explained in Chap. 5 and also no limitations are imposed for the inert species. The importance of convection was already justified, but an arbitrary number of inert species in the gaseous phase is extremely important for combustion applications, where different combustion products and/or intermediary species may be present and directly impact the mass transfer behavior through the far-away specified conditions. Additionally, the resulting formulation also presents a simpler analytical structure, favoring a simpler numerical implementation.

Then, we propose a heat transfer formulation that, when following the hypotheses #1-#7 from Chap. 1, is general in the sense that no further structural hypotheses are necessary. In particular, it will be shown that this formulation is able to organically incorporate enthalpy diffusion effects, and that it degenerates to the heat transfer formulation of Abramzon and Sirignano for the single-component limit. From a numerical implementation standpoint, this result is highly desirable, as the same formulation can be used regardless of the number of components. This is also important for situations where the droplet starts in a stratified multi-component scenario but tends to become single-component as volatile species evaporate.

8.1 A general Stefan-Maxwell mass transfer model

As discussed on Chap. 2, ideally the Stefan-Maxwell equations should be used for the diffusion velocity closure. The model that uses the least constraining structure while still employing the Stefan-Maxwell equations with typical hypotheses for droplet mass transfer models is the one proposed by (Tonini and Cossali 2016). However, that formulation does not take into account convection effects and supposes that only one inert species can be present on the gaseous phase. Therefore, we depart from a similar point, but taking a different path, in order to incorporate these considerations. Still, the model by Tonini and Cossali will be detailed and derived in Chap. 9 for reference.

First, we use the information contained in the integrated species conservation Eq. 1.11. The obtained Stefan-Maxwell equations Eqs. 2.12, apart from the hypotheses used for their derivation, are still general. This means that they are still "disconnected" from the droplet mass transfer formulation, and we start by making this connection. To do this, first Eq. 1.11 can be arranged for the molecular velocities:

$$\mathrm{v}_i^m = \frac{\dot{m}_i}{4\pi r^2 \rho Y_i}, \tag{8.1}$$

Substitution of Eq. 8.1 in the Stefan-Maxwell equation for the difference of molecular velocities Eq. 2.12a leads to:

$$4\pi r^2 \rho \frac{dX_i}{dr} = -\sum_{k=1}^{N} \frac{X_i X_k}{\tilde{D}_{i,k}} \left[\frac{\dot{m}_i}{Y_i} - \frac{\dot{m}_k}{Y_k} \right], \tag{8.2}$$

where we have left the original multi-component binary diffusion coefficients $\tilde{D}_{i,k}$ instead of the simplified binary mixture ones $D_{i,k}$ since our proposed derivation does not need to make this hypothesis.

Conversion from mass fractions on the RHS to molar fractions and substitution for the molar density $c = \rho/W$ and a molar evaporation rate $\dot{n}_i = \dot{m}_i/W_i$ leads to:

$$4\pi r^2 c \frac{dX_i}{dr} = -\sum_{k=1}^{N} \frac{[X_k \dot{n}_i - X_i \dot{n}_k]}{\tilde{D}_{i,k}}. \tag{8.3}$$

Since when $k = i$ the term in the summation cancels out, the equation above is also equivalent to:

$$4\pi r^2 c \frac{dX_i}{dr} = -\sum_{\substack{k=1 \\ k\neq i}}^{N} \frac{[X_k \dot{n}_i - X_i \dot{n}_k]}{\tilde{D}_{i,k}}. \tag{8.4}$$

By making the change of variable $\xi = 1/r$ and by splitting the summation into its two parts, the above equation can be rearranged as:

$$\boxed{\frac{dX_i}{d\xi} = \frac{1}{4\pi c}\left(\left[-\sum_{\substack{k=1 \\ k\neq i}}^{N} \frac{\dot{n}_k}{\tilde{D}_{i,k}}\right] X_i + \left[\dot{n}_i \sum_{\substack{k=1 \\ k\neq i}}^{N} \frac{X_k}{\tilde{D}_{i,k}}\right]\right)} \tag{8.5}$$

Now, to prepare for integration, the above equation can be recast in matrix form as:

$$\boxed{\frac{d\boldsymbol{\mathcal{X}}}{d\xi} = \mathcal{A}\boldsymbol{\mathcal{X}}} \tag{8.6}$$

with $\boldsymbol{\mathcal{X}}$ being the column vector for the molar fractions i.e. $\boldsymbol{\mathcal{X}} = [X_1, X_2, X_3, ... X_N]^T$ and the matrice $\mathcal{A}$ defined as:

$$\mathcal{A} = \frac{1}{4\pi c}\begin{bmatrix} -\sum\limits_{\substack{k=1 \\ k\neq 1}}^{N} \frac{\dot{n}_k}{\tilde{D}_{1,k}} & \frac{\dot{n}_1}{\tilde{D}_{1,2}} & \frac{\dot{n}_1}{\tilde{D}_{1,3}} & \cdots & \frac{\dot{n}_1}{\tilde{D}_{1,N}} \\ \frac{\dot{n}_2}{\tilde{D}_{2,1}} & -\sum\limits_{\substack{k=1 \\ k\neq 2}}^{N} \frac{\dot{n}_k}{\tilde{D}_{2,k}} & \frac{\dot{n}_2}{\tilde{D}_{2,3}} & \cdots & \frac{\dot{n}_2}{\tilde{D}_{2,N}} \\ \frac{\dot{n}_3}{\tilde{D}_{3,1}} & \frac{\dot{n}_3}{\tilde{D}_{3,2}} & -\sum\limits_{\substack{k=1 \\ k\neq 3}}^{N} \frac{\dot{n}_k}{\tilde{D}_{3,k}} & \cdots & \frac{\dot{n}_3}{\tilde{D}_{3,N}} \\ \vdots & \vdots & \vdots & \vdots & \vdots \\ \frac{\dot{n}_N}{\tilde{D}_{N,1}} & \frac{\dot{n}_N}{\tilde{D}_{N,2}} & \frac{\dot{n}_N}{\tilde{D}_{N,3}} & \cdots & -\sum\limits_{\substack{k=1 \\ k\neq N}}^{N} \frac{\dot{n}_k}{\tilde{D}_{N,k}} \end{bmatrix}. \tag{8.7}$$

Now, a single hypothesis is necessary to carry out the integration of this system of equations: constant molar density c with respect to ξ or, constant in space. Since c was defined as $c = \rho/W$, we point out that this is not equivalent as supposing constant ρ in space (unless the molar weight is also assumed to be constant in space).

Therefore, by assuming $c(\xi)$ constant, the system of equations Eq. 8.6 can be integrated to yield:

$$\boldsymbol{\mathcal{X}} = \exp[\mathcal{A}\xi]\,\boldsymbol{\mathcal{C}} \tag{8.8}$$

with a suitable constant of integration $\boldsymbol{\mathcal{C}}$, which is a second unknown paired with the matrix $\mathcal{A}$. Note that $\boldsymbol{\mathcal{C}}$ is also a column vector with the same dimension as $\boldsymbol{\mathcal{X}}$ and therefore the order of the multiplication in Eq. 8.8 matters.

To proceed with the solution, it is known that, at the surface of droplet $\xi = 1/R_d$, the molar fractions vector must be $\boldsymbol{\mathcal{X}} = \boldsymbol{\mathcal{X}}^s = [X_1^s, X_2^s, X_3^s, ... X_N^s]^T$. The second evaluation will now be made using film theory. Namely, at the coordinate $\xi = 1/(R_d + \delta_{max})$, we must have $\boldsymbol{\mathcal{X}} = \boldsymbol{\mathcal{X}}^\infty = [X_1^\infty, X_2^\infty, X_3^\infty, ... X_N^\infty]^T$, with $\delta_{max} = \max(\delta_1, \delta_2..., \delta_N)$. The boundary layer thickness δ_{max} is the largest boundary layer thickness among those of all species, thus guaranteeing that all of them have reached the far-away state i.e. $X_k = X_k^\infty$.

The problem is now reduced to solving the following set of equations simultaneously:

$$\boldsymbol{\mathcal{X}}^s = \exp\left[\frac{1}{R_d}\mathcal{A}\right]\boldsymbol{\mathcal{C}}, \tag{8.9}$$

$$\boldsymbol{\mathcal{X}}^\infty = \exp\left[\frac{1}{(R_d + \delta_{min})}\mathcal{A}\right]\boldsymbol{\mathcal{C}}. \tag{8.10}$$

From the boundary layer theory of Chap. 5, when only diffusional effects are taken into account (no Stefan flow) the mass transfer boundary layer thickness for each species is $\delta_i = 2R_d/(Sh_i - 2)$. Therefore, we can conclude that $\delta_{max} = 2R_d/(Sh_{min} - 2)$ with $Sh_{min} = \min(Sh_1, Sh_2, ...Sh_N)$, leading to:

$$\boldsymbol{\mathcal{X}}^s = \exp\left[\frac{1}{R_d}\mathcal{A}\right]\boldsymbol{\mathcal{C}}, \tag{8.11}$$

$$\boldsymbol{\mathcal{X}}^\infty = \exp\left[\frac{Sh_{min} - 2}{Sh_{min}R_d}\mathcal{A}\right]\boldsymbol{\mathcal{C}}. \tag{8.12}$$

Finally, it is then possible to account for Stefan flow effects using for example the methodology of (Abramzon and Sirignano 1989) i.e. Eqs. 5.33 to obtain the modified Sherwood numbers:

$$\begin{aligned} \boldsymbol{\mathcal{X}}^s &= \exp\left[\frac{1}{R_d}\mathcal{A}\right]\boldsymbol{\mathcal{C}}, \\ \boldsymbol{\mathcal{X}}^\infty &= \exp\left[\frac{Sh^*_{min} - 2}{Sh^*_{min}R_d}\mathcal{A}\right]\boldsymbol{\mathcal{C}}. \end{aligned} \tag{8.13}$$

To solve these two systems of equations, a vector with guesses for all molar transfer rates is provided to construct a matrix $\mathcal{A}^{guess}$, paired with a guess for the constant vector, $\boldsymbol{\mathcal{C}}^{guess}$.

For a first iteration in a typical droplet phase-change problem, the matrix $\mathcal{A}_0^{guess}$ can be initialized by computing mass transfer rates for each species using any other simpler

model and then converting them to molar transfer rates through $\dot{n}_k = \dot{m}_k / W_k$. Then, $\boldsymbol{\mathcal{C}}_0^{guess}$ can be initialized through a matrix inversion for one of Eqs. 8.13, for instance:

$$\boldsymbol{\mathcal{C}}_0^{guess} = \left(\exp \left[\frac{Sh^*_{min} - 2}{Sh^*_{min} R_{d,0}} \mathcal{A}_0^{guess} \right] \right)^{-1} \boldsymbol{\mathcal{X}}_0^{\infty}, \tag{8.14}$$

or even simpler, it can be initialized using the non-convective case i.e. $\boldsymbol{\mathcal{C}}_0^{guess} = \boldsymbol{\mathcal{X}}_0^{\infty}$.

For subsequent iterations, the $\boldsymbol{\mathcal{C}}$ from the last iteration is used as a first guess for the non-linear solver, and this can also be done for the molar transfer rates $\dot{n}_k$ to construct the matrix $\mathcal{A}^{guess}$. Once the system is solved and $\mathcal{A}$ is found, the individual molar transfer rates are found from its entries and then the individual mass evaporation rates $\dot{m}_k$. These can be summed leading to the global evaporation rate $\dot{m}$, closing the mass transfer problem.

In this way, the methodology proposed in this section is able to compute the mass transfer without the need to use simplifying approaches for the mass velocities closure discussed in Chap. 2. Furthermore, not only the hypotheses of no convection and only one inert species from (Tonini and Cossali 2016) have been relaxed, but the final analytical formulation is simpler, with only one matrix to compute. Therefore, this model establishes a reference droplet mass transfer model for comparing different simplifying hypothesis for the diffusion velocities closures on general scenarios. Simplified models are still useful due to the lower numerical cost and ease of implementation, and so their derivations and specific advantages will be layed out in Chaps. 9 and 10.

8.2 A general heat transfer formulation with respect to the mass diffusion closure

As seen in Eqs. 1.15, 1.16 for the energy formulation for instance, the individual diffusion velocities explicitly appear. This suggests that results of the mass transfer model of choice, that would lead to the obtention of an expression of the diffusion velocities, could explicitly inject functional dependencies on the enthalpy diffusion term based on their simplifying choices. This may justify why this term has often been neglected for energy formulations, as was typically done before the Abramzon-Sirignano model in single-component treatments, for example.

However, as will be demonstrated below, the integration of the energy conservation equation yields a general result with respect to the choice of mass diffusion closure. Meaning, regardless of the choice made for the diffusion velocities or coefficients, the final energy result will have no explicit functional dependencies to them. As explained at the beggining of this chapter, the energy derivation procedure is carried out independently of the mass transfer model of choice, and it is the purpose of this model to generalize the energy result to any mass transfer formulation. Therefore, this section should be viewed

as independent of the derivations of the previous section, and applies in conjunction with any multi-component mass transfer model that shares the same set of hypotheses #1-#7 displayed in Part I.

To start, Eq. 1.15 is rewritten below with the middle term in the LHS recast with all of its terms inside the summation:

$$\dot{m}h_s + \sum_{k=1}^{N}\left[4\pi r^2 \rho Y_k \mathrm{v}_k^{D,Y}\right] h_{s,k} - 4\pi r^2 \lambda \frac{dT}{dr} = \dot{\mathcal{Q}}. \tag{8.15}$$

On the above, it is now possible to see the explicit appearance of the LHS of the integration for the species conservation, Eq. 1.11. The result of this first integration is general with respect to all droplet mass transfer models based on the species conservation equation. When the substitution of Eq. 1.11 into Eq. 8.15 is made as follows, the mass transfer is being injected into the energy formulation, but in an implicit manner, as no choices concerning diffusion velocities $\mathrm{v}_i^{D,Y}$ have yet been made.

Performing the substitution leads to:

$$\dot{m}h_s + \sum_{k=1}^{N}\left[\left(\dot{m}_k - \dot{m}Y_k\right) h_{s,k}\right] - 4\pi r^2 \lambda \frac{dT}{dr} = \dot{\mathcal{Q}}. \tag{8.16}$$

The summation term in the LHS can be split and the whole equation rearranged as:

$$\dot{m}\left[h_s - \left(\sum_{k=1}^{N} Y_k h_{s,k}\right)\right] + \sum_{k=1}^{N} \dot{m}_k h_{s,k} - 4\pi r^2 \lambda \frac{dT}{dr} = \dot{\mathcal{Q}}, \tag{8.17}$$

The sensible enthalpy for the whole gaseous mixture can then be written as the sum of its components i.e. $h_s = \sum_{k=1}^{N} Y_k h_{s,k}$, cancelling out the first term and yielding:

$$\boxed{\sum_{k=1}^{N} \dot{m}_k h_{s,k} - 4\pi r^2 \lambda \frac{dT}{dr} = \dot{\mathcal{Q}}} \tag{8.18}$$

Eq. 8.18 above represents the generality of the energy formulation for multi-component droplets with respect to the mass diffusion closure, provided that the same simplifying hypotheses to obtain Eqs. 1.11 and 1.15 are made. It states that the heat transfer rate reaching the surface of the droplet is equal to difference between the sum of the enthalpy diffusive fluxes and the heat conduction in the gaseous phase. In particular, the enthalpy diffusion term can be of great importance, since the individual mass transfer rates of each component $\dot{m}_k$ are present and can have positive or negative sign contributions due to evaporation or condensation. It should be noted that other works such as (Lupo and Duwig 2018) for instance have also managed to include enthalpy diffusion effects

via other theoretical tools. However, due to the simplicity and generality of the derived expression, it is preferred here.

As done in Chap. 1 for Eq. 1.18, it is useful to convert this formulation from sensible enthalpy to temperature, to allow for a second integration. Eq. 8.18 then becomes:

$$\sum_{k=1}^{N} \dot{m}_k c_{p,k}(T - T^s) - 4\pi r^2 \lambda \frac{dT}{dr} = \dot{\mathcal{Q}}. \tag{8.19}$$

By also supposing constant thermal conductivity λ in space, Eq. 8.19 can then be integrated by separation of variables from the surface of the droplet $r = R_d$ where $T = T^s$ towards an arbitrary coordinate R with temperature T:

$$\int_{R_d}^{R} \frac{dr}{r^2} = 4\pi\lambda \int_{T^s}^{T} \frac{dT}{\sum_{k=1}^{N} \dot{m}_k c_{p,k}(T - T^s) - \dot{\mathcal{Q}}} \tag{8.20}$$

The above integration yields:

$$\left(\frac{1}{R_d} - \frac{1}{R}\right) = 4\pi \frac{\lambda}{\sum_{k=1}^{N} \dot{m}_k c_{p,k}} \ln\left|\frac{\sum_{k=1}^{N} \dot{m}_k c_{p,k}(T^s - T) + \dot{\mathcal{Q}}}{\dot{\mathcal{Q}}}\right|. \tag{8.21}$$

By defining the multi-component Spalding thermal transfer number as:

$$B_T = \frac{\sum_{k=1}^{N} \dot{m}_k c_{p,k}(T^s - T^\infty)}{\dot{\mathcal{Q}}}, \tag{8.22}$$

Eq. 8.21 becomes:

$$\left(\frac{1}{R_d} - \frac{1}{R}\right) = 4\pi \frac{\lambda}{\sum_{k=1}^{N} \dot{m}_k c_{p,k}} \ln|1 + B_T|. \tag{8.23}$$

In particular, attention is drawn to the appearance of an absolute value operator on the RHS. This is due to the rigorous definition of the performed analytical integration:

$$\int \frac{1}{x} dx = \ln x + \mathcal{C}_1 \quad \text{if} \quad x > 0; \tag{8.24}$$

$$\int \frac{1}{x} dx = \ln(-x) + \mathcal{C}_2 \quad \text{if} \quad x < 0, \tag{8.25}$$

where $\mathcal{C}_1, \mathcal{C}_2$ are constants of integration. For a multi-component mixture it is physically possible to have $B_T < -1$, making the use of the absolute value operator mandatory for such cases.

Integrating Eq. 8.23 up until infinity $R \to \infty$ leads to:

$$\sum_{k=1}^{N} \dot{m}_k c_{p,k} = 4\pi R_d \lambda \ln|1 + B_T|. \tag{8.26}$$

Alternatively, the integration can be carried out until $R = R_d + \delta_T$, where δ_T is the thickness of the thermal boundary layer, following the film-theory strategy of Chap 5 to incorporate convection effects. Eq. 8.23 then becomes:

$$\sum_{k=1}^{N} \dot{m}_k c_{p,k} = 4\pi R_d \left[\frac{R_d + \delta_T}{\delta_T}\right] \lambda \ln|1 + B_T|. \tag{8.27}$$

Similarly, Eq. 8.27 can be recast into a more usable form by using the thermal boundary layer thickness for the pure diffusive case:

$$\delta_T = \frac{2R_d}{Nu - 2}, \tag{8.28}$$

In so doing, Eq. 8.27 becomes:

$$\sum_{k=1}^{N} \dot{m}_k c_{p,k} = 4\pi R_d \left[\frac{Nu}{2}\right] \lambda \ln|1 + B_T|. \tag{8.29}$$

The result of Eq. 8.23 was derived with Stefan flow effects taken into account, and so for consistency the same must be done for the Nusselt number. We use the same strategy of (Abramzon and Sirignano 1989) i.e. Eq. 5.33 to add these effects by using a modified Nusselt number Nu^* leading to the Stefan-flow corrected version of Eq. 8.29:

$$\sum_{k=1}^{N} \dot{m}_k c_{p,k} = 4\pi R_d \left[\frac{Nu^*}{2}\right] \lambda \ln|1 + B_T| \tag{8.30}$$

Eq. 8.30 represents a result that can actually be implemented in CFD codes to model droplet heat transfer, and it can be coupled with any mass transfer model that shares the same hypotheses. Due to the absolute value operator, it is best solved numerically through the implementation of two equations, isolating for the heat transfer rate $\mathcal{Q}$:

$$\begin{aligned} \dot{\mathcal{Q}} &= \frac{\sum_{k=1}^{N} \dot{m}_k c_{p,k}(T^s - T)}{\exp\left[\frac{\sum_{k=1}^{N} \dot{m}_k c_{p,k}}{2\pi R_d Nu^* \lambda}\right] - 1}, \quad \text{if } \; 1 + B_T > 0, \\ \dot{\mathcal{Q}} &= -\left(\frac{\sum_{k=1}^{N} \dot{m}_k c_{p,k}(T^s - T)}{\exp\left[\frac{\sum_{k=1}^{N} \dot{m}_k c_{p,k}}{2\pi R_d Nu^* \lambda}\right] + 1}\right), \quad \text{if } \; 1 + B_T < 0. \end{aligned} \tag{8.31}$$

This particular use for our result is encouraged because it leads to a single implementation that can be used for different models and because it avoids an explicit, functional spillage from errors introduced from mass transfer modelling choices. Also, of note is the fact that since the mass and heat transfer approaches are functionally decoupled, that

it is possible to use this proposed energy formulation with an alternative mass transfer formulation that does take into account Soret effects, as there only required hypotheses for the energy concern the Dufour term.

Now we show that Eq. 8.33 above degenerates to the single-component formulation of Abramzon-Sirignano. To do so, we note that Eq. 8.33 can be rearranged if a fractional evaporation rate $\epsilon_k = \dot{m}_k/\dot{m}$ is used instead of the individual mass transfer rates $\dot{m}_k$; this is useful since it allows for the isolation of the global mass transfer rate, leading to a classical form:

$$\dot{m} = 4\pi R_d \left[\frac{Nu^*}{2}\right] \frac{\lambda}{\sum_{k=1}^{N} \epsilon_k c_{p,k}} \ln|1 + B_T|. \tag{8.32}$$

In the single-component case, if the index v is used for the fuel vapor in the gaseous phase, naturally $\sum_{k=1}^{N} \epsilon_k c_{p,k} = c_{p,v}$, and so Eq. 8.32 becomes:

$$\dot{m} = 4\pi R_d \left[\frac{Nu^*}{2}\right] \frac{\lambda}{c_{p,v}} \ln|1 + B_T|. \tag{8.33}$$

In parallel, for the single-component case developed with the same hypotheses for the species and energy equations, Eq. 5.35 for the relationship between Spalding numbers must hold. From the definition of single-component the Spalding mass transfer number in Eq. 4.14, it is straighforward to see that to have $B_M < -1$, it would be necessary to have mass fractions superior to one, which is impossible by definition. Therefore, from the relationship expressed through Eq. 5.35 it follows that $B_T < -1$ is also impossible for the single-component case.

The absolute value from our expression Eq. 8.33 can therefore be dropped for the single-component case, leading to an identical formulation for the droplet energy transfer formulation proposed by (Abramzon and Sirignano 1989). In this way, the energy formulation proposed in this section is able to consistently scale the droplet heat transfer from a multi-component treatment to a single-component one, while incoporating Stefan flow, convection effects and the contribution of the enthalpy diffusion.

8.3 Summary

In this chapter, two novel formulations were proposed for the mass and heat transfer of droplets, following classical hypotheses. For the mass formulation, an expression was derived following the framework established in (Tonini and Cossali 2016), by directly integrating the Stefan-Maxwell equations. Convection effects were included organically, and an arbitrary number of inert species can be used.

As for the heat transfer formulation, it was derived independently from the mass counterpart, and the inclusion of enthalpy diffusion effects effectively eliminates any functional dependency from diffusion velocity closures. It can thus be used not only with our

proposed mass transfer formulation, but with any other that shares the same set of hypotheses. In this way, both proposed formulations can be seen to be independent of the diffusion velocity closure problem posed in Chap. 2. In Table 8.1 the intermediary results and the main formulations are displayed as a reference.

$$\frac{dX_i}{d\xi} = \frac{1}{4\pi c}\left(\left[-\sum_{\substack{k=1\\k\neq i}}^{N}\frac{\dot{n}_k}{\tilde{D}_{i,k}}\right]X_i + \left[\dot{n}_i\sum_{\substack{k=1\\k\neq i}}^{N}\frac{X_k}{\tilde{D}_{i,k}}\right]\right)$$

$$\frac{d\boldsymbol{\mathcal{X}}}{d\xi} = \mathcal{A}\boldsymbol{\mathcal{X}}$$

$$\mathcal{A} = \frac{1}{4\pi c}\begin{bmatrix} -\sum\limits_{\substack{k=1\\k\neq 1}}^{N}\frac{\dot{n}_k}{\tilde{D}_{1,k}} & \frac{\dot{n}_1}{\tilde{D}_{1,2}} & \cdots & \frac{\dot{n}_1}{\tilde{D}_{1,N}} \\ \frac{\dot{n}_2}{\tilde{D}_{2,1}} & -\sum\limits_{\substack{k=1\\k\neq 2}}^{N}\frac{\dot{n}_k}{\tilde{D}_{2,k}} & \cdots & \frac{\dot{n}_2}{\tilde{D}_{2,N}} \\ \vdots & \vdots & \vdots & \vdots \\ \frac{\dot{n}_N}{\tilde{D}_{N,1}} & \frac{\dot{n}_N}{\tilde{D}_{N,2}} & \cdots & -\sum\limits_{\substack{k=1\\k\neq N}}^{N}\frac{\dot{n}_k}{\tilde{D}_{N,k}} \end{bmatrix}, \quad \boldsymbol{\mathcal{X}} = \begin{bmatrix} X_1 \\ X_2 \\ \vdots \\ X_N \end{bmatrix}$$

$$\boldsymbol{\mathcal{X}}^s = \exp\left[\frac{1}{R_d}\mathcal{A}\right]\boldsymbol{\mathcal{C}},$$

$$\boldsymbol{\mathcal{X}}^\infty = \exp\left[\frac{Sh^*_{min}-2}{Sh^*_{min}R_d}\mathcal{A}\right]\boldsymbol{\mathcal{C}}$$

$$\sum_{k=1}^{N}\dot{m}_k h_{s,k} - 4\pi r^2\lambda\frac{dT}{dr} = \dot{\mathcal{Q}}$$

$$\sum_{k=1}^{N}\dot{m}_k c_{p,k} = 4\pi R_d\left[\frac{Nu^*}{2}\right]\lambda\ln|1+B_T|$$

$$\dot{\mathcal{Q}} = \frac{\sum_{k=1}^{N}\dot{m}_k c_{p,k}(T^s - T)}{\exp\left[\frac{\sum_{k=1}^{N}\dot{m}_k c_{p,k}}{2\pi R_d Nu^*\lambda}\right]-1}, \text{ if } 1+B_T > 0,$$

$$\dot{\mathcal{Q}} = -\left(\frac{\sum_{k=1}^{N}\dot{m}_k c_{p,k}(T^s - T)}{\exp\left[\frac{\sum_{k=1}^{N}\dot{m}_k c_{p,k}}{2\pi R_d Nu^*\lambda}\right]+1}\right), \text{ if } 1+B_T < 0$$

Figure 8.1: Summary of droplet mass and heat transfer expressions for Chap. 8.

Chapter 9

Multi-component evaporation models in the litterature

In this chapter, the multi-component droplet mass transfer models present in (Newbold and Amundson 1973), (Law 1976), (Ebrahimian and Habchi 2011), (Tonini and Cossali 2015) and (Tonini and Cossali 2016) are shown and derived. All of these models can also be classified as discrete component models (DCMs), since they use the integrated result for the species conservation equations and provide expressions for the mass transfer rate of each fuel species. We limit the developments here to the mass transfer only, even though some authors also include energy/heat transfer discussions. This is because of the general energy result derived in Chap. 8, that applies to all models here.

First, the model in (Law 1976) is detailed. Law's model is quite simple in the sense that it supposes that all species have the same diffusional behaviour. To that extent, this is referred to as a "preferential diffusion" approach in contrast to "differential diffusion" models where each species is allowed to have its own diffusion coefficient. All remaining models in this chapter follow the differential diffusion paradigm.

Then, Ebrahimian and Habchi's model is derived as proposed in their original work, focusing on the Hirschfelder and Curtiss diffusion closure Eq. 2.41. Their main contribution resides on the inclusion of a correction velocity, that allows for the use of typical differential diffusion approaches while still organically preserving global mass conservation. They also propose a conversion for the molar fraction gradients to mass fractions gradients with the goal of improving the consistency of the Hirschfelder-Curtiss law in view of the diffusion velocity closure specifically for droplet mass transfer models.

In sequence, the model in (Tonini and Cossali 2015) is derived and its main characteristics summarized. The main contribution here was the proposition of a discrete component formulation that incorporates convection effects and that is general with respect to the diffusion coefficient approach. They also proposed an intermediary approach between the preferential and differential diffusion ones, wherein the global mass transfer rate is

computed supposing that all species have the same diffusion coefficient, and then the individual mass transfer rates of each species are computed each having their own diffusion coefficients.

Then, the model in (Newbold and Amundson 1973) is derived. To our knowledge, this was one of the first differential diffusion DCMs in the litterature. The author uses an original framework to simplify the Stefan-Maxwell equations while also incorporating the species conservation equation. The ensuing integration was carried out only for non-convective environments and a simplifying hypothesis of single inert species was also used.

Finally, the model previously mentioned in Chap. 8 of (Tonini and Cossali 2016) is presented. As explained, it was derived by assuming only a single inert species as well, and for non-convective environments, leading to a different yet useful formulation.

The first objective of this chapter follows a bibliographical nature. We sought to compile in concise manner all the derivation procedures for all of these models, which are among the most used DCMs currently. Even though a reference mass transfer model was established in Chap. 8, all of these models are useful since they can be significant less expensive in terms of computational resources. Accordingly, the formulations developed here will also serve as a useful reference for the next chapter, where these formulations will be extended to become more robust in line with a pragmatical approach for spray combustion investigations in CFD codes.

9.1 Law (1976) model

In (Law 1976), the author devises a rigorous treatment for spherical diffusion flames surrounding a droplet. The general theory states a flame front with infinitely small thickness at $r = R_{fl}$, where a combustion chemical reaction takes place infinitely fast. The domain is further divided into an evaporative region described by the coordinate range $R_d < r < R_{fl}$ and then the rest of the domain, $R_{fl} < r < \infty$. The flame is described as a diffusion flame, such that its position is always defined by the stoichiometric reaction between fuel and oxidizer, and the required theoretical tools follow the same approach as that of (Spalding 1953) and (Godsave 1953).

Here, we focus on the result of the multi-component model provided. For the purposes of computing combustion quantities at the flame front, it is assumed that only two species are relevant in terms of chemical reactions, the fuel F and the oxidizer O, characterizing a binary gaseous mixture. However, the droplet is allowed to have any number of actual fuel species, that vaporize and meet at the flame front. In this sense, the species F is seen as a sum of all vapor species; the sum must be characterized in terms of mass fractions to ensure mass conservation.

The author then presents the following expression for the fractional evaporation rate:

$$\epsilon_i = Y_i^s + (Y_i^s - Y_i^{fl}) \left(\frac{1 - Y_F^s}{Y_F^s - Y_F^{fl}} \right). \tag{9.1}$$

To obtain the above, we depart from the integrated conservation equation for the species, Eq. 1.14. Then, it is assumed that all species have the same diffusion coefficient $\bar{D}$. As shown in Chap. 2, this assumption leads to the same expression of Fick's law for the diffusion closure. In the radial coordinate, this is expressed as:

$$Y_i \mathrm{v}_i^{D,Y} = -\bar{D} \frac{dY_i}{dr}. \tag{9.2}$$

Substituting this for the diffusion velocity on Eq. 1.14 leads to:

$$Y_i \frac{\dot{m}}{4\pi} - r^2 \rho \bar{D} \frac{dY_i}{dr} = \frac{\dot{m}_i}{4\pi}. \tag{9.3}$$

By further defining Y_F as:

$$\sum_{k=1}^{N_F} Y_k = Y_F, \tag{9.4}$$

where $N_F < N$ is the number of fuel species, then Eqs. 9.3 can be summed for all N_F fuels, leading to:

$$Y_F \frac{\dot{m}}{4\pi} - r^2 \rho \bar{D} \frac{dY_F}{dr} = \frac{\dot{m}}{4\pi}, \tag{9.5}$$

noting that on the RHS $\sum_{k=1}^{N_F} \dot{m}_k = \sum_{k=1}^{N} \dot{m}_k = \dot{m}$ since inert species have no contribution.

Eq. 9.5 can be integrated as done in Part II i.e. Eq. 4.10, with the product $\rho\bar{D}$ constant in space, from the surface of the droplet R_d towards ∞ leading to:

$$\dot{m} = 4\pi R_d \bar{D} \ln\left(1 + \bar{B}_M\right), \tag{9.6}$$

with the average Spalding number defined for the average fuel species F as:

$$\bar{B}_M = \frac{Y_F^s - Y_F^\infty}{1 - Y_F^s}. \tag{9.7}$$

Eq. 9.6 already allows for the computation of the global mass transfer rate using information from all fuel species; however, it is possible to backtrack and obtain the contribution of each species. To do so, we note that Eq. 9.5 can also be integrated as it is towards infinity for each fuel:

$$\int_{R_d}^{\infty} \frac{dr}{r^2} = 4\pi\rho\bar{D} \int_{Y_i^s}^{Y_i^\infty} \frac{dY_i}{\dot{m}Y_i - \dot{m}_i}. \tag{9.8}$$

Now, as justified in Chap. 8 for the energy formulation, the integrand on the RHS $\dot{m}Y_i - \dot{m}_i$ may be negative. Therefore, rigorously an absolute value operator should be introduced, but this was not done on the original mass transfer model proposed by Law. Following the original procedure, the final result is thus:

$$\dot{m} = 4\pi R_d \bar{D} \ln\left(1 + B_{M,i}\right), \tag{9.9}$$

with the individual Spalding number of each fuel defined as:

$$B_{M,i} = \frac{Y_i^s - Y_i^\infty}{\epsilon_i - Y_i^s}, \tag{9.10}$$

with ϵ_i being the fractional mass transfer rate of each species as defined in Eq. 1.12. The global mass transfer rate at the LHS of Eqs. 9.6 and 9.9 must be the same, and thus equalizing these results leads to $B_M = B_{M,i}$, which can be expanded for the fractional mass transfer rate as:

$$\epsilon_i = Y_i^s + (Y_i^s - Y_i^\infty)\left(\frac{1 - Y_F^s}{Y_F^s - Y_F^\infty}\right), \tag{9.11}$$

and this is the same result as Eq. 9.1, with the difference that the original integration was carried out inside the flame region as it was a combustion application.

Due to the simplicity of the above result, it is still being used in many spray combustion applications, as shown recently in (Shastry, Cazeres, Rochette, Riber, and Cuenot 2021) for instance. However, its main drawback is the hypothesis of same diffusion coefficient for all species, which is somewhat contradictory with the advantages that a discrete component model seeks. Therefore, for the remainder of this chapter, models that relax this hypothesis will be discussed.

9.2 Ebrahimian and Habchi (2011) model

The contribution in (Ebrahimian and Habchi 2011) can be divided into two parts. First, the model is able to analytically take into account a correction velocity that allows for a natural achivement of global mass conservation. Then, the model also proposes a way to convert the Hirschfelder-Curtiss diffusion velocity closure, since its original formula cannot be directly used on the species conservation equation. To do so, the authors devise a way to convert gradients in molar fraction to mass fraction, in analogy with the binary case.

One particularity of their results is that the spatial integration is only carried out once, whereas typically droplet mass transfer models carry out a second integration which in turn is usually made inside a boundary layer, or film, region. This means that a supplementary hypothesis of constant product ρD in space, which is often made, would not be necessary.

To reach their point of departure, we rewrite below the species conservation equation with no chemical reaction:

$$\frac{\partial \rho Y_i}{\partial t} + \nabla \cdot [\rho Y_i \mathbf{v}_i^m] = 0, \tag{9.12}$$

Since the molecular velocity is $\mathbf{v}_i^m = \mathbf{u} + \mathbf{v}_i^{D,Y}$, this can be split up to send the diffusional component of the velocity to the RHS, as such:

$$\frac{\partial \rho Y_i}{\partial t} + \nabla \cdot [\rho Y_i \mathbf{u}] = -\nabla \cdot \left[\rho Y_i \mathbf{v}_i^{D,Y}\right], \tag{9.13}$$

Now, when summing up equations Eq. 9.13 for all N species, global mass conservation must be retrieved, namely:

$$\frac{\partial \rho}{\partial t} + \nabla \cdot [\rho \mathbf{u}] = 0, \tag{9.14}$$

However, as Ebrahimian and Habchi point out, the Hirschfelder-Curtiss mass diffusion closures employed do not respect the above statement. Namely, when using Eq. 2.41 for the diffusion velocities, we obtain $\sum_{k=1}^{N} Y_k \mathbf{v}^{D,Y} \neq 0$ which violates Eq. 9.14.

This, of course, needs to be corrected in some way, since mass conservation is of paramount importance for reactive flows, and a procedure for doing so is offered in the work of (Ebrahimian and Habchi 2011). To solve for the inconsistency, they note that, in the binary case with species $1, 2$, the conversion of molar fractions to mass fractions can be expressed as follows:

$$\nabla X_1 = \left[\frac{W}{W_1} - \frac{Y_1 W^2}{W_1^2} + Y_1 \frac{W^2}{W_1 W_2}\right] \nabla Y_1 \tag{9.15}$$

Noting that in the RHS above $Y_1 \frac{W^2}{W_1 W_2}$ is the only term that depends on the "other" species, namely species 2, the authors have proposed the following generalization to the multi-component case in analogy with the binary one:

$$\nabla X_i = \left[\frac{W}{W_i} - \frac{Y_i W^2}{W_i^2} + Y_i \frac{W}{W_i} \sum_{\substack{k=1 \\ k \neq i}}^{N} \frac{W}{W_k}\right] \nabla Y_i \tag{9.16}$$

Substituting Eq. 9.16 on Eq. 2.41 to convert the molar fraction gradient leads to:

$$X_i \mathbf{v}_i^{D,Y} = -D_{i,m} \left[\frac{W}{W_i} - \frac{Y_i W^2}{W_i^2} + Y_i \sum_{\substack{k=1 \\ k \neq i}}^{N} \frac{W}{W_k}\right] \nabla Y_i, \tag{9.17}$$

with $D_{i,m}$ expressed as in Eq. 2.42. Now, on the LHS, the molar fraction can be converted to mass fraction $X_i = Y_i \frac{W}{W_i}$ as customary. Perfoming this conversion leads to:

$$Y_i \mathbf{v}_i^{D,Y} = -D_{i,m} \left[1 - X_i + Y_i \sum_{\substack{k=1 \\ k \neq i}}^{N} \frac{W}{W_k} \right] \nabla Y_i. \tag{9.18}$$

Now, the sum on the last term on the RHS can be recast by noting that $\frac{W}{W_k} = \frac{X_k}{Y_k}$, leading to mass diffusion closure proposed in (Ebrahimian and Habchi 2011):

$$Y_i \mathbf{v}_i^{D,Y} = -D_{i,m} \left[1 - X_i + Y_i \sum_{\substack{k=1 \\ k \neq i}}^{N} \frac{X_k}{Y_k} \right] \nabla Y_i, \quad D_{i,m} = \frac{(1 - Y_i)}{\sum\limits_{\substack{k=1 \\ k \neq i}}^{N} X_k / D_{i,k}} \tag{9.19}$$

In parallel, to ensure global mass conservation it is possible to include an advective mass correction velocity $\mathbf{u}_c$, as suggested in (Poinsot and Veynante 2012) for instance. To obtain the expression for this velocity, we add it to the RHS of Eq. 9.13:

$$\frac{\partial \rho}{\partial t} + \nabla \cdot [\rho \mathbf{u}] = -\nabla \cdot \left[\rho \left(\sum_{k=1}^{N} Y_k \mathbf{v}_k^{D,Y} + \mathbf{u}_c \right) \right], \tag{9.20}$$

And so, in order for the sum on the RHS to be zero such that global mass conservation is ensured, it is necessary to have:

$$\mathbf{u}_c = -\sum_{k=1}^{N} Y_k \mathbf{v}_k^{D,Y}. \tag{9.21}$$

In this way, the "corrected" individual species conservation equations would become:

$$\frac{\partial \rho Y_i}{\partial t} + \nabla \cdot \left[\rho Y_i \left(\mathbf{u} + \mathbf{u}_c + \mathbf{v}_i^{D,Y} \right) \right] = 0, \tag{9.22}$$

It should be emphasized that Eq. 9.22 can be viewed as "general", in the sense that if a diffusion velocity is chosen such that it automatically respects global mass conservation, then the correction velocity degenerates to zero and the classical form is retrieved.

As customary, the next step is to integrate Eq. 9.22 to obtain the mass transfer rates for each species. To do so, quasi-stationarity and spherical symmetry are assumed. With these hypotheses, Eq. 9.22 can be integrated once over the spatial coordinate as done in Chap. 1 to yield:

$$4\pi r^2 \rho Y_i \left(\mathrm{u} + \mathrm{u}_c + \mathrm{v}_i^{D,Y} \right) = \dot{m}_i, \tag{9.23}$$

The Stefan-flow advective velocity u can be substituted from the integration of global mass conservation Eq. 1.10 yielding:

$$Y_i\dot{m} + 4\pi r^2 \rho \left(Y_i \mathrm{u}_c + Y_i \mathrm{v}_i^{D,Y} \right) = \dot{m}_i, \tag{9.24}$$

Substituting the proposed modification of the Hirschfelder-Curtiss mass diffusion closure Eq. 9.19 with assumed spherical symmetry on Eq. 9.24 and with the correction velocity expressed through Eq. 9.21 leads to:

$$\dot{m}_i = Y_i\dot{m} + 4\pi r^2 \rho \left(Y_i \sum_{j=1}^{N} D_{j,m} \left[1 - X_j + Y_j \sum_{\substack{k=1 \\ k\neq i}}^{N} \frac{X_j}{Y_j} \right] \frac{dY_j}{dr} - D_{i,m} \left[1 - X_i + Y_i \sum_{\substack{k=1 \\ k\neq i}}^{N} \frac{X_k}{Y_k} \right] \frac{dY_i}{dr} \right), \tag{9.25}$$

In particular, the above expression can be evaluated at the surface of the droplet $r = R_d$, where $Y_k, X_k = Y_k^s, X_k^s \ \forall\, k$:

$$\dot{m}_i = Y_i^s\dot{m} + 4\pi R_d^2 \rho^s \left(Y_i^s \sum_{j=1}^{N} D_{j,m}^s \left[1 - X_j^s + Y_j^s \sum_{\substack{k=1 \\ k\neq i}}^{N} \frac{X_j^s}{Y_j^s} \right] \frac{dY_j}{dr}\bigg|^s - \right.$$
$$\left. - D_{i,m}^s \left[1 - X_i^s + Y_i^s \sum_{\substack{k=1 \\ k\neq i}}^{N} \frac{X_k^s}{Y_k^s} \right] \frac{dY_i}{dr}\bigg|^s \right), \tag{9.26}$$

Of note is the fact that the density ρ^s and diffusion coefficients $D_{k,m}^s \ \forall\, k$ are all also evaluated at the surface of the droplet, with the corresponding composition and temperature.

The next step concerns the evaluation of the gradients at the surface of the droplet, since this information is not directly computable with non-discretized models. This can be done via boundary layer Sherwood numbers for each species, generalized from Eq. 5.10a:

$$Sh_i = -\frac{2R_d \frac{dY_i}{dr}\big|^s}{Y_i^s - Y_i^\infty}. \tag{9.27}$$

Substituing the above on Eq. 9.26 leads to:

$$\dot{m}_i = Y_i^s\dot{m} + 2\pi R_d \rho^s \left(D_{i,m}^s \left[1 - X_i^s + Y_i^s \sum_{\substack{k=1 \\ k\neq i}}^{N} \frac{X_k^s}{Y_k^s} \right] Sh_i \left(Y_i^s - Y_i^\infty \right) - \right.$$
$$\left. - Y_i^s \sum_{j=1}^{N} D_{j,m}^s \left[1 - X_j^s + Y_j^s \sum_{\substack{k=1 \\ k\neq i}}^{N} \frac{X_k^s}{Y_k^s} \right] Sh_j \left(Y_j^s - Y_j^\infty \right) \right), \tag{9.28}$$

In order to isolate for the global mass transfer rate $\dot{m}$, the preceding equation is summed only for the fuel species, namely, species l which have $\dot{m}_l \neq 0$:

$$\frac{\dot{m}}{2\pi R_d \rho^s}\left[1-\sum_{\substack{l=1,\\ l\in\text{fuels}}}^{N} Y_l\right] = \sum_{\substack{l=1,\\ l\in\text{fuels}}}^{N} D^s_{l,m}\left[1-X^s_l+Y^s_l\sum_{\substack{k=1\\k\neq l}}^{N}\frac{X^s_k}{Y^s_k}\right] Sh_l\left(Y^s_l-Y^\infty_l\right) - \\ -\sum_{\substack{l=1,\\ l\in\text{fuels}}}^{N} Y^s_l\sum_{j=1}^{N} D^s_{j,m}\left[1-X^s_j+Y^s_j\sum_{\substack{k=1\\k\neq i}}^{N}\frac{X^s_k}{Y^s_k}\right] Sh_j\left(Y^s_j-Y^\infty_j\right) \quad (9.29)$$

Once this global mass transfer rate is obtained, it can be substituted in Eq. 9.28 to yield the individual mass transfer rates. This modelling approach is able to incorporate convection effects as done in (Abramzon and Sirignano 1989), through the Sherwood numbers. However, Abramzon and Sirignano point out in their work that the Sherwood number computed from the gradient may not necessarily be the same as the one developed from correlations.

9.3 Tonini and Cossali (2015) model

In (Tonini and Cossali 2015), the authors condense the full set of integrated species conservation equations into a single equation to be solved for the global mass transfer rate. To do so, first the global mass transfer rate is solved and then it is substituted for the mass transfer rates of each individual species in a "cascading" manner, similar to what was done in the models of Law and Ebrahimian and Habchi. Contrary to the procedure of Ebrahimian and Habchi however is the fact that a second integration is carried out and the final result of Tonini and Cossali's model is a non-linear equation. Also, there is no use of a correction velocity; rather, a common strategy is employed to preserve global mass conservation which will be briefly highlighted.

To reach their result, we depart from the integrated species conservation equation, Eq. 1.14. The authors have used the following diffusion velocity closure:

$$Y_i \mathbf{v}_i^{D,Y} = -D_{i,m}\nabla Y_i, \qquad D_{i,m} = \frac{1}{\sum\limits_{\substack{k=1\\k\neq i}}^{N} Y_k/D_{i,k}}, \quad (9.30)$$

which has been referred to as Blanc's law, as in (Sazhin 2017) for instance. Also, the authors have opted to express the individual mass transfer rates through fractional evaporation rates i.e. $\dot{m}_i = \epsilon_i \dot{m}$.

In so doing, Eq. 1.14 becomes:

$$Y_i\dot{m} - 4\pi r^2 \rho D_{i,m}\frac{dY_i}{dr} = \epsilon_i \dot{m}. \quad (9.31)$$

By supposing constant $\rho D_{i,m}$ is space, the above equation can be rearranged through the separation of variables technique to integrate over the radial coordinate from the surface of the droplet $r = R_d$ towards infinity $r \to \infty$:

$$\dot{m} \int_{R_d}^{\infty} \frac{dr}{r^2} = 4\pi\rho D_{i,m} \int_{Y_i^s}^{Y_i^\infty} \frac{dY_i}{Y_i - \epsilon_i}. \tag{9.32}$$

Similar to Law's model, the authors have also neglected the absolute value operator. The integration procedure then leads to:

$$\dot{m} = 4\pi R_d \rho D_{i,m} \ln\left(\frac{Y_i^\infty - \epsilon_i}{Y_i^s - \epsilon_i}\right). \tag{9.33}$$

To obtain their final result, we first isolate for the fractional evaporation rates:

$$\epsilon_i = \frac{Y_i^\infty - Y_i^s \exp\left(\frac{\dot{m}}{4\pi R_d \rho D_{i,m}}\right)}{1 - \exp\left(\frac{\dot{m}}{4\pi R_d \rho D_{i,m}}\right)}. \tag{9.34}$$

To obtain the exact expression in their publication, the above equation can equivalently be written as:

$$\epsilon_i = \frac{Y_i^s - Y_i^\infty \exp\left(-\frac{\dot{m}}{4\pi R_d \rho D_{i,m}}\right)}{1 - \exp\left(-\frac{\dot{m}}{4\pi R_d \rho D_{i,m}}\right)}. \tag{9.35}$$

Then, the equations for all N species are summed; on the LHS, the trivial result $\sum_{k=1}^{N} \epsilon_k = 1$ is found, leading to:

$$1 = \sum_{k=1}^{N} \left[\frac{Y_i^s - Y_i^\infty \exp\left(-\frac{\dot{m}}{4\pi R_d \rho D_{i,m}}\right)}{1 - \exp\left(-\frac{\dot{m}}{4\pi R_d \rho D_{i,m}}\right)}\right]. \tag{9.36}$$

This is a non-linear equation with a single variable, the global mass transfer rate $\dot{m}$, and so it can be solved as such.

It should be noted that in (Tonini and Cossali 2015), the authors index their species starting at $k = 0$, and not $k = 1$, and fix $k = 0$ to be a single inert species, with $k = 1, 2, ...N-1$ being the fuels in a mixture composed of N species. In their work, their summation also starts at $k = 1$, meaning they exclude the influence of the inert species. For this specific result no impacts are expected since $\epsilon = 0$ for any inert species.

The authors have also recast Eq. 9.36 in another form which may be of simpler implementation and/or handling for a numerical non-linear solver; to retrieve it, first the term

inside the RHS sum is written as:

$$\frac{Y_i^s - Y_i^\infty \exp\left(-\frac{\dot{m}}{4\pi R_d \rho D_{i,m}}\right)}{1-\exp\left(-\frac{\dot{m}}{4\pi R_d \rho D_{i,m}}\right)} = \frac{Y_i^s + (Y_k^\infty - Y_k^\infty) + Y_i^\infty \exp\left(-\frac{\dot{m}}{4\pi R_d \rho D_{i,m}}\right)}{1-\exp\left(-\frac{\dot{m}}{4\pi R_d \rho D_{i,m}}\right)} =$$
$$= \frac{(Y_i^s - Y_k^\infty) + \left(Y_i^\infty - Y_i^\infty \exp\left(-\frac{\dot{m}}{4\pi R_d \rho D_{i,m}}\right)\right)}{1-\exp\left(-\frac{\dot{m}}{4\pi R_d \rho D_{i,m}}\right)} = \frac{Y_i^s - Y_k^\infty}{1-\exp\left(-\frac{\dot{m}}{4\pi R_d \rho D_{i,m}}\right)} + Y_k^\infty \tag{9.37}$$

And so inserting this inside the sum, Eq. 9.36 becomes:

$$1 = \sum_{k=1}^{N} \left[\frac{Y_i^s - Y_k^\infty}{1-\exp\left(-\frac{\dot{m}}{4\pi R_d \rho D_{i,m}}\right)} + Y_k^\infty \right]. \tag{9.38}$$

The sum can then be split with the term Y_k^∞ being sent to the LHS and the remaninig one with the exponential being multiplied by -1 both on the numerator and denominator to yield, finally:

$$1 - \sum_{k=1}^{N} Y_k^\infty = \sum_{k=1}^{N} \frac{Y_k^\infty - Y_i^s}{\exp\left(-\frac{\dot{m}}{4\pi R_d \rho D_{i,m}}\right) - 1}, \tag{9.39}$$

This is the main result in (Tonini and Cossali 2015). As explained at the beggining of this section, the overall procedure is to first compute the global mass transfer rate through the non-linear Eq. 9.39 and then substitute it onto Eq. 9.35 to obtain the fractional evaporation rates (and thus, the mass transfer rates) of each species.

To complement this formulation, a simplified procedure was also offered by the authors. They proposed a method that avoids having to compute a non-linear equation for the global mass transfer rate, while still preserving the individual fractional evaporation rates's structure. Conceretely, they compute the global mass transfer rate by using an assumption of equal diffusion coefficient for all species first, i.e. using Eq. 9.6. In this way, the average Spalding mass transfer number $\bar{B}_M$ and the presence of a single diffusion coefficient $\bar{D}$ would represent the fact that, for the purposes of computing the global mass transfer rate, a binary diffusion description would suffice.

Once this global mass transfer rate is computed, it is substituted in Eq. 9.35 for each species, thus somewhat still preserving the structure of Tonini and Cossali's main result which includes the individual $D_{i,m}$. To maximize the consistency with the discrete component approach, the average diffusion coefficient is computed as a mass average between the individual ones computed from their form of Blanc's law for the diffusion coefficient

as in Eq. 9.30, namely:

$$\bar{D} = \frac{\sum\limits_{\substack{k=1,\\ k\in\text{fuels}}}^{N} Y_k D_{k,m}}{\sum\limits_{\substack{k=1,\\ k\in\text{fuels}}}^{N} Y_k}, \tag{9.40}$$

and so therefore this represents an alternative method to compute an average diffusion coefficient, compared to the multi-component extension of the Wilke and Lee method Eq. 2.18 in Chap. 2. In (Tonini and Cossali 2015) the authors conclude by saying that in general the results of both proposed methodologies are very close, at least in low-temperature scenarios and when no fuels are present at infinity, i.e. $Y_k^{\infty} = 0$ for all fuel species.

To include convection effects, an approach analogous to the binary case of (Abramzon and Sirignano 1989) is proposed, through a correction factor for the non-convective case. For instance, Eq. 9.39 is first solved for the global mass transfer rate, and then Eqs. 9.35 are solved for each of the fractional evaporation rates which can then be converted back to mass transfer rates i.e. $\dot{m}_k = \epsilon_k \dot{m}$.

Then, the mass transfer rates are updated as:

$$\dot{m}_i^{conv} = \left[\frac{Sh_i^*}{2}\right] \dot{m}_i, \tag{9.41}$$

where $\dot{m}_i^{conv}$ is the corrected mass transfer rate to account for convection effects and Sh_i^* is the Sherwood number of each species. The correction strategy follows the same structure as in the Abramzon-Sirignano model, but the average Spalding transfer number $\bar{B}_M$ is used instead of the individual $B_{M,i}$:

$$Sh_k^* = 2 + \frac{Sh_{k,0} - 2}{F_M}, \quad F_M = \left(1 + \bar{B}_M\right)^{0.7} \frac{\ln(1 + \bar{B}_M)}{\bar{B}_M}, \tag{9.42}$$

The corrected global mass transfer rate can then be computed through $\dot{m}^{conv} = \sum_{k=1}^{N} \dot{m}_k^{conv}$ and then updated values for the fractional evaporation rates can be found if needed through $\epsilon_k^{conv} = \dot{m}_k^{conv} / \dot{m}^{conv}$.

9.4 Newbold and Amundson (1973) model

The main novelty in (Newbold and Amundson 1973) consists in an expression for the droplet mass transfer rate obtained through the integration of a simplified version of the Stefan-Maxwell equations, instead of the customary second integration for the species

conservation equation. Spherical symmetry is assumed, and by defining a species mass flux $\mathcal{M}_i = \rho Y_i \mathrm{v}_i^m$, the integration result of Eq. 1.11 can be recast as:

$$\mathcal{M}_i = \frac{\dot{m}_i}{4\pi r^2}. \tag{9.43}$$

An equivalent species molar flux is similarly defined as being $\mathcal{N}_i = cX_i \mathrm{v}_i^m$.

With the relationship between mass and molar densities $\rho/c = W$ and the conversion from mass to molar fractions $Y_i = X_i W_i / W$, the following relationship between the fluxes is retrieved:

$$\mathcal{N}_i = \frac{\mathcal{M}_i}{W_i} = \frac{\dot{m}_i}{4\pi r^2 W_i}. \tag{9.44}$$

Now, the next step is to use the Stefan-Maxwell equations in terms of molar fluxes $\mathcal{N}_i$, Eq. 2.12d. The authors state that this equation cannot be integrated as such, and they essentially propose that the binary diffusion coefficients $D_{i,j}$ can be assumed to depend only on one species. The concept of "effective binary diffusivity" is introduced, and a diffusion coefficient $D_{i,m}$ is used, similar to the approaches of Ebrahimian and Habchi and Tonini and Cossali.

Using $D_{i,j} = D_{i,m}$, the diffusion coefficients now depend only on species i and can exit the summation on Eq. 2.12d:

$$\mathcal{N}_i = X_i \sum_{k=1}^{N} \mathcal{N}_k - cD_{i,m} \frac{dX_i}{dr}. \tag{9.45}$$

Now, Eq. 9.44 can in particular be used to define a relationship between the molar flux at the surface of the droplet $r = R_d$ where $\mathcal{N}_i = \mathcal{N}_i^s$ and $R > R_d$:

$$\frac{\mathcal{N}_i^s}{R_d^2} = \frac{\mathcal{N}_i}{R^2}. \tag{9.46}$$

Substituting Eq. 9.46 onto Eq. 9.45 for each individual molar flux $\mathcal{N}_k$ leads to:

$$\mathcal{N}_i^s = X_i \sum_{k=1}^{N} \mathcal{N}_k^s - cD_{i,m} \frac{R^2}{R_d^2} \frac{dX_i}{dr}. \tag{9.47}$$

Now, a change of variables is made from the coordinate R to $\xi = 1/R$, leading to the following equation:

$$\mathcal{N}_i^s = X_i \sum_{k=1}^{N} \mathcal{N}_k^s + \frac{cD_{i,m}}{R_d^2} \frac{dX_i}{d\xi}. \tag{9.48}$$

This equation can be further rearranged and integrated by separation of variables if the product between molar density and the diffusion coefficient $cD_{i,m}$ is supposed to be constant in space. In so doing, an indefinite integral is then computed:

$$\frac{R_d^2}{cD_{i,m}} \int d\xi = \int \frac{dX_i}{-X_i \sum_{k=1}^{N} \mathcal{N}_k^s + \mathcal{N}_i^s}. \tag{9.49}$$

The result yields:

$$\left[\frac{R_d^2}{cD_{i,m}}\right] \xi + \mathcal{C}_1 = -\frac{1}{\sum_{k=1}^{N} \mathcal{N}_k^s} \ln\left(\mathcal{N}_i^s - X_i \sum_{k=1}^{N} \mathcal{N}_k^s\right), \tag{9.50}$$

where $\mathcal{C}_1$ is a constant of integration. By substituting back $r = 1/\xi$ and rearranging for the molar fraction, the expression becomes:

$$X_i(r) = -\frac{\mathcal{C}_2}{\sum_{k=1}^{N} \mathcal{N}_k^s} \exp\left[-\frac{\sum_{k=1}^{N} \mathcal{N}_k^s R_d^2}{cD_{i,m}} \frac{1}{r}\right] + \frac{\mathcal{N}_i^s}{\sum_{k=1}^{N} \mathcal{N}_k^s}. \tag{9.51}$$

Now $\mathcal{C}_2 = \exp(\mathcal{C}_1)$ can be evaluated for instance by setting $r \to \infty$, where $X_i = X_i^{\infty}$:

$$X_i^{\infty} = -\frac{\mathcal{C}_2}{\sum_{k=1}^{N} \mathcal{N}_k^s} + \frac{\mathcal{N}_i^s}{\sum_{k=1}^{N} \mathcal{N}_k^s} \to \mathcal{C}_2 = \mathcal{N}_i^s - X_i^{\infty} \sum_{k=1}^{N} \mathcal{N}_k^s. \tag{9.52}$$

Substituting $\mathcal{C}_2$ back on Eq. 9.51 and rearranging leads to:

$$X_i(r) = \left(X_i^{\infty} - \frac{\mathcal{N}_i^s}{\sum_{k=1}^{N} \mathcal{N}_k^s}\right) \exp\left[-\frac{\sum_{k=1}^{N} \mathcal{N}_k^s R_d^2}{cD_{i,m}} \frac{1}{r}\right] + \frac{\mathcal{N}_i^s}{\sum_{k=1}^{N} \mathcal{N}_k^s}. \tag{9.53}$$

The final objective is to evaluate the molar fluxes at the surface of the droplet, $\mathcal{N}_i^s$ for each species. In this way, Eq. 9.53 can be evaluated at $r = R_d$ where $X_i = X_i^s$ to yield, after some modifications:

$$\mathcal{N}_i^s = \left(\sum_{k=1}^{N} \mathcal{N}_k^s\right) \left(\frac{X_i^s \exp\left[\frac{\sum_{k=1}^{N} \mathcal{N}_k^s R_d}{cD_{i,m}}\right] - X_i^{\infty}}{\exp\left[\frac{\sum_{k=1}^{N} \mathcal{N}_k^s R_d}{cD_{i,m}}\right] - 1}\right). \tag{9.54}$$

Then, for a particular inert species Ω, the molar flux at the surface of the droplet must be zero i.e. $\mathcal{N}_{\Omega}^s = 0$. For this to be true, from Eq. 9.54 the following must be valid:

$$\frac{X_{\Omega}^{\infty}}{X_{\Omega}^s} = \exp\left[\frac{\sum_{k=1}^{N} \mathcal{N}_k^s R_d}{cD_{\Omega,m}}\right]. \tag{9.55}$$

Then it is assumed that Ω is the only inert species i.e. $X_\Omega = 1 - \sum_{\substack{k=1 \\ k\neq\Omega}}^{N} X_k$. In this way, the LHS of the previous equation can be rewritten as:

$$\frac{1 - \sum_{\substack{k=1 \\ k\neq\Omega}}^{N} X_k^\infty}{1 - \sum_{\substack{k=1 \\ k\neq\Omega}}^{N} X_k^s} = \exp\left[\frac{\sum_{k=1}^{N} \mathcal{N}_k^s R_d}{cD_{\Omega,m}}\right] = \zeta, \tag{9.56}$$

with ζ being introduced for better readability. It is now possible to isolate for the sum of all fluxes at the surface of the droplet:

$$\sum_{k=1}^{N} \mathcal{N}_k^s = \frac{cD_{\Omega,m}}{R_d} \ln\zeta. \tag{9.57}$$

Finally, substituting this result on Eq. 9.54 leads to the main result in (Newbold and Amundson 1973):

$$\mathcal{N}_i^s = \frac{cD_{\Omega,m}}{R_d} \left(\frac{X_i^s \zeta^{\frac{D_{\Omega,m}}{D_{i,m}}} - X_i^\infty}{\zeta^{\frac{D_{\Omega,m}}{D_{i,m}}} - 1} \right) \ln\zeta. \tag{9.58}$$

From the definition of mass and molar fluxes at the beggining of this section, it is then possible to retrieve the mass transfer rates of each species through:

$$\dot{m}_i = 4\pi R_d^2 \frac{\mathcal{N}_i^s}{W_i}. \tag{9.59}$$

This result is important because it introduces an alternative framework with respect to all mass transfer formulations displayed so far. In a sense, it can be viewed as a "molar" approach to compute the droplet mass transfer, and in effect, a different hypothesis is used, namely constant $cD_{i,m}$ instead of constant $\rho D_{i,m}$ as done for instance in the model of (Tonini and Cossali 2015). This distinction for the constant properties can be useful depending on the exact application.

9.5 Tonini and Cossali (2016) model

In (Tonini and Cossali 2016), the authors have developed a non-convective droplet mass transfer model based on the direct resolution of the Stefan-Maxwell equations. This was introduced previously as the motivation for mass transfer model of Chap. 8, and the derivation to their contribution is now offered.

We depart from Eq. 2.12d and define a molar transfer rate $\dot{n}_i = \mathcal{N} 4\pi r^2$. In so doing, we obtain:

$$4\pi r^2 c \frac{dX_i}{dr} = -\sum_{k=1}^{N} \frac{[X_k \dot{n}_i - X_i \dot{n}_k]}{D_{i,k}}. \tag{9.60}$$

The authors then define the following auxiliary quantities:

$$\xi = \frac{R_d}{r}, \tag{9.61}$$

$$\dot{n}_i^{adim} = \frac{\dot{n}_i}{4\pi R_d c D_{ref}}, \tag{9.62}$$

where D_{ref} is a suitable reference diffusion coefficient. Using these on 9.60 yields:

$$\frac{dX_i}{d\xi} = D_{ref} \sum_{k=1}^{N} \frac{\left[X_k \dot{n}_i^{adim} - X_i \dot{n}_k^{adim}\right]}{D_{i,k}}. \tag{9.63}$$

A supplementary set of variables is then defined:

$$\dot{n}_{tot}^{adim} = \sum_{k=1}^{N} \dot{n}_k^{adim}, \tag{9.64}$$

$$\nu_k = \frac{\dot{n}_k^{adim}}{\dot{n}_{tot}^{adim}}, \tag{9.65}$$

$$\phi_{i,k} = \frac{D_{ref}}{D_{i,k}}, \tag{9.66}$$

Substituting the above onto Eq. 9.63 leads to the following formulation:

$$\frac{dX_i}{d\xi} = \dot{n}_{tot}^{adim} \sum_{k=1}^{N} \phi_{i,k} \left[X_k \nu_i - X_i \nu_k\right]. \tag{9.67}$$

They then suppose that a single inert species is present, say Ω, such that it is the only one respecting $\nu_\Omega = 0$. Eq. 9.67 can then be opened up to become:

$$\frac{dX_i}{d\xi} = \dot{n}_{tot}^{adim} \sum_{\substack{k=1 \\ k \neq \Omega}}^{N} \left(\phi_{i,k} \left[X_k \nu_i - X_i \nu_k\right]\right) + \dot{n}_{tot}^{adim} \nu_i \phi_{i,\Omega} X_\Omega \tag{9.68}$$

The hypothesis of a single inert species again is useful since leads to the following relationship:

$$X_\Omega = 1 - \sum_{\substack{k=1 \\ k \neq \Omega}}^{N} X_k, \tag{9.69}$$

and then the summation on the RHS of Eq. 9.69 has the same indexes to be reinserted into the main sum of Eq. 9.68, leading to:

$$\frac{dX_i}{d\xi} = \dot{n}_{tot}^{adim} \sum_{\substack{k=1 \\ k\neq\Omega}}^{N} \left(\left[\phi_{i,k} - \phi_{i,\Omega} \right] X_k \nu_i - \phi_{i,k} X_i \nu_k \right) + \dot{n}_{tot}^{adim} \nu_i \phi_{i,\Omega} \tag{9.70}$$

The final objective is to integrate the equation for X_i and so the RHS is rearranged to contain a multiplicative factor besides X_i leading to:

$$\frac{dX_i}{d\xi} = \left(-\dot{n}_{tot}^{adim} \sum_{\substack{k=1 \\ k\neq\Omega}}^{N} \phi_{i,k} \nu_k \right) X_i + \dot{n}_{tot}^{adim} \nu_i \left(\phi_{i,\Omega} + \sum_{\substack{k=1 \\ k\neq\Omega}}^{N} \left(\left[\phi_{i,k} - \phi_{i,\Omega} \right] X_k \right) \right) \tag{9.71}$$

In order to completely isolate the multiplicative term besides X_i, the second term of the RHS is broken apart to remove its dependency on the i-th species, placing it inside the first sum to yield:

$$\frac{dX_i}{d\xi} = \left(\dot{n}_{tot}^{adim} \left[(\phi_{i,i} - \phi_{i,\Omega}) \nu_i - \sum_{\substack{k=1 \\ k\neq\Omega}}^{N} \phi_{i,k} \nu_k \right] \right) X_i + \dot{n}_{tot}^{adim} \nu_i \left(\phi_{i,\Omega} + \sum_{\substack{k=1 \\ k\neq i,\Omega}}^{N} \left(\left[\phi_{i,k} - \phi_{i,\Omega} \right] X_k \right) \right) \tag{9.72}$$

The authors make a further assumption that $\phi_{i,i} = \phi_{i,\Omega}$, leading to:

$$\frac{dX_i}{d\xi} = \left(-\dot{n}_{tot}^{adim} \sum_{\substack{k=1 \\ k\neq\Omega}}^{N} \phi_{i,k} \nu_k \right) X_i + \dot{n}_{tot}^{adim} \nu_i \left(\phi_{i,\Omega} + \sum_{\substack{k=1 \\ k\neq i,\Omega}}^{N} \left(\left[\phi_{i,k} - \phi_{i,\Omega} \right] X_k \right) \right), \tag{9.73}$$

Finally, this formulation can be rewritten as:

$$\frac{dX_i}{d\xi} = \dot{n}_{tot}^{adim} \left[\left(-\sum_{\substack{k=1 \\ k\neq\Omega}}^{N} \phi_{i,k} \nu_k \right) X_i + \sum_{\substack{k=1 \\ k\neq i,\Omega}}^{N} \nu_i \left[\phi_{i,\Omega} - \phi_{i,\Omega} \right] X_k \right] + \dot{n}_{tot}^{adim} \nu_i \phi_{i,\Omega}, \tag{9.74}$$

which can be recasted in matrix form as:

$$\frac{d\boldsymbol{\mathcal{X}}}{d\xi} = \mathcal{A}\boldsymbol{\mathcal{X}} + \mathcal{B} \tag{9.75}$$

With $\boldsymbol{\mathcal{X}} = [X_1, X_2, ... X_{N-1}]^T$ and the matrice $\mathcal{A}$ defined as:

$$\mathcal{A} = \dot{n}_{tot}^{adim} \begin{bmatrix} -\sum_{\substack{k=1 \\ k\neq\Omega}}^{N} \phi_{1,k}\nu_k & \nu_1(\phi_{1,2} - \phi_{1,\Omega}) & ... & \nu_1(\phi_{1,N} - \phi_{1,\Omega}) \\ \nu_2(\phi_{2,1} - \phi_{2,\Omega}) & -\sum_{\substack{k=1 \\ k\neq\Omega}}^{N} \phi_{2,k}\nu_k & ... & \nu_2(\phi_{2,N} - \phi_{1,\Omega}) \\ \vdots & \vdots & \vdots & \vdots \\ \nu_N(\phi_{N,1} - \phi_{N,\Omega}) & \nu_N(\phi_{N,2} - \phi_{N,\Omega}) & ... & -\sum_{\substack{k=1 \\ k\neq\Omega}}^{N} \phi_{N,k}\nu_k \end{bmatrix}, \tag{9.76}$$

and the matrice $\mathcal{B}$ defined as:

$$\mathcal{B} = \dot{n}_{tot}^{adim} \begin{bmatrix} \nu_1\phi_{1,\Omega} \\ \nu_2\phi_{2,\Omega} \\ \vdots \\ \nu_N\phi_{N,\Omega} \end{bmatrix}, \tag{9.77}$$

Eq. 9.75 has a general solution of the form:

$$\boldsymbol{\mathcal{X}} = \exp\left[\mathcal{A}\xi\right]\mathbf{C}_0 - \mathcal{A}^{-1}\mathcal{B}. \tag{9.78}$$

Notice that when solving Eq. 9.75 we do not include the inert gas Ω, such that the column matrix $\boldsymbol{\mathcal{X}}$ has $N-1$ rows for example. This is a set of $N-1$ equations for N variables, since $\dot{n}_{tot}^{adim}$ is itself also unknown. The last equation to be satisfied is therefore simply $\sum_{k=1}^{N} v_k = 1$. As expected, this solution procedure contains many structural similarities with the solution proposed in Chap. 8, most notably the need of solving a system of non-linear equations at each time step to compute mass transfer rates.

Chapter 10

Towards a general mass transfer description: extension of models in the litterature

In Chap. 9, the models of (Law 1976), (Ebrahimian and Habchi 2011), (Tonini and Cossali 2015) and (Newbold and Amundson 1973) were detailed. Throughout the derivation procedure, multiple limitations were highlighted. In particular, attention was given to the importance of the absolute value operator. Indeed, when deriving the general energy equation in Chap. 8, it was pointed out that for general multi-component scenarios, the integration of the logarithm function that appears consistently for the simplified droplet phase-change models should introduce an absolute value operator. As shown in (Filho, Santos, Vié, and Filho 2022), this can be critical for spray combustion applications, specifically when condensation occurs. For condensation to occur, one possibility is when mass fractions of fuels at the far-away state to be higher than those at the surface, and since most droplet phase-change investigations are conducted by setting these to zero, it is natural that this was overlooked. Therefore, the main discrete component evaporation models for multi-component models in the litterature are improved to handle any type of mass transfer in this chapter.

Also in (Filho, Santos, Vié, and Filho 2022) some cases were investigated wherein the overall droplet mass transfer behavior can go from evaporation to condensation or vice-versa during the droplet lifetime. When this happens, we have $\dot{m}$ approaching (and then crossing) zero with a non-zero time derivative (in contrast with the end of the droplet lifetime, where it approaches zero with the derivative also converging to zero). This means that the fractional evaporation rate $\epsilon_i = \dot{m}_i/\dot{m}$ will become ill-defined in these cases, since the individual $\dot{m}_i \not\to 0$ whereas $\dot{m} \to 0$. Therefore, for the enhancements proposed in this chapter all formulations will be given in terms of individual mass transfer rates $\dot{m}_i$ instead of fractional evaporation rates ϵ_i to avoid this singularity.

A second enhancement that will be brought here is the inclusion of convection effects.

Indeed, the model in (Law 1976) and (Newbold and Amundson 1973) did not contain convection effects naturally, so this extension will be carried out here. Also, it will be shown that the methodology used to include convection effects in (Tonini and Cossali 2012) is not consistent with the proposed method of integration, and so a more robust formulation is proposed.

We also extend the formulation of (Newbold and Amundson 1973) to include an arbitrary number of inert species since as discussed in Chap. 8 this can be particularly relevant for spray combustion applications. The methodology proposed in (Ebrahimian and Habchi 2011), which was specifically developed for the Hirschfelder-Curtiss model, is also extended to a general diffusion coefficient method, augmenting its versatility. Concerning the model in (Tonini and Cossali 2016), it was already extended in Chap. 8 to become the reference mass transfer model.

10.1 Extending the model of Law (1976)

First we extend Law's model to incorporate the absolute value operator. From Eq. 9.6, the first argument that might need the absolute value is $1 + \bar{B}_M$. It may now be useful to expand the definition of the average Spalding number Eq. 9.7 as:

$$\bar{B}_M = \frac{\sum_{k\in\text{fuels}} Y_k^s - \sum_{k\in\text{fuels}} Y_k^\infty}{1 - \sum_{k\in\text{fuels}} Y_k^s}. \tag{10.1}$$

From Eq. 10.1 above, it is straightforward to see that it is impossible to have $\bar{B}_M < -1$, and so the absolute value operator is not needed for the global mass transfer rate integration.

As for the individual species conservation equations, the argument is now $1 + B_{M,i}$, with the individual Spalding numbers from Eq. 9.10 recast below to avoid singularities:

$$B_{M,i} = \dot{m}\left[\frac{Y_i^s - Y_i^\infty}{\dot{m}_i - \dot{m}Y_i^s}\right]. \tag{10.2}$$

From Eq. 10.2 we see that in some conditions it may be possible to have $B_{M,i} < -1$, and so in general the absolute value operator is needed.

If the argument is positive, then $B_{M,i} = \bar{B}_M$, leading to:

$$\boxed{\dot{m}_i = \dot{m}\left[Y_i^s + \frac{(Y_i^s - Y_i^\infty)}{\bar{B}_M}\right]} \tag{10.3}$$

Conversely, if the integrand is negative, it must follow that $-(1 + B_{M,i}) = 1 + \bar{B}_M$,

leading to:

$$\dot{m}_i = \dot{m}\left[\frac{Y_i^s(1-\bar{B}_M)+Y_i^\infty}{2+\bar{B}_M}\right] \tag{10.4}$$

and since $\bar{B}_M > -1$, it is straightforward to see that both the numerator and denominator are always strictly positive, leading to $\dot{m}_i > 0$ (and thus, condensation of species i) whenever $1 + B_{M,i} < 0$.

A second improvement to Law's model is the inclusion of convection effects. Following the procedure of Chap. 5 for the film theory, the integration of Eq. 9.5 would now be done inside the film, that is, from the surface of the droplet R_d towards $R_d + \delta_M$. In so doing, the following result is obtained:

$$\dot{m} = 4\pi R_d\left[\frac{Sh}{2}\right]\rho\bar{D}\ln(1+\bar{B}_M), \tag{10.5}$$

where Sh is the Sherwood number corresponding to mass transfer generated from all fuel species. Again, no absolute value is necessary since $1 + \bar{B}_M$ cannot be negative. In parallel, the same procedure is applied to the integration of each species' individual conservation equations, by assuming constant product $\rho\bar{D}$:

$$\int_{R_d}^{R_d+\delta_{M,i}}\frac{dr}{r^2} = 4\pi\rho\bar{D}\int_{Y_i^s}^{Y_i^\infty}\frac{dY_i}{\dot{m}Y_i-\dot{m}_i}. \tag{10.6}$$

Substituting the Sherwood numbers Sh_i for the boundary layer thicknesses $\delta_{M,i}$ finally leads to:

$$\dot{m} = 4\pi R_d\left[\frac{Sh_i}{2}\right]\rho\bar{D}\ln|1+B_{M,i}|. \tag{10.7}$$

Now, equating Eqs. 10.5 and 10.7 leads to:

$$Sh\ln(1+\bar{B}_M) = Sh_i\ln|1+B_{M,i}|, \tag{10.8}$$

which is even more complex.

Opening up both possibilities for the absolute value operator leads to:

$$\dot{m}_i = \dot{m}\left[\frac{Y_i^\infty - Y_i^s(1+\bar{B}_M)^{Sh/Sh_i}}{1-(1+\bar{B}_M)^{Sh/Sh_i}}\right],\ \text{if} 1+B_{M,i}>0; \tag{10.9a}$$

$$\dot{m}_i = \dot{m}\left[\frac{Y_i^\infty + Y_i^s(1+\bar{B}_M)^{Sh/Sh_i}}{1+(1+\bar{B}_M)^{Sh/Sh_i}}\right],\ \text{if} 1+B_{M,i}<0. \tag{10.9b}$$

If we neglect the absolute value operator and also suppose that all species have the same Sherwood number, the original expression for the fractional evaporation rates Eq. 9.11 can still be used, as done in (Shastry, Cazeres, Rochette, Riber, and Cuenot 2021) and (Bonanni and Ihme 2022) for instance. In so doing, convection would have no impact on the relative contribution from each species' to the global mass transfer rate, even though the individual mass transfer rates would of course be impacted through Eq. 10.7.

To correct for the presence of Stefan-flow effects, the same treatment proposed by Abramzon and Sirignano as in Eq. 5.33 can be used, leading to the following final relation:

$$Sh^*(1+\bar{B}_M) = Sh_i^*|1+B_{M,i}|, \tag{10.10}$$

where it should be noted that if the correction factor F_M is used as in Eq. 5.31, then each species will also have its own correction factor $F_{M,i}$ since they each have their own Spalding mass transfer number. Eqs. 10.9 then become simply:

$$\begin{aligned} \dot{m}_i &= \dot{m}_i \left[\frac{(Sh^*(1+\bar{B}_M)Y_i^s - Sh_i^* Y_i^\infty}{Sh^*(1+\bar{B}_M) - Sh_i^*} \right], \text{ if} 1+B_{M,i} > 0; \\ \dot{m}_i &= \dot{m}_i \left[\frac{(Sh^*(1+\bar{B}_M)Y_i^s + Sh_i^* Y_i^\infty}{Sh^*(1+\bar{B}_M) + Sh_i^*} \right], \text{ if} 1+B_{M,i} < 0. \end{aligned} \tag{10.11}$$

10.2 Extending the model of Ebrahimian and Habchi (2012)

In this section, we generalize the suggested procedure of (Ebrahimian and Habchi 2011) to include a correction velocity on the mass transfer formulation, regardless of the choice of the diffusion coefficient, expanding their original result. If a general mass equation is assumed in analogy with Fick's law:

$$Y_i \mathrm{v}_i^{D,Y} = -D_{i,m} \frac{dY_i}{dr}, \tag{10.12}$$

Then, Eq. 9.24 with Eq. 9.21 yields:

$$\dot{m}_i = Y_i \dot{m} + 4\pi r^2 \rho \left(Y_i \sum_{j=1}^{N} D_{j,m} \frac{dY_j}{dr} - D_{i,m} \frac{dY_i}{dr} \right) \tag{10.13}$$

Again, this can be in particular evaluated at the surface of the droplet:

$$\dot{m}_i = Y_i^s \dot{m} + 4\pi R_d^2 \rho^s \left(Y_i^s \sum_{j=1}^{N} D_{j,m}^s \frac{dY_j}{dr}\bigg|^s - D_{i,m}^s \frac{dY_i}{dr}\bigg|^s \right) \tag{10.14}$$

If the Sherwood number's definition Eq. 9.27 is employed, this evolves to:

$$\dot{m}_i = Y_i^s \dot{m} + 2\pi R_d \rho^s \left(D_{i,m}^s Sh_i \left(Y_i^s - Y_i^\infty\right) - Y_i^s \sum_{j=1}^{N} D_{j,m}^s Sh_j \left(Y_j^s - Y_j^\infty\right) \right) \tag{10.15}$$

And finally, summing up for all fuel species then leads to:

$$\frac{\dot{m}}{2\pi R_d \rho^s} = \frac{\left[\sum\limits_{\substack{l=1,\\ l \in \text{fuels}}}^{N} D^s_{l,m} Sh_l \left(Y^s_l - Y^\infty_l\right) - \sum\limits_{\substack{l=1,\\ l \in \text{fuels}}}^{N} Y^s_l \sum_{j=1}^{N} D^s_{j,m} Sh_j \left(Y^s_j - Y^\infty_j\right) \right]}{\left[1 - \sum\limits_{\substack{l=1,\\ l \in \text{fuels}}}^{N} Y^s_l \right]} \tag{10.16}$$

which is general with respect to the mass diffusion coefficient, provided that Eq. 10.12 is used for the diffusion closure, which is customary to allow for an analytical integration, as will be shown in (Tonini and Cossali 2015) model for instance. This will be useful to compare the contribution of (Ebrahimian and Habchi 2011) with other droplet mass transfer models that do not necessarily use the Hirschfelder-Curtiss approach.

In particular, the general framework here proposed through Eq. 10.16 can still be used to retrieve the original contribution of Ebrahimian et al. if the classical Hirschfelder-Curtiss diffusion coefficient is exchanged for a "corrected" one, to account for the conversion of molar to mass fractions:

$$D_{i,m} = \left[1 - X_i + Y_i \sum_{\substack{k=1 \\ k \neq i}}^{N} \frac{X_i}{Y_i} \right] \frac{(1 - Y_i)}{\sum\limits_{\substack{k=1 \\ k \neq i}}^{N} X_k / D_{i,k}}. \tag{10.17}$$

A brief comment shall be made here concerning a potential extension to our proposed general energy formulation, Eq. 8.18. Following the rationale of Ebrahimian and Habchi, our expression can in particular be evaluated at the surface of the droplet to yield:

$$\sum_{k=1}^{N} \dot{m}_k h^s_{s,k} - 4\pi R_d^2 \lambda^s \frac{dT}{dr}\bigg|^s = \dot{\mathcal{Q}}. \tag{10.18}$$

Now, the temperature gradient can also be obtained from the Nusselt number formal definition:

$$Nu = -\frac{2R_d \frac{dT}{dr}\big|^s}{T^s - T^\infty}. \tag{10.19}$$

Substitution of Eq. 10.19 into Eq. 10.18 leads to:

$$\sum_{k=1}^{N} \dot{m}_k h^s_{s,k} + 2\pi R_d \lambda^s Nu (T^s - T^\infty) = \dot{\mathcal{Q}} \tag{10.20}$$

This equation represents an alternative energy formulation that is also general with respective to the choices in the mass counterpart, while at the same time avoiding a second integration and all the hypotheses that come with it. However, the Nusselt number must be accurately computed at the surface of the droplet for its use. In this way, using direct numerical simulation tools it could be possible to obtain correlations for this specific form of the Nusselt number which could viabilize the use of this form of the energy equation.

10.3 Extending the model of Tonini and Cossali (2015)

Recall that, in contrast with the heat transfer formulation, for a discrete component model, each species has its own equation. This means that depending on the circumstances, some species may change signs according to the absolute value operator whereas other will not. Therefore, the single, non-linear expression provided in (Tonini and Cossali 2015) is not valid in general; it can only be used if all fuel species respect $1 + B_{M,i}$ at the same time.

Also, we show below that a more consistent incorporation of convective effects can be achieved. Indeed, integration of the individual species conservation equations leads to the same result of Eq. 10.6. This time around, the absolute value operator is isolated as:

$$|1 + B_{M,i}| = \exp\left[\frac{\dot{m}}{2\pi R_d Sh_i^* \rho D_{i,m}}\right], \tag{10.21}$$

with $B_{M,i}$ defined as Eq. 10.2 as well and using modified Sherwood numbers Sh_i^* that take Stefan flow into account.

Opening up for both possibilities of the absolute value operator leads to:

$$\begin{aligned} \dot{m}_i &= \dot{m}\left(\frac{Y_i^\infty - Y_i^s \exp\left[\frac{\dot{m}}{2\pi R_d Sh_i^* \rho D_{i,m}}\right]}{1 - \exp\left[\frac{\dot{m}}{2\pi R_d Sh_i \rho D_{i,m}}\right]}\right), \text{ if } 1 + B_{M,i} > 0, \\ \dot{m}_i &= \dot{m}\left(\frac{Y_i^\infty + Y_i^s \exp\left[\frac{\dot{m}}{2\pi R_d Sh_i^* \rho D_{i,m}}\right]}{1 + \exp\left[\frac{\dot{m}}{2\pi R_d Sh_i \rho D_{i,m}}\right]}\right), \text{ if } 1 + B_{M,i} < 0. \end{aligned} \tag{10.22}$$

Comparing this procedure for the inclusion of convection effect for the positive-argument half of Eq. 10.22 with the authors' original formulation Eq. 9.41, it is possible to see that they use the Sherwood number as a multiplicative factor for the individual mass transfer rates. However, the exponential structure of Eq. 10.21, obtained from the integration procedure using film theory, actually shows that the Sherwood number should be embedded inside the exponential. This was also explored in (Filho, Santos, Vié, and Filho 2022).

10.4 Extending the model of Newbold and Amundson (1973)

We now seek to retrieve a formulation that includes convection effects and an arbitrary number of inert species while still preserving the strategy proposed by Newbold and Amundson. To do so, first we rewrite Eq. 9.44 as $\mathcal{N}_i = \dot{n}_i/4\pi r^2$, such that $\mathcal{N}_i^s = \dot{n}_i/4\pi R_d^2$. Then, Eq. 10.23 can be modified to:

$$\dot{n}_i = X_i\dot{n} - cD_{i,m}4\pi r^2\frac{dX_i}{dr}. \tag{10.23}$$

If the product $cD_{i,m}$ is assumed constant, this equation can be rearranged for integration through separation of variables as follows:

$$\int_{R_d}^{R_d+\delta_{M,i}}\frac{dr}{r^2} = 4\pi cD_{i,m}\int_{X_i^s}^{X_i^\infty}\frac{dX_i}{\dot{m}X_i - \dot{n}_i}. \tag{10.24}$$

It is possible to see that Eq. 10.24 has an identical structure of Eq. 10.6, but with molar fractions instead of mass fractions, and the molar density c instead of the mass density ρ. Therefore, integration with a modified Sherwood number Sh_i^* will yield:

$$|1 + B_{M,i}^X| = \exp\left[\frac{\dot{m}}{2\pi R_d Sh_i^* cD_{i,m}}\right], \tag{10.25}$$

with the molar Spalding transfer number defined as:

$$B_{M,i}^X = \dot{n}\left[\frac{X_i^s - X_i^\infty}{\dot{n}_i - \dot{n}X_i^s}\right]. \tag{10.26}$$

Similarly, this leads to the following formulations:

$$\begin{aligned}
\dot{n}_i &= \dot{n}\left(\frac{X_i^\infty - X_i^s\exp\left[\frac{\dot{n}}{2\pi R_d Sh_i cD_{i,m}}\right]}{1 - \exp\left[\frac{\dot{n}}{2\pi R_d Sh_i^* cD_{i,m}}\right]}\right), \text{ if } 1 + B_{M,i}^X > 0,\\
\dot{n}_i &= \dot{n}\left(\frac{X_i^\infty + X_i^s\exp\left[\frac{\dot{n}}{2\pi R_d Sh_i cD_{i,m}}\right]}{1 + \exp\left[\frac{\dot{n}}{2\pi R_d Sh_i^* cD_{i,m}}\right]}\right), \text{ if } 1 + B_{M,i}^X < 0.
\end{aligned} \tag{10.27}$$

These equations represent the extension to Newbold and Amundson's model.

It should be noted that in (Tonini and Cossali 2016) the authors provided the non-convective version of the positive-argument half of Eq. 10.27 above, referring to it as the molar version of Fick's law. Indeed, we emphasize here that the derivation procedures for the mass and molar formulations have different sequences. To obtain Eqs. 10.22, it was necessary to first simplify the Stefan-Maxwell equations and use the Hougen's analogy with the binary case (further discussed on Sec. 11.1). Then, the ensuing result is substituted on the species conservation equation, allowing for a second integration. Conversely, to obtain Eqs. 10.27, we use the result of the first integration of the species conservation equation on the simplified Stefan-Maxwell equations using Hougen's analogy, and then we integrate the simplified Stefan-Maxwell equations.

10.5 Summary of expressions

In this chapter, extensions to models of Chap. 9 were provided, focusing on the inclusion of the absolute value operator for general mass transfer scenarios and the organic addition of convection effects. The Ebrahimian-Habchi model was extended for any diffusion coefficient following a general Fick's law diffusion velocity closure while still using a correction velocity, and the Newbold-Amundson model was further extended to handle an arbitrary number of inert species. In Table 10.1 we summarize the main results.

Ext N-C Law	$\dot{m}_i = \dot{m}\left[Y_i^s + \frac{(Y_i^s - Y_i^\infty)}{\bar{B}_M}\right],\ \text{if} 1 + B_{M,i} > 0$ $\dot{m}_i = \dot{m}\left[\frac{Y_i^s(1-\bar{B}_M) + Y_i^\infty}{2 + \bar{B}_M}\right]$
Ext Law	$\dot{m}_i = \dot{m}_i\left[\frac{(Sh^*(1+\bar{B}_M)Y_i^s - Sh_i^* Y_i^\infty}{Sh^*(1+\bar{B}_M) - Sh_i^*}\right],\ \text{if} 1 + B_{M,i} > 0$ $\dot{m}_i = \dot{m}_i\left[\frac{(Sh^*(1+\bar{B}_M)Y_i^s + Sh_i^* Y_i^\infty}{Sh^*(1+\bar{B}_M) + Sh_i^*}\right],\ \text{if} 1 + B_{M,i} < 0$
Ext E-H	$\frac{\dot{m}}{2\pi R_d \rho^s} = \frac{\left[\sum\limits_{\substack{l=1,\\ l\in\text{fuels}}}^{N} D_{l,m}^s Sh_l\left(Y_l^s - Y_l^\infty\right) - \sum\limits_{\substack{l=1,\\ l\in\text{fuels}}}^{N} Y_l^s \sum_{j=1}^{N} D_{j,m}^s Sh_j\left(Y_j^s - Y_j^\infty\right)\right]}{\left[1 - \sum\limits_{\substack{l=1,\\ l\in\text{fuels}}}^{N} Y_l^s\right]}$
Ext T-C	$\dot{m}_i = \dot{m}\left(\frac{Y_i^\infty - Y_i^s \exp\left[\frac{\dot{m}}{2\pi R_d Sh_i^* \rho D_{i,m}}\right]}{1 - \exp\left[\frac{\dot{m}}{2\pi R_d Sh_i \rho D_{i,m}}\right]}\right),\ \text{if}\ 1 + B_{M,i} > 0$ $\dot{m}_i = \dot{m}\left(\frac{Y_i^\infty + Y_i^s \exp\left[\frac{\dot{m}}{2\pi R_d Sh_i^* \rho D_{i,m}}\right]}{1 + \exp\left[\frac{\dot{m}}{2\pi R_d Sh_i \rho D_{i,m}}\right]}\right),\ \text{if}\ 1 + B_{M,i} < 0$
Ext N-A	$\dot{n}_i = \dot{n}\left(\frac{X_i^\infty - X_i^s \exp\left[\frac{\dot{n}}{2\pi R_d Sh_i c D_{i,m}}\right]}{1 - \exp\left[\frac{\dot{n}}{2\pi R_d Sh_i^* c D_{i,m}}\right]}\right),\ \text{if}\ 1 + B_{M,i}^X > 0$ $\dot{n}_i = \dot{n}\left(\frac{X_i^\infty + X_i^s \exp\left[\frac{\dot{n}}{2\pi R_d Sh_i c D_{i,m}}\right]}{1 + \exp\left[\frac{\dot{n}}{2\pi R_d Sh_i^* c D_{i,m}}\right]}\right),\ \text{if}\ 1 + B_{M,i}^X < 0$

Figure 10.1: Summary of droplet mass and heat transfer expressions for Chap. 8.

Chapter 11

Characterizing multi-component diffusion coefficients

In Chap. 9, some discrete component evaporation models proposed by the litterature were derived and detailed. Then, in Chap. 10, they were extended for more general applications, including any regime of mass transfer and a consistent inclusion of convection effects.

All of these models do not fully solve the Stefan-Maxwell equations, and to do so, simplifying hypotheses are necessary for the diffusion velocities, or more concretely, the diffusion coefficients. For all differential diffusion models, the hypothesis that the multi-component binary diffusion coefficients can be approximated by a coefficient dependant explicitly only on a single species is made i.e. $\tilde{D}_{i,k} = D_i$. It is the purpose of this chapter to detail the general procedure that allows for this simplification to be made; this will be referred to here as "Hougen's binary analogy", tracing back to (Hougen, Watson, and Ragatz 1952). This framework will be common to all shown diffusion coefficients.

Then, the different diffusion coefficient models in the litterature are derived and discussed in detail. These include the Blanc model after (Blanc 1908), the Wilke model after (Fairbanks and Wilke 1950) and the Hirschfelder and Curtiss model after (Hirschfelder and Curtiss 1949). We also propose a novel formulation for the diffusion coefficient complimentary to Blanc's model which can be useful for certain scenarios. Finally, some numerical investigations are carried out to pinpoint which of these formulations best agree with the Stefan-Maxwell mass transfer reference of Chap. 8.

11.1 Hougen's general simplifying theory: an analogy with the binary case

As noted in (Klingenberg 2015), the preceding strategy for the differential diffusion coefficients was possibly first suggested in the works of (Hougen, Watson, and Ragatz

1952), where the authors supposed that each species would have the same diffusion coefficient towards all other species, but this would vary in a species-by-species basis, namely, $\tilde{D}_{i,k} \approx D_i$. The approach suggested in (Hougen, Watson, and Ragatz 1952) is that the overall molecular fluxes for a given species i on the multi-component mixture m could be expressed in a simplified manner as follows (Klingenberg 2015):

$$\mathcal{N}_i = X_i \sum_{k=1}^{N} \mathcal{N}_k - cD_{i,m}\nabla X_i, \tag{11.1}$$

In parallel, the overall molecular flux for species 1 in a binary mixture composed of species $1, 2$ is (Klingenberg 2015):

$$\mathcal{N}_1 = X_1 \left(\mathcal{N}_1 + \mathcal{N}_2\right) - cD_{1,2}\nabla X_1, \tag{11.2}$$

In this way, by comparison Eq. 11.1 essentially states that the diffusive fluxes are being represented as an upscaled analogy with Fick's law for binary diffusion, with the diffusion coefficient $D_{i,m}$ characterising a binary diffusion between each species and the remaining mixture. Performing some conversions, Eq. 11.1 becomes:

$$X_i \mathbf{v}_i^m = X_i \sum_{k=1}^{N} X_k \mathbf{v}_k^m - D_{i,m}\nabla X_i. \tag{11.3}$$

Now, by noticing the definition of the advective molar velocity $\mathbf{u}^X$ as per Eq. 2.3, Eq. 11.3 can be rearranged to:

$$\mathbf{v}_i^m = \mathbf{u}^X - D_{i,m}\frac{\nabla X_i}{X_i}. \tag{11.4}$$

Using the molar equality of Eq. 2.1 leads to the following expression for the molar diffusion velocities:

$$X_i \mathbf{v}_i^{D,X} = -D_{i,m}\nabla X_i. \tag{11.5}$$

In a binary mixture, the following can be written in terms of molar fluxes:

$$X_1 \mathbf{v}_1^{D,X} = -D_{1,2}\nabla X_1. \tag{11.6}$$

In this way, it is possible to see that Eq. 11.5 is an analogy with the binary closure for the diffusive term. Now, in the binary case the following is also true:

$$Y_1 \mathbf{v}_1^{D,Y} = -D_{1,2}\nabla Y_1 \tag{11.7}$$

for the mass counterpart, and so the mass equivalent of Eq. 11.5 can be assumed to hold in this binary analogy context, namely:

$$Y_i \mathbf{v}_i^{D,Y} = -D_{i,m}\nabla Y_i. \tag{11.8}$$

The results of Eqs. 11.5 and 11.8 summarize Hougen's binary analogy.

These developments do not make any assumptions on how the velocity and mass/molar fraction fields vary in space; however, the droplet heat and mass transfer developments carried out in this manuscript assume spherical symmetry. Therefore, the following relations can be constructed to summarize the previous approach for mass and molar diffusion fluxes:

$$Y_i \mathrm{v}_i^{D,Y} = -D_{i,m} \frac{dY_i}{dr}, \tag{11.9}$$

$$X_i \mathrm{v}_i^{D,X} = -D_{i,m} \frac{dX_i}{dr}. \tag{11.10}$$

and in particular Eq. 11.9 is the main result that describes the mass diffusion closure under the hypothesis of Hougen et al. In particular, we note that the same diffusion coefficient $D_{i,m}$ is present regardless of mass or molar diffusive fluxes. By employing this closure, the modelling efforts can now be concentrated on how to compute the diffusion coefficients $D_{i,m}$ accurately.

11.2 Blanc's model

Historically, one of the first developments that can be worked to yield a diffusion coefficient in this context goes back to the works of (Blanc 1908). The original paper studies the mobility of ions in a gaseous mixture; in a sense, it is not interested in the diffusion properties of other species but rather only on that of the ions inside that mixture. This information was concretely conveyed as diffusion coefficient in the works of (Sandler and Mason 1968), albeit with no derivation. To obtain that expression, the Stefan-Maxwell equations for molar diffusion velocities are used, and the following hypothesis is made:

- All species except i have null molar diffusion velocities, namely $\mathbf{v}_k^{D,X} = 0, \forall k \neq i$.

In so doing, Eq. 2.9 becomes:

$$\nabla X_i = -X_i \mathbf{v}_i^{D,X} \sum_{\substack{k=1 \\ k \neq i}}^{N} \frac{X_k}{D_{i,k}}. \tag{11.11}$$

For the case of spherical symmetry, this equation can be rearranged to:

$$X_i \mathrm{v}_i^{D,X} = -\left[\sum_{\substack{k=1 \\ k \neq i}}^{N} \frac{X_k}{D_{i,k}} \right]^{-1} \frac{dX_i}{dr}, \tag{11.12}$$

which by comparison with Eq. 11.10 leads to the definition of the diffusion coefficient named here as the Blanc's model:

$$D_{i,m} = \frac{1}{\sum\limits_{\substack{k=1 \\ k \neq i}}^{N} X_k / D_{i,k}}. \tag{11.13}$$

In the works of (Tonini and Cossali 2015) and (Sazhin 2017), it is possible to see an analogous definition for the Blanc's model using mass insted of molar fractions:

$$D_{i,m} = \frac{1}{\sum\limits_{\substack{k=1 \\ k \neq i}}^{N} Y_k / D_{i,k}}. \tag{11.14}$$

This was possibly motivated from the fact that, to obtain Blanc's model, the Stefan-Maxwell equations must be developed using molar fractions and velocities, with the mass diffusion closure requiring mass fractions. Therefore, it is reasonable to think that, from this direct perspective, a "conversion" towards a mass fraction based formulation would be needed to use the original result suggested by Blanc. However, as argued before, the binary analogy ensures that the same diffusion coefficient is obtained (and should be used), regardless of molar or mass formulations, and so Eq. 11.13 is preferred.

11.3 A complimentary diffusion coefficient for Blanc's model

Motivated by the binary analogy inherent to Hougen's approach used for all diffusion coefficents models, we propose an alternative formulation for the computation of the diffusion coefficient $D_{i,m}$. The point of departure is Eq. 2.25 for the conversion of mass to molar gradients. Since it is constructed for a binary mixture, it can be rewritten for species 1 as:

$$\nabla X_1 = \left[\frac{X_1(1 - X_1)}{Y_1(1 - Y_1)} \right] \nabla Y_1. \tag{11.15}$$

The binary analogy, with the introduction of the diffusion coefficient $D_{i,m}$ allows us to interpret the mass diffusion as if it is happening in a binary sense, from a species i towards the remainder of the mixture m. In this context, for the purposes of computing a diffusion coefficient, the following approximation is made:

$$\nabla X_i = \frac{X_i X_m}{Y_i Y_m} \nabla Y_i = \frac{X_i(1 - X_i)}{Y_i(1 - Y_i)} \nabla Y_i. \tag{11.16}$$

Subsituting Eq. 11.16 onto the LHS of Eq. 2.8 leads to:

$$\frac{(1 - X_i)}{Y_i(1 - Y_i)} \frac{dY_i}{dr} = -\sum_{k=1}^{N} \frac{X_k}{D_{i,k}} \left[\mathrm{v}_i^{D,Y} - \mathrm{v}_k^{D,Y} \right]. \tag{11.17}$$

Now, the complimentary hypothesis to Blanc's law is made:

- All species except i have null mass diffusion velocities, namely $\mathbf{v}_k^{D,Y} = 0, \forall\, k \neq i$.

This then leads to:

$$\frac{(1-X_i)}{Y_i(1-Y_i)}\frac{dY_i}{dr} = -Y_i \mathrm{v}_i^{D,Y} \sum_{\substack{k=1 \\ k\neq i}}^{N} \frac{X_k}{D_{i,k}}. \tag{11.18}$$

Rearranging into a form analogous to 11.9 then produces an alternative diffusion coefficient:

$$D_{i,m} = \left(\frac{1-X_i}{1-Y_i}\right)\left(\sum_{k=1}^{N}\frac{X_k}{D_{i,k}}\right)^{-1}. \tag{11.19}$$

In a sense, this formulation is complementary to Blanc's law because it allows for the obtention of a new formulation wherein *mass* diffusion velocities are supposed to be null instead of *molar* ones which can be useful depending on the application.

11.4 Wilke's model

Even though Blanc's publication came first chronologically, the binary analogy through a diffusion coefficient was perhaps first materialized in the works of (Fairbanks and Wilke 1950), where the coefficient D_i is named the "effective" diffusion coefficient. The publication mentions a previous work by co-author Wilke that derived the showcased expression, however the paper seems to not be acessible. Due to this fact, the diffusion coefficient expression derived here is referred to as the Wilke model.

The main idea is to depart from Eq. 11.3 and isolate for the gradient of molar fraction. Then, this is equated to the RHS of the Stefan-Maxwell equations for molecular velocities Eq. 2.12a to obtain:

$$\frac{\mathbf{v}_i^m - \sum_{k=1}^{N} X_k \mathbf{v}_k^m}{D_{i,m}} = \sum_{k=1}^{N}\frac{X_k}{D_{i,k}}[\mathbf{v}_i^m - \mathbf{v}_k^m]. \tag{11.20}$$

Then, the following hypothesis is made:

- All species except i have the same molecular velocity, i.e. $\mathbf{v}_k^m = \mathbf{w}, \forall\, k \neq i$.

In so doing, the numerator of the LHS of Eq. 11.20 becomes:

$$\begin{aligned}\mathbf{v}_i^m - \sum_{k=1}^{N} X_k \mathbf{v}_k^m = \mathbf{v}_i^m - \mathbf{v}_i^m X_i - \mathbf{w}\sum_{\substack{k=1 \\ k\neq i}}^{N} X_k = \\ = \mathbf{v}_i^m - \mathbf{v}_i^m X_i - \mathbf{w}(1-X_i) = (\mathbf{v}_i^m - \mathbf{w})(1-X_i).\end{aligned} \tag{11.21}$$

The RHS becomes:

$$\sum_{k=1}^{N} \frac{X_k}{D_{i,k}}[\mathbf{v}_i^m - \mathbf{v}_k^m] = \mathbf{v}_i^m \sum_{k=1}^{N} \frac{X_k}{D_{i,k}} - \sum_{k=1}^{N} \frac{X_k \mathbf{v}_k^m}{D_{i,k}} =$$
$$= \frac{\mathbf{v}_i^m X_i}{D_{i,i}} + \mathbf{v}_i^m \sum_{\substack{k=1 \\ k\neq i}}^{N} \frac{X_k}{D_{i,k}} - \frac{\mathbf{v}_i^m X_i}{D_{i,i}} - \mathbf{w} \sum_{\substack{k=1 \\ k\neq i}}^{N} \frac{X_k}{D_{i,k}} = (\mathbf{v}_i^m - \mathbf{w}) \sum_{\substack{k=1 \\ k\neq i}}^{N} \frac{X_k}{D_{i,k}} \quad (11.22)$$

Substituting the above results, Eq. 11.20 becomes:

$$\frac{(\mathbf{v}_i^m - \mathbf{w})(1 - X_i)}{D_{i,m}} = (\mathbf{v}_i^m - \mathbf{w}) \sum_{\substack{k=1 \\ k\neq i}}^{N} \frac{X_k}{D_{i,k}}. \quad (11.23)$$

By cancelling out the term $(\mathbf{v}_i^m - \mathbf{w})$ from both sides of the equation, we obtain the following definition of the diffusion coefficient:

$$D_{i,m} = \frac{(1 - X_i)}{\sum\limits_{\substack{k=1 \\ k\neq i}}^{N} X_k / D_{i,k}}. \quad (11.24)$$

The same expression is offered in (Klingenberg 2015), without a precise derivation but enough infomation to allow for one. Comparing both formulations Eq. 11.13 and Eq. 11.24, it is possible to see that the only difference is the factor $(1-X_i)$ on the numerator. Essentially, this explicitly injects the molar fraction information from species i into the computation of the diffusion coefficient, since the summation excludes contributions from species i.

In the limiting case of $X_i \to 0$, Eqs. 11.24 and 11.13 retrieve the exact same result. Further, in the opposite limiting case, namely $X_i \to 1$, it is easy to see that Eq. 11.13 diverges; since $\sum_{k=1}^{N} X_k = 1$, if $X_i \to 1$ then $X_k \to 0 \forall k \neq i$. However, the limiting behavior for Eq. 11.24 is bounded, as shown below. Suppose $\mathcal{L}$ is defined as such limit:

$$\mathcal{L} = \lim_{X_i \to 1} (1 - X_i) \left(\sum_{\substack{k=1 \\ k\neq i}}^{N} \frac{X_k}{D_{i,k}} \right)^{-1} \quad (11.25)$$

By naming $D_{i,k}^{\max} = \max(D_{i,k}), \forall k \neq i$, it follows naturally that:

$$(1 - X_i)\left(\sum_{\substack{k=1 \\ k\neq i}}^{N} \frac{X_k}{D_{i,k}}\right)^{-1} \leq (1 - X_i)\left(\sum_{\substack{k=1 \\ k\neq i}}^{N} \frac{X_k}{D_{i,k}^{\max}}\right)^{-1} = \\ = D_{i,k}^{\max} \frac{(1 - X_i)}{\sum\limits_{\substack{k=1 \\ k\neq i}}^{N} X_k} = D_{i,k}^{\max}, \quad (11.26)$$

and therefore from Eq. 11.25, $\mathcal{L} \leq D_{i,k}^{\max}$. It is then straightforward to show that, conversely, $\mathcal{L} \geq D_{i,k}^{\min}$ if we define $D_{i,k}^{\min} = \min(D_{i,k}), \forall j \neq k$ and therefore:

$$D_{i,k}^{\min} \leq \mathcal{L} \leq D_{i,k}^{\max}, \quad (11.27)$$

which proves that the formulation proposed by Eq. 11.24 will always converge to a physically sensible quantity for the limiting case $X_i \to 1$. It should be noted that still the convergence is not ideal since in theory for $X_i \to 1$, $D_{i,m} \to D_{i,i}$ should be retrieved; since the auto-diffusion coefficient is not present in Eq. 11.24, this convergence behavior is not generally attainable.

In the context of multi-component droplet heat and mass transfer, the hypothesis of vapor-liquid equilibrium at the surface of the droplet allows for the computation of mass fractions of each species at the surface based on its saturation vapor pressure. As some species approach their boiling temperature, impacts of the diverging behavior of Blanc's model would be expected, since $Y_i^s \to 1$ as $T^s \to T_{b,i}$, with $T_{b,i}$ being the boiling temperature of species i.

However, in practice this ends up not happening, and the reason is two-fold. First, the droplet may effectively never reach boiling temperatures, as the wet-bulb behavior is observed. Second and perhaps most importantly, there is the usage of the one-third rule inside the boundary layer (except for the Ebrahimian and Habchi model). As explained in Chap. 5, this rule averages mass fractions using values from the surface and far away from the droplet, which are typically set to 0, or are way smaller than those computed at the surface when reaching temperatures nearing the boiling one. Still, this sensibility is noted here for more general applications.

11.5 Hirschfelder and Curtiss's model

A third possibility for the diffusion coefficient can be traced back to the publication of (Hirschfelder and Curtiss 1949). Therein, the authors provide the following expression

for the mass diffusion velocity:

$$\mathbf{v}_i^{D,Y} = \frac{n^2\left(1 - n_i W_i/\rho\right)}{n_i \sum\limits_{\substack{k=1 \\ k\neq i}}^{N} n_k/D_{i,k}} \nabla\left(\frac{n_i}{n}\right), \tag{11.28}$$

where n is the total number of moles in the mixture, n_i is the number of moles of species i and W_i its molecular weight. By noticing that $\frac{n_i W_i}{\rho} = Y_i$ and $\frac{n_i}{n} = X_i$, the above can be rearranged as:

$$\mathbf{v}_i^{D,Y} = \frac{1}{X_i} \frac{(1 - Y_i)}{\sum\limits_{\substack{k=1 \\ k\neq i}}^{N} X_k/D_{i,k}} \nabla X_i. \tag{11.29}$$

The expression for the diffusion velocity in Eq. 11.29 was derived in (Coffee and Heimerl 1981) using a similar reasoning as done for the obtention of the Wilke model, but this time with a same mass diffusion velocity (instead of same molecular velocity):

- All species except i have the same mass diffusion velocity, i.e. $\mathbf{v}_k^{D,Y} = \mathbf{w}^{D,Y}, \forall k \neq i$.

Indeed, departing from Eq. 2.12a using $\mathbf{v}_i^{D,Y} = \mathbf{w}^{D,Y}\, \forall k \neq i$ leads to:

$$\nabla X_i = -X_i \left(\mathbf{v}_i^{D,Y} - \mathbf{w}^{D,Y}\right) \sum_{\substack{k=1 \\ k\neq i}}^{N} X_k/D_{i,k} \tag{11.30}$$

In parallel, from the condition of mass conservation 2.4 we find:

$$\sum_{k=1}^{N} Y_k \mathbf{v}_k^{D,Y} = 0 \rightarrow Y_i \mathbf{v}_i^{D,Y} + \left[\sum_{\substack{k=1 \\ k\neq i}}^{N} Y_i\right] \mathbf{w}^{D,Y} = Y_i \mathbf{v}_i^{D,Y} + (1 - Y_i)\mathbf{w}^{D,Y} = 0 \rightarrow \mathbf{w}^{D,Y} = -\frac{Y_i \mathbf{v}_i^{D,Y}}{1 - Y_i} \tag{11.31}$$

Substituting this result on Eq. 11.30 and isolating for the diffusion velocity leads to the expression of Eq. 11.29. In subsequent works, an extrapolation has been made that this induces a diffusion coefficient referred to as the "Hirschfelder-Curtiss" model:

$$D_{i,m} = \frac{(1 - Y_i)}{\sum\limits_{\substack{k=1 \\ k\neq i}}^{N} X_k/D_{i,k}}, \tag{11.32}$$

However, Eq. 11.29 would then become:

$$X_i \mathbf{v}_i^{D,Y} = -D_{i,m} \nabla X_i, \tag{11.33}$$

which as pointed out in (Ebrahimian and Habchi 2011) could not in general be used in the binary analogy, as a mass diffusion velocity is used for the molar fraction gradient formulation.

As noted in (Giovangigli 1991), apparently the expression for the diffusion velocity Eq. 11.29 was originally imposed rather than analitically derived, due to the fact that it simplifies the matrix that must be inverted when solving the Stefan-Maxwell system of equations in the context of multi-component flows that discretize the gaseous phase. This is in contrast with our current interests, where the droplet heat and mass transfer models are integrated in space.

As discussed in Chap. 9 and as shown in Chap. 10, in (Ebrahimian and Habchi 2011) the authors propose that a conversion from molar to mass fractions that can essentially be translated into the following corrected diffusion coefficient for the Hirschfelder-Curtiss model:

$$D_{i,m} = \left[1 - X_i + Y_i \sum_{\substack{k=1 \\ k \neq i}}^{N} \frac{X_i}{Y_i}\right] \frac{(1 - Y_i)}{\sum_{\substack{k=1 \\ k \neq i}}^{N} X_k / D_{i,k}}. \tag{11.34}$$

We also note here that, if Eq. 11.16 that we propose for the conversion of molar to mass gradients is used on Eq. 11.33, then the Wilke diffusion coefficient model Eq. 11.24 is retrieved. Now, recall that the Hirschfelder-Curtiss model is derived by assuming that all species except for i have the same mass diffusion velocity, and the Wilke model is derived assuming that all species except i have the same molecular velocity. Therefore, this would suggest that Eq. 11.16 for the gradient conversion would be valid if both of these conditions are satisfied at the same time.

11.6 The velocity inconsistency problem

For all the models discussed in this chapter, hypotheses were made concerning either the molecular velocities, the mass diffusion velocities, or the molar diffusion velocities, to simplify the Stefan-Maxwell equations. Following Hougen's binary analogy, they lead to expressions for diffusion coefficients $D_{i,m}$ between each species i and the remainder of the mixture m.

For typical multi-component applications however, this can lead to an inconsistency problem. For example, if a droplet composed of ethanol and water is evaporating into air, the gaseous phase is composed of a ternary mixture, composed of two fuels and one inert species. For any discrete component model, one equation would need to be solved for each fuel species i.e. one for water and one for ethanol. If we elect to use any differential diffusion model, this would mean that we would need to compute the diffusion coefficients

from water towards the mixture $D_{water,m}$ and the one from ethanol towards the mixture $D_{ethanol,m}$.

Now, assume that Wilke's model is being used to compute $D_{water,m}$. In so doing, we are enforcing that ethanol and air, the remainder of the mixture, have the same molecular velocity i.e. $\mathrm{v}^m_{ethanol} = \mathrm{v}^m_{air} = \mathrm{w}^m_1$ which would be different from the one of water, v^m_{water}. Then, if we were to also use Wilke's model to compute the diffusion coefficient for ethanol, we would now have to assume that $\mathrm{v}^m_{water} = \mathrm{v}^m_{air} = \mathrm{w}^m_2$ which can easily be seen as inconsistent with the scenario used to compute the diffusion coefficient for water. For this gaseous mixture, the only case in which this would not be inconsistent would be when all molecular velocities are equal, which leads to a trivial solution to the Stefan-Maxwell equations that is not useful. It is straightforward to see that a similar problem arises for any other diffusion coefficient model of this chapter.

There are two scenarios which can solve this problem. First, is to use different diffusion coefficients expressions for each species. In this way, each species would enforce a hypothesis about a particular velocity that would not clash with other hypotheses. The caveat here is that, of course, only a handful of diffusion coefficients models are present, and so this is not practical for gaseous mixtures containing multiple species. Another issue is that unless some studies are carried for fully-solved multi-component gaseous mixtures beforehand, the choice concerning which species would be described by which coefficient (and therefore its hypothesis) would be arbitrary.

A second scenario that presents no inconsistency is the case where we seek to describe the diffusional behavior of a single species in a gaseous mixture having multiple components. For example, the case where a single-component droplet evaporates towards a gaseous mixture that has multiple other inert species, not only air. This was the case of the original work of (Blanc 1908), where the author is only concerned with the mobility of ions. Therefore, this approach can be seen as a useful extension for surrogate models that assume that all fuel species can be treated as a single fuel. For spray combustion applications, this would be useful since combustion products and many other intermediary reacting species are present and could more explicitly impact the phase-change through the far-away condition.

Interestingly, even though the mathematical inconsistency is verified, numerical investigations show that these diffusion coefficients actually approximate the Stefan-Maxwell equations fairly well, as will be shown in the next section. Also, another hypothesis made in Blanc's work was that the ion species were present in trace amounts. Therefore, we could also interpret that if multiple fuel species are present but in small quantities relative to the remaining inert gases, then they would physically not interact with other species enough, therefore making this inconsistent assumption "sufficiently" valid.

11.7 Comparison between different diffusion coefficients

We now compare the following expressions, summarized below for easy reference:

1. Blanc

$$D_{i,m} = \frac{1}{\sum\limits_{\substack{k=1 \\ k\neq i}}^{N} X_k/D_{i,k}}.$$

2. Wilke

$$D_{i,m} = \frac{(1-X_i)}{\sum\limits_{\substack{k=1 \\ k\neq i}}^{N} X_k/D_{i,k}}.$$

3. Hirschfelder and Curtiss - Ebrahimian and Habchi correction (HC-EH)

$$D_{i,m} = \left[1 - X_i + Y_i \sum_{\substack{k=1 \\ k\neq i}}^{N} \frac{X_i}{Y_i}\right] \frac{(1-Y_i)}{\sum\limits_{\substack{k=1 \\ k\neq i}}^{N} X_k/D_{i,k}}.$$

We leave out the Hisrchfelder-Curiss non-corrected expression, Eq. 11.32 due to its analytical inconsistency, and also the complimentary Blanc model Eq. 11.19 because it produced large deviations, possibly indicating that for typical operating conditions it does not represent a valid hypothesis.

The numerical investigations are carried out against the full solution of the Stefan-Maxwell equations, detailed in Chap. 8 and taken here to be the reference. Investigations for these coefficients were carried out for both the extended mass and molar formulations, represented through $\dot{m}$ and $\dot{n}$ respectively, and reproduced below:

- Mass formulation - $\dot{m}$

$$\dot{m}_i = \dot{m}\left(\frac{Y_i^{\infty} - Y_i^{s}\exp\left[\frac{\dot{m}}{2\pi R_d Sh_i \rho D_{i,m}}\right]}{1-\exp\left[\frac{\dot{m}}{2\pi R_d Sh_i \rho D_{i,m}}\right]}\right), \text{ if } 1 + B_{M,i}^{Y} > 0,$$

$$\dot{m}_i = \dot{m}\left(\frac{Y_i^{\infty} + Y_i^{s}\exp\left[\frac{\dot{m}}{2\pi R_d Sh_i \rho D_{i,m}}\right]}{1+\exp\left[\frac{\dot{m}}{2\pi R_d Sh_i \rho D_{i,m}}\right]}\right), \text{ if } 1 + B_{M,i}^{Y} < 0.$$

- Molar formulation - $\dot{n}$

$$\dot{n}_i = \dot{n}\left(\frac{X_i^\infty - X_i^s \exp\left[\frac{\dot{n}}{2\pi R_d Sh_i c D_{i,m}}\right]}{1-\exp\left[\frac{\dot{n}}{2\pi R_d Sh_i c D_{i,m}}\right]}\right), \text{ if } 1+B_{M,i}^X > 0,$$

$$\dot{n}_i = \dot{n}\left(\frac{X_i^\infty + X_i^s \exp\left[\frac{\dot{n}}{2\pi R_d Sh_i c D_{i,m}}\right]}{1+\exp\left[\frac{\dot{n}}{2\pi R_d Sh_i c D_{i,m}}\right]}\right), \text{ if } 1+B_{M,i}^X < 0.$$

The Spalding mass and molar transfer numbers are:

$$B_{M,i}^Y = \dot{m}\left[\frac{Y_i^s - Y_i^\infty}{\dot{m}_i - \dot{m}Y_i^s}\right],$$

$$B_{M,i}^X = \dot{n}\left[\frac{X_i^s - X_i^\infty}{\dot{n}_i - \dot{n}X_i^s}\right].$$

Law's extended model was left out since it follows a preferential diffusion approach. Ebrahimian and Habchi's extended model was left out since it is not as suitable as the mass and molar approaches for comparison with the Stefan-Maxwell equations for the purposes of obtaining the best diffusion coefficient expression. The three compared mass transfer models (Stefan-Maxwell, mass and molar) all use the same energy formulation, also detailed in Chap. 8.

The numerical investigations were carried with initial conditions common to all of them, listed in Table 11.1 below.

Parameter	Value
Initial droplet diameter $\mathcal{D}_{d,0}$	$40\mu m$
Initial droplet temperature $T_{d,0}$	$300K$
Surrounding gas temperature T^∞	$800K$
Initial droplet velocity $U_{d,0}$	$0m/s$
Surrounding gas velocity U^∞	$25m/s$
Atmospheric pressure p	$101325Pa$

Figure 11.1: Initial conditions common to all investigations of this section

Four different initial droplet compositions were studied, with percentages in volume. These are displayed in Table 11.2. For each droplet composition of Table 11.2, two different surrounding compositions were investigated, pure air (Air) and a "vapor" (V) condition where fuel vapors are present in a high humidity environment. To detail this vapor condition, we detail the concept of relative vapor presence (RVP), characterised

Initial droplet composition	Percentual in volume
Ethanol/Water (E/W)	50% E and 50% W
Acetone/Water (A/W)	50% A and 50% W
Ethanol/Acetone/Water (E/A/W)	33.3% E, 33.3% A and 33.4% W
Ethanol/n-Dodecane/Water (E/D/W)	33.3% E, 33.3% D and 33.4% W

Figure 11.2: Denomination and description of the different initial droplet compositions

through the parameter $0 < \phi^{\mathrm{RVP}} < 1$, which allows us to compute the molar fractions of each species at the far-away condiiton through:

$$X_i^{\infty} = \phi^{\mathrm{RVP}} \left(\frac{\mathrm{p}_{sat,i}(T = 300K)}{\mathrm{p}} \right). \tag{11.35}$$

In this way, if $\phi^{\mathrm{RVP}} = 1.0$, we would have the maximum molar mass fraction possible $X_{i,\max}^{\infty}$ at the gaseous state for species i at $T = 300K$, the starting droplet temperature. This concept is most useful when used in isolation; if more than one species is present at the far-away state, then the maximum ϕ^{RVP} for each one is expected to be less than 1. This means that the sum of all X_i^{∞} could eventually be greater than 1 if care is not taken. We chose a high humidity condition for water (as it is the most realistic) and values that are physically revelant for remaining fuel species. Also, since the droplet temperature will rise, $X_{i,\max}^{\infty}$ should also increase which will only alleviate more the physical constraints.

The vapor conditions "V" are thus detailed in Table 11.3 for each droplet composition.

Composition denomination	Relative vapor presence
V-E/W	$\phi_{\mathrm{E}}^{\mathrm{RVP}} = 0.25$ and $\phi_{\mathrm{W}}^{\mathrm{RVP}} = 0.8$ $X_{\mathrm{ethanol}}^{\infty} \approx 0.0218$ and $X_{\mathrm{water}}^{\infty} \approx 0.028$
V-A/W	$\phi_{\mathrm{A}}^{\mathrm{RVP}} = 0.25$ and $\phi_{\mathrm{W}}^{\mathrm{RVP}} = 0.8$ $X_{\mathrm{A}}^{\infty} \approx 0.082$ and $X_{\mathrm{W}}^{\infty} \approx 0.028$
V-E/A/W	$\phi_{\mathrm{E}}^{\mathrm{RVP}} = 0.25$, $\phi_{\mathrm{A}}^{\mathrm{RVP}} = 0.25$ and $\phi_{\mathrm{W}}^{\mathrm{RVP}} = 0.8$ $X_{\mathrm{E}}^{\infty} \approx 0.0218$, $X_{\mathrm{A}}^{\infty} \approx 0.082$ and $X_{\mathrm{W}}^{\infty} \approx 0.028$
V-E/D/W	$\phi_{\mathrm{E}}^{\mathrm{RVP}} = 0.25$, $\phi_{\mathrm{D}}^{\mathrm{RVP}} = 0.25$ and $\phi_{\mathrm{W}}^{\mathrm{RVP}} = 0.8$ $X_{\mathrm{E}}^{\infty} \approx 0.0218$, $X_{\mathrm{D}}^{\infty} \approx 4.98\mathrm{x}10^{-5}$ and $X_{\mathrm{W}}^{\infty} \approx 0.028$

Figure 11.3: Description of surrounding atmosphere compositions for each case

For all cases in Table 11.3, the remaining molar fraction at infinity was attributed to

a single inert species "air", detailed in appendix C. For the cases where only air is present, we use the nomenclaure "Air-E/W" for example for the ethanol-water droplet composition.

11.7.1 Discussion of results

In Fig. 11.5, we can see that for the E/W droplet evaporating into air, in general all models predict a fairly good agreement for the global mass transfer rate, the non-dimensional surface and the heat transfer rate. However, we readily see that the HC-EH model overshoots the mass transfer rate of ethanol and undershoots the mass transfer rate of water, which evens out for the global mass transfer rate. This suggests that it can be misleading to analyze only global metrics for multi-component droplets. The biggest difference can be seen for the droplet temperature profiles. Since all models use the same energy coupling with the liquid phase, this is explained through a hyper-sensitivity on the heat transfer rate; even though they seem to be identical, a slight difference leads to 3-4K for the final temperature here. Overall, we see that all models capture the same physics. We see the initial heat-up time followed by a first plateau where ethanol (the most volatile species) dominates the evaporation. Then, a second, less extreme heat-up follows at the end of which only water remains until the droplet has evaporated. As expected, for this single-component extreme, all models perform similarly.

In Fig. 11.6 we see the same case with fuel vapors; the same trends are observed. In general, the presence of vapors tends to damp the differences between models by a small margin. Throughout all cases for the E/W droplet, no difference can be seen between the mass and the molar approaches, and a better agreement for the droplet temperature is observed for Wilke's model. All other metrics seem to be captured reasonably well for Blanc model.

In Figs. 11.7 and 11.8 we now see results for the A/W droplet. The HC-EH coefficient now distantiates more from the other formulations at the beggining of the droplet's lifetime. The initial evaporation rate of acetone that it predicts is almost double than that of other models, and it fails to capture a decrease then an increase; it starts at the bottom and then only increases. The other trends seem to be similar when comparing with the E/W case. Since acetone is more volatile than ethanol, we see that there is no time for a first plateau to consolidate on the droplet's temperature. we also see a slight discrepance between mass and molar formulations for both Blanc and Wilke model at the beggining of the droplet's lifetime, but nothing too substantial.

In Figs. 11.9 and 11.10 we now see results for the ternary droplet E/A/W. In general the same trends are captured; the HC-EH model is the worst predictor overall, mass and molar formulations tend to be indistinguishable and Wilke is the better predictor of temperature behavior. The presence of fuel vapors tend to dampen the differences between the HC-EH and other models.

In Fig. 11.11, a different scenario is presented for the second ternary droplet E/D/W. This time around, the HC-EH model is the better predictor of global mass transfer rate. Upon further inspection, we see however that it accurately predicts the mass transfer rate of water, with those of n-dodecane and ethanol consistently delayed in comparison with the Stefan-Maxwell reference. Conversely, the Blanc and Wilke models fall consistently behind, with Wilke model closer to the reference. Both the Blanc and Wilke models predict a fairly similar final temperature whereas the HC-EH predicts around 20K less for the final temperature, again highlighting a potential sensibility to the heat transfer rate. It should also be noted that the mass transfer rate of water has a huge peak on the last 2-2.5 ms of evaporation time (when the droplet's diameter is around $6\mu m$). Interestingly, the n-dodecane and the ethanol have similar mass transfer rate behaviors until around 9.5-10.5ms, where a severe drop-off happens for ethanol followed by its return to zero, indicating that all ethanol suddenly evaporates. The n-dodecane follows afterwards, without a sudden drop-off. The residual water present in the droplet then suddenly evaporates as it faces a super-heated droplet above its boiling point.

Finally, in Fig. 11.12 we see the greatest differences between all approaches. First we see that the HC-EH model fails to capture the correct physics, with vastly different behaviors. Then, we also see that the molar and mass formulations for Blanc model are virtually identical, whereas there is clear separation for Wilke model, with the mass formulation consistently closer to the Stefan-Maxwell reference. Again we see the same steep drop-off for ethanol followed by its extinction, then a smooth decline for n-dodecane followed by a severe water evaporation. This might be because the n-dodecane and water mixture is immiscible, and therefore the n-dodecane would diffuse towards the outer spherical layer, with pure water at its core, leading to a single-component evporation behaviour for single-component (with surface temperatures superior to that of the water boiling point) and then a sudden change to single-component evaporation of water. It should be noted that these results cannot be numerically accurate, since the infinite diffusivity and conductivity approaches cannot fully describe such behavior, and so care must be taken when analyzing the later part of this droplet evaporation process. In this situation, no model was able to reproduce the Stefan-Maxwell results, but the Wilke model is the closest, especially with the mass formulation. In conclusion, these results suggest that the Wilke model is the best candidate for these diffusion coefficient models. With the exception of the more complex case of the V-E/D/W droplet, it correctly captures all relevant metrics, and is the closest one even for this complex case. Due to these results and the analytical stability demonstrated through the discussion starting in Eq. 11.25, we elect to use the Wilke model Eq. 11.24 as the diffusion coefficient for all remaining investigations in this manuscript.

We also display below Table 11.4 with the benchmarked simulation time t_{run} for the mass formulation using Wilke rule and the Stefan-Maxwell simulation, for their quickest and longest runs. The time it takes to run the Stefan-Maxwell simulations is around 12 times greater for the quickest run and 17 times greater for the longest run. We also see

that the heterogeneous ternary droplet E-D-W is more complex to solve, and even more in the vapor "V" atmosphere. This will be further investigated in the next chapter.

Composition denomination	$\dot{m}$-Wilke	Stefan-Maxwell
Air-A/W	$t_{run} = 6.35s$	$t_{run} = 77.5s$
V-E/D/W	$t_{run} = 91.2s$	$t_{run} = 1550s$

Figure 11.4: Benchmark simulation time t_{run} for the $\dot{m}$ model (using Wilke diffusion coefficient model) and the Stefan-Maxwell reference model.

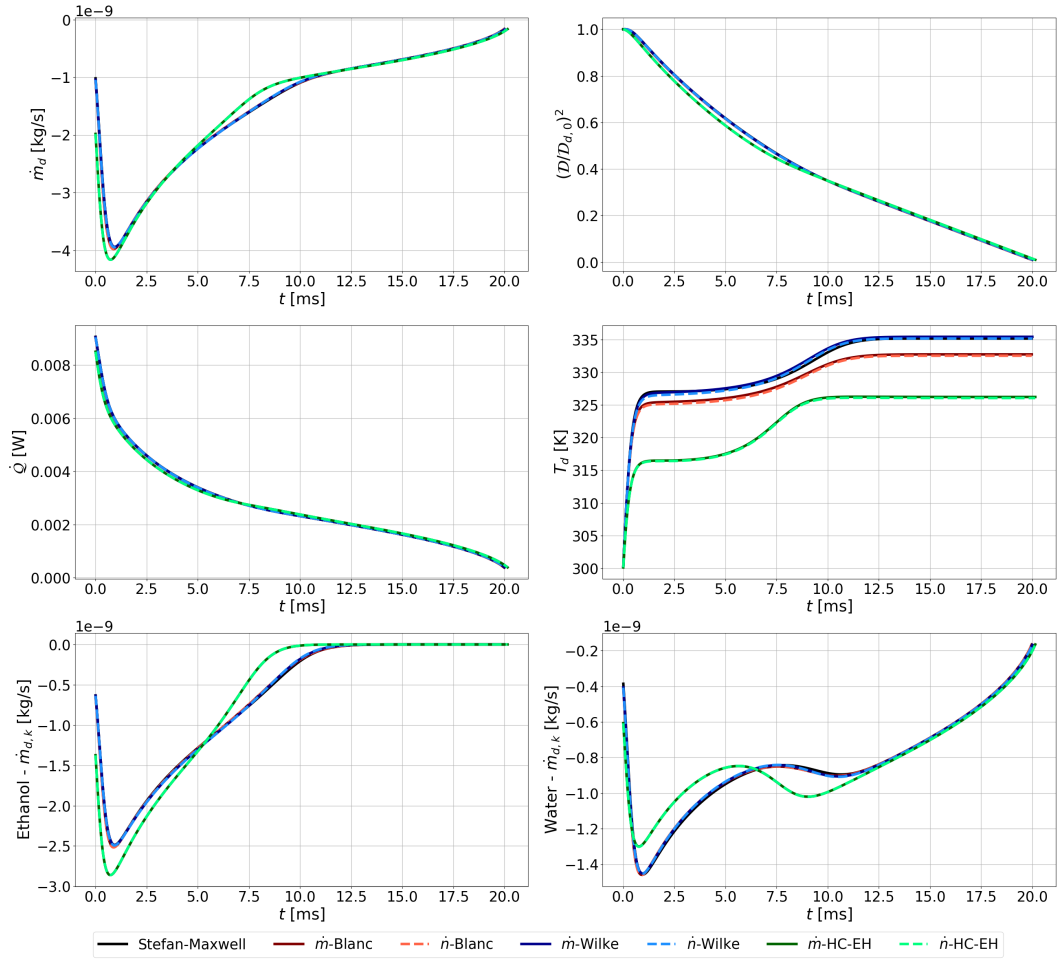

Figure 11.5: Simulation of Air-E/W configuration (see Table 11.2) with initial conditions of Table 11.1. Results displayed for the global mass transfer rate $\dot{m}$, the normalized surface $(\mathcal{D}_d/\mathcal{D}_{d,0})^2$, the heat transfer rate $\dot{\mathcal{Q}}$, the droplet's temperature T_d and the mass transfer rates $\dot{m}_k$ of ethanol and water.

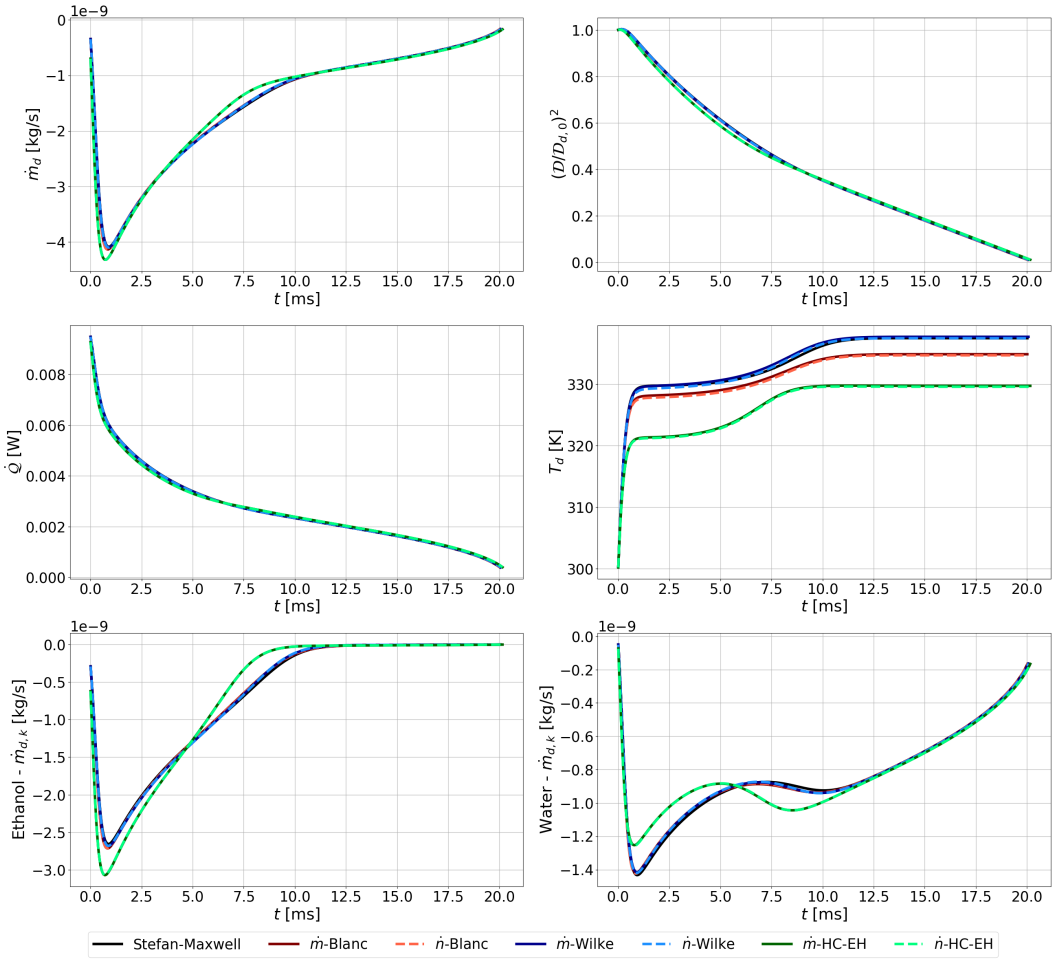

Figure 11.6: Simulation of V-E/W configuration (see Table 11.2 and Table 11.3) with initial conditions of Table 11.1. Results displayed for the global mass transfer rate $\dot{m}$, the normalized surface $(\mathcal{D}_d/\mathcal{D}_{d,0})^2$, the heat transfer rate $\dot{\mathcal{Q}}$, the droplet's temperature T_d and the mass transfer rates $\dot{m}_k$ of ethanol and water.

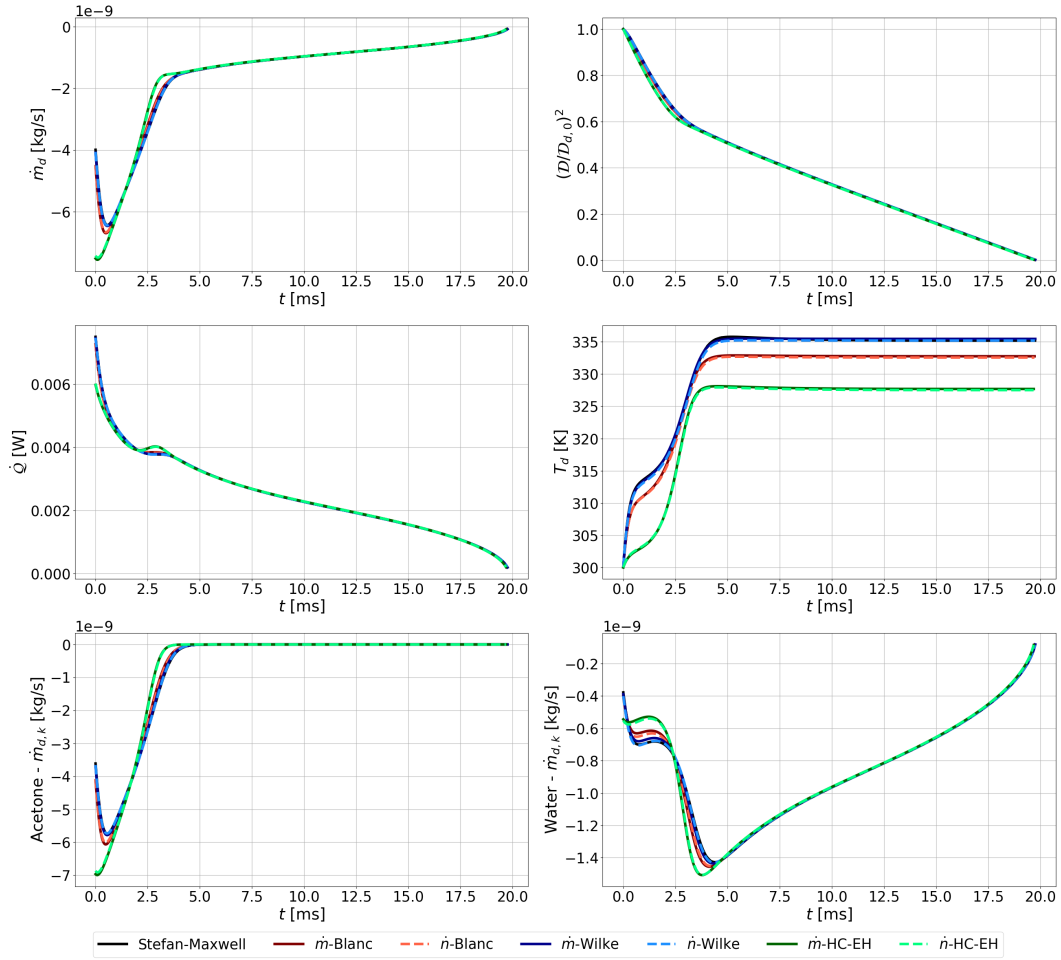

Figure 11.7: Simulation of Air-A/W configuration (see Table 11.2) with initial conditions of Table 11.1. Results displayed for the global mass transfer rate $\dot{m}$, the normalized surface $(\mathcal{D}_d/\mathcal{D}_{d,0})^2$, the heat transfer rate $\dot{\mathcal{Q}}$, the droplet's temperature T_d and the mass transfer rates $\dot{m}_k$ of acetone and water.

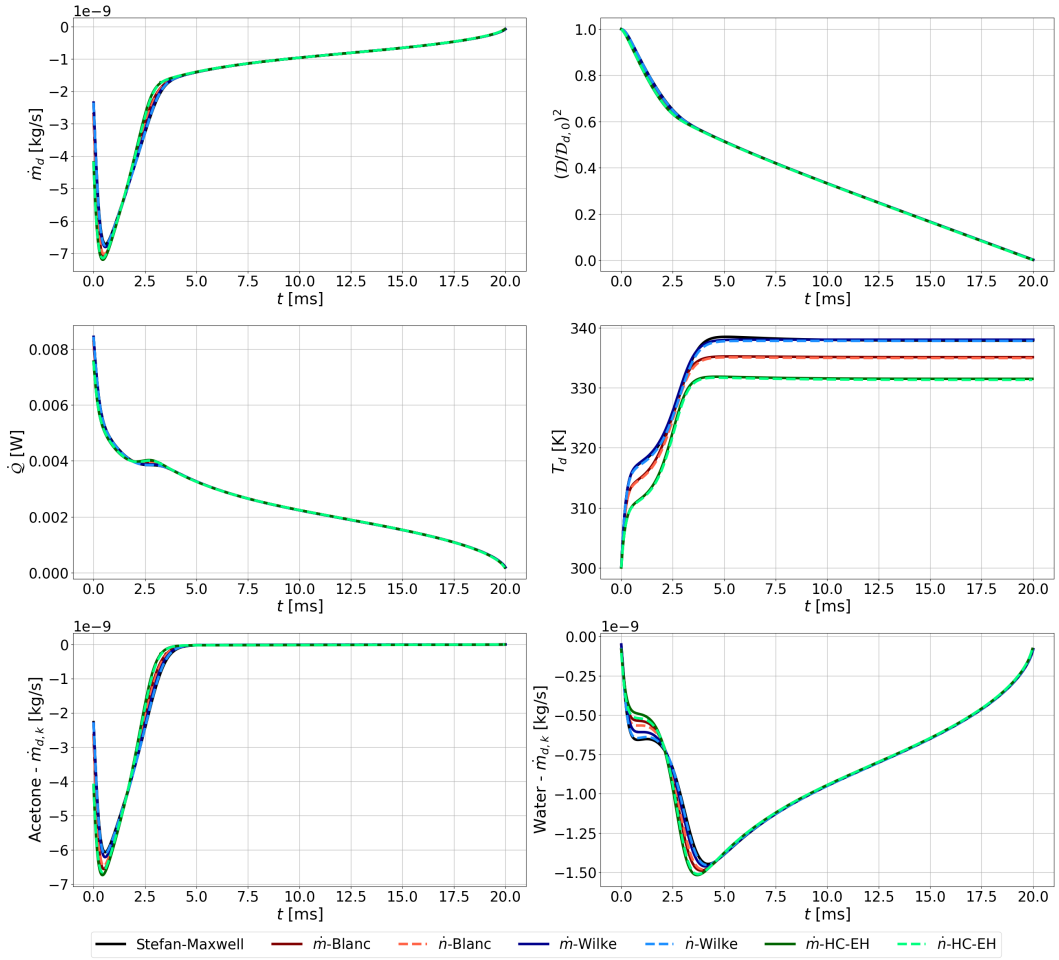

Figure 11.8: Simulation of V-A/W configuration (see Table 11.2 and Table 11.3) with initial conditions of Table 11.1. Results displayed for the global mass transfer rate $\dot{m}$, the normalized surface $(\mathcal{D}_d/\mathcal{D}_{d,0})^2$, the heat transfer rate $\dot{\mathcal{Q}}$, the droplet's temperature T_d and the mass transfer rates $\dot{m}_k$ of acetone and water.

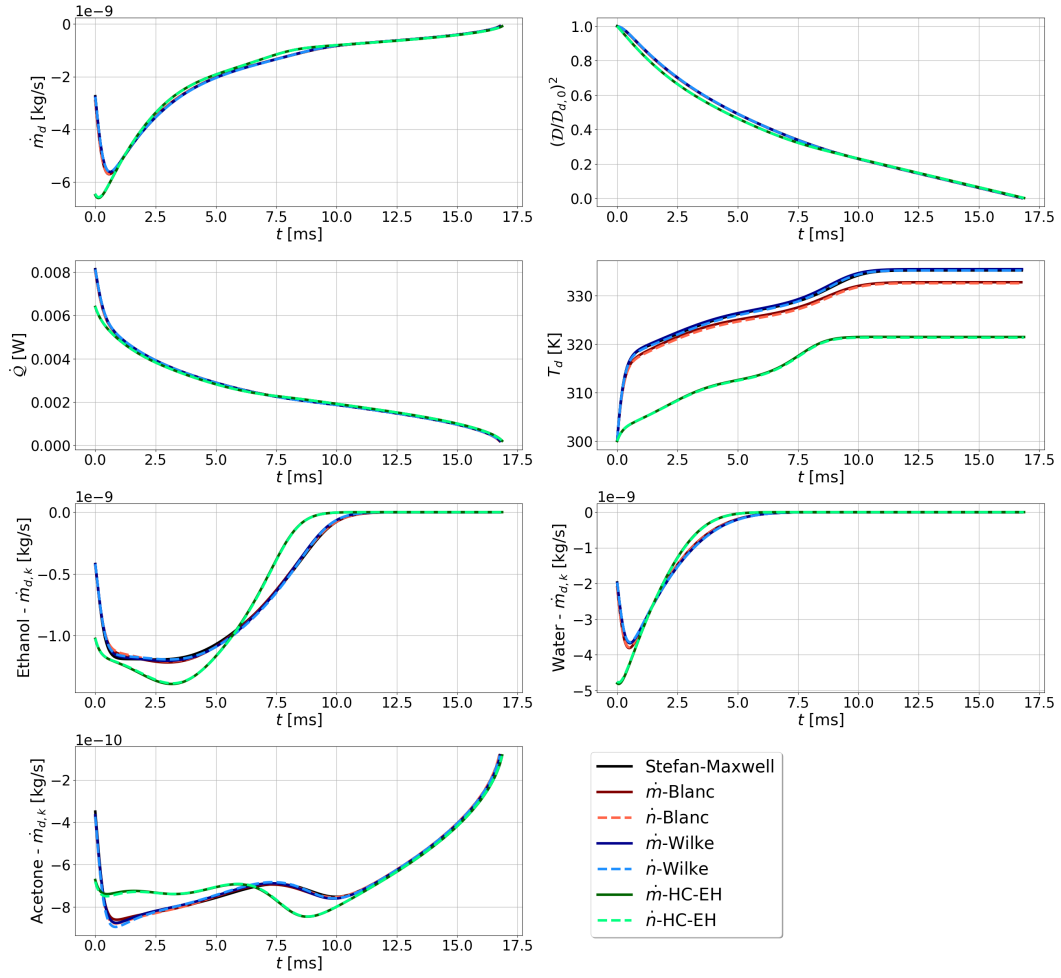

Figure 11.9: Simulation of Air-E/A/W configuration (see Table 11.2) with initial conditions of Table 11.1. Results displayed for the global mass transfer rate $\dot{m}$, the normalized surface $(\mathcal{D}_d/\mathcal{D}_{d,0})^2$, the heat transfer rate $\dot{\mathcal{Q}}$, the droplet's temperature T_d and the mass transfer rates $\dot{m}_k$ of ethanol, acetone and water.

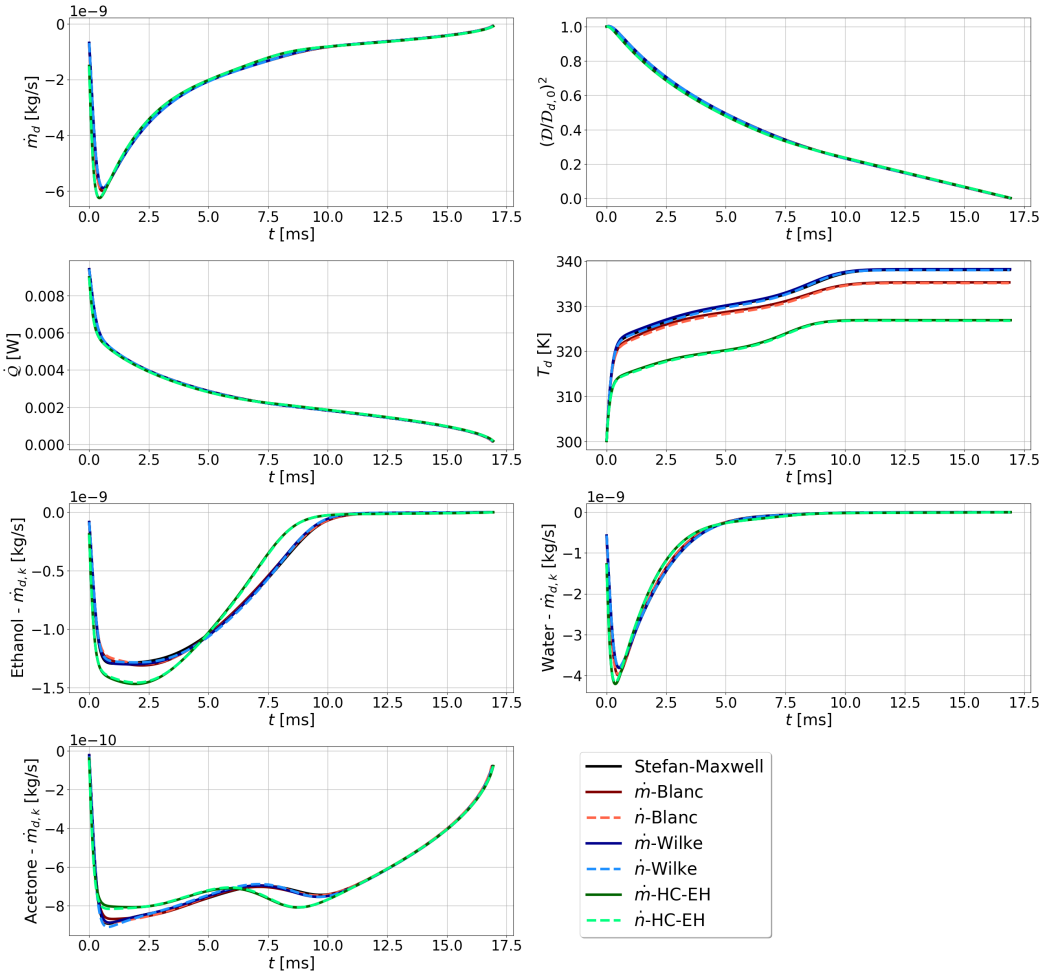

Figure 11.10: Simulation of V-E/A/W configuration (see Table 11.2 and Table 11.3) with initial conditions of Table 11.1. Results displayed for the global mass transfer rate $\dot{m}$, the normalized surface $(\mathcal{D}_d/\mathcal{D}_{d,0})^2$, the heat transfer rate $\dot{\mathcal{Q}}$, the droplet's temperature T_d and the mass transfer rates $\dot{m}_k$ of ethanol, acetone and water.

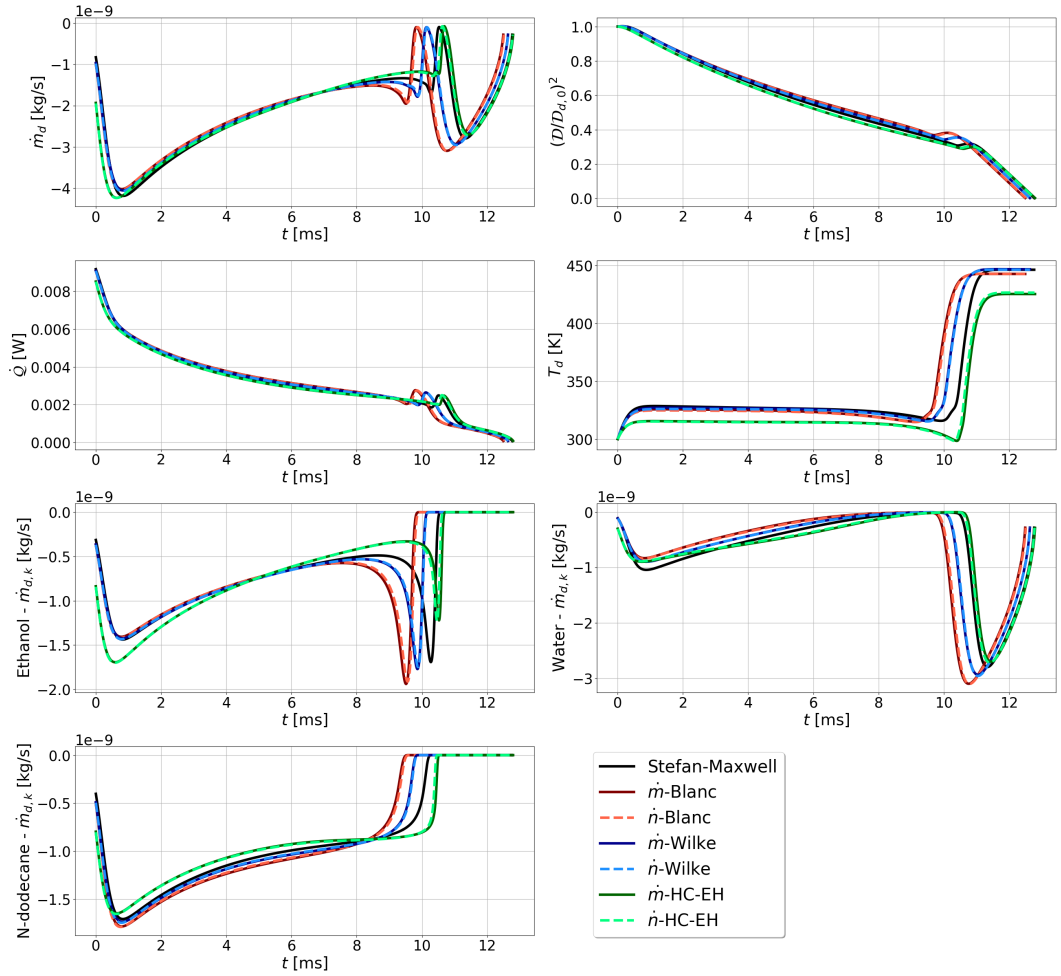

Figure 11.11: Simulation of Air-E/D/W configuration (see Table 11.2) with initial conditions of Table 11.1. Results displayed for the global mass transfer rate $\dot{m}$, the normalized surface $(\mathcal{D}_d/\mathcal{D}_{d,0})^2$, the heat transfer rate $\dot{\mathcal{Q}}$, the droplet's temperature T_d and the mass transfer rates $\dot{m}_k$ of ethanol, n-dodecane and water.

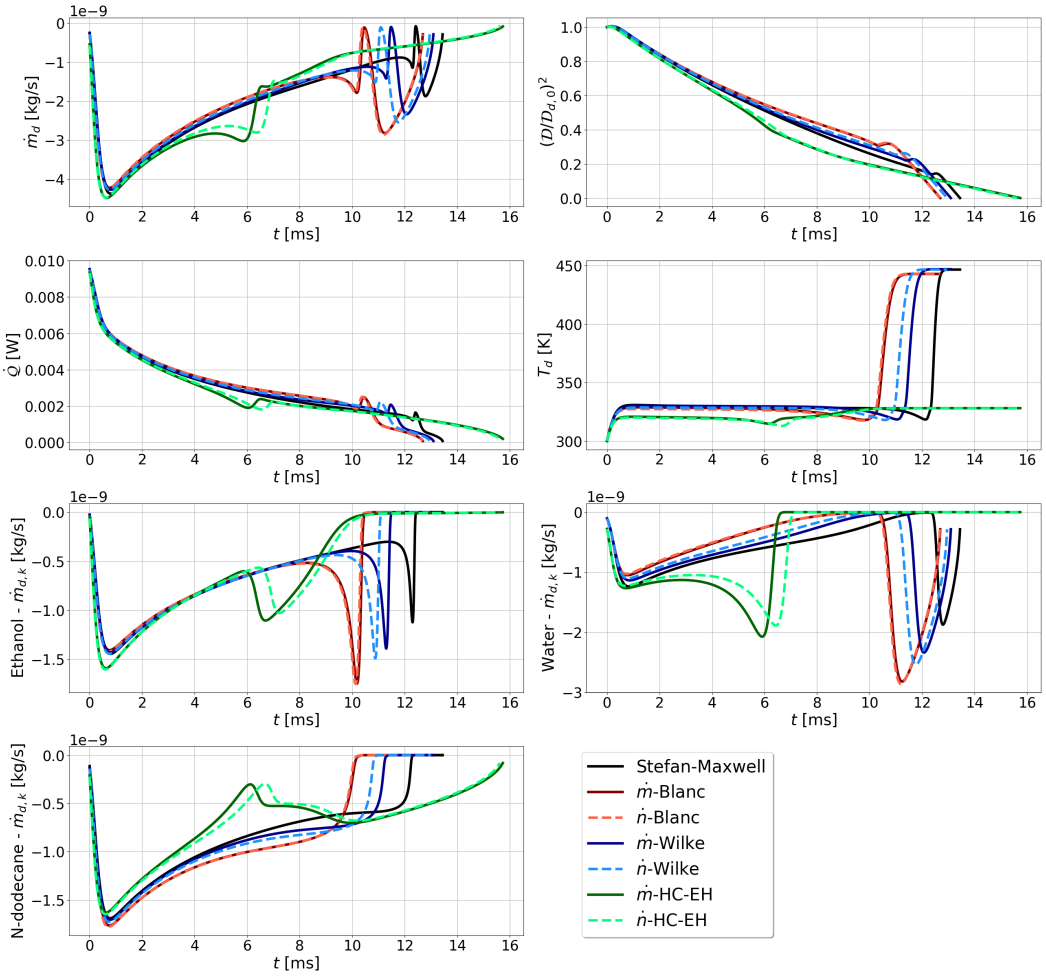

Figure 11.12: Simulation of V-E/D/W configuration (see Table 11.2 and Table 11.3) with initial conditions of Table 11.1. Results displayed for the global mass transfer rate $\dot{m}$, the normalized surface $(\mathcal{D}_d/\mathcal{D}_{d,0})^2$, the heat transfer rate $\dot{\mathcal{Q}}$, the droplet's temperature T_d and the mass transfer rates $\dot{m}_k$ of ethanol, n-dodecane and water.

Chapter 12

Numerical investigations for simplified models

The purpose of this chapter is to now compare all mass transfer model formulations proposed in Chap. 10 using a common diffusion coefficient (Chap. 11) for a vast sweep of parameters relevant to spray combustion applications. It was shown in Chap. 11 that the Stefan-Maxwell formulation can be one order of magnitude more expensive in terms of computational time. Therefore, the numerical investigations carried here have the purpose to elect, among the simplified approaches, which one can most accurately reproduce those reference results while still preserving a lower computational cost.

First, we define the parameter sweep and the physical scenarios. Then, we conduct simulations first for non-convective, then highly convective conditions. Investigations are carried out for droplets composed of ethanol, acetone, n-dodecane and water, including conditions where fuel vapors are present.

12.1 Cases description

First, we list in Table 12.1 the parameters that are commmon to all simulations. The droplet velocity will be fixed to zero for simplicity, with the ambient velocity being varied for the convective scenario.

Parameter	Value
Initial droplet temperature $T_{d,0}$	$300K$
Initial droplet velocity $U_{d,0}$	$0m/s$
Pressure p	$101325Pa$

Figure 12.1: Common initial conditions for all investigations of this section.

Then, the remaining parameters will be varied, following the values seen in Table 12.2. To keep the analysis more concise, only extreme value representative of spray combustion

applcations are chosen here, labeled as "low" and "high" values.

Parameter	Low value	High value
Initial droplet diameter $\mathcal{D}_{d,0}$	$10\mu m$	$100\mu m$
Surrounding gas temperature T^{∞}	$300.01K$	$1600K$
Surrounding gas velocity U^{∞}	$0m/s$	$100m/s$

Figure 12.2: Sweep of parameters for all simulations.

The droplet initial compositions investigated in this study are displayed in Table 12.3. We opted to highlight situations wherein no component dominates the initial mixture, to capture the most varied scenarios. For each droplet, two compositions at infinity are tested, summarized in Table 12.4.

Initial droplet composition	Percentual in volume
Ethanol/Water (E/W)	50% E and 50% W
Acetone/Water (A/W)	50% A and 50% W
Ethanol/Acetone/Water (E/A/W)	33.3% E, 33.3% A and 33.4% W
Ethanol/n-Dodecane/Water (E/D/W)	33.3% E, 33.3% D and 33.4% W

Figure 12.3: Denomination and description of the different initial droplet compositions.

Composition denomination	Relative vapor presence
V-E/W	$\phi_{\mathrm{E}}^{\mathrm{RVP}} = 0.25$ and $\phi_{\mathrm{W}}^{\mathrm{RVP}} = 0.8$ $X_{\mathrm{E}}^{\infty} \approx 0.0218$ and $X_{\mathrm{W}}^{\infty} \approx 0.028$
V-A/W	$\phi_{\mathrm{A}}^{\mathrm{RVP}} = 0.25$ and $\phi_{\mathrm{W}}^{\mathrm{RVP}} = 0.8$ $X_{\mathrm{A}}^{\infty} \approx 0.082$ and $X_{\mathrm{W}}^{\infty} \approx 0.028$
V-E/A/W	$\phi_{\mathrm{E}}^{\mathrm{RVP}} = 0.25$, $\phi_{\mathrm{A}}^{\mathrm{RVP}} = 0.25$ and $\phi_{\mathrm{W}}^{\mathrm{RVP}} = 0.8$ $X_{\mathrm{E}}^{\infty} \approx 0.0218$, $X_{\mathrm{A}}^{\infty} \approx 0.082$ and $X_{\mathrm{W}}^{\infty} \approx 0.028$
V-E/D/W	$\phi_{\mathrm{E}}^{\mathrm{RVP}} = 0.25$, $\phi_{\mathrm{D}}^{\mathrm{RVP}} = 0.25$ and $\phi_{\mathrm{W}}^{\mathrm{RVP}} = 0.8$ $X_{\mathrm{E}}^{\infty} \approx 0.0218$, $X_{\mathrm{D}}^{\infty} \approx 4.98\mathrm{x}10^{-5}$ and $X_{\mathrm{W}}^{\infty} \approx 0.028$

Figure 12.4: Description of surrounding atmosphere compositions for each case.

The definition of the relative vapor presence (RVP) factor can be found in Eq. 11.35. The remainder of the molar fractions at infinity are assigned to air. The idea here is to have a reference scenario with only pure air (referred to as "Air"), but also a more extreme situation (referred to as "V") where vapors from all fuels are present, with water

as a majority to represent a high relative humidity environment.

Finally, each numerical investigation is ran for a total of five droplet mass transfer models. The first is the Stefan-Maxwell reference listed in Chap. 8 and the remaining four are listed below again for easy reference:

1. Extended Tonini-Cossali model (Ext-TC)

$$\dot{m}_i = \dot{m}\left(\frac{Y_i^\infty - Y_i^s \exp\left[\frac{\dot{m}}{2\pi R_d Sh_i \rho D_{i,m}}\right]}{1-\exp\left[\frac{\dot{m}}{2\pi R_d Sh_i \rho D_{i,m}}\right]}\right), \text{ if } 1+B_{M,i}^Y > 0,$$

$$\dot{m}_i = \dot{m}\left(\frac{Y_i^\infty + Y_i^s \exp\left[\frac{\dot{m}}{2\pi R_d Sh_i \rho D_{i,m}}\right]}{1+\exp\left[\frac{\dot{m}}{2\pi R_d Sh_i \rho D_{i,m}}\right]}\right), \text{ if } 1+B_{M,i}^Y < 0.$$

2. Extended Newbold-Amundson model (Ext-NA)

$$\dot{n}_i = \dot{n}\left(\frac{X_i^\infty - X_i^s \exp\left[\frac{\dot{n}}{2\pi R_d Sh_i c D_{i,m}}\right]}{1-\exp\left[\frac{\dot{n}}{2\pi R_d Sh_i c D_{i,m}}\right]}\right), \text{ if } 1+B_{M,i}^X > 0,$$

$$\dot{n}_i = \dot{n}\left(\frac{X_i^\infty + X_i^s \exp\left[\frac{\dot{n}}{2\pi R_d Sh_i c D_{i,m}}\right]}{1+\exp\left[\frac{\dot{n}}{2\pi R_d Sh_i c D_{i,m}}\right]}\right), \text{ if } 1+B_{M,i}^X < 0.$$

3. Extended Ebrahimian-Habchi model (Ext-EH)

$$\frac{\dot{m}}{2\pi R_d \rho^s}\left[1-\sum_{\substack{l=1,\\ l\in\text{fuels}}}^{N} Y_l^s\right] = \sum_{\substack{l=1,\\ l\in\text{fuels}}}^{N} D_{l,m}^s Sh_l\left(Y_l^s - Y_l^\infty\right) - \sum_{\substack{l=1,\\ l\in\text{fuels}}}^{N} Y_l^s \sum_{j=1}^{N} D_{j,m}^s Sh_j\left(Y_j^s - Y_j^\infty\right),$$

$$\dot{m}_i = Y_i^s \dot{m} + 2\pi R_d \rho^s \left(D_{i,m}^s Sh_i\left(Y_i^s - Y_i^\infty\right) - Y_i^s \sum_{j=1}^{N} D_{j,m}^s Sh_j\left(Y_j^s - Y_j^\infty\right)\right).$$

4. Extended Law model (Ext-Law)

$$\dot{m}_i = \dot{m}\left[\frac{Y_i^\infty - Y_i^s (1+\bar{B}_M)^{Sh/Sh_i}}{1-(1+\bar{B}_M)^{Sh/Sh_i}}\right], \text{ if} 1+B_{M,i} > 0;$$

$$\dot{m}_i = \dot{m}\left[\frac{Y_i^\infty + Y_i^s (1+\bar{B}_M)^{Sh/Sh_i}}{1+(1+\bar{B}_M)^{Sh/Sh_i}}\right], \text{ if} 1+B_{M,i} < 0.$$

In this way, for each droplet composition of Table 12.3, a total of 80 simulations are performed, corresponding to the 2 possible diameters, 2 possible temperatures at infinity, 2 possible velocities at infinity, 2 possible compositions at infinity, each of which are carried out for the 5 different mass transfer models.

12.2 Results

12.2.1 Ethanol-Water droplets

We first analyze the non-convective results for droplets composed of ethanol and water (E/W). In Fig. 12.5, results are shown for the Air-E/W configuration with starting diameter, $\mathcal{D}_{d,0} = 10\mu m$ and surrounding temperature $T^{\infty} = 300.01K$. Overall, we see that all models agree fairly well among themselves with the exception of Law's model. However, the preferential evaporation is still captured for all models, water evaporating first. It should be noted that this particular case does not have condensation (absolute value operator not necessary), nor convection ($Sh = Sh_i = 2$), which means that the traditional expression of Law's model Eq. 9.11 is retrieved. Even though the global mass transfer rate seems to be acceptable, this comes at the cost of underprecting the ethanol mass transfer rate and overpredicting the water mass transfer rate. The heat transfer rate also shows some impact, with the transient temperature being affected. The final droplet temperature is in agreement between all models.

In Fig. 12.6 we now have the same situation but with fuel vapors in the atmosphere i.e. the V-E/W configuration. In general, not much difference is seen comparing it to Fig. 12.5 for the pure air scenario. Law's model seems to better capture the mass transfer rates when compared to the previous case, except for the very beginning where we see that it predicts a lower, steeper evaporation rate. This in turn leads to an overshoot for the heat transfer rate and therefore an undershoot for the temperature. The presence of vapors in the atmosphere overall increases significantly the droplet lifetime, and the differences, even though small, propagate and become noticeable in terms of the surface evolution for Law's model.

In Fig. 12.7 we now investigate a high temperature, pure air scenario. Comparing it with Fig. 12.5 for the low temperature equivalent, it is now possible to see a bigger gap between all models, especially the Law and the extended Ebrahimian-Habchi ones. Only a slight difference is visible between the extended Tonini-Cossali and Newbold-Amundson formulations, and both of them also are good approximations for the Stefan-Maxwell reference. A more complex physical situation is depicted, and Law and Ext-EH consistently overestimate then underestimate the ethanol mass transfer rate (and vice-versa for the water mass transfer rate), with the Law model having more deviations. Still, the Law model reaches the same final droplet temperature whereas the Ext-EH overpredicts it. The same conclusions for larger diameters (not shown here). Here, we reiterate that the main differences from the extended Ebrahimian-Habchi model to the extended Tonini-Cossali and Newbold-Amundson ones for the non-convective case are two-fold. First, it does not make a second spatial integration, which means that the properties are evaluated only at the surface of the droplet. Therefore, there is no need to use the one-third rule, or any other spatial averaging rule. Secondly, it takes into account the correction velocity. However, upon inspecting Figs. 12.5 and 12.6, we saw that differences between all models were negligeable for the low-temperature scenario

whereas they start to become impactful here. Therefore, a greater difference between the Ext-EH model towards the others is indeed expected for this high temperature scenario since other models will have properties evaluated at a reference temperature superior than that at the surface of the droplet. This also suggests that for this droplet composition the correction velocity does not have a strong impact, or else differences would also appear on the low-temperature scenario.

12.2.2 Acetone-Water droplets

Results for the acetone and water (A/W) droplet are now displayed in Figs. 12.8-12.9, where we vary the surrounding temperature and keep other parameters constant. The same trends were observed for the variation of surrounding composition and initial diameter as those for the E/W droplet, so theses results are not shown. Law's model seems to perform slightly better here for the baseline case in Fig. 12.8 when compared to the baseline E/W case of Fig. 12.5. For the high temperature case, still both Law and Ext-EH preserve the tendency of greater discrepancy, with Ext-EH again predicting a higher final droplet temperature due to the heat transfer rate sensibility. In general we also see similar droplet lifetimes when compared to the E/W droplet, since water tends to overlast both more volatile fuels.

12.2.3 Ethanol-Acetone-Water droplets

In Figs. 12.10, 12.11 and 12.12 results are displayed for the non-convective ternary ethanol, acetone and water (E/A/W) droplet. In Fig. 12.10 we first have the baseline case, with initial diameter $\mathcal{D}_{d,0} = 10\mu m$ and surrounding temperature $T^{\infty} = 300.01$. The same trend is observed: all models perform reasonably well with the exception of the Law model. Interestingly, for the Law model, the mass transfer rate of acetone has the best prediction when compared to that of ethanol and water, even when all of these species are present together.

In Fig. 12.11, we see the same behavior as before, namely, the presence of vapors tends to damp the differences between models. All models succesfully capture the steep behavior for all species at the beggining of the droplets lifetime, particularly the ethanol mass transfer rate, even though the Law model overshoots it by some margin. In Fig. 12.12 we now see the impact of the high temperature. Again, the same conclusions can be drawn: the extended Ebrahimian-Habchi model starts to veer away, but not so much as the Law model, with the exception of the final droplet temperature. Still, both the extended TC and NA models behave quite similarly between themselves and in comparison to the Stefan-Maxwell reference.

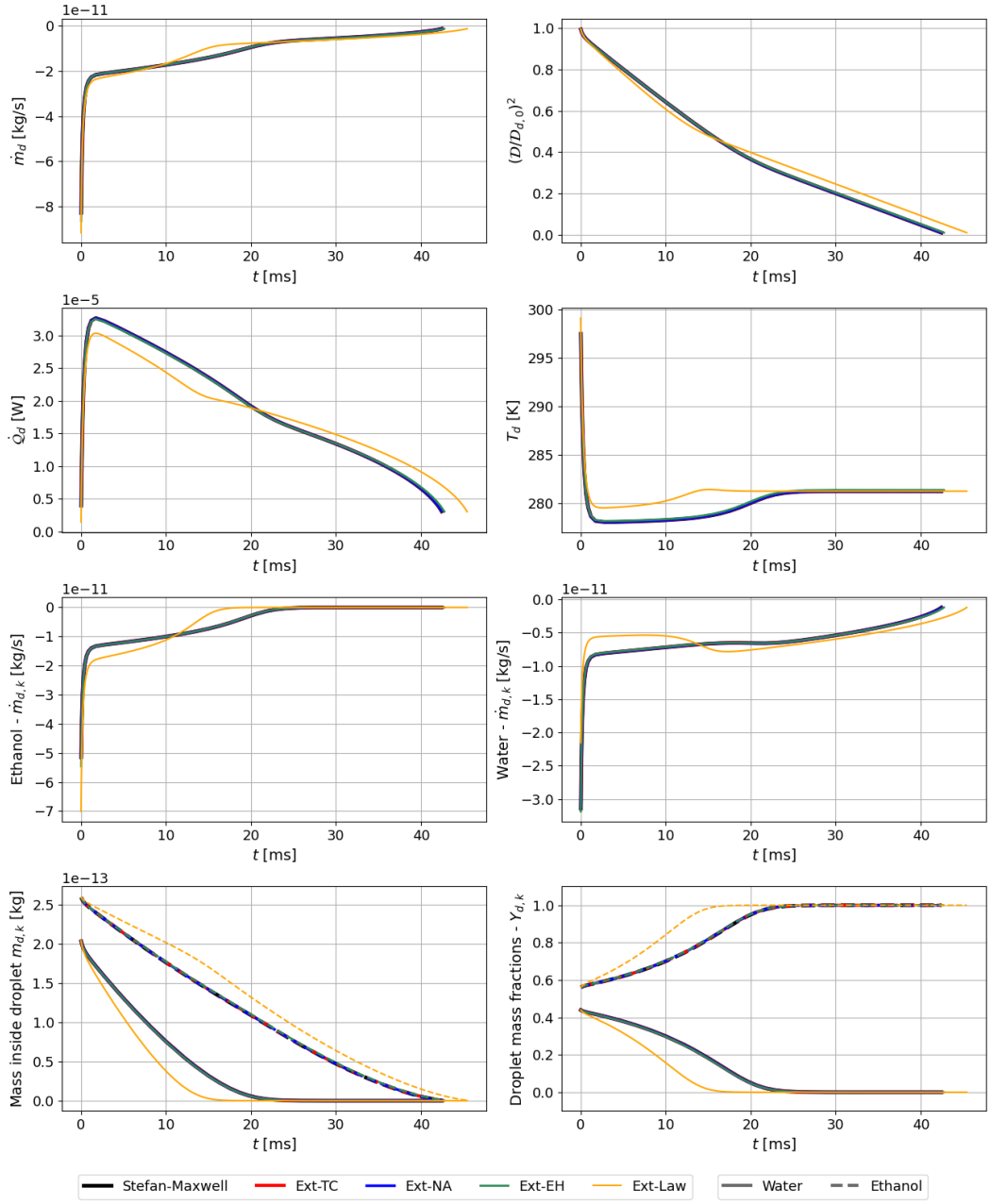

Figure 12.5: Simulation of Air-E/W configuration (see Table 12.4) with common conditions of Table 12.1 and initial diameter $\mathcal{D}_{d,0} = 10\mu m$, surrounding temperature $T^{\infty} = 300.01K$ and surrounding velocity $U^{\infty} = 0m/s$. Results displayed for the global mass transfer rate $\dot{m}$, the normalized surface $(\mathcal{D}_d/\mathcal{D}_{d,0})^2$, the heat transfer rate $\dot{\mathcal{Q}}$, the droplet's temperature T_d, the mass transfer rates $\dot{m}_k$ of ethanol and water, the masses of ethanol and water m_k inside the droplet and its corresponding mass fractions $Y_{d,k}$.

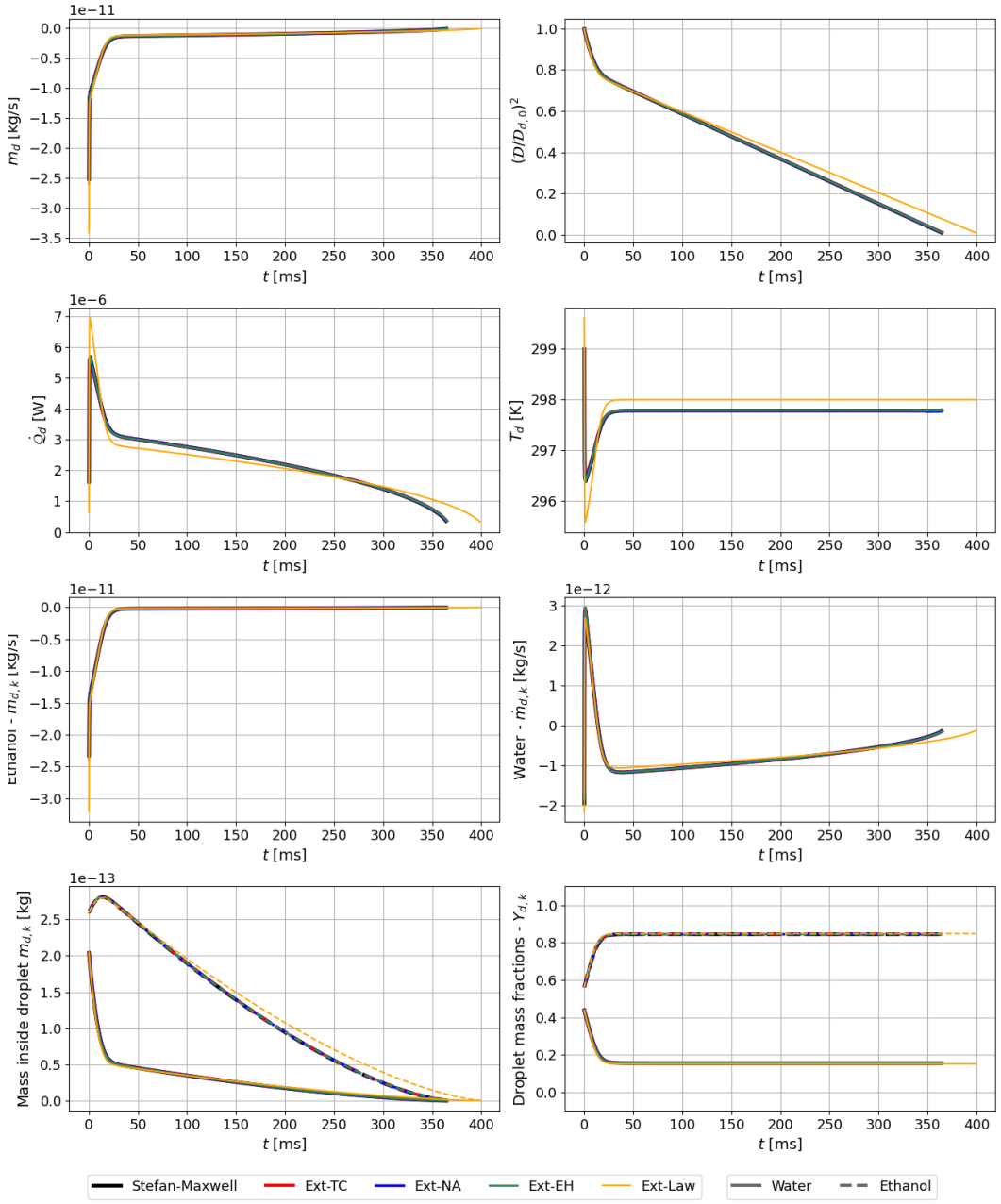

Figure 12.6: Simulation of V-E/W configuration (see Table 12.4) with common conditions of Table 12.1 and initial diameter $\mathcal{D}_{d,0} = 10\mu m$, surrounding temperature $T^{\infty} = 300.01K$ and surrounding velocity $U^{\infty} = 0m/s$. Results displayed for the global mass transfer rate $\dot{m}$, the normalized surface $(\mathcal{D}_d/\mathcal{D}_{d,0})^2$, the heat transfer rate $\dot{\mathcal{Q}}$, the droplet's temperature T_d, the mass transfer rates $\dot{m}_k$ of ethanol and water, the masses of ethanol and water m_k inside the droplet and its corresponding mass fractions $Y_{d,k}$.

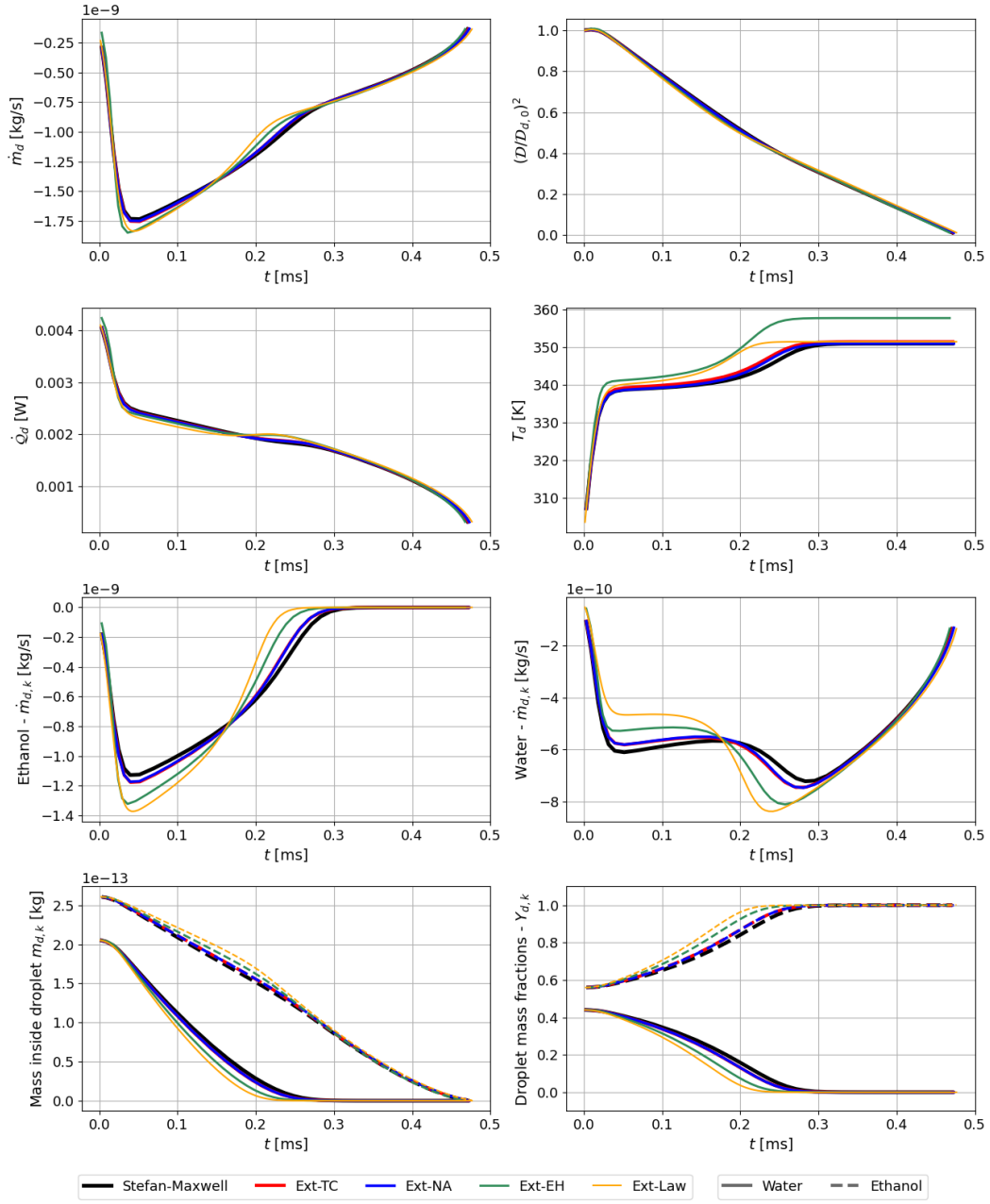

Figure 12.7: Simulation of Air-E/W configuration (see Table 12.4) with common conditions of Table 12.1 and initial diameter $\mathcal{D}_{d,0} = 10\mu m$, surrounding temperature $T^{\infty} = 1600K$ and surrounding velocity $U^{\infty} = 0m/s$. Results displayed for the global mass transfer rate $\dot{m}$, the normalized surface $(\mathcal{D}_d/\mathcal{D}_{d,0})^2$, the heat transfer rate $\dot{\mathcal{Q}}$, the droplet's temperature T_d, the mass transfer rates $\dot{m}_k$ of ethanol and water, the masses of ethanol and water m_k inside the droplet and its corresponding mass fractions $Y_{d,k}$.

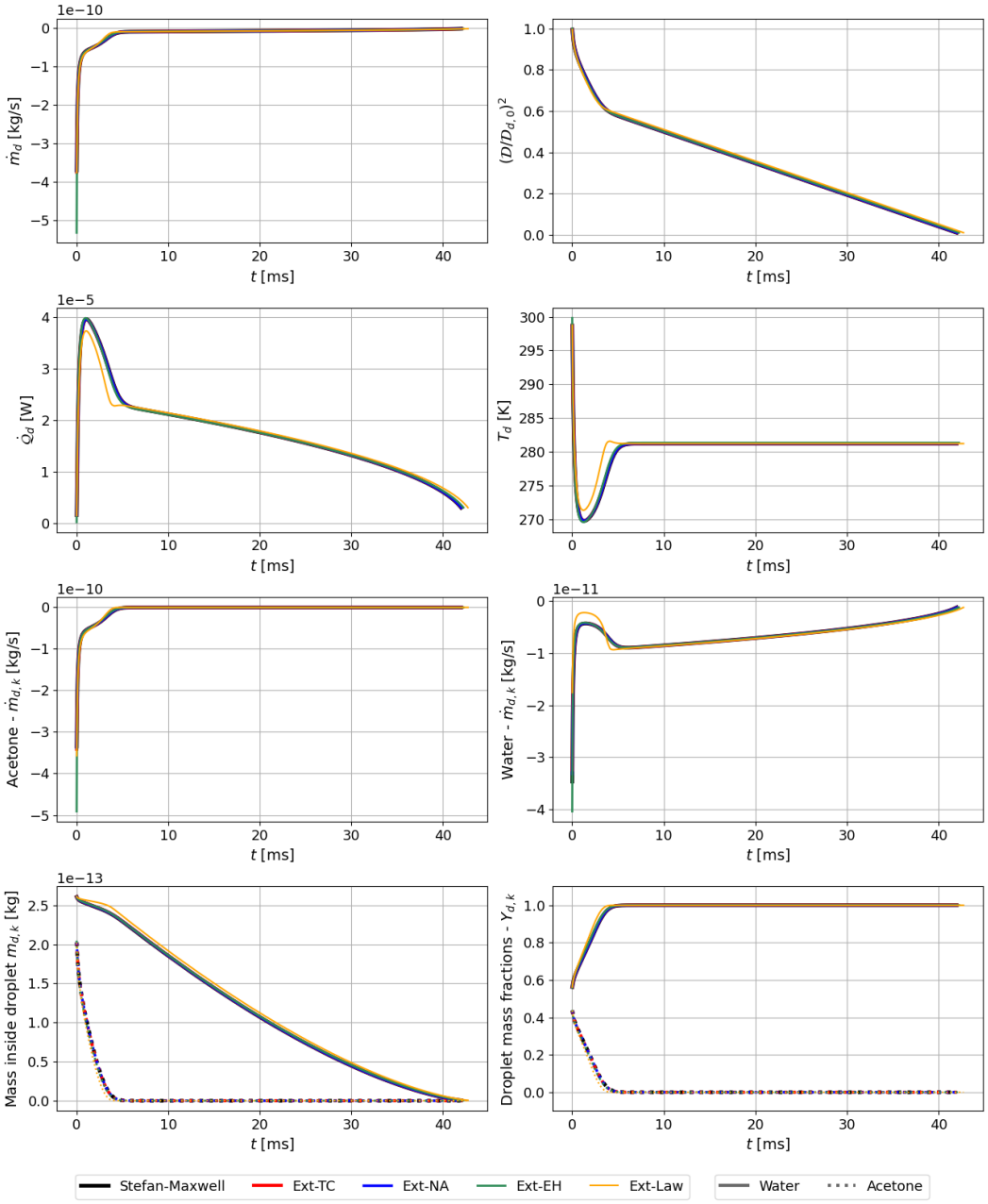

Figure 12.8: Simulation of Air-A/W configuration (see Table 12.4) with common conditions of Table 12.1 and initial diameter $\mathcal{D}_{d,0} = 10\mu m$, surrounding temperature $T^{\infty} = 300.01K$ and surrounding velocity $U^{\infty} = 0m/s$. Results displayed for the global mass transfer rate $\dot{m}$, the normalized surface $(\mathcal{D}_d/\mathcal{D}_{d,0})^2$, the heat transfer rate $\dot{\mathcal{Q}}$, the droplet's temperature T_d, the mass transfer rates $\dot{m}_k$ of acetone and water, the masses of acetone and water m_k inside the droplet and its corresponding mass fractions $Y_{d,k}$.

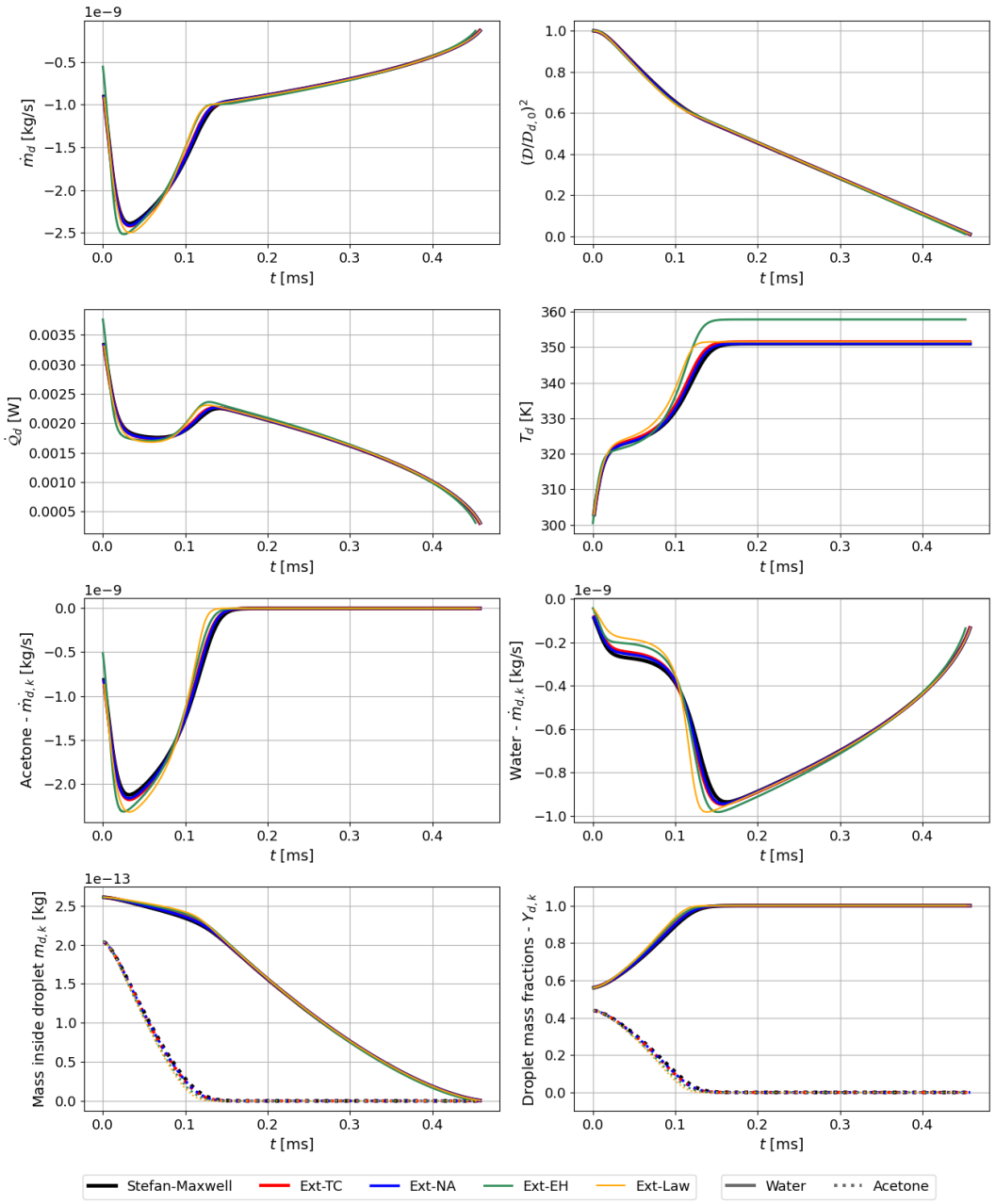

Figure 12.9: Simulation of Air-A/W configuration (see Table 12.4) with common conditions of Table 12.1 and initial diameter $\mathcal{D}_{d,0} = 10\mu m$, surrounding temperature $T^{\infty} = 1600K$ and surrounding velocity $U^{\infty} = 0m/s$. Results displayed for the global mass transfer rate $\dot{m}$, the normalized surface $(\mathcal{D}_d/\mathcal{D}_{d,0})^2$, the heat transfer rate $\dot{\mathcal{Q}}$, the droplet's temperature T_d, the mass transfer rates $\dot{m}_k$ of acetone and water, the masses of acetone and water m_k inside the droplet and its corresponding mass fractions $Y_{d,k}$.

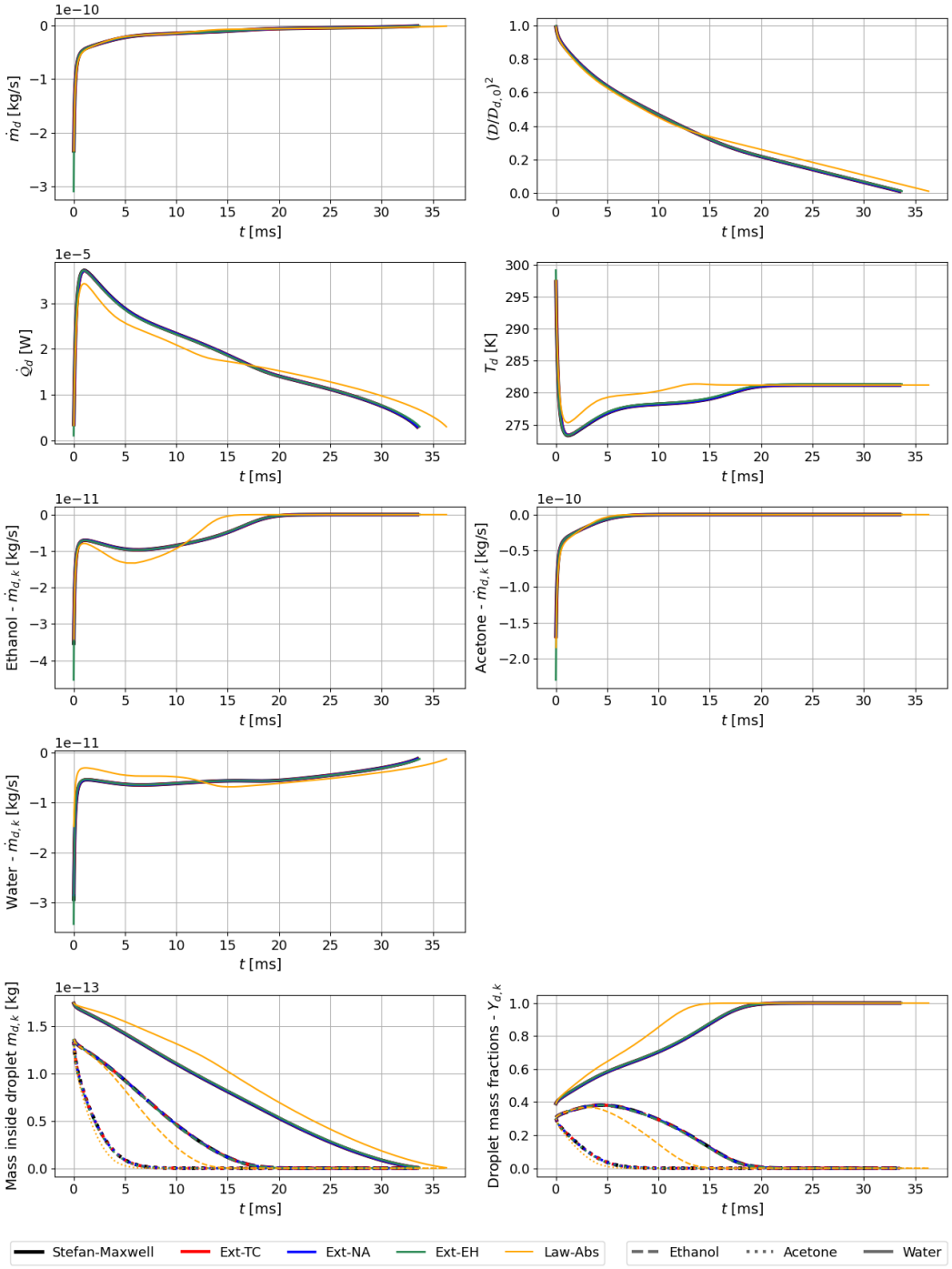

Figure 12.10: Simulation of Air-E/A/W configuration (see Table 12.4) with common conditions of Table 12.1 and initial diameter $\mathcal{D}_{d,0} = 10\mu m$, surrounding temperature $T^{\infty} = 300.01$ and surrounding velocity $U^{\infty} = 0m/s$. Results displayed for the global mass transfer rate $\dot{m}$, the normalized surface $(\mathcal{D}_d/\mathcal{D}_{d,0})^2$, the heat transfer rate $\dot{\mathcal{Q}}$, the droplet's temperature T_d, the mass transfer rates $\dot{m}_k$ of ethanol, acetone and water, the masses of ethanol, acetone and water m_k inside the droplet and its corresponding mass fractions $Y_{d,k}$.

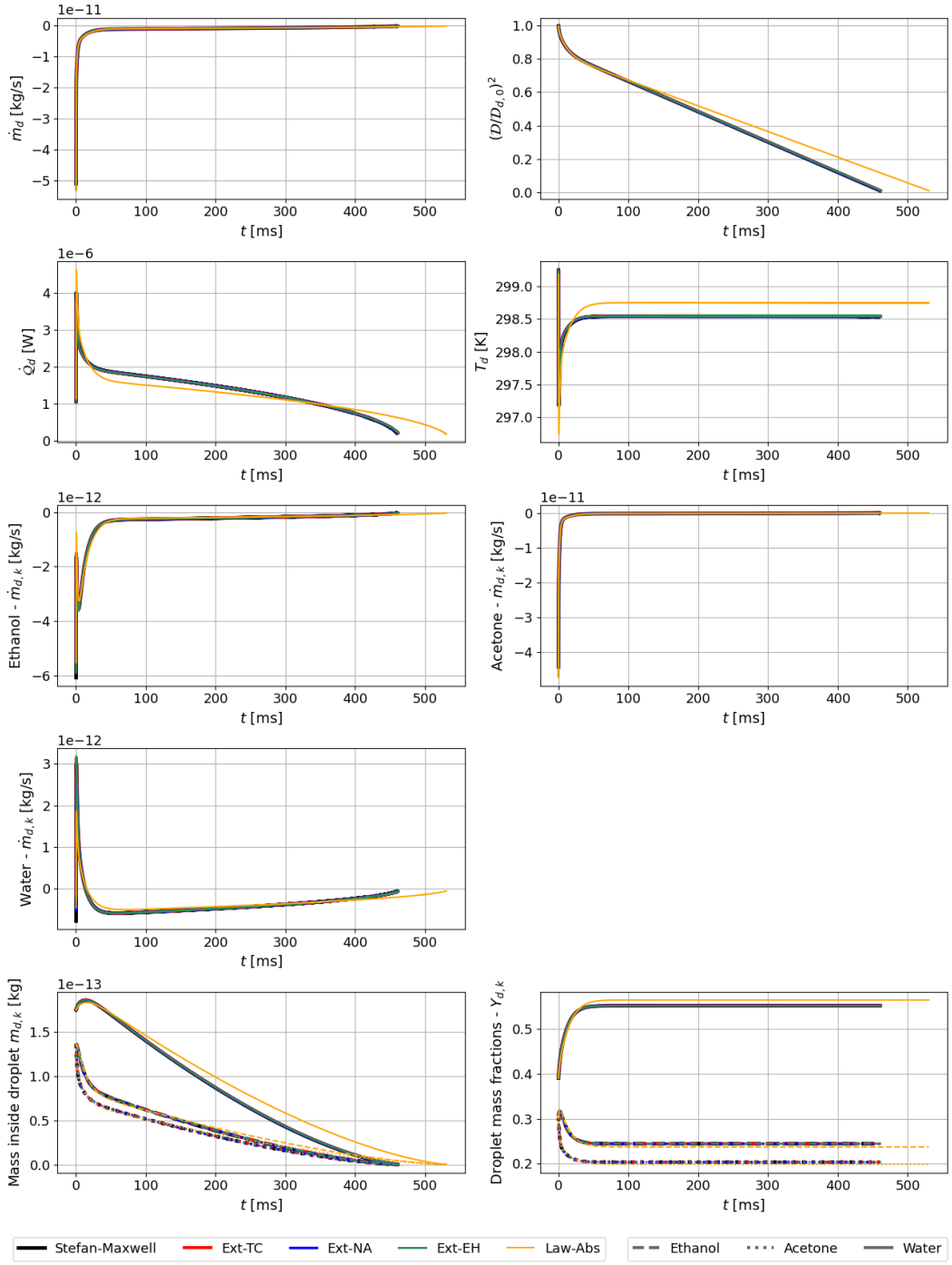

Figure 12.11: Simulation of V-E/A/W configuration (see Table 12.4) with common conditions of Table 12.1 and initial diameter $\mathcal{D}_{d,0} = 10\mu m$, surrounding temperature $T^{\infty} = 300.01K$ and surrounding velocity $U^{\infty} = 0m/s$. Results displayed for the global mass transfer rate $\dot{m}$, the normalized surface $(\mathcal{D}_d/\mathcal{D}_{d,0})^2$, the heat transfer rate $\dot{\mathcal{Q}}$, the droplet's temperature T_d, the mass transfer rates $\dot{m}_k$ of ethanol, acetone and water, the masses of ethanol, acetone and water m_k inside the droplet and its corresponding mass fractions $Y_{d,k}$.

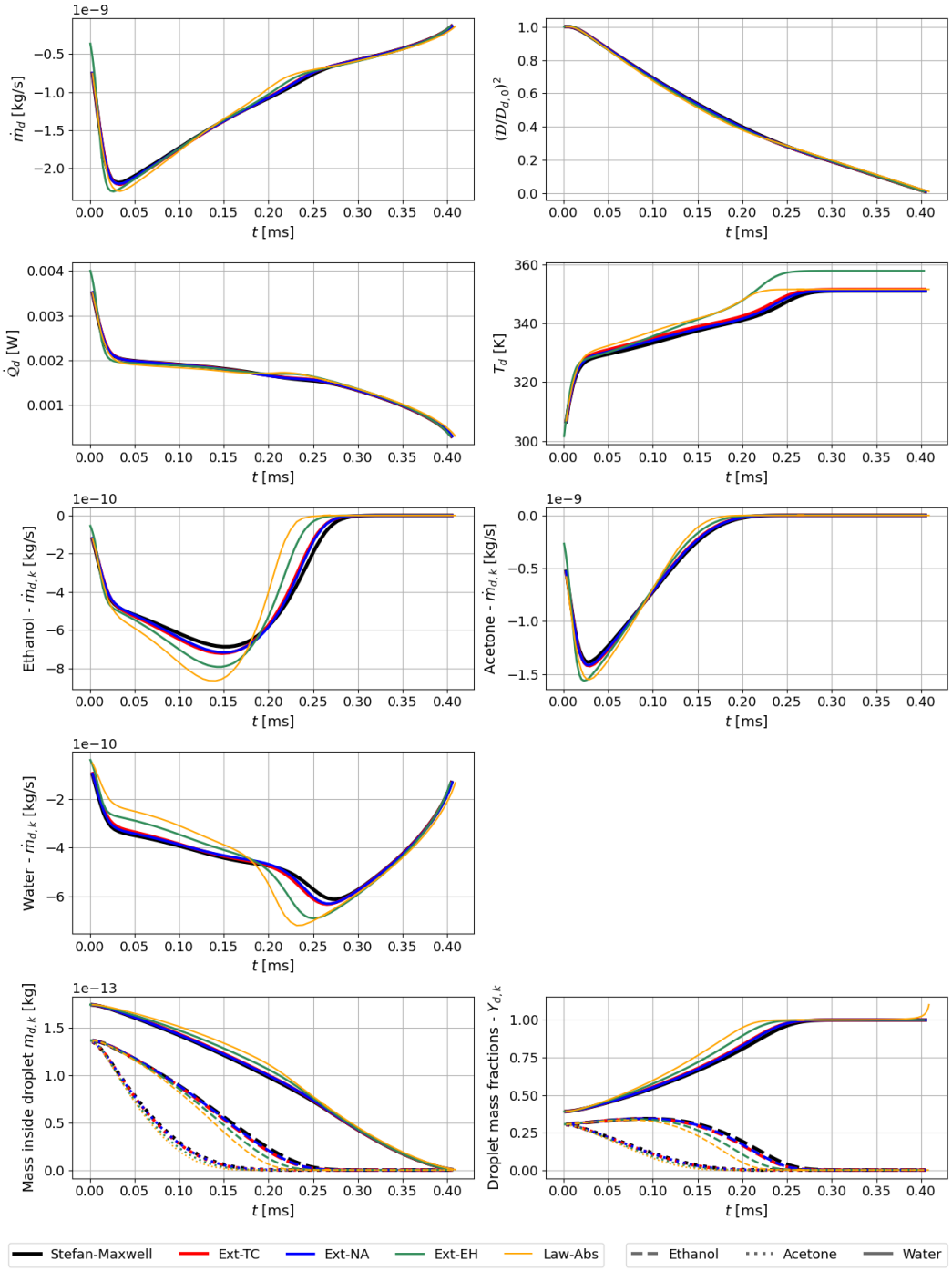

Figure 12.12: Simulation of Air-E/A/W configuration (see Table 12.4) with common conditions of Table 12.1 and initial diameter $\mathcal{D}_{d,0} = 10\mu m$, surrounding temperature $T^{\infty} = 1600K$ and surrounding velocity $U^{\infty} = 0m/s$. Results displayed for the global mass transfer rate $\dot{m}$, the normalized surface $(\mathcal{D}_d/\mathcal{D}_{d,0})^2$, the heat transfer rate $\dot{Q}$, the droplet's temperature T_d, the mass transfer rates $\dot{m}_k$ of ethanol, acetone and water, the masses of ethanol, acetone and water m_k inside the droplet and its corresponding mass fractions $Y_{d,k}$.

As for convective results, there is a first important consideration that can be seen in Fig. 12.13. Towards the end of the droplet lifetime, we see that the Ext-Law model starts to have mass fractions superior to one (or even negative). This shows that this analytical extension can actually be ill-posed, and this is due to the relationship between the global Sherwood number and the Sherwood number of each individual species. To better understand this, we look at Eq. 10.9a (since in this case the absolute value operator was not needed). When summing up the LHS and the RHS for all species, the global mass transfer rate cancels out and we must have:

$$1 = \sum_{k=1}^{N} \left[\frac{Y_k^{\infty} - Y_k^s (1 + \bar{B}_M)^{Sh/Sh_k}}{1 - (1 + \bar{B}_M)^{Sh/Sh_k}} \right]. \tag{12.1}$$

The RHS above can be expanded and the whole expression simplified to:

$$\sum_{k=1}^{N} \left[\frac{Y_k^{\infty} - Y_k^s}{1 - (1 + \bar{B}_M)^{Sh/Sh_k}} \right] = 0. \tag{12.2}$$

It is then possible to see that for this relationship to be true, a specific relationship would need to take place between the Sherwood numbers. In general, it is not possible to guarantee that this holds, because these numbers are computed using average properties for the whole mixture (for the global Sherwood) versus individual properties, and this becomes even more complex if the Sherwood numbers are corrected to take Stefan-flow effects into account, as using the Abramzon-Sirignano approach leads to corrections based on the Spalding transfer numbers i.e. $\bar{B}_M$ versus $B_{M,i}$. Therefore, for convective results, we opt to only use the extension of Law's model for the absolute value, namely Eqs. 10.3 and 10.4, and for clarity we use the label "Law-Abs" when this is the case.
For the overall convective results, it was consistently seen that the small droplets with $\mathcal{D}_{d,0} = 10\mu m$ relax too quickly towards the velocity $U^{\infty} = 100 m/s$, and so differences when compared to the non-convective case are negligible. Also, the convection trends were similar when comparing the E/W, A/W and E/A/W droplets. Therefore, for simplicity we showcase in Fig. 12.14 the convective high-temperature counterpart for the $\mathcal{D}_{d,0} = 100\mu m$ E/A/W droplet, since for the bigger droplet a more noticeable impact was seen. Qualitatively, it is possible to see slight behavior changes, with both ethanol and acetone "compressed" into a quicker relative evaporation. The differences between both Law and Ext-EH and the other models also seem to relatively be slightly more pronounced. Still, the effect of convection is not as pronounced as that of temperature, in generating differences between models.

12.2.4 Ethanol-Dodecane-Water droplets

Now, in Figs. 12.15,12.16 and 12.17 results are displayed for the more complex scenario, the ethanol, n-dodecane and water droplet. This case is more complex because of the interactions between the molecular structures in the liquid phase, which here is taken into account via the UNIFAC method. Therefore, for simplicity we exclude Law's model from

the analysis since it was previously shown that it already was not able to consistently capture the inherent physics, and this is even more true for this case.
In Fig. 12.15 we have the baseline simulation, with pure air in the surrounding atmosphere, initial diameter $\mathcal{D}_{d,0} = 10\mu m$, surrounding temperature $T^{\infty} = 300.01$ and surrounding velocity $U^{\infty} = 0m/s$. It is possible to see that all models present a fair agreement, being indistinguishable in all metrics. The simulation was cut short because the droplet eventually becomes pure n-dodecane and, due to the low temperature, its mass transfer rate becomes really small.

In Fig. 12.16 we change to the vapor rich atmosphere. This time, the Ext-EH presents slight differences, consistently predicting earlier and sharper results for the mass transfer rates. Interestingly, the Ext-TC model this time around loses the Stefan-Maxwell reference, whereas the Ext-NA model is able to follow it. The difference, even though also slight, is mostly observed on the heat transfer rate.

Then, in Fig. 12.17 we now go back to the pure air atmosphere to see the impact of the high temperature environment, with $T^{\infty} = 1600K$. Here all models present substantial differences, which is not the expected trend from the other droplet compositions. In general, all models are able to capture the underlying physics, in which a sudden increase on the water mass transfer rate is observed, followed by a sudden decrease on the ethanol mass transfer rate, with a steady decrease then sudden increase of the n-dodecane mass transfer rate. However, we see that the Ext-EH model predicts this series of events earlier than the Ext-TC formulation, which is then earlier than the Ext-NA formulation which finally manifests earlier than the Stefan-Maxwell reference. The present physics leads to a complex behavior for the global mass transfer rate and the heat transfer rate, but all models with the exception of Ext-EH predict the same final temperature, as seen for previous droplets. We also see that the droplet becomes composed of pure water towards the end of its lifetime.

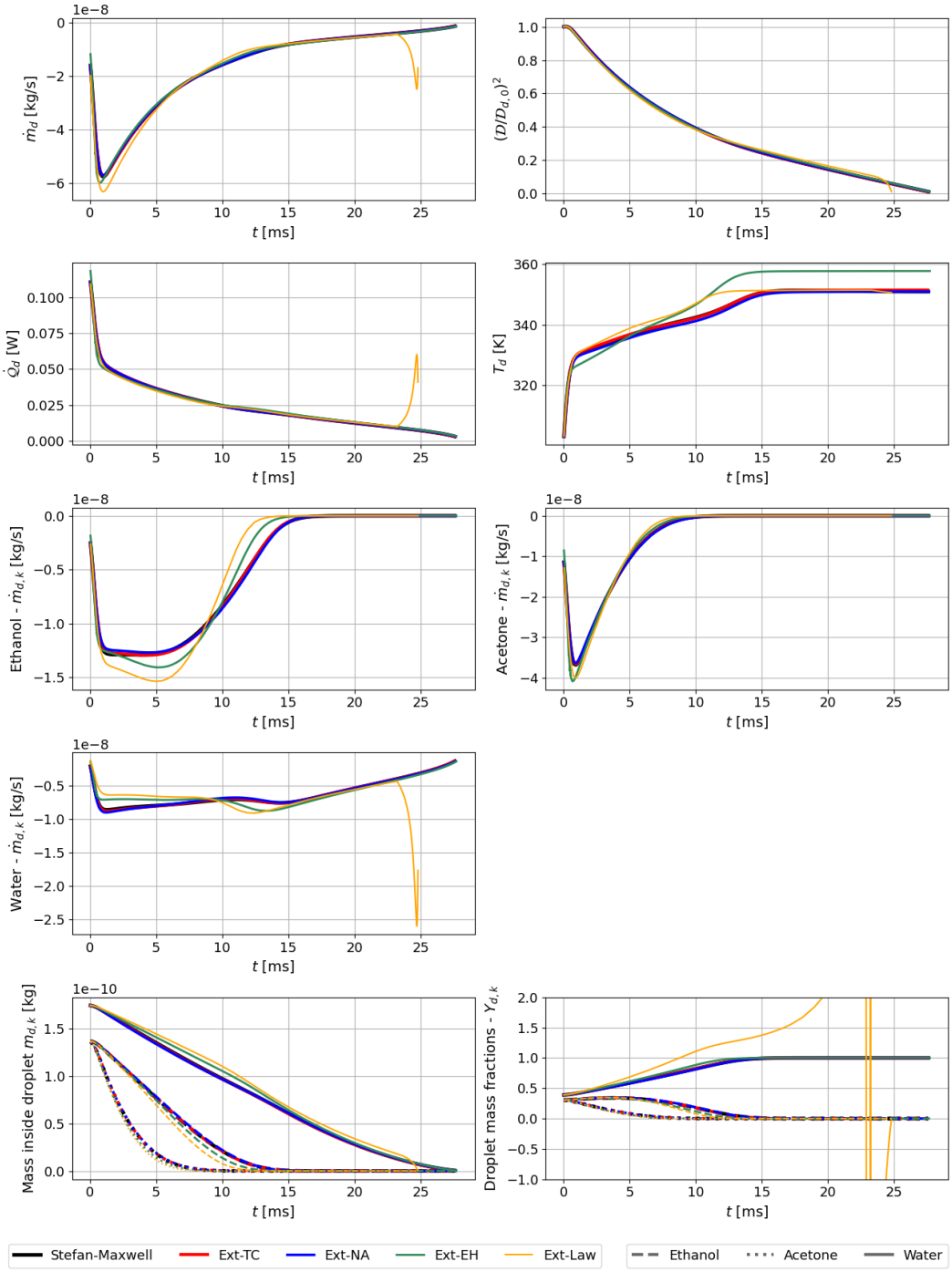

Figure 12.13: Simulation of Air-E/A/W configuration (see Table 12.4) with common conditions of Table 12.1 and initial diameter $\mathcal{D}_{d,0} = 100\mu m$, surrounding temperature $T^{\infty} = 1600K$ and surrounding velocity $U^{\infty} = 100m/s$. Results displayed for the global mass transfer rate $\dot{m}$, the normalized surface $(\mathcal{D}_d/\mathcal{D}_{d,0})^2$, the heat transfer rate $\dot{\mathcal{Q}}$, the droplet's temperature T_d, the mass transfer rates $\dot{m}_k$ of ethanol, acetone and water, the masses of ethanol, acetone and water m_k inside the droplet and its corresponding mass fractions $Y_{d,k}$.

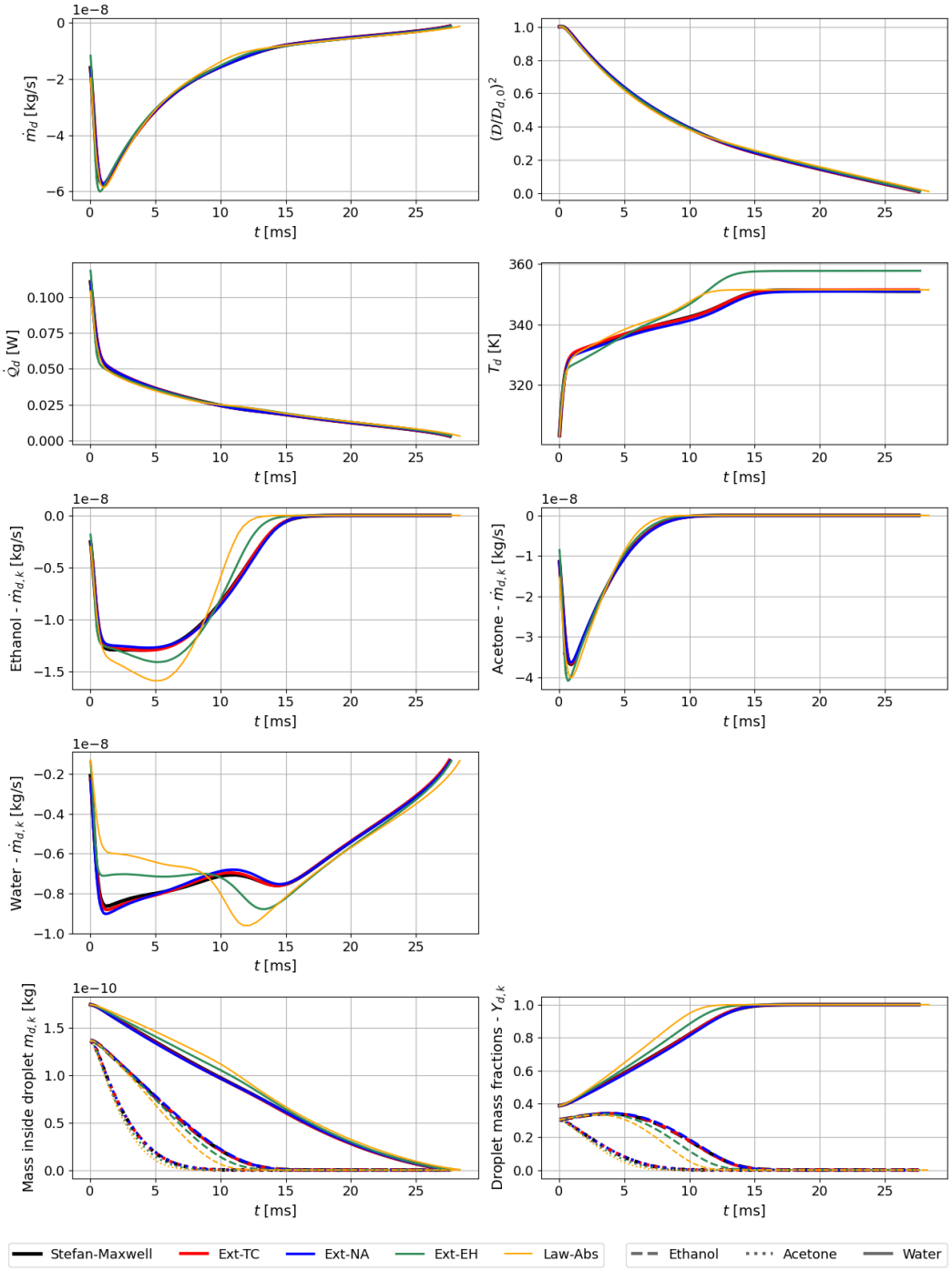

Figure 12.14: Simulation of Air-E/A/W configuration (see Table 12.4) with common conditions of Table 12.1 and initial diameter $\mathcal{D}_{d,0} = 100\mu m$, surrounding temperature $T^\infty = 1600K$ and surrounding velocity $U^\infty = 100m/s$. Results displayed for the global mass transfer rate $\dot{m}$, the normalized surface $(\mathcal{D}_d/\mathcal{D}_{d,0})^2$, the heat transfer rate $\dot{Q}$, the droplet's temperature T_d, the mass transfer rates $\dot{m}_k$ of ethanol, acetone and water, the masses of ethanol, acetone and water m_k inside the droplet and its corresponding mass fractions $Y_{d,k}$.

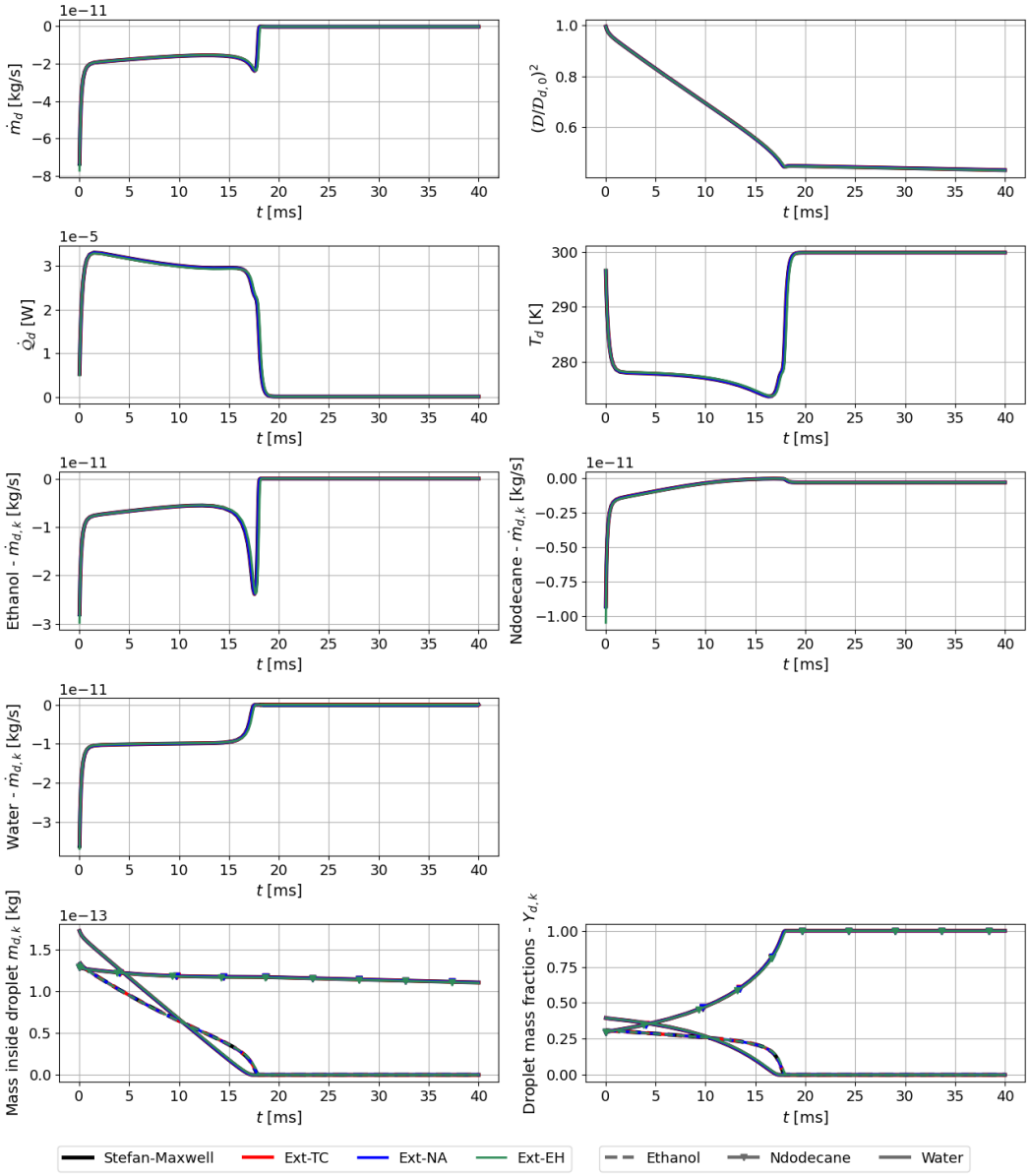

Figure 12.15: Simulation of Air-E/D/W configuration (see Table 12.4) with common conditions of Table 12.1 and initial diameter $\mathcal{D}_{d,0} = 10\mu m$, surrounding temperature $T^{\infty} = 300.01K$ and surrounding velocity $U^{\infty} = 0m/s$. Results displayed for the global mass transfer rate $\dot{m}$, the normalized surface $(\mathcal{D}_d/\mathcal{D}_{d,0})^2$, the heat transfer rate $\dot{\mathcal{Q}}$, the droplet's temperature T_d, the mass transfer rates $\dot{m}_k$ of ethanol, n-dodecane and water, the masses of ethanol, n-dodecane and water m_k inside the droplet and its corresponding mass fractions $Y_{d,k}$.

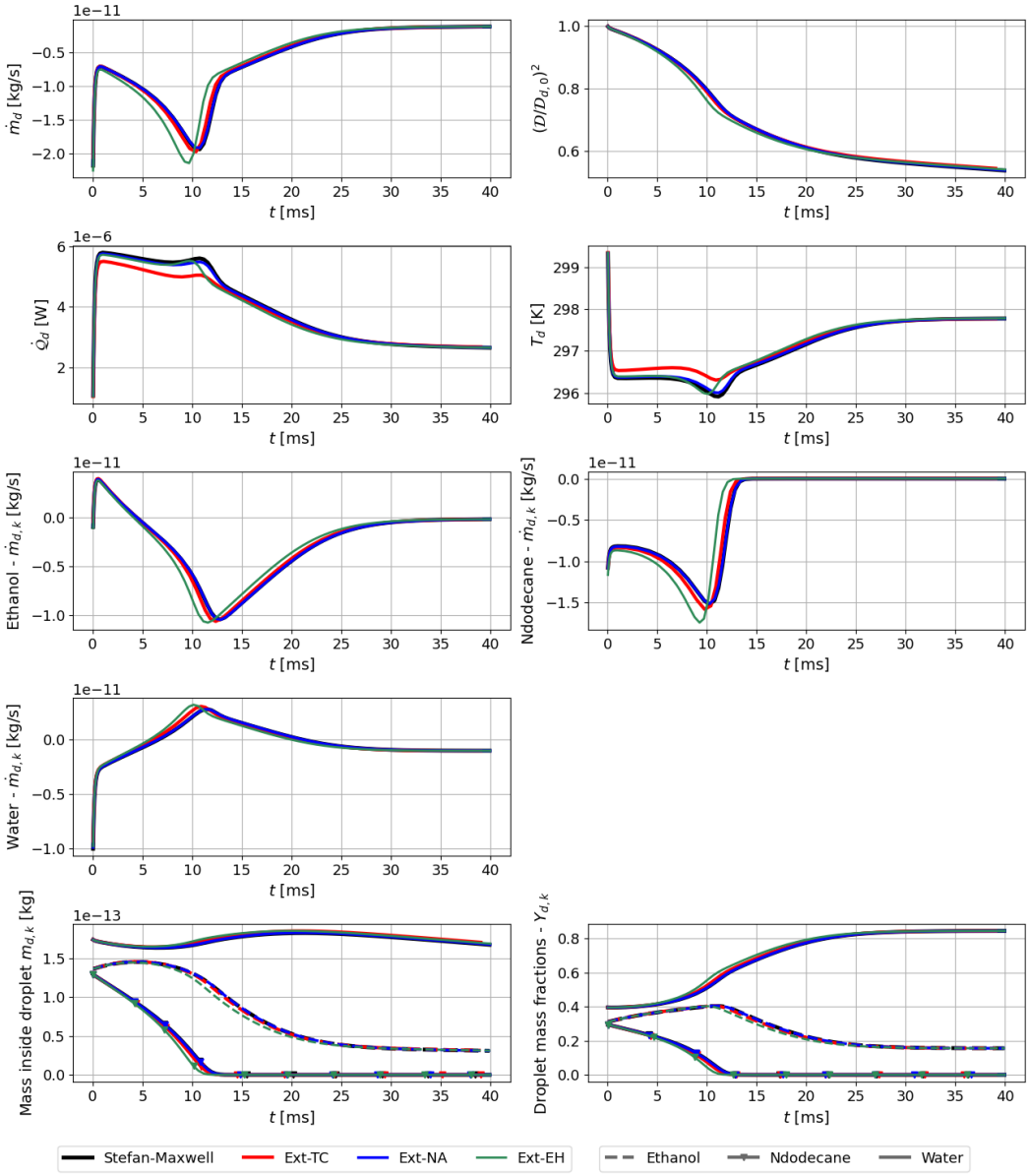

Figure 12.16: Simulation of Air-E/D/W configuration (see Table 12.4) with common conditions of Table 12.1 and initial diameter $\mathcal{D}_{d,0} = 10\mu m$, surrounding temperature $T^{\infty} = 1600K$ and surrounding velocity $U^{\infty} = 0m/s$. Results displayed for the global mass transfer rate $\dot{m}$, the normalized surface $(\mathcal{D}_d/\mathcal{D}_{d,0})^2$, the heat transfer rate $\dot{\mathcal{Q}}$, the droplet's temperature T_d, the mass transfer rates $\dot{m}_k$ of ethanol, n-dodecane and water, the masses of ethanol, n-dodecane and water m_k inside the droplet and its corresponding mass fractions $Y_{d,k}$.

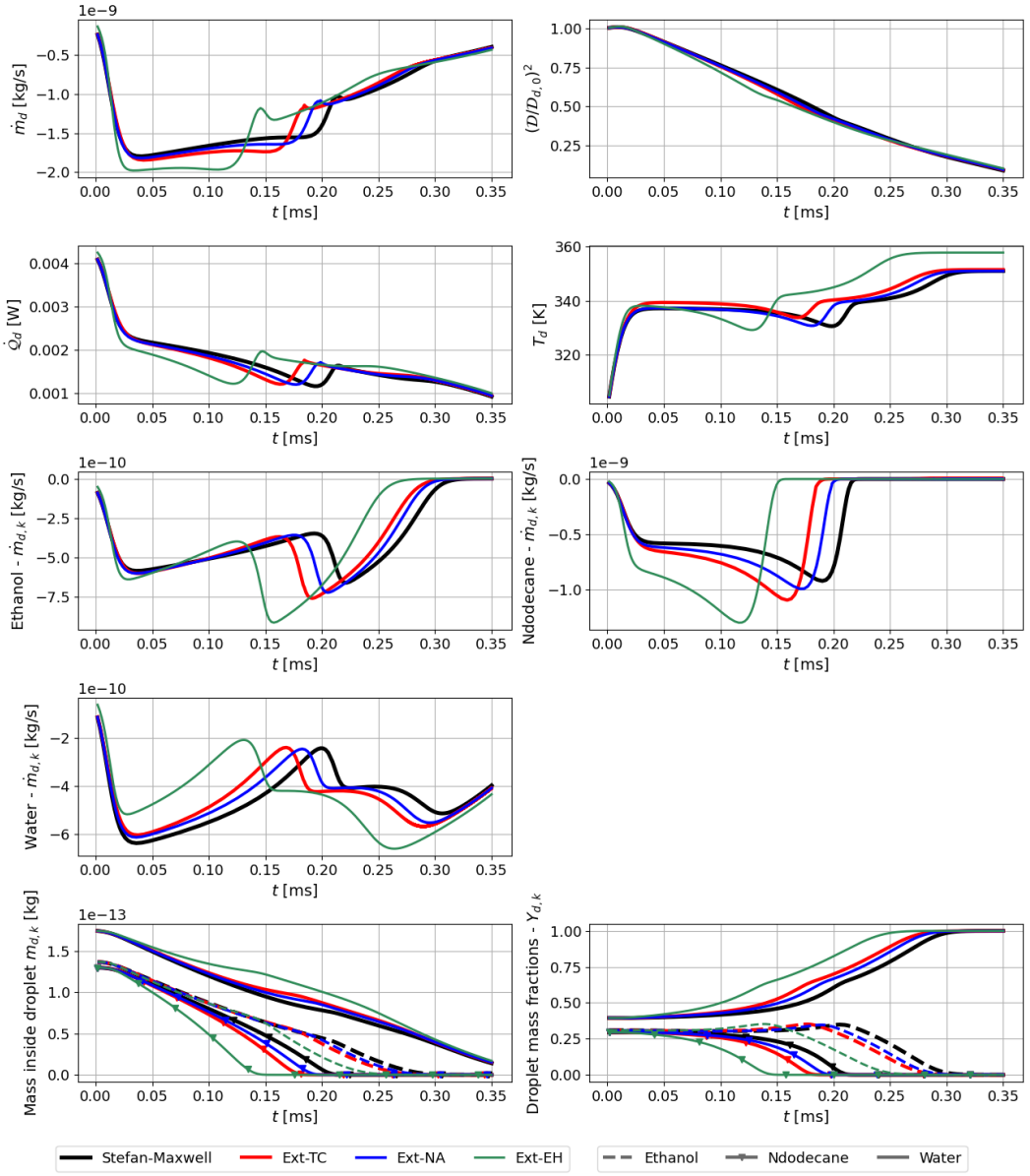

Figure 12.17: Simulation of V-E/D/W configuration (see Table 12.4) with common conditions of Table 12.1 and initial diameter $\mathcal{D}_{d,0} = 10\mu m$, surrounding temperature $T^{\infty} = 300.01K$ and surrounding velocity $U^{\infty} = 0m/s$. Results displayed for the global mass transfer rate $\dot{m}$, the normalized surface $(\mathcal{D}_d/\mathcal{D}_{d,0})^2$, the heat transfer rate $\dot{\mathcal{Q}}$, the droplet's temperature T_d, the mass transfer rates $\dot{m}_k$ of ethanol, n-dodecane and water, the masses of ethanol, n-dodecane and water m_k inside the droplet and its corresponding mass fractions $Y_{d,k}$.

12.3 Summary

In chapter 10, extensions to the most used discrete component models in the litterature were offered. Also, in chapter 11 the Wilke model for the diffusion coefficient was shown to be the most accurate one, with respect to the Stefan-Maxwell reference. Having eliminated this degree of freedom, in this chapter we studied an array of different configurations representative of extreme spray combustion scenarios.

In general, it was found that the extension of Tonini and Cossali's model, as well as the extension to Newbold and Amundson's model were the best approximations to the reference. Also, it was shown that the convection extension for Law's model is ill-defined, due to the relationship between the global and individual Sherwood numbers. Still, Law's model consistently yielded the largest deviations, even for non-convective and non-condensing regimes. The second largest deviations were consistently seen for the extension of the Ebrahimian and Habchi model; however, it should be reiterated that the expression for the Sherwood number there used should probably not be the same as the ones used for other mass transfer models, and so this can possibly indicate where a correction is due. Therefore, considering the current structure of the models as described in this manuscript, both the mass (Ext-TC) and molar (Ext-NA) formulations are recommended. To choose between them, a preliminary study can be carried out, if possible, to determine which among the mass or molar densities vary less spatially, in order to be coherent with the simplifying hypothesis needed for their derivation.

Concerning numerical resources, in Table 12.18, we see the average running times for the ethanol, acetone and water (E/A/W) droplet investigated in this chapter. Two averages are offered, since there were two edge cases with fuel vapor at infinity where all models took considerably more time due to the complex physics. When including edge cases, all models fall within 8-11% of the computational time compared to the Stefan-Maxwell reference; excluding the edge cases, this ratio rises to 18-19 %, with a lesser difference between models. The conclusion here is that Law's model should not be used since it produces worse physics with a similar computational time, possible due to the slow convergence to the required tolerance (the same for the numerical integration of all models). Among the three other candidates, they all have the same numerical cost generally, and so depending on the application and/or the underlying hypotheses, any one could be preferred at least in terms of numerical costs.

Stefan-Maxwell average run-time	$t_{avg} = 74.4s$
Ext-TC average run-time	$t_{avg} = 7.9s$
Ext-NA average run-time	$t_{avg} = 7.5s$
Ext-EH average run-time	$t_{avg} = 6.3s$
Law-Abs average run-time	$t_{avg} = 6.1s$
Stefan-Maxwell average run-time excl. edge cases	$t_{avg} = 15.5s$
Ext-TC average run-time excl. edge cases	$t_{avg} = 3.0s$
Ext-NA average run-timeexcl. edge cases	$t_{avg} = 2.8s$
Ext-EH average run-time excl. edge cases	$t_{avg} = 2.9s$
Law-Abs average run-time excl. edge cases	$t_{avg} = 2.8s$

Figure 12.18: Average run time metrics for E/A/W droplet simulations of Chap. 8.

Conclusions and Perspectives

One of the main objectives of this manuscript was to provide a starting reference for the derivation of droplet phase-change models. Indeed, different authors may have different visions as to where exactly the derivation procedure should start, and so a single procedure would be beneficial in this sense. Also, specific details of the derivation process are not always given, which can deter the comprehension of the reader. Such details may not seem of paramount importance when looking at the bigger picture. However a rigorous foundation is not only welcome, but also allows us to focus on the weaknesses of the different hypotheses, and thus, where to look to propose improvements. In this way, the conservation equations are presented in their most general form, with all core simplifications clearly stated from the beginning, and to what they translate both physically and mathematically.

These core assumptions of course already open up the door to multiple possible enhancements. For example, a natural path is the work carried out today in (Tonini and Cossali 2022), where authors extend their Stefan-Maxwell formulation to spheroidal shapes, relaxing the necessity of perfectly spherical droplets. This degree of freedom may already vastly extend the reach of droplet phase-change modelling, and so an extension to include convection effects as well as an arbitrary number of inert species as done in this manuscript for the spherical case would also enrich the discussion.

Due to the high temperature, enclosed scenarios that typically characterise spray combustion applications, radiation is also a particular point of interest where improvements can be sought. One course of strategy was suggested in (Dombrovsky, Sazhin, Sazhina, Feng, Heikal, Bardsley, and Mikhalovsky 2001) and (Abramzon and Sazhin 2006), where radiation could be injected following a simple analytical form leading to an integrated source term composed of polynomial parameters. The main advantage is the pragmatic result, that could be readily deployed in CFD codes. In (Sazhin 2017), particular attention was drawn to the fact that droplets should be regarded as semi-transparent objects for radiation developments. In this way, correlations for more substances can be obtained for the proposed model or new, alternative formulations can be developed to extend their ranges of validity.

Then, still in part I, the external closures required for the practical use of a droplet phase-

change model are listed. These encompass a whole new set of additional hypotheses, but in the end are still crucial for the obtention of simple droplet phase-change models. Particular attention was given to the Stefan-Maxwell equations, since they underpin the main challenges for multi-component droplet mass transfer models. Here, one possible avenue would be to study the impact of the correction factor $\Delta_{i,j}$ used to compute a second approximation for the binary diffusion coefficients in the multi-component mixture. It was shown in (Sandler and Mason 1968) that this factor is frequently small enough, but some overshoots can be found for some particular molecular configurations, and due to the complexity of combustion scenarios and the great distribution of droplets sizes and composition, this could represent an appreciable effect.

The vapor-liquid equilibrium was also studied following the activity coefficient approach. A natural extension here would be to consider non-equilibrium effects, including extensions for the multi-component case. A possible point of departure would be the works of (Bellan and Harstad 1987a), (Bellan and Harstad 1987b) and (Miller, Harstad, and Bellan 1998). Also, instead of activity coefficients, (Poling, Prausnitz, and O'Connell 2001) suggests that equations of state can also be used, which should provide an alternative venue of attack, specially when incorporating pressure effects. This can be seen for instance for the computation of thermodynamic properties in (Voutsas, Louli, Boukouvalas, Magoulas, and Tassios 2006), where the author compares the Peng-Robinson equation with the UNIFAC method. To this note, the $\mathcal{F}$ correction factor in the activity coefficient approach could also be modeled to include pressure variation effects. Finally, the UNIFAC methodology could benefit from a framework dedicated to spray combustion applications; it was shown that it is highly convenient, but still some formulations for the interaction groups are known to not be able to predict some relevant phenomena, such as micro-emulsions (Troncoso and Acosta 2015).

Then followed a bibliographical study concerning correlations for drag coefficients and the non-dimensional Nusselt and Sherwood numbers, for rigid and fluid spheres, including droplets with phase-change. The bibliographical evolution seems to indicate that the literature has given the required attention to this topic, but fine-tuned versions of these correlations could still be generated by using direct numerical solution (DNS) techniques for three-dimensional fully solved single droplets. The idea would be to construct a spherical volume of control, and capture volume-averaged mass and heat transfer rates and compute average Nusselt and Sherwood numbers for various regimes of Reynolds numbers, for both the convective flow and the outward/inward flow due to phase-change itself (Reynolds blowing number). These correlations would essentially allow us to still preserve the analytical simplicity and current structure of already developed spherical models, but tune them to be able to yield source terms more representative of realistic scenarios.

In Part II, the main single-component droplet heat and mass transfer models were derived. Here, the idea was to provide to the reader a concise and thorough journey into

how these models were derived. It quickly becomes clear that building blocks were progressively added, in modular fashion: first models that neglect all convection, then Stefan flow effects are added, with film theory following afterwards. This development culminates in the work of (Abramzon and Sirignano 1989), which summarises the main results not only for single-component droplet heat and mass transfer models but also important sub-models. Here, the main contribution was to use this model as a reference ground to conduct investigations for multiple correlations concerning convective applications. Again, DNS tools could be used to further solidify which choices are more suitable for ranges of applications, and universal correlations that take into account the inner recirculation and phase-change for realistic ranges of Reynolds numbers could be obtained. Also, some attention was drawn to the one-third rule and the averaging of constant spatial properties. This averaging law has typically been extended for all properties, and a similar weight is given to both temperature and composition. As shown in (Finneran 2021), this assumption is far from trivial, and further studies can be carried out, possibily also aided by DNS tools, to construct more rigorous and specific averaging laws.

In Part III, the main contribution of this manuscript is presented. A great focus was given on multi-component droplet phase-change models, since recently this has been one of the main challenges for spray combustion. First, we derived and displayed general mass and heat transfer models with respect to the diffusion velocity closure. An extension for the Stefan-Maxwell model proposed in (Tonini and Cossali 2016) was realized, providing a simpler functional expression which is able to include convection effects as well as an arbitrary number of fuel and inert species in the gaseous phase. From this derivation, multiple perspectives arise, as the different approaches for the mass transfer integration, which are most cost effective, can now be fine tuned to still capture the relevant physics. Particular emphasis was also given to the general formulation obtained for the integration of the energy conservation equation. Due to the analytical uncoupling between species and energy formulations, it was shown that a single, rigorously obtained heat transfer expression, can be coupled with all droplet mass transfer models in this manuscript. This includes the single-component treatment of Abramzon and Sirignano, since the proposed formulation was shown to correctly degenerate to that model in the single-component limit. This alleviates the modelling efforts and allow for the isolation of impacts concerning sub-modelling choices for the mass diffusion problem. These mass and heat transfer formulations provide a complete, rigorous framework of reference for droplet phase-change modelling in the zero-dimensional context.

A complete derivation was then laid out for cornerstone models in the litterature, including (Law 1976), (Ebrahimian and Habchi 2011), (Tonini and Cossali 2015), (Newbold and Amundson 1973) and (Tonini and Cossali 2016). Therein, it was possible to see the inherent contributions and simplifying assumptions of each one. All of these models were then extended in their key weaknesses, including the consistent addition of convection effects and the absolute value operator for general mass transfer scenarios, where strong condensation may occur. We also extended the Ebrahimian and Habchi methodology

to any diffusion coefficient, not only the Hirschfelder-Curtiss law as proposed originally. Their proposed methodology also allows for a different perspective to our general energy formulation, which does not require a second spatial integration and therefore avoids the hypothesis of constant properties in space (and their averaging).

Then, a thorough derivation for all diffusion coefficient methodologies used in the context of droplet phase-change modelling was carried out. In particular, it was shown that Blanc's law presents a sensibility in some limiting cases, and that the diffusion coefficient obtained from the Hirschfelder-Curtiss law is not analytically suitable for the integration of the species conservation equations. Still, each model is derived by placing different constraints to the molecular, mass diffusion, or molar diffusion velocities, and in this way a new diffusion coefficient expression was proposed which is complimentary to Blanc's law. Overall, for a broad range of applications, the diffusion coefficient from (Fairbanks and Wilke 1950) was recommended.

Once this standard diffusion coefficient was established, numerical investigations were carried for extreme conditions still representative of spray combustion scenarios. All models used the same general energy formulation, isolating the influence of the mass transfer formulation choice. It was found out that generally the simplified framework of Law's model is not enough to capture the underlying physics, and that the Ebrahimian and Habchi extended model still needs fine-tuning, possibly for the Sherwood number computation. The extension of the Tonini-Cossali and Newbold-Amundson models consistently yielded close results to the Stefan-Maxwell reference, indicating that they can be used and still retrieve reasonable accuracy.

Finally, for future studies it is also possible to incorporate new, relevant physical phenomena to the previously developed droplet phase-change models. One recent example is the treatment of micro-explosions provided in (Antonov, Kuznetsov, Sazhin, and Strizhak 2022), and also droplet modelling focused on combustion scenarios as seen in (Bonanni and Ihme 2022) and (Both, Mira, and Lehmkuhl 2022).

Appendix A

The liquid-phase closure

In Chap. 1, the conservation equations were specifically worked on only for the gaseous phase. Therefore, a closure must be devised for the liquid-phase to describe how the mass and the heat transfer rates will be communicated to the droplet. This appendix details how the droplet's temperature, composition and diameter are updated at each time step during the numerical integration.

One of the consequences of the decoupling between both phases, allowed mainly due to the quasi-steadiness assumption, is that this liquid-phase closure is arbitrary, meaning, there is freedom of modelling choices for the interior of the droplet (provided that modelling hypotheses do not clash). However, it ideally should still be aligned with the hypotheses made for the gaseous phase, for consistency. The spherical symmetry hypothesis for instance essentially establishes that no velocity field can be present inside the droplet since it could only contain components in the radial direction (expansion or contraction). This of course is not true in general, as seen in Chap. 6.

Still, it would not be inconsistent to employ a strategy wherein the liquid phase is discretized even though the gaseous phase has been integrated; the key would be to correctly couple both phases through relations at the surface of the droplet. This has been done for instance in (Abramzon and Sirignano 1989) wherein the authors propose that it is still possible to solve only for the diffusion of temperature inside the droplet and still account for inner convection effects if the conductivity is corrected accordingly - this approach has been referred to as the "effective conductivity". Still, this would require a one-dimensional spatial discretization.

For simplicity, in this manuscript we assume infinite liquid thermal conductivity and infinite mass diffusivity for the liquid phase, with liquid thermodynamic properties also assumed to be constant and homogeneous within a time-step. These hypotheses usually can be justified for some spray combustion scenarios, typically through an analysis including relevant physical time-scales, as done for instance in (Sazhin, Feng, Heikal, Goldfarb, Gol'dshtein, and Kuzmenko 2001), (McIntosh, Gol'dshtein, Goldfarb, and Zi-

noviev 1998), (Sanchez 2012). Concretely, these simplifications are made to avoid spatial discretizations or more complex analytical integrations, in sync with the modelling strategies made for the gaseous phase to reduce numerical costs.

For the energy part, integrations in the gaseous phase will yield the heat transfer rate reaching the surface of the droplet, $\dot{\mathcal{Q}}$. From the perspective of the droplet, $\dot{\mathcal{Q}}_d = -\dot{\mathcal{Q}}$. By neglecting radiation and the Dufour effect, this heat transfer rate can be modelled as being further subdivided onto a sensible part related to temperature change, and a latent part, related to phase-change:

$$\dot{\mathcal{Q}}_d = \dot{\mathcal{Q}}_{d,S} + \dot{\mathcal{Q}}_{d,L}. \tag{A.1}$$

The infinite liquid thermal conductivity means that the temperature is always supposed to be uniform inside the droplet and adjust infintely fast (no inner thermal gradients). This is represented through the modelling of the sensible component of the heat entering the droplet in Eq. A.1 as follows:

$$\dot{\mathcal{Q}}_{d,S} = m_d c_L \frac{dT_d}{dt}, \tag{A.2}$$

with c_L being the droplet's liquid mixture specific heat at constant pressure and T_d the droplet's temperature. The droplet phase-change contribution to the heat transfer rate is usually modeled through a latent heat of vaporization L_{vap}, also called enthalpy of vaporization:

$$\dot{\mathcal{Q}}_{d,L} = \dot{m} L_{vap}. \tag{A.3}$$

In this way, an expression for updating the droplet's temperature through Eq. A.1 can be devised once an analytical expression for $\dot{\mathcal{Q}}$ (and therefore, $\dot{\mathcal{Q}}_d$) has been found through the droplet heat transfer model of choice.

For the species, the infinite mass diffusivity hypothesis dictates that mass fractions for each component inside the droplet are also updated instantaneouly, with no inner gradients. In practice, once the mass transfer rates for each species $\dot{m}_i$ and the global mass transfer rate $\dot{m}$ are computed, the mass of each species inside the droplet is updated from $m_{d,i}^t$ to $m_{d,i}^{t+dt}$ and the global droplet's mass is updated to m_d^t to m_d^{t+dt}. Then, the new mass fractions inside the droplet are simply taken to be the ratio of these updates masses i.e. $Y_{d,i}^{t+dt} = \frac{m_{d,i}^{t+dt}}{m_d^{t+dt}}$.

In (Sazhin, Krutitskii, Martynov, Mason, Heikal, and Sazhina 2007) and (Sazhin, Gusev, Krutitskii, and Heikal 2011) it is possible to find analytical solutions for simplified droplet heat transfer problems that couple the liquid and the gaseous-phase in transient scenarios. In (Sazhin, Krutitskii, Abdelghaffar, Sazhina, Mikhalovsky, Meikle, and Heikal 2004), the analytical study is concentrated only in the liquid phase. It was proposed in (Dombrovsky and Sazhin 2003) that parabolical temperature profiles could be imposed

for the liquid phase, to obtain satisfactory results while not having to compute complex analytical solutions; this was further adressed in (Snegirev 2013) Also, in (Sazhin, Elwardany, Sazhina, and Heikal 2011), the authors analyze the hypotheses of infinite liquid conductivity and mass diffusivity.
Concerning the update of the droplet's diameter, due to the assumptions made for the liquid-phase above, it is possible to obtain an expression that is independent of the choice of the droplet's mass transfer rate $\dot{m}$ computed from the gaseous phase. This is typically done through the so-called "d^2 law". In (Fuchs 1959) we can find one of the first times this development was mathematically formalized, and it essentially states that the droplet's surface area, or equivalently the squared power of its diameter, decreases following a constant factor during an evaporation process.

The derivation departs from the following considerations. First, the mass of a spherical droplet can be computed as follows, supposing that its density ρ_L is homogeneous:

$$m_d = \frac{4}{3}\pi R_d^3 \rho_L. \tag{A.4}$$

Then, suppposing that this density ρ_L is also constant in time, the variation of the droplet's mass in time can be computed as:

$$\frac{dm_d}{dt} = 4\pi R_d^2 \frac{dR_d}{dt}\rho_L. \tag{A.5}$$

Now, noticing that:

$$\frac{dR_d^2}{dt} = 2R_d \frac{dR_d}{dt}, \tag{A.6}$$

Eq. A.5 can be recast as:

$$\frac{dm_d}{dt} = \dot{m}_d = 2\pi R_d \frac{dR_d^2}{dt}\rho_L. \tag{A.7}$$

In the literature, typically the evaporation constant $\mathcal{K}$ is defined as being:

$$\mathcal{K} = -\frac{d\mathcal{D}^2}{dt}, \tag{A.8}$$

where $\mathcal{D}$ is the droplet's diameter. Using this notation, and recalling that $\dot{m}_d = -\dot{m}$ leads to the following general formulation:

$$\mathcal{K} = \frac{2\dot{m}}{\pi R_d \rho_L}. \tag{A.9}$$

Eq. A.8 can then be integrated between instant t where the droplet's diameter is $\mathcal{D}_t$ to instant $t + dt$ with $\mathcal{D}_{t+dt}$, leading to:

$$\mathcal{D}_{t+dt}^2 = \mathcal{D}_t^2 - \mathcal{K}dt, \tag{A.10}$$

or, the square of the diameter (or the surface area) follows a constant rate of change. As noted for instance in (Sazhin 2014), this is strictly valid only when the droplet has a constant temperature and is moving very slowly.

This of course supposes that the coordinate of the droplet radius does not change with time during the integration, which is valid for CFD solvers. This overall conclusion was also mentioned on (Godsave 1953), where the author actually defined $\mathcal{K}$ as the evaporation constant. This is one of the most well-known results for droplet evaporation, due to its simplicity and also because experimental data typically corroborates this result, as shown for instance in (Godsave 1953).

Appendix B

Assessing the quasi-steadiness assumption

When laying out the simplified versions of the conservation equations in Chap. 1, the quasi-steadiness assumption was readily made in order to avoid the temporal derivatives. This assumption is usually made with the justification that processes in the liquid phase tend to take 1-2 orders of magnitude longer than those in the gaseous phase. Since the droplet phase-change problem is intrinsically coupled between liquid and gas phase, the quasi-steadiness hypothesis essentially is saying that processes in the gas-phase can be seen to adapt infinitely fast in this context, and so only spatial gradients would be kept. This assumption is widely used to allow for the obtention of droplet heat and mass transfer models, and some authors have taken care to justify quantitatively as to why this is the case, as shown in this subsection for problems without the inclusion of advective Stefan-flow effects.

In the works of (Fuchs 1959), the analytical solution to the following partial differential equation is proposed:

$$\frac{\partial Y_1}{\partial t} = D_{1,2}\left(\frac{\partial^2 Y_1}{\partial r^2} + \frac{2}{r}\frac{\partial Y_1}{\partial r}\right), \tag{B.1}$$

with the following boundary conditions:

$$Y_1(t=0, r > R_d) = Y_1^{\infty}, \tag{B.2}$$
$$Y_1(t>0, r = R_d) = Y_1^{s}. \tag{B.3}$$

This problem correspond to solving the quasi-steady species conservation equation when $\mathrm{u}^Y = 0$, which, from global mass conservation, must lead to $\partial\rho/\partial t = 0$, also when the density ρ is assumed to be constant in space. In this way, the solution provided is:

$$Y_1(t, r > R_d) = Y_1^{\infty} + \frac{R_d}{r}(Y_1^s - Y_1^{\infty})\left[1 - \mathrm{erf}\left(\frac{r - R_d}{2\sqrt{D_{1,2}t}}\right)\right], \tag{B.4}$$

where the error function erf is defined as:

$$\mathrm{erf}(z) = \frac{2}{\sqrt{\pi}} \int_0^z e^{-\alpha^2} d\alpha. \tag{B.5}$$

In the original work of (Fuchs 1959), Eq. B.4 had a typo, but the results shown by author just afterwards corroborate the above result. To better understand the structure of this solution, it is useful to define the following variable:

$$u = \frac{r - R_d}{2\sqrt{D_{1,2}t}}, \tag{B.6}$$

such that:

$$\frac{\partial}{\partial u}[\mathrm{erf}u] = \frac{2e^{-u^2}}{\sqrt{\pi}}, \tag{B.7}$$

$$\frac{\partial}{\partial r}[\mathrm{erf}u] = \frac{\partial}{\partial u}[\mathrm{erf}u]\frac{\partial u}{\partial r} = \frac{2e^{-u^2}}{\sqrt{\pi}} \frac{1}{2\sqrt{D_{1,2}t}}. \tag{B.8}$$

In this way, the gradient of the mass fraction can be computed from Eq. B.4 to be:

$$\frac{dY_1}{dr} = -\frac{R_d}{r}(Y_1^s - Y_1^\infty) \left[\frac{1 - \mathrm{erf}u}{r} + \frac{e^{-u^2}}{\sqrt{\pi D_{1,2}t}} \right]. \tag{B.9}$$

If the mass transfer rate is assumed to still be computable using Maxwell's expression Eq. 4.2 i.e.:

$$\dot{m} = -4\pi R_d^2 \rho D_{1,2} \left. \frac{dY_1}{dr} \right|_{r=R_d}, \tag{B.10}$$

then, the evaluation of the gradient at the surface of the droplet in non-stationary conditions would be, from Eq. B.9 above:

$$\left. \frac{dY_1}{dr} \right|_{r=R_d} = \frac{(Y_1^\infty - Y_1^s)}{R_d} \left[1 + \frac{R_d}{\sqrt{\pi D_{1,2}t}} \right], \tag{B.11}$$

This leads to the non-stationary mass vaporization rate expression without Stefan flow:

$$\dot{m} = 4\pi R_d \rho D_{1,2}(Y_1^s - Y_1^\infty) \left[1 + \frac{R_d}{\sqrt{\pi D t}} \right]. \tag{B.12}$$

Comparison between the non-stationary vaporization rate $\dot{m}_{\partial t}$ from Eq. B.12 and the steady-stat vaporization rate $\dot{m}$ from Eq. 4.7 leads to:

$$\frac{\dot{m}_{\partial t}}{\dot{m}} = 1 + \frac{R_d}{\sqrt{\pi D_{1,2}t}}. \tag{B.13}$$

Now, to give a rough estimate, it is possible to quantify a time-scale τ_t after which quasi-stationarity has been satisfactorily achieved, namely, if $t >> \tau_t = R_d^2/(\pi D_{1,2})$ A common order of magnitude for the mass diffusion coefficient is $D_{1,2} \approx 10^{-5} m^2/s$. A droplet radius representative of spray combustion would have $R_d \approx 10\mu m$. This yields $\tau_t \approx 3\mu s$ as a reference time-scale. As seen for example in (Santos, Filho, and Vié 2021), the droplet evaporation lifetime for typical cases can be estimated to be of the order of magnitude $\tau_{evap} \approx 10ms$. Therefore, the ratio $\tau_t/\tau_{evap} \approx 3\text{x}10^{-4}$ is a good first indication that the quasi-starionarity assumption may be employed.

In (Sazhin 2014), the author has developed the same rationale for the non-stationary equation for energy, which would be in this case:

$$\frac{\partial T}{\partial t} = \kappa \left(\frac{\partial^2 T}{\partial r^2} + \frac{2}{r} \frac{\partial T}{\partial r} \right), \tag{B.14}$$

where κ is the thermal diffusivity defined as being:

$$\kappa = \frac{\lambda}{\rho c_p}. \tag{B.15}$$

Comparing Eqs. B.14 and B.1, supposing analogous boundary conditions leads to a straighforward solution for the temperature profile in the gas phase:

$$T(t, r > R_d) = T^{\infty} + \frac{R_d}{r}(T^s - T^{\infty}) \left[1 - \text{erf} \left(\frac{r - R_d}{2\sqrt{\kappa t}} \right) \right]. \tag{B.16}$$

By also noting that the following can be defined for the case without Stefan-flow effects:

$$\dot{\mathcal{Q}} = -4\pi R_d^2 \lambda \left. \frac{dT}{dr} \right|_{r=R_d}, \tag{B.17}$$

The same rationale done for the species above can be applied for the non-stationary heat transfer rate $\dot{\mathcal{Q}}_{\partial t}$ versus the stationary one, $\dot{\mathcal{Q}}$, to yield its ratio:

$$\frac{\dot{\mathcal{Q}}_{\partial t}}{\dot{\mathcal{Q}}} = 1 + \frac{R_d}{\sqrt{\pi \kappa t}}. \tag{B.18}$$

Common orders of magnitude for gases are $\lambda \approx 1\text{x}10^{-2} W/(m.K)$, $\rho \approx 1 kg/m^3$, $c_p \approx 1\text{x}10^3$ leading to $\kappa \approx 1\text{x}10^{-5}$, similar to the mass diffusion coefficient. Therefore, the same conclusions generally apply for the use of the quasi-stationarity hypothesis.

Appendix C

Species and properties database

In this appendix, first the fuel species chosen for numerical investigations in this manuscript are listed, with their main characteristics and intrinsic properties. The used formulations for the computation of thermodynamic and transport properties are also shown, all extracted from (e. V. 2010). To carry out a complete droplet phase-change model investigation using the models of this manuscript, the following properties are required:

- Liquid density ρ_l;
- Liquid specific heat at constant pressure c_l;
- Liquid enthalpy of vaporization L_{vap}
- Liquid saturation vapor presure p_{vap};
- Gaseous density ρ_g;
- Gaseous specific heat at constant pressure c_p;
- Gaseous binary diffusion coefficients at binary gaseous mixture $D_{i,j}$
- Gaseous conductivity λ_g;
- Gaseous viscosity μ_g.

Additionally, even though the liquid viscosity μ_l is not necessary for the modelling computations per se, it will still be displayer here since it is used to compute the viscosity ratio for convection correlations for fluid spheres.

Four fuel species have been chosen, deemed to be able to capture a great range of possible interactions: water, ethanol (representant of alcohols), acetone (representant of ketones) and n-dodecane (representant of heavy hydrocarbons). Further, ethanol is also typically used as a fuel, mainly for automotive applications, whereas n-dodecane is often chosen to model the main component of aeronautical kerosene. The inert species are air which can be defined as a single, average species, and also separately nitrogen, oxygen and carbon dioxide, which is a typical combustion product. Sample evaluations of the properties above for each species are provided at $T = 300K$ for both gas and liquid, and at $T = T_b - 10$ to give an upper limit for the liquid-phase (close to boiling point) and $T = 1500K$ for the gas-phase upper limit. Unless otherwise stated, the properties formulations listed here are the default. Finally, formulas used to compute locally average properties when more than one species is present are listed.

C.1 General species data

Species	Formula	W [g/mol]	T_b [K]	T_c [K]	p_c [bar]	ρ_c [kg/m^3]
Water	H_2O	18.02	373.15	647.1	220.64	322
Ethanol	C_2H_5OH	46.07	351.52	513.9	61.48	276
Acetone	$(CH_3)_2CO$	58.08	329.25	508.1	46.92	274
N-dodecane	$C_{12}H_{26}$	170.34	489.45	658.1	18.18	238
Air	-	28.97	-	132.53	37.86	343
Nitrogen	N_2	28.01	-	126.19	33.96	313
Oxygen	O_2	32	-	154.6	50.46	427
Carbon dioxide	CO_2	44.01	-	304.13	73.77	468

C.2 Liquid sample properties

Below, the superscript "0" is for $T_l = 300K$ and "+" is for $T_L = T_b - 10$, with the boiling temperature of each species.

-	Water	Ethanol	Acetone	N-dodecane
ρ_l^0 [kg/m^3]	996.5	784.4	783.4	743.7
ρ_l^+ [kg/m^3]	963.6	746.4	761.2	603.0
c_l^0 [J/(kg $\cdot$ K)]	4182.5	2594.5	2147.4	2219.0
c_l^+ [J/(kg $\cdot$ K)]	4204.4	3079.6	2198.5	2922.0
L_{vap}^0 [J/kg] (x10^5)	24.359	9.191	5.325	3.601
L_{vap}^+ [J/kg] (x10^5)	22.816	8.664	5.125	2.625
p_{vap}^0 [Pa]	3539.4	8850.6	33254.2	20.1722
p_{vap}^+ [Pa]	70152.7	67693.5	71129.4	79412.4
μ_l^0 [kg/(m $\cdot$ s)] (x10^{-4})	8.651	10.264	2.993	13.305
μ_l^+ [kg/(m $\cdot$ s)] (x10^{-4})	3.162	5.079	2.523	2.234

C.3 Gas sample properties

Below, the superscript "0" is for $T_g = 300K$ and "+" is for $T_g = 1500$.

-	Water	Ethanol	Acetone	N-dodecane
ρ_g^0 [kg/m^3]	0.732	1.872	2.359	6.920
ρ_g^+ [kg/m^3]	0.146	0.374	0.472	1.384
c_p^0 [J/(kg · K)]	1868.6	1604.1	1290.8	1642.4
c_p^+ [J/(kg · K)]	2610.0	3641.8	3200.6	4234.7
λ_g^0 [J/kg] (x10^{-2})	1.855	1.520	5.325	0.7524
λ_g^+ [J/kg] (x10^{-2})	18.484	28.550	24.958	19.931
μ_g^0 [kg/(m · s)] (x10^{-6})	9.930	8.988	7.537	4.140
μ_g^+ [kg/(m · s)] (x10^{-6})	61.435	35.856	38.353	23.865

-	Air	Nitrogen	Oxygen	CarbonDioxide
ρ_g^0 [kg/m^3]	1.177	1.138	1.300	1.788
ρ_g^+ [kg/m^3]	0.235	0.228	0.260	0.358
c_p^0 [J/(kg · K)]	1005.5	1039.3	919.6	845.6
c_p^+ [J/(kg · K)]	1213.0	1245.9	1141.1	1317.3
λ_g^0 [J/kg] (x10^{-2})	2.651	2.556	2.673	1.670
λ_g^+ [J/kg] (x10^{-2})	9.046	9.239	10.195	9.069
μ_g^0 [kg/(m · s)] (x10^{-6})	18.550	17.838	20.778	15.059
μ_g^+ [kg/(m · s)] (x10^{-6})	54.498	54.184	63.438	52.028

In the table below, binary diffusion coefficients are computed for all pairs of species at $T_g = 300K$; the lower triangle is omitted since $D_{ji} = D_{ij}$.

$D_{i,j}[\mathrm{m}^2/\mathrm{s}]$ (x10^{-5})	H_2O	C_2H_5OH	$(CH_3)_2CO$	$C_{12}H_{26}$	Air	N_2	O_2	CO_2
H_2O	3.234	1.620	1.406	0.7122	2.531	2.605	2.655	2.106
C_2H_5OH	-	0.809	0.700	0.356	1.239	1.274	1.266	1.006
$(CH_3)_2CO$	-	-	0.603	0.304	1.069	1.099	1.087	0.863
$C_{12}H_{26}$	-	-	-	0.147	0.535	0.549	0.532	0.422
Air	-	-	-	-	1.943	2.001	2.019	1.591
N_2	-	-	-	-	-	2.061	2.081	1.639
O_2	-	-	-	-	-	-	2.098	1.638
CO_2	-	-	-	-	-	-	-	1.281

Finally, binary diffusion coefficients are computed below for each pair at $T_g = 1500K$.

$D_{i,j}[\mathrm{m}^2/\mathrm{s}]$ (x10^{-5})	H_2O	C_2H_5OH	$(CH_3)_2CO$	$C_{12}H_{26}$	Air	N_2	O_2	CO_2
H_2O	54.07	27.08	23.51	11.91	42.31	43.55	44.39	35.21
C_2H_5OH	-	13.53	11.69	5.951	20.71	21.29	21.17	16.82
$(CH_3)_2CO$	-	-	10.08	5.086	17.87	18.38	18.18	14.42
$C_{12}H_{26}$	-	-	-	2.457	8.937	9.180	8.891	7.049
Air	-	-	-	-	32.49	33.46	33.75	26.60
N_2	-	-	-	-	-	34.46	34.79	27.41
O_2	-	-	-	-	-	-	35.08	27.39
CO_2	-	-	-	-	-	-	-	21.42

C.4 Individual local properties

Correlations for the computation of each one are provided just after; their expressions and coefficients for each species are extracted from (e. V. 2010). The reduced temperature used in many correlations is defined as:

$$T_r = \frac{T}{T_c}, \tag{C.1}$$

and the universal gas constant used here is $R = 8314.46262 J/(mol \cdot K)$.

C.4.1 Liquid density

$$\rho_l = \rho_{c,i} + A(1-T_r)^{0.35} + B(1-T_r)^{\frac{2}{3}} + C(1-T_r) + D(1-T_r)^{\frac{4}{3}} \tag{C.2}$$

C.4.2 Liquid specific heat at constant pressure

$$c_l = \frac{R}{W_i}\left[\frac{A}{1-T_r} + B + C(1-T_r) + D(1-T_r)^2 + E(1-T_r)^3 + F(1-T_r)^4\right] \tag{C.3}$$

C.4.3 Liquid enthalpy of vaporization

$$L_{vap} = T_c \frac{R}{W_i}\left[A(1-T_r)^{\frac{1}{3}} + B(1-T_r)^{\frac{2}{3}} + C(1-T_r) + D(1-T_r)^2 + E(1-T_r)^6\right] \tag{C.4}$$

C.4.4 Liquid saturation vapor pressure

$$\ln\left(\frac{\mathrm{p}_{sat}}{\mathrm{p}_c}\right) = \frac{1}{T_r}\left(A(1-T_r) + B(1-T_r)^{1.5} + C(1-T_r)^3 + D(1-T_r)^6\right), \tag{C.5}$$

C.4.5 Gaseous density

$$\rho_g = \frac{\mathrm{p}W_i}{RT} \tag{C.6}$$

C.4.6 Gaseous specific heat at constant pressure

$$c_p = \frac{R}{W_i}\left[B + (C-B)\left(\frac{T}{A+T}\right)^2\right]\left[1 - \frac{A}{A+T}\left(D + E\left(\frac{T}{A+T}\right) + F\left(\frac{T}{A+T}\right)^2 + G\left(\frac{T}{A+T}\right)^3\right)\right] \tag{C.7}$$

C.4.7 Gaseous binary diffusion coefficients at binary gaseous mixture

$$D_{i,j} = 0.00143 \frac{T^{1.75}}{\mathrm{p}} \left[\frac{\left(\frac{1}{W_i} + \frac{1}{W_j}\right)^{1/2}}{\sqrt{2}\left(\delta_i^{1/3} + \delta_j^{1/3}\right)^2} \right] \mathrm{x}10^{-4}, \tag{C.8}$$

where the pressure p must be expressed in bar and the 10^{-4} factor appears to convert from cm^2/s to m^2/s.

C.4.8 Gaseous conductivity

$$\lambda_g = A + BT + CT^2 + DT^3 + ET^4 \tag{C.9}$$

C.4.9 Gaseous viscosity

$$\mu_g = A + BT + CT^2 + DT^3 + ET^4 \tag{C.10}$$

C.5 Local mixture properties

Averaging rules for a given point where multiple species are present are detailed below for a general property η, covering most individual properties stated at the beggining of this appendix. For an average diffusion coefficient, examples are given in Chap. 2 and Chap. 9. As for the saturation vapor pressure and the latent heat of vaporization, there is no functional need to compute averages of these quantities.

C.5.1 Proportional mass averaging method

$$\eta_{mixt} = \sum_{k=1}^{N} Y_k \eta_k \tag{C.11}$$

This method is used to compute the average specific heat for both the liquid and gaseous phases i.e. $\eta_k = c_l, c_p$.

C.5.2 Inverse proportional mass averaging method

$$\eta_{mixt} = \left[\sum_{k=1}^{N} \frac{Y_k}{\eta_k} \right]^{-1} \tag{C.12}$$

This method is used to compute the average density for both the liquid and gaseous phases i.e. $\eta_k = \rho_l, \rho_g$.

C.5.3 Wilke's molar rule

$$\eta_{mixt} = \sum_{k=1}^{N} \left[\frac{X_k \eta_k}{\sum_{m=1}^{N} X_k \phi_{km}} \right], \tag{C.13a}$$

$$\phi_{km} = \frac{\left[1 + (\eta_k/\eta_m)^{1/2} (W_m/W_k)^{1/4}\right]^2}{\left[8(1 + (W_k/W_m))\right]^{1/2}}. \tag{C.13b}$$

This method is used to compute the average conductivity and viscosity for the gaseous phase i.e. $\eta_k = \lambda_g, \mu_g$.

Appendix D

Summary of single-component formulations

Below are listed different formulations for mass and heat transfer obtained so far. This includes the heat and mass transfer rates, the gradients, and the Nusselt and Sherwood numbers that can be defined for each case, as will be specified below. To simplify, all energy expressions that include Stefan flow will showcase the specific heat $c_{p,v}$ instead of the global c_p, meaning, we include enthalpy diffusion effects when also including Stefan flow effects. To obtain the version that neglects enthalpy diffusion, it suffices to switch these specific heats.

D.1 Heat and mass transfer rates

1. Diffusion + no Stefan flow + integration to infinity: Eq. 4.7 for $\dot{m}_D^\infty$ and Eq. 4.25 for $\dot{\mathcal{Q}}_\lambda^\infty$.

$$\dot{m}_D^\infty = 4\pi R_d \rho D_{1,2}(Y_1^s - Y_1^\infty), \tag{D.1a}$$

$$\dot{\mathcal{Q}}_\lambda^\infty = 4\pi R_d \lambda (T_1^s - T^\infty). \tag{D.1b}$$

2. Diffusion + no Stefan flow + integration inside film: Eq. 5.7a for $\dot{m}_D^\delta$ and Eq. 5.7b for $\dot{\mathcal{Q}}_\lambda^\delta$

$$\dot{m}_D^\delta = 2\pi R_d Sh_D^\delta \rho D_{1,2}(Y_1^s - Y_1^\infty), \tag{D.2a}$$

$$\dot{\mathcal{Q}}_\lambda^\delta = 2\pi R_d Nu_\lambda^\delta \lambda (T_1^s - T^\infty). \tag{D.2b}$$

3. Diffusion + Stefan flow + integration to infinity: Eq. 4.12 for $\dot{m}_{\mathrm{u},D}^\infty$ and Eq. 4.35 for $\dot{\mathcal{Q}}_{\mathrm{u},\lambda}^\infty$

$$\dot{m}_{\mathrm{u},D}^\infty = 4\pi R_d \rho D_{1,2} \ln\left(\frac{1 - Y_1^\infty}{1 - Y_1^s}\right), \tag{D.3a}$$

$$\dot{\mathcal{Q}}_{\mathrm{u},\lambda}^\infty = \frac{\dot{m} c_{p,v}(T^s - T^\infty)}{\exp\left(\frac{\dot{m} c_{p,v}}{4\pi R_d \lambda}\right) - 1}. \tag{D.3b}$$

4. Diffusion + Stefan flow + integration inside film but same thickness as pure diffusive case: Eq. 5.13a for $\dot{m}_{\mathrm{u},D}^{\delta=}$ and Eq. 5.16 for $\dot{\mathcal{Q}}_{\mathrm{u},\lambda}^{\delta=}$

$$\dot{m}_{\mathrm{u},D}^{\delta=} = 2\pi R_d Sh_{\mathrm{u},D}^{\delta} \rho D_{1,2} \ln\left(\frac{1-Y_1^{\infty}}{1-Y_1^{s}}\right), \tag{D.4a}$$

$$\dot{\mathcal{Q}}_{\mathrm{u},\lambda}^{\delta=} = \frac{\dot{m} c_{p,v}(T^s - T^{\infty})}{\exp\left(\frac{\dot{m} c_{p,v}}{2\pi R_d Nu_{\mathrm{u},\lambda}^{\delta} \lambda}\right) - 1}. \tag{D.4b}$$

5. Diffusion + Stefan flow + integration inside film but corrected thickness: Eq. 5.13a for $\dot{m}_{\mathrm{u},D}^{\delta\neq}$ and Eq. 5.26 for $\dot{\mathcal{Q}}_{\mathrm{u},\lambda}^{\delta\neq}$

$$\dot{m}_{\mathrm{u},D}^{\delta\neq} = 2\pi R_d Sh_{\mathrm{u},D}^{\delta\neq} \rho D_{1,2} \ln\left(\frac{1-Y_1^{\infty}}{1-Y_1^{s}}\right), \tag{D.5a}$$

$$\dot{\mathcal{Q}}_{\mathrm{u},\lambda}^{\delta\neq} = \frac{\dot{m} c_{p,v}(T^s - T^{\infty})}{\exp\left(\frac{\dot{m} c_{p,v}}{2\pi R_d Nu_{\mathrm{u},\lambda}^{\delta\neq} \lambda}\right) - 1}. \tag{D.5b}$$

D.2 Gradients at the surface of the droplet

1. Diffusion + no Stefan flow

$$\left.\frac{dY_1}{dr}\right|_{\rho D}^{s} = -\frac{\dot{m}}{4\pi R_d^2 \rho D_{1,2}}, \tag{D.6a}$$

$$\left.\frac{dT}{dr}\right|_{\lambda}^{s} = -\frac{\dot{\mathcal{Q}}}{4\pi R_d^2 \lambda}. \tag{D.6b}$$

2. Diffusion + Stefan flow

$$\left.\frac{dY_1}{dr}\right|_{\mathrm{u}_r,\rho D}^{s} = -\frac{\dot{m}(1-Y_1)}{4\pi R_d^2 \rho D_{1,2}}, \tag{D.7a}$$

$$\left.\frac{dT}{dr}\right|_{\mathrm{u}_r,\lambda}^{s} = -\frac{\dot{m} c_{p,v}(T^s - T^{\infty}) + \dot{\mathcal{Q}}}{4\pi R_d^2 \lambda}. \tag{D.7b}$$

D.3 Nusselt and Sherwood numbers

- Diffusion + no Stefan flow + integration to infinity: Sh_D^{∞} and Nu_{λ}^{∞}

$$Sh_D^{\infty} = 2, \tag{D.8a}$$

$$Nu_{\lambda}^{\infty} = 2. \tag{D.8b}$$

- Diffusion + no Stefan flow + integration inside film: Sh_D^δ and Nu_λ^δ

$$Sh_D^\delta = \frac{\dot{m}_{\rho D}^\delta}{2\pi R_d \rho D_{1,2}} \frac{1}{(Y_1^s - Y_1^\infty)}, \tag{D.9a}$$

$$Nu_\lambda^\delta = \frac{\dot{q}_{g_\lambda}^\delta}{2\pi R_d \lambda} \frac{1}{(T^s - T^\infty)}. \tag{D.9b}$$

- Diffusion + Stefan flow + integration to infinity: $Sh_{\mathrm{u}_r,\rho D}^\infty$ and $Nu_{\mathrm{u}_r,\lambda}^\infty$

$$Sh_{\mathrm{u},D}^\infty = \frac{\dot{m}_{\mathrm{u},D}^\infty}{2\pi R_d \rho D_{1,2}} \left(\frac{1 - Y_1^s}{Y_1^s - Y_1^\infty} \right) = 2 \frac{\ln(1 + B_M)}{B_M}, \tag{D.10a}$$

$$Nu_{\mathrm{u},\lambda}^\infty = \frac{\dot{m}_{\mathrm{u},\lambda}^\infty c_{p,v}}{2\pi R_d \lambda} \left(1 + \frac{1}{\exp\left(\frac{\dot{m}_{\mathrm{u},\lambda}^\infty c_{p,v}}{4\pi R_d \lambda} \right) - 1} \right) = 2(1 + B_T) \frac{\ln(1 + B_T)}{B_T}. \tag{D.10b}$$

- Diffusion + Stefan flow + integration inside film but same thickness as pure diffusive case, isolating the Sh/Nu from Eqs. (5.42a) and (5.42b): $Sh_{\mathrm{u}_r,\rho D}^{\delta=}$ and $Nu_{\mathrm{u}_r,\lambda}^{\delta=}$

$$Sh_{\mathrm{u},D}^{\delta=} = \frac{\dot{m}_{\mathrm{u},D}^{\delta=}}{2\pi R_d \rho D_{1,2} \ln\left(\frac{1 - Y_1^s}{Y_1^s - Y_1^\infty} \right)} = \frac{\dot{m}_{\mathrm{u},\rho D}^{\delta=}}{2\pi R_d \rho D_{1,2} \ln(1 + B_M)}, \tag{D.11a}$$

$$Nu_{\mathrm{u},\lambda}^{\delta=} = \frac{\dot{m}_{\mathrm{u},\lambda}^{\delta=}}{2\pi R_d \frac{\lambda}{c_{p,v}} \ln\left(\frac{\dot{m}_{\mathrm{u},\lambda}^{\delta=} c_{p,v} (T^s - T^\infty) + \dot{\mathcal{Q}}_{\mathrm{u},\lambda}^{\delta=}}{\dot{\mathcal{Q}}_{\mathrm{u},\lambda}^{\delta=}} \right)} = \frac{\dot{m}_{\mathrm{u},\lambda}^{\delta=}}{2\pi R_d \frac{\lambda}{c_{p,v}} \ln(1 + B_T)} \tag{D.11b}$$

- Diffusion + Stefan flow + integration inside film but same thickness as pure diffusive case, computing Sh/Nu from gradients Eqs. (5.45a) and (5.45b): $Sh_{\mathrm{u}_r,\rho D}^{\nabla,\delta=}$ and $Nu_{\mathrm{u}_r,\lambda}^{\nabla,\delta=}$

$$Sh_{\mathrm{u},D}^{\nabla,\delta=} = \frac{\dot{m}_{\mathrm{u},D}^{\delta=}}{2\pi R_d \rho D_{1,2}} \left(\frac{1 - Y_1^s}{Y_1^s - Y_1^\infty} \right) = 2 \frac{\ln(1 + B_M)}{B_M}, \tag{D.12a}$$

$$Nu_{\mathrm{u},\lambda}^{\nabla,\delta=} = \frac{\dot{m}_{\mathrm{u},\lambda}^{\delta=} c_{p,v}}{2\pi R_d \lambda} \left(1 + \frac{1}{\exp\left(\frac{\dot{m}_{\mathrm{u},\lambda}^{\delta=} c_{p,v}}{4\pi R_d \lambda} \right) - 1} \right) = 2(1 + B_T) \frac{\ln(1 + B_T)}{B_T}. \tag{D.12b}$$

- Diffusion + Stefan flow + integration inside film but corrected thickness, isolating

the Sh/Nu from Eqs. (5.42a) and (5.42b): $Sh^{\delta\neq}_{\mathrm{u}_r,\rho D}$ and $Nu^{\delta\neq}_{\mathrm{u}_r,\lambda}$:

$$Sh^{\delta\neq}_{\mathrm{u},D} = \frac{\dot{m}^{\delta\neq}_{\mathrm{u},D}}{2\pi R_d \rho D_{1,2} \ln\left(\frac{1-Y_1^s}{Y_1^s - Y_1^\infty}\right)} = \frac{\dot{m}^{\delta\neq}_{\mathrm{u},D}}{2\pi R_d \rho D_{1,2} \ln(1+B_M)}, \tag{D.13a}$$

$$Nu^{\delta\neq}_{\mathrm{u},\lambda} = \frac{\dot{m}^{\delta\neq}_{\mathrm{u},\lambda}}{2\pi R_d \frac{\lambda}{c_{p,v}} \ln\left(\frac{\dot{m}^{\delta\neq}_{\mathrm{u}_r,\lambda} c_{p,v}(T^s - T^\infty) + \dot{\mathcal{Q}}^{\delta\neq}_{\mathrm{u},\lambda}}{\dot{\mathcal{Q}}^{\delta\neq}_{\mathrm{u},\lambda}}\right)} = \frac{\dot{m}^{\delta\neq}_{\mathrm{u},\lambda}}{2\pi R_d \frac{\lambda}{c_{p,v}} \ln(1+B_T)} \tag{D.13b}$$

- Diffusion + Stefan flow + integration inside film but corrected thickness, computing Sh/Nu from gradients Eqs. (5.45a) and (5.45b): $Sh^{\nabla,\delta\neq}_{\mathrm{u}_r,\rho D}$ and $Nu^{\nabla,\delta\neq}_{\mathrm{u}_r,\lambda}$

$$Sh^{\nabla,\delta\neq}_{\mathrm{u},D} = \frac{\dot{m}^{\delta\neq}_{\mathrm{u},D}}{2\pi R_d \rho D_{1,2}} \left(\frac{1-Y_1^s}{Y_1^s - Y_1^\infty}\right) = 2\frac{\ln(1+B_M)}{B_M}, \tag{D.14a}$$

$$Nu^{\nabla,\delta\neq}_{\mathrm{u},\lambda} = \frac{\dot{m}^{\delta\neq}_{\mathrm{u},\lambda} c_{p,v}}{2\pi R_d \lambda} \left(1 + \frac{1}{\exp\left(\frac{\dot{m}^{\delta\neq}_{\mathrm{u},\lambda} c_{p,v}}{4\pi R_d \lambda}\right) - 1}\right) = 2(1+B_T)\frac{\ln(1+B_T)}{B_T}. \tag{D.14b}$$

References

Abianeh, O. S. and C. P. Chen (2012). A discrete multicomponent fuel evaporation model with liquid turbulence effects. *International Journal of Heat and Mass Transfer 55*, 6897–6907.

Abrams, D. S. and J. M. Prausnitz (1975). Statistical thermodynamics of liquid mixtures: A new expression for the excess gibbs energy of partly or completely miscible systems. *AIChE Journal 21*, 116–128.

Abramzon, B. and S. Sazhin (2006). Convective vaporization of a fuel droplet with thermal radiation absorption. *Fuel 85*, 32–46.

Abramzon, B. and W. A. Sirignano (1989). Droplet vaporization model for spray combustion calculations. *Int. J. Heat Mass Transf. 32*, 1605–1618.

Acrivos, A. and T. D. Taylor (1962). Heat and mass transfer from single spheres in stokes flow. *Physics of Fluids 5*, 387–394.

Aggarwal, S. K., A. Y. Tong, and W. A. Sirignano (1984). A comparison of vaporization models in spray calculations. *AIAA Journal 22*, 1448–1457.

Alis, R. (2018). Simulation numérique directe de gouttes et de groupes de gouttes qui s'évaporent dans un écoulement laminaire ou turbulent.

Antoine, C. (1888). Tensions de vapeurs: nouvelle relation entre les tensions et les températures. *Comptes Rendus des Séances de l'Académie des Sciences 107*.

Antonov, D. V., G. V. Kuznetsov, S. S. Sazhin, and P. A. Strizhak (2022). Puffing/micro-explosion in droplets of rapeseed oil with coal micro-particles and water. *Fuel 316*, 123009.

Bader, A., P. Keller, and C. Hasse (2013). The influence of non-ideal vapor-liquid equilibrium on the evaporation of ethanol/iso-octane droplets. *International Journal of Heat and Mass Transfer 64*, 547–558.

Bellan, J. and K. Harstad (1987a, 1). Analysis of the convective evaporation of nondilute clusters of drops. *Int. J. Heat Mass Transf. 30*, 125–136.

Bellan, J. and K. Harstad (1987b). The details of the convective evaporation of dense and dilute clusters of drops. *International Journal of Heat and Mass Transfer 30*, 1083–1093.

Bellan, J. and M. Summerfield (1976). Quasi-steady gas phase assumption for a burning droplet. *AIAA Journal 14*, 973–975.

Bellan, J. and M. Summerfield (1978, 1). Theoretical examination of assumptions commonly used for the gas phase surrounding a burning droplet. *Combust. Flame 33*,

107–122.

Blanc, A. (1908). Recherches sur les mobilités des ions dans les gaz. *Journal de Physique Théorique et Appliquée 7*.

Bonanni, M. and M. Ihme (2022). Interaction of preferential evaporation and low-temperature chemistry in multicomponent counterflow spray flames. *Proceedings of the Combustion Institute 000*, 1–9.

Boniou, V., T. Schmitt, and A. Vié (2022). Comparison of interface capturing methods for the simulation of two-phase flow in a unified low-mach framework. *International Journal of Multiphase Flow 149*.

Both, A., D. Mira, and O. Lehmkuhl (2022). Evaporation of volatile droplets subjected to flame-like conditions. *International Journal of Heat and Mass Transfer 187*.

Bég, O. A., V. R. Prasad, B. Vasu, N. B. Reddy, Q. Li, and R. Bhargava (2011). Free convection heat and mass transfer from an isothermal sphere to a micropolar regime with soret/dufour effects. *International Journal of Heat and Mass Transfer 54*, 9–18.

Chauveau, C., X. Chesneau, and I. Gökalp (1995). High pressure vaporization and burning of methanol droplets in reduced gravity. *Advances in Space Research 16*, 157–160.

Chauveau, C., F. Halter, A. Lalonde, and I. Gökalp (2008). An experimental study on the droplet vaporization: effects of heat conduction through the support fiber.

Chiang, C. H., M. S. Raju, and W. A. Sirignano (1992). Numerical analysis of convecting, vaporizing fuel droplet with variable properties. *International Journal of Heat and Mass Transfer 35*, 1307–1324.

Cliffe, K. A. and D. A. Lever (1985). Isothermal flow past a blowing sphere. *International Journal for Numerical Methods in Fluids 5*, 709–725.

Coats, D. and F. Fendell (1968). Compressible slow viscous flow past a vaporizing droplet. *AIAA J. 6*, 1953–1960.

Coffee, T. P. and J. M. Heimerl (1981). Transport algorithms for premixed, laminar steady-state flames. *Combustion and Flame 43*, 273–289.

Daïf, A., M. Bouaziz, X. Chesneau, and A. A. Chérif (1998). Comparison of multicomponent fuel droplet vaporization experiments in forced convection with the sirignano model. *Experimental Thermal and Fluid Science 18*, 282–290.

Dombrovsky, L. A. and S. S. Sazhin (2003). A parabolic temperature profile model for heating of droplets. *Journal of Heat Transfer 125*.

Dombrovsky, L. A., S. S. Sazhin, E. M. Sazhina, G. Feng, M. R. Heikal, M. E. Bardsley, and S. V. Mikhalovsky (2001). Heating and evaporation of semi-transparent diesel fuel droplets in the presence of thermal radiation. *Fuel 80*, 1535–1544.

Downing, C. G. (1966). The evaporation of drops of pure liquids at elevated temperatures: Rates of evaporation and wet-bulb temperatures. *AIChE Journal 12*, 760–766.

e. V., V. (Ed.) (2010). *VDI Heat Atlas* (2nd ed.). Springer.

Ebrahimian, V. and C. Habchi (2011). Towards a predictive evaporation model for multi-component hydrocarbon droplets at all pressure conditions. *International*

Journal of Heat and Mass Transfer 54, 3552–3565.

Eckel, G., J. Grohmann, L. Cantu, N. Slavinskaya, T. Kathrotia, M. Rachner, P. L. Clercq, W. Meier, and M. Aigner (2019). Les of a swirl-stabilized kerosene spray flame with a multi-component vaporization model and detailed chemistry. *Combustion and Flame 207*, 134–152.

Eisenklam, P., S. A. Arunachalam, and J. A. Weston (1967). Evaporation rates and drag resistance of burning drops. *Symposium (International) on Combustion 11*, 715–728.

Faeth, G. M. (1968). Flame zone development of monopropellant droplets. *Combustion and Flame 12*, 411–416.

Faeth, G. M. (1977). Current status of droplet and liquid combustion. *Prog. Energy Combust. Sci. 3*, 191–224.

Fairbanks, D. F. and C. R. Wilke (1950). Diffusion coefficients in multicomponent gas mixtures. *Industrial & Engineering Chemistry 42*, 471–475.

Farrell, A. E., R. J. Plevin, B. T. Turner, A. D. Jones, M. O'Hare, and D. M. Kammen (2006). Ethanol can contribute to energy and environmental goals. *Science 311*, 506–508.

Fedorenko, R. M., D. V. Antonov, P. A. Strizhak, and S. S. Sazhin (2022). Time evolution of composite fuel/water droplet radii before the start of puffing/micro-explosion. *International Journal of Heat and Mass Transfer 191*, 122838.

Feng, Z. G. and E. E. Michaelides (2001). Heat and mass transfer coefficients of viscous spheres. *International Journal of Heat and Mass Transfer 44*, 4445–4454.

Filho, F. L. S., G. C. K. Filho, J. A. van Oijen, A. Sadiki, and J. Janicka (2019). A novel strategy to accurately represent the carrier gas properties of droplets evaporating in a combustion environment. *International Journal of Heat and Mass Transfer 137*, 1141–1153.

Filho, F. L. S., A. C. Santos, A. Vié, and G. C. K. Filho (2022). A new robust modeling strategy for multi-component droplet heat and mass transfer in general ambient conditions. *International Journal of Heat and Mass Transfer 194*, 123102.

Finneran, J. (2021). On the evaluation of transport properties for droplet evaporation problems. *International Journal of Heat and Mass Transfer 181*, 121858.

Finneran, J., C. P. Garner, and F. Nadal (2021). Deviations from classical droplet evaporation theory. *Proceedings of the Royal Society A: Mathematical, Physical and Engineering Sciences 477*.

Fredenslund, A., R. L. Jones, and J. M. Prausnitz (1975). Group-contribution estimation of activity coefficients in nonideal liquid mixtures. *AIChE Journal 21*, 1086–1099.

Frössling, N. (1938). Über die verdunstung fallender tropfen. *Gerlands Beitr. Zur Geophys 52*, 170–216.

Fuchs, N. A. (1959). Evaporation and droplet growth in gaseous media.

Fuller, E. N., K. Ensley, and J. C. Giddings (1969). Diffusion of halogenated hydrocarbons in helium. the effect of structure on collision cross sections. *Journal of Physical Chemistry 73*, 3679–3685.

Fuller, E. N. and J. Giddings (1965). A comparison of methods for predicting gaseous diffusion coefficients. *Journal of Chromatographic Science 3*, 222–227.

Fuller, E. N., P. D. Schettler, and J. C. Giddings (1966). A new method for prediction of binary gas-phase diffusion coefficients. *Industrial and Engineering Chemistry 58*, 18–27.

Giovangigli, V. (1991). Convergent iterative methods for multicomponent diffusion. *IMPACT of Computing in Science and Engineering 3*, 244–276.

Godsave, G. A. (1953). Studies of the combustion of drops in a fuel spray-the burning of single drops of fuel. *Symposium (International) on Combustion 4*, 818–830.

Gogos, G., S. Soh, and D. N. Pope (2003). Effects of gravity and ambient pressure on liquid fuel droplet evaporation. *International Journal of Heat and Mass Transfer 46*, 283–296.

Grace, J. and M. W. R. Clift (1978). *Bubbles, drops and particles*.

Gradinger, T. B. and K. Boulouchos (1998). A zero-dirnensional model for spray droplet vaporization high pressures and temperatures. *International Journal of Heat and Mass Transfer 9310*.

Habchi, C. and V. Ebrahimian (2012). Gravitational effects on multi-component droplet evaporation. *Microgravity Science and Technology 24*, 229–235.

Hadamard, J. M. (1911). Mouvement permanent lent d'une sphère liquide et visqueuse dans un liquide visqueux. *Comptes rendus hebdomadaires des séances de l ' Académie des sciences, Série B*.

Hamielec, A. E., T. W. Hoffman, and L. L. Ross (1967). Numerical solution of the navier-stokes equation for flow past spheres: Part i. viscous flow around spheres with and without radial mass efflux. *AIChE Journal 13*, 212–219.

Haywood, R. J., R. Nafziger, and M. Renksizbulut (1989). A detailed examination of gas and liquid phase transient processes in convective droplet evaporation. *Journal of Heat Transfer 111*, 495–502.

Hirschfelder, J. O. and C. F. Curtiss (1949). Flame propagation in explosive gas mixtures. *Third Symposium (International) on Combustion, Reinhold, New York*, 121–127.

Hougen, O. A., K. M. Watson, and R. A. Ragatz (1952). *Chemical Process Principles*. John Wiley and Sons, Inc.

Hubbard, G. L., V. E. Denny, and A. F. Mills (1975). Droplet evaporation: Effects of transients and variable properties. *Int. J. Heat Mass Transf. 18*, 1003–1008.

IEA (2021). World energy outlook 2021. *IEA Publications*, 15.

Jenny, P., D. J. E. M. Roekaerts, and N. Beishuizen (2012). Modeling of turbulent dilute spray combustion. *Prog. Energy Combust. Sci. 38*, 846–887.

Kallendorf, C., A. Fath, M. Oberlack, and Y. Wang (2015). Exact solutions to the interfacial surfactant transport equation on a droplet in a stokes flow regime. *Physics of Fluids 27*.

Klingenberg, R. B. B. W. E. S. E. N. L. D. J. (2015). *Introductory Transport Phenomena*. Wiley.

Kuerten, J. G. M. (2016). Point-particle dns and les of particle-laden turbulent flow -

a state-of-the-art review. *Flow, Turbulence and Combustion 97*, 689–713.

Langmuir, I. (1918). The evaporation of small spheres. *Physical Review 12*, 368–370.

Lapple, C. E. and C. B. Shepherd (1940). Calculation of particle trajectories. *Industrial and Engineering Chemistry 32*, 605–617.

Law, C. K. (1976). Multicomponent droplet combustion with rapid internal mixing. *Combustion and Flame 26*, 219–233.

Law, C. K., S. Prakash, and W. A. Sirignano (1977). Theory of convective, transient, multicomponent droplet vaporization. *Symposium (International) on Combustion 16*, 605–617.

Law, C. K., T. Y. Xiong, and C. Wang (1987). Alcohol droplet vaporization in humid air. *International Journal of Heat and Mass Transfer 30*, 1435–1443.

Linstrom, P. J. and W. G. Mallard (2014). *NIST Chemistry webBook, NIST Standard Reference Database Number 69*. National Institute of Standards and Technology.

Liu, L., Y. Liu, M. Mi, Z. Wang, and L. Jiang (2016). Evaporation of a bicomponent droplet during depressurization. *International Journal of Heat and Mass Transfer 100*, 615–626.

Liu, Z., M. Jia, X. Xi, H. Liu, and P. Yi (2022). Simulation of the evaporation/boiling transition for the vaporization of a bi-component droplet under wide-temperature environments. *International Journal of Heat and Mass Transfer 193*.

Lupo, G. and C. Duwig (2018). A numerical study of ethanol-water droplet evaporation. *Journal of Engineering for Gas Turbines and Power 140*, 1–9.

Marmottant, P. H. and E. Villermaux (2004). On spray formation. *Journal of Fluid Mechanics 498*, 73–111.

Mason, E. A. and T. R. Marrero (1970). The diffusion of atoms and molecules. *Advances in Atomic and Molecular Physics 6*.

Maxwell, J. C. (1877). Diffusion. *Encyclopaedia Britannica 7*, 214–221.

McIntosh, A. C., V. Gol'dshtein, I. Goldfarb, and A. Zinoviev (1998). Thermal explosion in a combustible gas containing fuel droplets. *Combustion Theory and Modelling 2*, 153–165.

Mercier, D. (2021). Large eddy simulation of coupled dispersed phase flows : a statistically-consistent formalism.

Mesquita, L. C. C. (2021). Simulation and analysis of the shape, performance, and stability of flames in a two-stage lean-burn aeronautical combustor.

Michaelides, E. E. (2006). *Particles, bubbles and drops: Their motion, heat and mass transfer*. World Scientific.

Miller, R. S., K. Harstad, and J. Bellan (1998). Evaluation of equilibrium and non-equilibrium evaporation models for many-droplet gas-liquid flow simulations. *International Journal of Multiphase Flow*.

Mohr, S. H., J. Wang, G. Ellem, J. Ward, and D. Giurco (2015). Projection of world fossil fuels by country. *Fuel 141*, 120–135.

Morsi, S. A. and A. J. Alexander (1972). An investigation of particle trajectories in two-phase flow systems. *Journal of Fluid Mechanics 55*, 193–208.

Neufeld, P. D., A. R. Janzen, and R. A. Aziz (1972). Empirical equations to calcu-

late 16 of the transport collision integrals omega(l,8)* for the lennard-jones (12-6) potential. *The Journal of Chemical Physics 57*, 1100–1102.

Newbold, F. R. and N. R. Amundson (1973). A model for evaporation of a multicomponent droplet. *AIChE Journal 19*, 22–30.

Oliver, D. L. and J. N. Chung (1987). Flow about a fluid sphere at low to moderate reynolds numbers. *Journal of Fluid Mechanics 177*, 1–18.

O'rourke, P. J. and A. A. Amsden (1987). The tab method for numerical calculation of spray droplet breakup international fuels and lubricants meeting and exposition toronto, ontario. *SAE Technical Paper Series 872089*, 12.

Oseen, C. W. (1910). Über die stokes'sche formel, und über eine verwandte aufgabe in der hydrodynamik. *Ark. f. Mat. Astr. og Fys 6*.

Pinheiro, A. P. and J. M. Vedovoto (2019). Evaluation of droplet evaporation models and the incorporation of natural convection effects. *Flow, Turbulence and Combustion 102*, 537–558.

Poinsot, T. and D. Veynante (2012). *Theoretical and Numerical Combustion* (3 ed.).

Poling, B., J. M. Prausnitz, and J. P. O'Connell (2001). *The properties of gases and liquids* (5th ed.). McGRAW-HILL.

Proudman, I. and J. R. Pearson (1957). Expansions at small reynolds numbers for the flow past a sphere and a circular cylinder. *Journal of Fluid Mechanics 2*, 237–262.

Putnam, A. (1961). Integratable form of droplet drag coeficient. *ARS J. 31*, 1467–1468.

Ranz, W. E. and W. R. Marshall (1952). Evaporation from drops i. *Chemical Engineering Progress 48*, 141–146.

Renksizbulut, M. and R. J. Haywood (1988). Transient droplet evaporation with variable properties and internal circulation at intermediate reynolds numbers. *International Journal of Multiphase Flow 14*, 189–202.

Renksizbulut, M., R. Nafziger, and X. Li (1991). A mass transfer correlation for droplet evaporation in high-temperature flows. *Chemical Engineering Science 46*, 2351–2358.

Renksizbulut, M. and M. C. Yuen (1983a). Experimental study of droplet evaporation in a high-temperature air stream. *Journal of Heat Transfer 105*, 384–388.

Renksizbulut, M. and M. C. Yuen (1983b). Numerical study of droplet evaporation in a high-temperature stream. *Journal of Heat Transfer 105*, 389–397.

Renon, H. and J. Prausnitz (1968). Local compositions in thermodynamic excess functions for liquid mixtures. *AICHE Journal 14*, 135–144.

Reveillon, J. and L. Vervisch (2005). Analysis of weakly turbulent dilute-spray flames and spray combustion regimes. *Journal of Fluid Mechanics 537*, 317–347.

Rodgers, R. C. and G. E. Hill (1978). Equations for vapour pressure versus temperature: Derivation and use of the antoine equation on a hand-held programmable calculator. *British Journal of Anaesthesia 50*, 415–424.

Rybczynski, W. (1911). Über die fortschreitende bewegung einer flüssigen kugel in einem zähen medium. *Bull. Acad. Sci. Cracovie A*, 40–46.

Saboni, A. and S. Alexandrova (2002). Numerical study of the drag on a fluid sphere. *AIChE Journal 48*, 2992–2994.

Saboni, A., S. Alexandrova, A. M. Spasic, and C. Gourdon (2007). Effect of the viscosity ratio on mass transfer from a fluid sphere at low to very high peclet numbers. *Chemical Engineering Science 62*, 4742–4750.

Sanchez, P. S. (2012). Modeling the dispersion and evaporation of sprays in aeronautical combustion chambers.

Sandler, S. I. and E. A. Mason (1968). Kinetic-theory deviations from blanc's law of ion mobilities. *The Journal of Chemical Physics 48*, 2873–2875.

Santos, A. C., F. L. S. Filho, and A. Vié (2021). Sensitivity analysis of droplet evaporation to convection effects modelling. *International Conference on Liquid Atomization and Spray Systems (ICLASS) 1*.

Sazhin, S. (2014). *Droplets and sprays* (1 ed.). Springer.

Sazhin, S. S. (2006). Advanced models of fuel droplet heating and evaporation. *Progress in Energy and Combustion Science 32*, 162–214.

Sazhin, S. S. (2017). Modelling of fuel droplet heating and evaporation: Recent results and unsolved problems. *Fuel 196*, 69–101.

Sazhin, S. S., A. E. Elwardany, E. M. Sazhina, and M. R. Heikal (2011). A quasi-discrete model for heating and evaporation of complex multicomponent hydrocarbon fuel droplets. *International Journal of Heat and Mass Transfer 54*, 4325–4332.

Sazhin, S. S., G. Feng, M. R. Heikal, I. Goldfarb, V. Gol'dshtein, and G. Kuzmenko (2001, 3). Thermal ignition analysis of a monodisperse spray with radiation. *Combustion and Flame 124*, 684–701.

Sazhin, S. S., I. G. Gusev, P. A. Krutitskii, and M. R. Heikal (2011). Transient heating of a semitransparent spherical body immersed into a gas with inhomogeneous temperature distribution. *International Journal of Thermal Sciences 50*, 1215–1222.

Sazhin, S. S., P. A. Krutitskii, W. A. Abdelghaffar, E. M. Sazhina, S. V. Mikhalovsky, S. T. Meikle, and M. R. Heikal (2004). Transient heating of diesel fuel droplets. *Int. J. Heat Mass Transf. 47*, 3327–3340.

Sazhin, S. S., P. A. Krutitskii, S. B. Martynov, D. Mason, M. R. Heikal, and E. M. Sazhina (2007). Transient heating of a semitransparent spherical body. *International Journal of Thermal Sciences 46*, 444–457.

Schiller, L. and Z. Naumann (1935). A drag coefficient correlation. *VDI Zeitung 77*, 318–320.

Schlichting, H. and K. Gersten (2017). *Boundary-Layer Theory* (9th ed.). Springer.

Schwarz, J. and J. Smolík (1994). Mass transfer from a drop-i. experimental study and comparison with existing correlations. *International Journal of Heat and Mass Transfer 37*, 2139–2143.

Shastry, V., Q. Cazeres, B. Rochette, E. Riber, and B. Cuenot (2021). Numerical study of multicomponent spray flame propagation. *Proceedings of the Combustion Institute 38*, 3201–3211.

Snegirev, A. Y. (2013). Transient temperature gradient in a single-component vaporizing droplet. *International Journal of Heat and Mass Transfer 65*, 80–94.

Spalding, D. B. (1953). The combustion of liquid fuels. *Symposium (international) on combustion 4*, 847–864.

Stokes, G. G. (1850). On the effect of the internal friction of fluids on the motion of pendulums. *Transactions of the Cambridge Philosophical Society 9*, 8.

Talbot, P., B. Sobac, A. Rednikov, P. Colinet, and B. Haut (2016). Thermal transients during the evaporation of a spherical liquid drop. *International Journal of Heat and Mass Transfer 97*, 803–817.

Tonini, S. and G. E. Cossali (2012). An analytical model of liquid drop evaporation in gaseous environment. *International Journal of Thermal Sciences 57*, 45–53.

Tonini, S. and G. E. Cossali (2015). A novel formulation of multi-component drop evaporation models for spray applications. *International Journal of Thermal Sciences 89*, 245–253.

Tonini, S. and G. E. Cossali (2016). A multi-component drop evaporation model based on analytical solution of stefan-maxwell equations. *International Journal of Heat and Mass Transfer 92*, 184–189.

Tonini, S. and G. E. Cossali (2022). An analytical model for the evaporation of multi-component spheroidal drops based on stefan–maxwell equations. *International Journal of Thermal Sciences 171*, 107223.

Troncoso, A. B. and E. Acosta (2015). The unifac model and the partition of alkyl and alkylphenol ethoxylate surfactants in the excess phases of middle phase microemulsions. *Fluid Phase Equilibria 397*, 117–125.

Verwey, C. and M. Birouk (2018). Experimental investigation of the effect of natural convection on the evaporation characteristics of small fuel droplets at moderately elevated temperature and pressure. *International Journal of Heat and Mass Transfer 118*, 1046–1055.

Voutsas, E., V. Louli, C. Boukouvalas, K. Magoulas, and D. Tassios (2006, 3). Thermodynamic property calculations with the universal mixing rule for eos/ge models: Results with the peng-robinson eos and a unifac model. *Fluid Phase Equilib. 241*, 216–228.

Wagner, W. (1973). New vapour pressure measurements for argon and nitrogen and a new method for establishing rational vapour pressure equations. *Cryogenics 13*, 470–482.

Wegener, M., N. Paul, and M. Kraume (2014). Fluid dynamics and mass transfer at single droplets in liquid/liquid systems. *International Journal of Heat and Mass Transfer 71*, 475–495.

Whitaker, S. (1972). Forced convection heat transfer correlations for flow in pipes, past flat plates, single cylinders, single spheres, and for flow in packed beds and tube bundles. *AIChE Journal 18*, 361–371.

Wilke, C. R. and C. Y. Lee (1955). Estimation of diffusion coefficients for gases and vapors. *Ind. Eng. Chem. 47*, 1253–1257.

Williams, F. A. (1960). On the assumptions underlying droplet vaporization and combustion theories. *The Journal of Chemical Physics 33*, 133–144.

Williams, F. A. (2018). *Combustion theory: The fundamental theory of chemically reacting flow systems, second edition.*

Wood, B. J., H. Wise, and S. H. Inami (1960). Heterogeneous combustion of multi-

component fuels. *Combustion and Flame 4*, 235–242.

Yuen, M. C. and L. W. Chen (1976). On drag of evaporating liquid droplets. *Combustion Science and Technology 14*, 147–154.

Zhang, L. and S.-C. Kong (2012). Multicomponent vaporization modeling of bio-oil and its mixtures with other fuels. *Fuel 95*, 471–480.